Universiteit Gent
Faculteit Wetenschappen
Vakgroep Anorganische en Fysische Chemie
Faculteit Ingenieurswetenschappen en Architectuur
Vakgroep Informatietechnologie

Optische eigenschappen van silicium-op-isolator-golfgeleiders gefunctionaliseerd met colloïdale ’quantum dots’

Optical properties of colloidal quantum dot functionalized silicon-on-insulator waveguides

---

Abdoulghafar Omari

Proefschrift tot het bekomen van de graad van
Doctor in de Ingenieurswetenschappen:
Toegepaste Natuurkunde
Academiejaar 2014-2015

Promotoren:

Prof. Dr. Ir. Zeger Hens	Universiteit Gent, Anorganische en fysische chemie
Prof. Dr. Ir. Dries Van Thourhout	Universiteit Gent, INTEC

Overige leden van de examencomissie :

Prof. Dr. Ir. Rik Van de Walle	Universiteit Gent, ELIS
Prof. Dr. Ir. Edouard Brainis	Universiteit Gent, Anorganische en fysische chemie
Prof. Dr. Ir. Kristiaan Neyts	Universiteit Gent, ELIS
Prof. Dr. Ir. Pascal Kockaert	Université Libre de Bruxelles
Dr. Ir. Iwan Moreels	Italian Institute of Technology

Universiteit Gent
Faculteit Wetenschappen
Vakgroep Anorganische en Fysische Scheikunde
Krijgslaan 281, S3
B-9000 Gent, België

Vakgroep Informatietechologie
Sint-Pietersnieuwstraat 41
B-9000 Gent, België

Dit werk kwam tot stand in het kader van een specialisatiebeurs van het IWT-Vlaanderen (Instituut voor de aanmoediging van Innovatie door Wetenschap en Technologie in Vlaanderen).

Aan ieder wie ik elk succes in mijn leven te danken heb

Dankwoord

Al het werk dat gedaan is doorheen al deze jaren zou niet succesvol verlopen zijn zonder hulp van bepaalde personen. Ten eerste wil ik mijn promotoren bedanken voor hun vertrouwen en om mij de vrijheid gegeven te hebben om dit werk tot een mooi einde te kunnen brengen. Zeger, jouw manier van aanpak, inzicht, uitleg en vooral jouw formidabele overtuigingskracht zijn zaken die ik niet zal vergeten. Dries bedankt om er altijd klaar te zijn met jouw inzichten en deskundige kennis als ik die nodig had. Verder wil ik alle overige leden bedanken van mijn comissie voor het lezen en evalueren van mijn thesis. Jullie commentaren zijn waardevol geweest om de kwaliteit van deze thesis te verbeteren. Daarvoor dank aan Prof. Edouard Brainis, Prof. Kristiaan Neyts, Prof. Pascal Kockaert, waar de vruchtbare samenwerking rond de niet-lineaire optische eigenschappen van de quantum dots mijn horizon in dit veld enorm heeft verbreed en Dr. Iwan Moreels, vriend en mentor, je was en bent nog altijd een enorme bron van inspiratie!

Bij het begin van een doctoraat lijkt alles op een kluwen, ik moest bij vele zaken van nul beginnen en niets was een sinecure. Alhoewel, de fascinatie voor nanokristallen was voor mij al begonnen tijdens mijn masterjaar. Daar ontdekte ik de wereld van deze kleine, haast atomaire deeltjes die verschillende kleuren kunnen stralen, met enorme mogelijkheden en waarmee je soms boeiende experimenten kan uitvoeren. Na mijn masterjaar werd ik nog meer geboeid. Het leek wel op een avontuur in verschillende domeinen : scheikunde, fysica, ingenieurstechnieken en dus besloot ik een beurs aan te vragen bij het IWT en heb ik meegedaan aan de selectieprocedure. Toen het bleek dat ik mijn beurs kreeg voor het project was ik vertrokken. In het begin was ik niet altijd wel-geëquipeerd met de juiste manier van handelen en moeilijkheden zijn onvermijdelijk. Toch zat ik in een team waar altijd mensen met inspirerende en creatieve oplossingen afkomen. Hereby, I would like to thank Kamal, who learned me how to synthesize CdTe nanocrystals. Yolanda, thanks for the many help with the synthesis of PbS nanocrystals. Verder wil ik al mijn vrienden en collega's bedanken van mijn groep FCN - Fysica en chemie van nanogestructureerde materialen. Sofie, bedankt voor jouw enorme enthousiasme en voor de vele hulp als ik die nodig had. Stijn, bedankt voor de leuke sfeer op kantoor. Pieter, bedankt voor de pertinente discussies en als tof gezelschap op reis. Furthermore, I would like to thank : Ruben, Chen, Antoine, Tangi, Kim, Elena, Kishu, Michael en Suzanne for the many nice moments together. To the 'new' members : Dorian, Willem en Emile, I don't know you that much, thanks for the short moments together and you are very welcome. It is clear that this group will further grow and flurish. Hereby I would like to thank the people who left the group, but where we had many discussions and fantastic moments together : Marco, Antti, Marina, Karel, Bram, Raquel, ...

In de Sterre zijn er nog tal van mensen die ik wil bedanken en die elk op hun manier hebben bijgedragen tot dit doctoraatswerk: Yu, Pat, Philip, Bart (altijd paraat voor technische ondersteuning), Pierre, Claudine en An (jullie zorden ervoor dat ik mij nooit zorgen hoefde te maken om de paperassen).

At the Photonics Research Group, a fantastic place where humor, outstanding science and deadly seriousness goes together, I have experienced many unforgettable moments and I wish to thank here many friends and colleagues : Bin en Zhechao for your help with the optical parts, Gunay for the many jokes together and to be there to help me with my measurement set-ups, Liesbet voor de oneindig vele SEM plaatjes, Jan-Willem, Jesper, Alfonso, Daan (jullie zijn allemaal aangename bureaugenoten), Sarvagya, Ananth, Bendix, Ashim, Jing, Kristien (excellent internet fixer), Weiqiang, Yunpeng, Dorian, Andrea, Sam en Pauline, Youssef and people come and go in this talented group and the list is endless : Ilses, Jeroen, Nannicha, Andrew, Pijush, Raphael, Bart, Eva, Amin en Leila, Stevan, Aditya, Antonio, Michael, Nebiyu, Rajesh, Steven, Francois, Peter Guns, Martin, ... Verder wil ik hierbij nog alle proffen bedanken (Roel, Wim, Gunter, Peter, Geert en Nicolas) voor hun toegankelijkheid en hulp tot oplossingen bij moeilijkheden.

Nu een doctoraat kan nooit succesvol verlopen zonder de nodige samenwerkingen. Hierbij wil ik nog bedanken : Prof. Rik Van Deun voor het gebruik van de fotoluminescentieopstelling, Dr. Francesco Masia van de Universiteit in Cardiff voor de FWM metingen en Said Rodriguez van de Philips Research Laboratories om mij te introduceren tot de wereld van plasmonische materialen. Verder bedankt aan Epixfab voor de fabrikage van mijn ontworpen optische chips en aan het IWT voor het steunen van mijn project.

Tot slot, *'last but not least'* wil ik mijn al mijn vrienden en familie zeer warm bedanken en speciaal mijn ouders voor hun oneindige steun en begrip. Dikke merci nog aan mijn zussen en broers.

Gent, November 2014
Abdoulghafar Omari

Contents

List of Figures **17**

List of Tables **21**

1 Introduction **47**

- 1.1 Introduction 47
- 1.2 Colloidal quantum dots 49
  - 1.2.1 Quantum confinement 51
  - 1.2.2 Colloidal heterostructured quantum dots 51
  - 1.2.3 Optical properties 54
- 1.3 Silicon photonics 55
  - 1.3.1 Silicon on insulator (SOI) 55
  - 1.3.2 Functionalization of SOI 56
- 1.4 Objective of this work 58
  - 1.4.1 Outline 59

Bibliography **61**

2 Synthesis of CdTe, PbS and PbS/CdS quantum dots **67**

- 2.1 Introduction 67
  - 2.1.1 The hot injection synthesis 67
  - 2.1.2 Quantum dots synthesized in this work 68
- 2.2 Synthesis of CdTe QDs 69
  - 2.2.1 Synthesis procedure 69
  - 2.2.2 Basic material properties 74
  - 2.2.3 An extended sizing curve 75

2.2.4 Extinction coefficients 77
2.2.5 Stability under ambient atmosphere 78
2.3 Synthesis of PbS QDs 78
2.3.1 Synthesis procedure 80
2.3.2 Basic material properties 82
2.3.3 Sizing curve 82
2.3.4 Extinction coefficients 82
2.3.5 Stability under ambient atmosphere 83
2.4 Synthesis of PbS/CdS QDs 83
2.4.1 Synthesis procedure 83
2.4.2 Basic material properties 84
2.4.3 Sizing curve 85
2.4.4 Extinction coefficients 85
2.4.5 Stability under ambient atmosphere 86
2.5 Conclusion 86

Bibliography **87**

3 Linear optical properties of multishell and graded shell quantum dots 91
3.1 Introduction 91
3.2 Theory 94
3.2.1 Maxwell-Garnett theory for μ 94
3.2.2 Local field factor of multi- and graded shell QDs 96
3.2.3 μ solution for a multishell QD 100
3.3 Absorption coefficient of CdTe QDs 105
3.3.1 μ at short wavelengths 105
3.3.2 μ at the bandgap 107
3.4 Absorption coefficient of CdSe/ CdSe$_x$S$_{1-x}$/ CdS QDs . 111
3.4.1 Diffusion induced alloying 111
3.4.2 μ at short wavelengths 113
3.5 Conclusion 115

Bibliography **117**

4 Nonlinear optical properties of PbS quantum dots 123
4.1 Introduction . . . 123
4.2 Analysis of non-linear optical properties by Z-scan . . . 125
4.2.1 Set-up and beam characterization . . . 125
4.2.2 Derivation of n_2 and β from the Z-scan traces . . . 127
4.2.3 Thermal effects . . . 128
4.3 Nonlinear refraction n_2 and β for PbS QDs . . . 129
4.3.1 Fabricated samples . . . 129
4.3.2 Excluding thermal effects . . . 131
4.3.3 Analyzing n_2 and β . . . 133
4.4 Simulation of the QD exciton population . . . 136
4.4.1 Bandgap exciton population of the QDs . . . 136
4.4.2 Occupancy rate equations . . . 137
4.5 Intensity dependence of the absorption coefficient (α) . . . 140
4.6 Four Wave Mixing (FWM) . . . 142
4.7 Dynamics of optical nonlinearities in PbS QDs . . . 144
4.8 Discussion . . . 148
4.9 Two photon absorption coupled nonlinearities . . . 149
4.10 Conclusions . . . 152

Bibliography 155

5 Optical properties of hybrid quantum dots waveguides 163
5.1 Introduction . . . 163
5.2 Hybrid QD/PWGs . . . 165
5.2.1 Fabrication . . . 165
5.2.2 Measurements . . . 170
5.2.3 Numerical description . . . 174
5.2.4 Simulations . . . 182
5.3 Hybrid QD/SWGs . . . 184
5.3.1 Fabrication . . . 184
5.3.2 Measurements . . . 186
5.3.3 Numerical description . . . 190
5.3.4 Simulations . . . 191

5.4 Conclusions 199

Bibliography **203**

6 Prospects of colloidal quantum dot absorption for photonic applications 207

6.1 Introduction 207

6.2 Light propagation in a dielecric medium 210

6.2.1 Maxwell's equations 211

6.2.2 Eigenmodes of a waveguide 212

6.3 Wavelength conversion 214

6.3.1 Wavelength conversion on SOI 214

6.3.2 Important parameters 216

6.4 Microsecond wavelength conversion 219

6.4.1 Occupancy rate equations 219

6.4.2 Figure of merit 221

6.4.3 Modulation Depth 221

6.5 Picosecond wavelength conversion 222

6.5.1 Occupancy rate equations 222

6.5.2 Figure of merit 225

6.5.3 Modulation Depth 228

6.5.4 Distribution of QD-excitons after a pulse 229

6.5.5 Condition of stable operation 232

6.5.6 Influence of the waveguide on the convertor . . . 233

6.6 Conclusion 236

Bibliography **237**

7 Colloidal QDs for plasmon applications **239**

7.1 Introduction 239

7.1.1 Rationale 239

7.1.2 Plasmonic phenomena 241

7.2 Experimental near field enhancement in gold nanoanttena arrays 243

7.2.1 Fabrication of the nanoantennas 243

7.2.2 Measurement of the near and far field extinction 244

7.2.3 Measurement of the photoluminescence enhancement 246

7.3 Simulations of the near field enhancement in plasmon arrays 247
  7.3.1 Simulation domain 247
  7.3.2 Simulation of the near field intensity enhancement 248
  7.3.3 Controlling the near field intensity enhancement 249
  7.3.4 Field profile at the anti-crossing condition 251
7.4 Conclusion 251

Bibliography 255

8 General conclusion 259
8.1 Conclusion 259
  8.1.1 Synthesis 259
  8.1.2 Linear optical properties 260
  8.1.3 Nonlinear optical properties 261
  8.1.4 Light absorption in hybrid/SOI waveguides . . . 262
8.2 Prospects 263

List of Publications 265

A Molar extinction coefficient of core/shell nanocrystal suspensions 269

List of Figures

1 PbS/CdS QD-spectrum and weergave van de QD/bedekte PWG 28
2 Weergave van de dwarsdoorsnede van het gesimuleerde elektrisch veld 30
3 PbS/CdS QD spectrum and representation of the QD/coated PWG 36
4 Cross-sectional representation of the simulated electric field 37

1.1 TEM image of PbSe QDs and series of PbSe absorption spectra 50
1.2 Series of CdSe QDs showing the change in emission color from red to blue 52
1.3 Structure of a CdSe core/(multi-)shell QD 53
1.4 Silicon-on-insulator layer structure of an (un)processed wafer ... 56
1.5 Various waveguide cross sections of different material shapes ... 57

2.1 Schematic illustrating the stages of nucleation and growth 69
2.2 Scheme depicting the synthesis of CdTe QDs 71
2.3 Synthesis of CdTe QDs at low injection temperature of 280°C ... 73
2.4 TEM image of large zb-CdTe QDs 73
2.5 Absorption spectra of CdTe nanocrystals with diameters ... 76
2.6 Series of CdTe spectra taken at different times during storage ... 79
2.7 Wavelength position of the first 1S-1S aborption peak of PbS QDs ... 80
2.8 TEM image of 6.2 nm PbS/CdS core/shell QDs 84

3.1 A schematic of a N-layered multishell dielectric particle presented ... 96
3.2 Partitioning or allocation of the boundarieso of a multilayered particle 103
3.3 Intrinsic absorption coefficient of different sized CdTe QDs ...108
3.4 Absorption coefficient at the bandgap as a function of the QD diameter 109
3.5 An ideal core/shell CdSe/CdS particle through which diffusion ...112
3.6 Intrinsic absorption coefficients for CdSe/CdSe$_x$S$_{1-x}$/CdS QDs 114
3.7 The experimental intrinsic absorption coefficient of CdSe/CdS QDs 116

4.1 Schematic representation of the Z-scan setup 127
4.2 Typical experimental OAI traces for PbS QDs 132
4.3 Intensity dependence of OAI for different samples 134
4.4 n_2-spectra around 1550 nm. λ_0 denotes the absorption peak ...134
4.5 The magnitude of β decreases with increasing I_0 135
4.6 Dependence of the nonlinear absorption on the intensity ...139
4.7 Schematic representation of the FWM setup 143
4.8 FWM field as a function of the averaged excitations per QD per pulse 145
4.9 Schematic of a thick z-scan experiment 151
4.10 Simulation of the TBI for a thick nonlinear medium 153

5.1 Cross sections of various silicon-on-insulator waveguides 164
5.2 Langmuir-Blodgett principle 166
5.3 LB-isotherms at surface pressures of 18 and 30mN/m . . 169
5.4 AFM profile of the LB deposition showing a sub-monolayer 169
5.5 Cartoon representation of the opitcal field coupled to the PWG 171
5.6 Enlarged SEM image of the PWG coated by a QD monolayer 172
5.7 Absorbance as a function of the of the strip length difference 173
5.8 Exp. absorption coefficient for a QD monolayer to a QD 7-layer 174
5.9 Replacement of the real QD film by an effective medium 175
5.10 The dielectric function of the core (PbS) of PbS/CdS QDs 179
5.11 QDs as point particles surrounded by an infinite extending host 181
5.12 Fourier image of the monolayer yields a hexagonal diffraction pattern 183
5.13 Cross-sectional representation of the simulated electric field 184
5.14 Comparison of the exp. and simulated absorption spectrum 185
5.15 Absorption spectra of the PWGs coated quantum dot multi-layers 186
5.16 SEM images of various QD coated strip waveguides . . . 187
5.17 Optical microscopy image of a sample with strip waveguides 188
5.18 Illustratinon of a monolayer conformally covering the SWGs 192
5.19 Simulated absorption coefficients for different layer parameters 195
5.20 Photoluminescence spectrum of the PbS/CdS QDs used in this work 196
5.21 Coupling efficiency η and $\frac{\eta QY}{2}$ as a function of the wavelength 198

6.1 Schematic illustration of managing a large network . . . 210
6.2 QD-coated strip waveguide illustrating the wavelength conversion 215

6.3 Figure of merit for the QD-wavelength convertor 218
6.4 The fraction of QDs with i excitons (c_i) as a function of time 224
6.5 The average number of excitons, DAR and FOM of an excited QD-layer 226
6.6 The distribution of the number of excitons i created after pulse 230

7.1 An array of gold nanorods on a glass substrate 244
7.2 Experimental dispersion relations for the nanoantenna array 245
7.3 Zeroth-order (a) transmittance T_0 (b) reflectance R_0 . . . 250
7.4 Zeroth-order transmittance T_0 and NFIE 252
7.5 Field enhancement and real part of the scattered field . . 252

A.1 Prefactor as function of the shell to the total volume ratio 272

List of Tables

2.1 CdTe QDs ICP-MS data... 75

3.1 CdTe size, ICP-MS, RBS and absorbance data 106
3.2 The core and total size of the CdSe/CdSe$_x$S$_{1-x}$/CdS alloyed QDs 113
3.3 CdSe and CdSe/CdSe ICP-MS data 115

4.1 n_2, β and figure of merit FOM for typical materials . . . 126
4.2 Summary of different samples used for the Z-scan and FWM experiments 130

5.1 The summarized properties of PbS/CdS core/shell samples used ... 201

6.1 The used time constants for implementing in the occupancy rate equations 222
6.2 Modulation depths of the wavelength convertor 228

Nederlandstalige samenvatting – Summary in Dutch –

Zoals de titel aanwijst, behandelen we in dit doctoraal onderzoek de optische eigenschappen van *colloïdale 'quantum dots'* voor geïntegreerde *silicium-fotonica*. Fotonica, of de studie van licht (fotonen) op de micro- en nanoschaal, speelt een belangrijke rol in de wereldwijde telecommunicatie. Optische vezels – werkpaard van het internet – hebben een potentieel om een gigantische hoeveelheid informatie met een grote bandbreedte te transporteren in de vorm van fotonpaketten. Deze capaciteit is echter momenteel beperkt door de componenten die de informatie verzenden, ontvangen en verwerken aan beide vezeleinden. Om succesvol te zijn, moeten deze systemen naast snelheid, meerdere functionaliteiten voorzien binnen een compacte grootte. Om deze doelstelling van miniaturizatie en performantie te bekomen, zijn on-chip-lage-kost-platformen vereist.

In deze context, bieden geïntegreerde fotonische schakelingen (PICs) op basis van silicium – onderzoeksgebied gekend als silicium-fotonica – uitgebreide mogelijkheden. Deze componenten zijn gebouwd op een silicium-op-isolator (SOI) platform, hetgeen toelaat dat licht geleid wordt door het hoge brekingsindexcontrast tussen het silicium en siliciumdioxide. Dit hoge brekingsindexcontrast resulteert in een hoge opsluiting van het licht en laat toe om zeer compacte golfgeleiders te produceren met een hoge dichtheid per eenheidsoppervlakte. Bijgevolg, kunnen we fotonische schakelingen bouwen, die dicht-geïntegreerd en zeer functioneel zijn.

Behalve compactheid, worden SOI-componenten gemaakt met dezelfde productietechnologie voor elektronische schakelingen(CMOS), die een revolutie teweegbrachten gedurende de afgelopen decennia, en dus heeft silicium-fotonica het potentieel om de infrastructuur van de CMOS-fabrikage tenvolle te benutten. Deze drijfkracht laat toe dat silicium-fotonica kosteneffectief wordt met betrekking tot materialen, componenten en energieverbruik. Silicium gebaseerde materialen hebben echter het nadeel dat ze moeilijk licht kunnen genereren nodig voor actieve componenten (lasers, LEDs, ...). Verder vertonen deze lage niet-lineaire optische eigenschappen, die nodig zijn voor optische signaalverwerking (routers, interconnects, ...). In dit opzicht, worden nieuwe manieren ontwikkelt om actieve en (passieve) niet-lineaire optische materialen te integreren met silicium en staan bekend als hybride technologieën. Een veelbelovende kandidaat onder die hybride technologieën zijn colloïdale ’quantum dots’ (QDs) geïntegreerd op SOI.

Colloïdale halfgeleider ’quantum dots’ of nanokristallen zijn een nieuwe klasse van mterialen, waarvan de fysische en materiaaleigenschappen sterk afhangen van hun grootte (2-20 nm), vorm, oppervlak en de kristalstructuur. Een belangrijke voordeel van QDs is hun flexibiliteit. De elektro-optische eigenschappen kunnen aangepast worden aan de toepassing - passief of actief - en integratie in SOI maakt gebruik van eenvoudige, natte technieken die grotendeels substraatonafhankelijk zijn. Daartegenover staat dat de technologie in zijn kinderschoenen staat. Alhoewel het potentieel van de techniek is aangetoond, is er op dit moment geen standaard materiaalsysteem voor de deklagen en moeten er nog vele hinderpalen overwonnen worden om de stap van materialen naar componenten te vergemakkelijken.

In deze samenvatting geven we een overzicht van de belangrijkste resultaten in de volgende onderzoeksgebieden : QD-fabrikage (synthese), optische eigenschappen van QDs, integratie van QDs met het SOI-platform en QD-fotonische toepassingen.

Colloïdale quantum dot synthese

Colloïdale ’quantum dots’ zijn gesynthethiseerd op basis van natte chemische procedures, waarbij specifiek de hete-injectie aanpak leidt to zeer monodisperse suspensies van nanokristallen. Deze procedure baseert zich op het gebruik van precursoren en liganden om de nucleatie en groei van nanokristallen te controleren en de resulterende suspensies te stabiliseren door sterische hindering. Sinds de introductie in 1993 voor de synthese van cadmium-chalcogenide nankristallen (CdS, CdSe en CdTe QDs), is de hete-injectie methode een gevestigde procedure geworden, die wijdverspreid gebruikt wordt.

In dit proefschrift, synthetiseren we colloïdale ’quantum dots’ aangepast voor toepassingen in de niet-lineaire optica in combinatie met het fotonische silicium-op-isolator platform, *i.e.*, in het golflengtegebied 1300-1600 nm. Dit betrekt materialen zoals PbS en PbS/CdS QDs – waarbij de bandgaptransitie afgestemd wordt op de fotonenergie – of CdTe QDs – waar de fotonenergie overeenstemt met de helft van de bandgapenergie.

In deze context, maken we CdTe QDs met diameters, die variëren van 3 tot 11 nm, gebruikmakend van de hete-injectie methode. De bandgap is afstembaar tussen 500 nm en 760 nm of 1.6 en 2.48 eV. De grote nanokristallen (7-11 nm) verkrijgen we door gebruik te maken van de continue injectie van precursoren bij een gecontroleerde reactietijd, om zo Ostwaldrijpening te mijden. Dankzij deze inspanningen construeren we de ’sizing curve’ van de CdTe QDs door een combinatie van UV-vis-absorptiespectroscopie en TEM-beeldvorming. Bovendien, synthetiseren we PbS kern PbS/CdS kern/schil QDs gebruikmakend van de hete-injectie methode. We verkijgen nanokristaldiameters van 2.5 t.e.m. 7.5 nm met absorptiepieken in het gebied 800-200 nm of 0.62-1.5 eV.

Optische eigenschappen van QDs

We analyseren de absorptiecoëfficiënt van CdTe QDs door combinatie van UV-vis-absorptiespectroscopie en elementen-analyse. Bij een korte golflengte van 410 nm, vertoont de intrinsieke absorptiecoëfficiënt geen kwantumopsluitings-effecten en de verkregen waarden zijn in goede overeenstemming met de bulkwaarde van CdTe. Het gemiddelde van deze waarden kan gebruikt worden als een betrouwbare standaard voor de concentratiebepaling van CdTe nanokristallen. Rond de bandgap-transitie vinden we geïntegreerde absorptiecoëfficiënten die omgekeerd evenredig schalen met het volume van de QDs. Bovendien tonen deze data aan dat er een afwijking is die oploopt tot een factor 3 vergeleken met waarden die wijdverspreid gebruikt worden in de literatuur.

We bepalen de intrinsieke absorptiecoëfficiënt van CdSe/CdS kern/schil en CdSe/CdSe$_x$S$_{1-x}$/CdS kern/legering/schil QDs. Gebruikmakend van Maxwell-Garnett theorie en een legeringsmodel, die de diffusie beschouwt tussen de Se- en S-atomen, respectievelijk bij de binnenste CdSe - en buitenste CdS-schil tonen we aan dat de intrinsieke absorptiecoëfficiënt van CdSe/CdS kern/schil QDs gebruikt kan worden voor CdSe/CdSe$_x$S$_{1-x}$/CdS kern/legering/schil QDs met een berekeningsfout die binnenin 5% ligt.

We bestuderen de niet-lineaire eigenschappen van PbS QD-suspensies i.f.v. de golflengte, optische intensiteit en QD-volumefractie gebruikmakend van de Z-scan methode met picoseconde pulsen. Vertekkende van de opbouwtijd van het karakeristieke temperatuursprofiel t_c, moduleren we het repetitietempo van de laser en sluiten we thermische lensvorming uit om direct de elektronische bijdrage te meten tot de niet-lineaire brekingsindex n_2. Deze is onafhankelijk van de intensiteit en volgt het absorptiespectrum van de QDs. Het prestatiegetal is groter dan 1 voor PbS QDs en is vergelijkbaar met PbSe QDs en lood-chalcogenide glazen. We beargumenteren dat de creatie van excitonen en de resulterende fotogeïnduceerde absorptie in de PbS QDs aan de oorsprong liggen van de waargenomen n_2 en de niet-lineaire absorptiecoëfficiënt (β). Gebruikmakend van de transiënte Four-Wave-Mixing-techniek (FWM) met 150 fs pulsen tonen we aan dat bij lage excitatie-intensiteiten de dynamica gedomineerd is door single-exciton-thermalisatie (ns) en recombinatie (μs). Bij hogere intensiteiten resulteert het FWM-signaal in een 100 ps respons. Dit toont aan dat colloïdale PbS QDs efficiënte en snelle niet-lineaire materialen zijn. Dit werk is geleverd in samenwerking met de OPERA-group van de ULB te Brussel en ’School of Physics and Astronomy’, Cardiff Universiteit.

Hybride golfgeleiders gefunctionalizeerd met QDs

We bestuderen lichtabsorptie in geplanariseerde SOI golfgeleiders (PWGs) gefunctionaliseerd met een deklaag van PbS/CdS QD mono- en multilagen (Fig.5.5). We kunnen de experimentele absorptiecoëfficiënten α_{QD} simuleren gebruikmakend van een aanpak waarbij de QD-laag vervangen wordt door een effectieve medium met een effective diëlektrische functie bepaald door dipoolkoppeling tussen naburende QDs. Deze aanpak laat de diëlekrische constante van de omgeving (host) ε_h alleen als de enige verstelbare parameter en biedt een generische schema om de optische eigenschappen te modelleren van composietmaterialen, die dichtgestapelde films van QDs bevatten. Gebruikmakend van ε_h om de experimentele - en gesimuleerde absorptiecoëfficiënten overeen te laten stemmen, vinden we dat ε_h systematisch toeneemt voor dikkere films. We interpreteren dit als een evolutie van ε_h van een extrinsieke eigenschap – bepaald door (beiden) de QD-films en de omgevende lagen – naar een intrinsieke eigenschap van de QD-laag. Voor zover wij weten is dit de eerste demonstratie van hoe ε_h – een typische parameter ingevoerd in effectieve mediumtheorieën – afhangt van de afmetingen van de gemodelleerde laag.

Bovendien bestuderen we lichtabsorptie van colloïdale PbS/CdS QDs in SOI-strip-golfgeleiders. Gebruikmakend van de Langmuir-Blodgett-depositie, worden dichtgestapelde monolagen gevormd op de strip-golfgeleiders. Door de golfgeleiderabsorbantie te analyseren, tonen we duidelijk de interactie aan van de QDs met de quasi-TE optische mode. We kunnen de experimentele absorptiecoëfficiënten – te wijten aan de aanwezigheid van QDs – simuleren gebruikmakend van de diëlektrische constante van de host bepaald in de QD-bedekte PWGs. Via FDTD-simulaties kunnen we corrigeren voor mogelijke emissie van QDs in de golfgeleiders, hetgeen verwaarloosbaar blijkt in onze werk. Bijgevolg levert de studie een

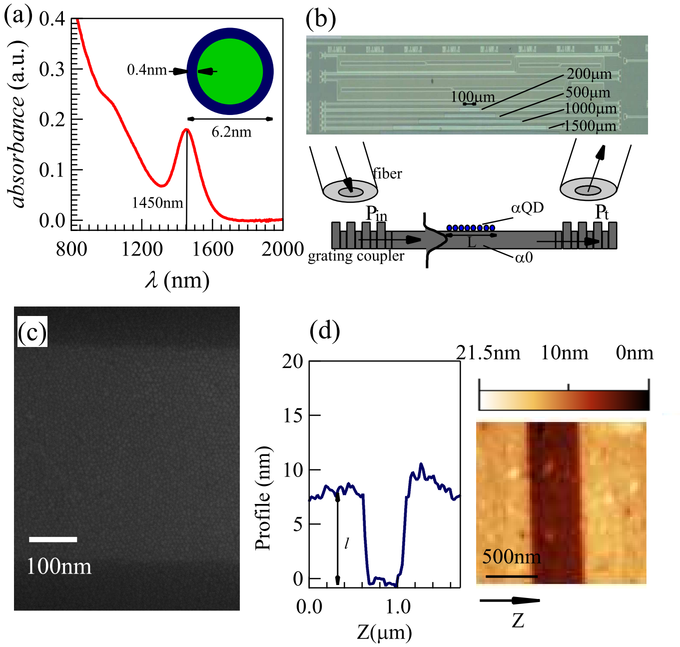

Figure 1: (a) PbS/CdS QD spectrum opgenomen in een verdunde QD-dispersie in tetracholoroethyleen. (b) Schematische weergave van het optische veld gekoppeld vanuit de vezel doorheen de grating in de geplanariseerde golfgeleider (PWG) bedekt met QDs. (c) SEM-beeld van een (bovenaanzicht) PWG bedekt door een QD-monolaag. (d) AFM-beeld en dwarsdoorsnede van een PWG bedekt door een QD-monolaag. Het beeld toont een offset (l) tussen het bovenoppervlak van de (lichtjes ingedeukte) PWG en de silica omringing.

complete aanpak van absorptie en eventuele emissie in (strip) golfgeleiders.

Quantum dots voor fotonische toepassingen

We demonstreren via simulaties het gebruik van loodzout QDs geëxciteerd rond hun bandgap als een golflengteconvertor in silicium-op-isolator-golfgeleiders. We introducreren belangrijke concepten om de prestatiegetallen voor trage microseconde en snelle picoseconde golflengteconversie. We bereiken prestatiegetalwaarden groter dan 25 en 3 voor de absorptiebleach en intraband gebaseerde convertor. Snelheden van $\approx$ 5 to 20 GHz zijn mogelijk voor de verschillende telecombanden : O-band (1274-1346 nm), C-band (1530-1565 nm) en L-band (1565-1625 nm). Door de bandgap van de QDs gepast af te stemmen, kunnen we golflengteconversie uitvoeren ofwel binnen de verschillende telecombanden ofwel van een korte naar een langere golflengteband. Alhoewel de bezettingsdistributie van de QDs verschillend is van Poisson, laat de introductie van de equivalente Poission-excitatie-grootheid ons toe om gemakkelijk het gemiddeld aantal excitonen per QD te bepalen. Dit biedt ons simpele uitdrukkingen om de stabiliteit van de achtergrond en de modulatie te controleren. Tot slot, besteden we in dit werk aandacht aan de vooruitzichten nodig voor de verdere optimalisatie van de golflengteconvertor.

We tonen aan dat een periodische rooster van plasmonische nanorods een nabije veldresonantie en een verre veld-geïnduceerde transparantie vertonen bij dezefde fotonenergie en in-het-vlak-momentum. We overwegen dat dit contra-intuïtief gedrag vele belangrijke functionaliteiten toelaat (*e.g.*, verhoogde lichtemissie en ’sensing’) die nu uitgevoerd worden door plasmonische EIT-analoge eigenschappen. Maar met het voordeel van een collectieve resonantie die ten koste komt van een dichte veldlokalisatie. We demonstreren experimenteel dit gedrag gebruikmakend van PbS QDs als lokale veldsensoren. Dit werk is uitgevoerd in samenwerking met S. Rodriguez van de FOM-instituut AMOLF-TU/e

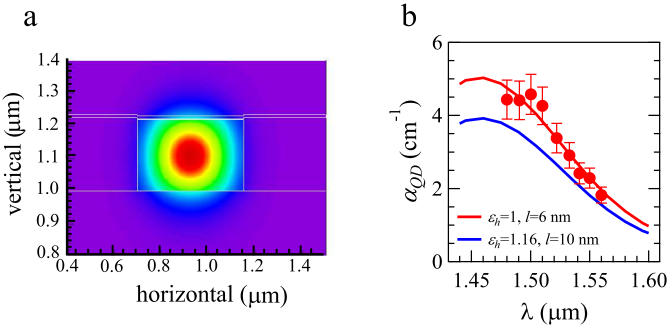

Figure 2: (a) Weergave van de dwarsdoorsnede van het gesimuleerde elektrisch veld voor 1520 nm licht geleidt door een PWG bedekt met een monolaag van QDs. (b) Vergelijking tussen de experimentele en gesimuleerde α_{QD} absorbantiespectrum van een QD-bedekte PWG voor twee verschillende combinaties van l and ε_h.

and 'Philips Research Laboratories' te Eindhoven.

Engelstalige samenvatting – English summary –

As the title signifies, we treat in this doctoral research the optical properties of *colloidal quantum dots* integrated on a *silicon-on-insulator* platform. Photonics, or the study of light (photons) on a micro and nanoscale, plays a key role in worldwide telecommunication. Optical fibers, backbone of internet, have a potential to convey a massive amount of information in the form of packets of photons at a high bandwidth. However, this capacity is currently limited by the components processing or receiving the information at both fiber ends. To be succesfull one needs besides speed, systems that provide a lot of functionalities within a compact size. To meet this goal of miniaturization and performance on-chip cost-effective platforms are required.

In this context, using photonic integrated circuits (PICs) based on silicon – research field known as silicon photonics – provide extended possibilities. These components are build on a silicon-on-insulator (SOI) platform, allowing the light to be guided by the high refractive index contrast between silicon and silicon dioxide. This high index contrast results in high confinement of light and permits that one can make ultracompact waveguides with a high density per unit area. Therefore yielding very dense and high functional photonic integrated circuits.

Apart from the compactness, SOI components are relying on the same technology used to produce electronic circuits (CMOS), witnessed to have revolutionized the electronic industry in the last few decades, and therefore silicon photonics has the potential to exploit these CMOS fabrication infrastructures. This driving force enables silicon photonics to

be cost effective with respect to materials, components and energy consumption. However, silicon based materials have a drawback that they are difficult in generating light for active devices (lasers, LEDs,...). Furthermore, they show low nonlinear optical properties, which are needed for optical signal processing (routers, interconnects,...). In this respect, new routes are being developed to integrate active and nonlinear materials with silicon, known as hybrid technologies to fabricate active and nonlinear devices. A promising candidate among those hybrid technologies are colloidal quantum dots (QDs) integrated on SOI.

Colloidal semiconductor quantum dots or nanocrystals are a new class of materials, whose physical and material properties are strongly dependent on their size (2-20 nm), shape, crystal structure, and surface characteristics. An important advantage of QDs is their flexibility. The electro-optical properties can be adjusted to the application - active or passive - in SOI and integration makes use of simple, wet techniques that are mainly independent of the substrate. In contrast, this technology is not very mature. In spite of its potential, there is no standard material system for coatings and many obstacles needs to be overcome to facilitate the step from materials towards devices.

In this summary we will provide an overview of the main results obtained on following research fields: QD-fabrication (synthesis) , optical properties of colloidal QDs, integration of QDs with the SOI platform and QD based photonic applications.

Synthesis

Colloidal quantum dots are synthesized using wet chemical procedures, where in particular the hot injection approach leads to highly monodisperse suspensions of nanocrystals. This procedure relies on precursors and ligands to control the nucleation and growth of the nanocrystals and stabilize the resulting suspension by steric hindrance. Since its introduction in 1993 for the synthesis of cadmium chalcogenide nanocrystals (CdS, CdSe and CdTe QDs), the hot injection method has become an established and widely used procedure. In this dissertation, we synthesize colloidal quantum dots engineered for applications in nonlinear optics in combination with the silicon-on-insulator photonics platform, *i.e.*, in the wavelength range 1300-1600 nm. This involves materials such as PbS and PbS/CdS QDs, where the bandgap transition can be matched to the photon energy or CdTe, where the photon energy can correspond to half the bandgap energy.

In this context, we make the CdTe QDs with sizes varying from 3 to 11 nm using the hot injection method. The bandgap is tunable between 500 nm and 760 nm, or 1.6-2.48 eV. The large nanocrystal sizes (7-11 nm) are obtained using a continuous injection of precursors at a controlled reaction time, avoiding Ostwald ripening. Thanks to these efforts, we construct the sizing curve of the CdTe QDs by combining UV-vis-absorption spectroscopy and TEM-imaging. Moreover, we synthesize PbS core and PbS/CdS core/shell QDs using the hot injection method. We obtain nanocrystal sizes from 2.5 till 7.5 nm with absorption peaks in the range 800-2000 nm or 0.62-1.5 eV.

Optical properties

We analyze the absorption coefficient of CdTe QDs by combining UV-vis absorption spectroscopy and elemental analysis. At short wavelength of 410 nm the intrinsic absorption coefficient does not show size quantization effects and the obtained values are in good agreement with the bulk value of CdTe. The average of these values can be used as a reliable standard for the concentration determination of CdTe nanocrystals. Around the bangap transition we find integrated absorption coefficients that scale inversely proportionally with the QD volume. In addition, these data showed a deviation up to a factor of 3 compared to the values widely used in literature.

We determine the intrinsic absorption coefficient of CdSe/CdS core/shell and CdSe/CdSe$_x$S$_{1-x}$/CdS core/alloy/shell QDs. Based on Maxwell-Garnett theory and an alloying model considering the diffusion of the Se and S atoms respectively at the inner and outer CdSe and CdS shell we show that the intrinsic absorption coefficient of CdSe/CdS core/shell

QDs can be used to a CdSe/CdSe$_x$S$_{1-x}$/CdS core/alloy/shell QDs within a 5% error of calculation.

We study the nonlinear properties of PbS QD suspensions as a function of wavelength, optical intensity and QD volume fraction using the Z-scan technique with picosecond pulses. Knowing the characteristic temperature profile buildup time t_c, we modulate the laser repetition rate and exclude thermal lensing to directly measure the electronic contribution to the nonlinear refractive index n_2. This quantity is independent from the intensity and follows the QD absorption spectrum. The figure of merit is larger than 1 for the PbS QDs and is comparable with PbSe QDs and lead chalcogenide glasses. We argue that the creation of excitons and the resulting photoinduced absorption in the PbS QDs lie at the origin of the observed n_2 and β. Using transient Four Wave Mixing with 150 fs pulses we prove that at low excitation intensities the dynamics is dominated by single exciton thermalization (ns) and recombination (μs). At higher intensities the FWM signal results in a 100 ps response. This shows that colloidal PbS QDs are efficient and fast nonlinear materials. This work is done in collaboration with OPERA-group from the ULB, Brussels and School of Physics and Astronomy, Cardiff university.

Hybrid QD-functionalized waveguides

We study light absorption in planarized SOI waveguides (PWGs) functionalized with a top coating of PbS/CdS QD mono- to multilayers (Fig.5.5). We can simulate the experimental absorption coefficients α_{QD} using an approach where the QD layer is replaced by an effective medium with an effective dielectric function determined by dipolar coupling between neighboring QDs. This approach leaves the host dielectric constant ε_h as the only adjustable parameter and provides a generic scheme to model optical properties of composite materials containing close packed QD films. Using ε_h to match experimental and simulated absorption coefficients (Fig. 5.13), we find that ε_h systematically increases for thicker films. We interpret this as an evolution of ε_h from an extrinsic property, both determined by the QD films and the surrounding layers, to a more intrinsic property of the QD layer. To the best of our knowledge, this is the first demonstration of how ε_h – a typical parameter introduced in effective medium theories – depends on the dimensions of the layer modeled.

In addition, we study light absorption of colloidal PbS/CdS QDs in SOI strip waveguides. Using Langmuir-Blodgett deposition, close-packed monolayers are formed on the strip waveguides. By analyzing the waveguide absorbance, we show a clear interaction of the QDs with the quasi-TE optical mode. We can simulate the experimental absorption coefficients due to the presence of the QDs using the host permittivity determined in the QD/coated PWGs. Through FDTD simulations we can correct for possible QD emission in the waveguides, which turns out to be negligible in our work. Therefore, the study allows for a complete engineering of absorption and possible emission in (strip) waveguides.

Quantum dots for photonic applications

We demonstrate through simulations the use of lead salt QDs excited around their bandgap as a wavelength convertor in silicon-on insulator waveguides. We introduce important concepts to simulate the figure of merits for slow microsecond and fast picosecond wavelength conversion. We achieve figure of merit values larger than 25 and 3 for the absorption bleach and intraband absorption based convertor, respectively. Operation speeds are possible of $\approx$ 5 to 20 GHz for the different telecom bands : O-band (1274-1346 nm), C-band (1530-1565 nm) and L-band (1565-1625 nm). By appropriately tuning the bandgap of the QDs, we can perform the wavelength conversion either within different telecom bands or from a short to a longer wavelength band. Although, the occupancy distribution is different from a Poisson, by introducing the equivalent Poisson excitation quantity it allows us to easy determine the average number of excitons. This provides us with simple expressions for controlling the background and modulation stability of the PbS/CdS QD wavelength convertor. Finally, in this work we highlight the prospects for further optimizing the wavelength convertor.

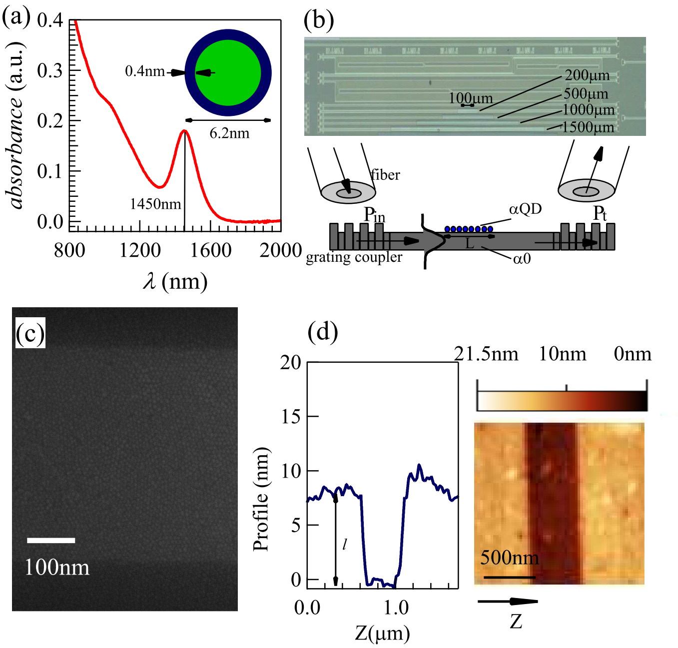

Figure 3: (a) PbS/CdS QD spectrum recorded on a dilute QD dispersion in TCE. (b) Cartoon representation of the optical field coupled from the fiber through the grating in the QD coated PWG. (c) SEM image of a (topview) PWG coated by a QD monolayer. (d) AFM image and cross section of a PWG coated by a QD monolayer, clearly showing the offset (l) between the top surface of the (slightly submerged) PWG and its silica cladding.

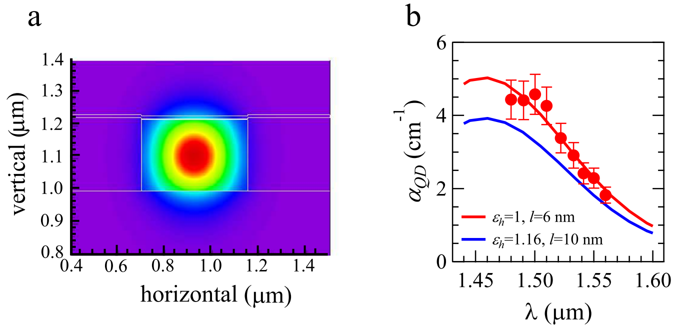

Figure 4: (a) Cross-sectional representation of the simulated electric field for 1520 nm light guided by a PWG coated by a QD monolayer. (b) Comparison of the experimental and simulated α_{QD} absorbance spectrum of a QD coated PWG for two different combinations of l and ε_h.

We show that a periodic array of plasmonic nanorods to exhibit a resonant NF and FF-induced transparency at the same photon energy and in-plane momentum. We envisage this counterintuitive behavior to enable many of the key functionalities (*e.g.*, enhanced light emission and sensing) pursued by plasmonic EIT analogs, but with the benefit of a collective resonance at the expense of tight field localization. We experimentally demonstrate this behavior by using PbS QDs as local field sensors. This work is done in collaboration with S. Rodriguez from FOM-institute AMOLF-TU/e and Philips Research Laboratories Eindhoven.

List of Acronyms

A

AS	Abosorption Saturation
AB	Absorption Bleach
AFM	Atomic Force Microscopy

C

CdOA	CadmiumOleate
CDM	Coupled Dipole Model
CMI	Continuous Multiple Injection (method)
CW	Continuous Wave

D

DPE	DiPhenyl Ether

E

ES	Excited State

F

FDTD	Finite Difference Time Domain (method)
FF	Far Field
FOM	Figure Of Merit
FWHM	Full Width at Half Maximum
FWM	Four Wave Mixing

G

GS	Ground State

H

HDA	HexaDecylAmine
HOMO	Highest Occupied Molecular Orbital

I

IMI	Iterative Matrix Inversion
ICP-MS	Inductively Coupled Plasma Mass Spectrometry

K

KK	Kramers-Krönig

L

LAN	Local Area Network
LB	Langmuir-Blodgett (deposition)

M

MG	Maxwell-Garnett

N

NIR	Near InfraRed
NF	Near Field
NFIE	Near Field Intensity Enhancement

O

OA	Oleic Acid
OAI	On-Axis Intensity
ODE	OctaDecene
OLA	OleylAmine

P

PbCl2	lead chloride
PIC	Photonic Inegrated Circuit
PS	Polystyrene
PL	PhotoLuminescence
PWG	Planarized WaveGuide

Q

QD	Quantum Dot
QY	Quantum Yield

R

RBS	Rütherford backscattering spectroscopy

S

SEM	Scanning Electron Microscopy
SLR	Surface Lattice Resonance
SOI	Silicon-on-Insulator
SWG	Strip WaveGuide

T

TCE	TetraChloroEthylene
TE	Transverse Electric (mode)
TEM	Transmission Electron Microscopy
TOP	Tri-n-OctylPhosphine
TOP-S	Tri-n-octylphosphine sulfide
TOP-Te	Tri-n-octylphosphine telluride
TPA	Two-Photon Absorption

W

WG	Waveguide

X

XRD	X-ray diffraction

-English Text-

1

Introduction

1.1 Introduction

In a modern society where news need to be spread instantaneously, education wants to enter new ways of teaching to better respond to sociocultural changes and teleworking should be incorporated in companies, an optimal knowledge exchange is indispensable. Therefore an increase in speed, memory and more chips for information processing is essential, which is technologically translated in a demand of more bandwidth, upscaling with smaller footprints and a lower cost for datacommunication networks. A solution for this is the replacement of relatively slow electronic components for dataprocessing by systems which process data optically very fast[1]. To be successfull, these systems must be based on the one hand on materials with appropriate physical properties - low absorption loss, fast response times, temperature resistance, ... - on the other hand they should be compatible with existing semiconductor micro- and nanoelectronics industry.

This semiconductor industry is facing major challenges in the medium term[2]. The need for continuing miniaturization in micro- and nanoelectronics requires the use of new techniques and materials. In this context, photonic integrated circuits (PICs) based on silicon provide extended possibilities. Photonics is the technology of generating and harnessing light and other forms of optical radiant energy whose quantum unit is the photon. Apart from the requirement for high performance at a lower cost, miniaturization of photonics is necessary to permanently enable integration with electronics. Si waveguides formed on silicon dioxide (silicon-on-insulator, SOI) have a high refractive, omni-directional index contrast. Therefore it is possible to perform different electronic functionalities, with compact optical circuits. Moreover, the production of SOI components is based on a technology developed for integrated electronic circuits (CMOS)[3;4]. A major drawback of SOI lies in the optical properties of silicon. Si is an indirect bandgap material and shows limited optical nonlinearities, inhibiting its use for applications relying on the emission of light and signal processing for optical communication, respectively.

The solution to these problems are sought in hybrid technologies, extending the SOI plaform with other materials. The current epitaxial techniques such as die-to-wafer bonding are quite successful but very expensive. An alternative that couples a large potential to a low cost is completing Si waveguides with a functional coating that is applied using inexpensive techniques such as spin - or dropcasting. Passive components have been demonstrated, for example by covering Si waveguides with a non-linear polymer[5] or graphene[6]. An alternative are coatings based on colloidal semiconductor nanocrystals or quantum dots (QDs).

An important advantage of colloidal QDs is their flexibility. The electro-optical properties can be adjusted to the application - active or passive - in SOI and integration makes use of simple, wet techniques that are mainly independent of the substrate. In contrast, this technology is not very mature. In spite of its potential, there is no standard material system for coatings and many barriers needs to be overcome to facilitate the step from materials towards devices. In this introduction we will give an overview of the fabrication and properties of colloidal QDs and SOI, discuss the important obstacles that should be overcome and outline the main work that is needed to pave the way for functionalizing the SOI platform and fabricate hybrid devices.

1.2 Colloidal quantum dots

Since the seminar of Richard Feynman, which dates back to 1959 at Caltech[7]: ’There’s Plenty of Room at the Bottom’ the interest in exploring nanotechnology was triggered. From the early 1980’s[1], this lead to an increased interest in the properties of semiconductor nanocrystals, later also called quantum dots (QDs)[8;9]. Nowadays, QDs have become important for a whole range of optical applications, including photovoltaics, photodetection, displays, nanoflash memories and optical amplifiers[10–13]. Besides electro-optical applications they show potential for other research branches such as biomedicine, the study of intracellular processes, high resolution imaging, biomarkers and tumor detection[14–17].

A semiconductor nanocrystal is a fragment of an inorganic, crystalline material having dimensions of the order of nanometers (Fig. 1.1(a)). Interesting to nanocrystals is that by the reduction of the dimensions the physical properties of the material changes due to a phenomenon called ’quantum confinement’ or ’size quantization’[9;18]. Under the influence of quantum confinement the band gap widens and the edges of the energy bands are reduced to a set of discrete levels with decreasing size. Thus, one obtains a sort of artificial atoms, of which the electro-optical properties are a function of the size of the particles. There are mainly two different methods for the production of QDs, conveniently called self-assembled QDs and colloidal QDs. Self-assembled QDs are made through the typical deposition techniques used in semiconductor technology (chemical vapor deposition, molecular beam epitaxy) in

---

[1] This year we are celebrating 30 years of quantum dots

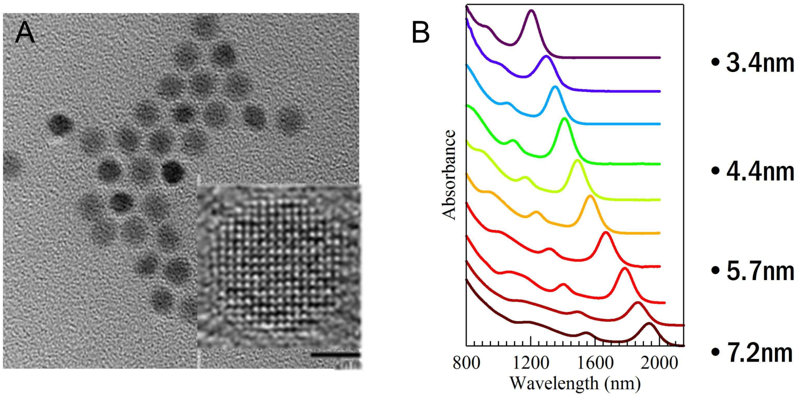

Figure 1.1: A. Transmission electron microscopy image of colloidal PbSe nanocrystals or quantum dots. The inset shows a high-resolution recording, whereby the individual atomic columns are clearly visible. Scale bar : 2 nanometers. B. Series of absorption spectra of PbSe quantum dots. The blue shift of the aborption peak with decreasing diameter illustrates the influence of the quantum confiment on the electro-optical properties. (courtesy of I. Moreels)

which one lets a thin coating contract into islands with nanometer dimensions[19]. Typical examples here are InAs QDs grown on InP or GaAs and Ge QDs grown on Si[20]. This approach gives very stable structures, as the QDs may be embedded in a solid matrix, but is expensive, little flexible and offers only limited control over size and shape of the QDs.

Colloidal QDs are created by chemical techniques, whereby the end result is a colloidal dispersion of nanocrystals[21]. This approach typically provides nanocrystals with dimensions of 1 to 10 nm, which are encased by an organic shell (capping) of ligands. An important advantage of the method is the maturity of the synthesis (monodispersion suspensions, control over size and shape, wide range of materials), which allows for a high degree of control over the electro-optical properties. Moreover the QDs allow for a flexible processing. This applies both at the level of individual quantum dots (change of ligands, coating with an additional inorganic shell) as well on the deposition of an ensemble of quantum dots in thin films via easy wet techniques as spin - and dropcasting. The combination of the adjustable electro-optical properties and easy processing makes QDs an attractive material for functionalization of SOI waveguides.

1.2.1 Quantum confinement

The origin of the quantum confinement can be traced back to the work of Brus[22–24]. If we assume a spherical semiconductor nanocrystal with a paricle radius R and calculate the energy spectrum by assuming the wavefunction of the electron-hole pairs (excitons) to be confined in an infinite potential well[25], we obtain the bandgap energy after solving the Schrödinger equation :

$$Eg = Eg_{bulk} + \frac{\bar{h}^2\pi^2}{8\mu R^2} - \frac{1.786e^2}{\epsilon R} \tag{1.1}$$

Here, μ is the reduced exciton mass and ϵ is the dielectric constant. The above equation is the Brus-equation. The first two terms are the particle-in-a-box energy, and the last term is the Coulomb energy that accounts for electron hole interaction. Inspecting expression 1.1 we observe a strong blueshift of the bandgap of the QDs by decreasing the particle size. Since the bangap depends on the size, the onset of absorption is also size dependent as illustrated in Fig. 1.1(b) for a series of PbSe QDs. The position of the luminescence peak is also controlled by the quantum dot size. This is demonstrated in Fig. 1.2 for a series of luminescent CdSe QDs, where the emitting color changes from red to blue and immediately highlights the potential use of semiconductor nanocrystals.

1.2.2 Colloidal heterostructured quantum dots

From the early fabrication of colloidal nanocrystals the hurdle of degrading electrical and optical properties with time appeared[21]. As the QD sizes are small, the surface to volume ratio is huge yielding free surface atoms with dangling bonds, introducing midgap states that are detrimental for the photoluminescence and make the nanocrystals prone to surface oxidation and leaking of the wavefunction. The hurdle has

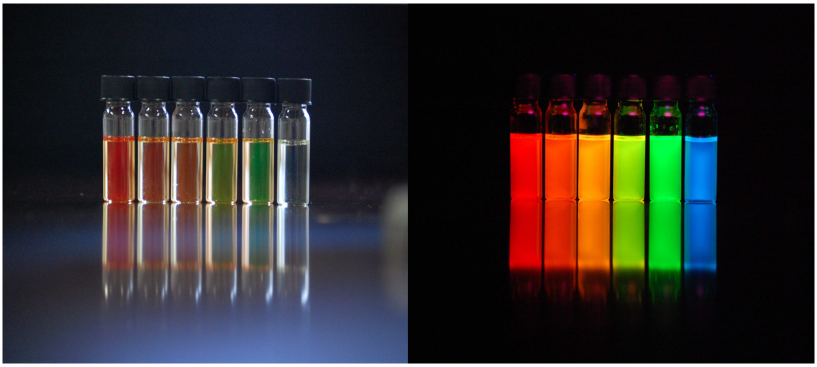

Figure 1.2: (Left) Series of CdSe QDs shining luminescently after UV illumination (right). By decreasing the particle size of the CdSe nanocrystals, the emission color is changed from red to blue. With the acknowledgement for S. Abe for the taken pictures.

been overcome at first by eliminating the free surface by a proper surface termination by organic ligands and later on by encapsulating the QDs with an inorganic shell material[26], confining the wavefunction well within the nanocrystal. (Fig. 1.3(a)). Nowadays, the current know-how of the colloidal quantum dots allows not only for a control of their size and stabilizing ligands, but various shapes (dots, rods, tetrapods, platelets, sheets, ...), combinations of these shapes to the so called 'heterostructured' QDs (core/shell, core/multishell, dot-in-rods, alloys, ...) are feasible in the visible and near-infrared range[27–30]. Moreover, one can extend the tunablity towards the types of the bandalignment of these heterosctructured QDs as illustrated in Fig. 1.3(b) : Type-I, type-$I^{1/2}$ and type-II[26;31–33]. In a Type I QD, both charge carriers (electron and holes) are confined in the core of a nanocrystal. This type is suitable for enhancing the chemical stability and the photoluminescence quantum yield. In a Type II QD, one of the charged carriers is confined in the core, while the other is confined in the shell. In the case of a Type $I^{1/2}$ QD, the band offset is small for one of the charge carriers to be only confined in the core. Consequently, one of the charge carriers will delocalize over the core and shell, while the other remains in the core. All these unique properties, combinations and types not only inspire

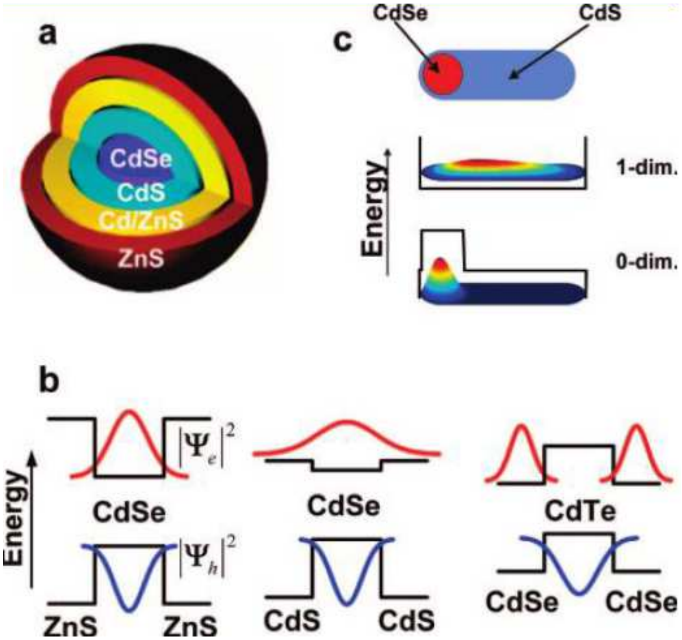

Figure 1.3: (a) Structure of a CdSe core/(multi-)shell QD yielding a very stable nanocrystal with a high photoluminescence quantum yield. (b) (left to right) Schematic representation of the band alignment in a Type-I, Type-I$^{1/2}$ and Type-II heterostructured nanocrystal, respectively. The amplitude squared of the wavefunction for the electron and hole are shown in red and blue, respectively. (c) An example of a CdSe dot in a CdS rod nanostructure where electron and hole wavefunctions have different confinement regimes : the electron and hole are confined in two and three dimensions, respectively. Graph is reproduced from Talapin et al.[17].

nanocrystal engineers for implementing them in a broad range of applications, but also challenges them for completely unravelling the QD basic material characteristics and their optical properties.

1.2.3 Optical properties

The optical properties of QDs can be simply divided in two categories : low power (linear) optical properties and high power (nonlinear) optical properties. Linear optical properties commonly observed properties of light at low power and are typically related to absorption and emission. Hereby, no new frequencies are generated and typically increasing the light intensity enhances the respons accordingly in these materials. In the first half of the 20th century, nonlinear properties were demonstrated in electricity and magnetism phenomena. As examples, amplifying radiowaves in radiotubes, the electrical properties of p-n junctions in transistors and saturation of ferromagnets. Optical applications based on nonlinear phenomena could only be envisaged after 1960, the year the laser was invented by Theodore Maiman[2] [34]. This invention made that high optical intensities became achievable to trigger the optical nonlinearities. To understand this, we consider following Taylor-expansion of the nonlinear polarization, which is the respons of the applied optical field $\bar{E}$:

$$\bar{P} = \epsilon_0\chi^{(1)}\bar{E} + \epsilon_0\chi^{(2)}\bar{E}^2 + \epsilon_0\chi^{(3)}\bar{E}^3 + ... \tag{1.2}$$

The nonlinear susceptiblities $\chi^{(2)}$,$\chi^{(3)}$ are very small as compared to the linear susceptibility $\chi^{(1)}$ and the higher order terms are undetectable, except if the energy densities are high enough to generate strong electrical fields.

Furthermore, one can show that in centro-symmetric crystals the second order susceptibility $\chi^{(2)}$ vanishes, yielding a nonlinear susceptibility that is in first order proportional to the intensity I. This corresponds to

---

[2] His first submission of the report was to the journal of Physical Review Letters and was turned down by the editors reflecting their limited understanding that time! Fortunate, his second submission to the Nature editors was accepted.

a change of the refractive index n and the absorption coefficient α. We refer to this as a Kerr-type nonlinearity :

$$n = n_0 + n_2 I = n_0 + \delta n \tag{1.3}$$

$$\alpha = \alpha_0 + \beta I \tag{1.4}$$

Here, n_0 and α_0 are the linear refractive index and absorption coefficient, respectively. The second term in 1.4 is only significant when nonlinear absorption appears. Based on the sign of β one can distinguish two phenomena : two-photon absorption (TPA) and absorption bleach (AB). When the sign of β is positive, two-photon absorption occurs. This is a process in which subsequently two photons are absorbed by a QD with a bandgap equal to twice the energy of the incoming photons. On the other hand – if the sign of β is negative – absorption bleach appears, when a decrease of absorption is noticed if the intensity increases.

1.3 Silicon photonics

1.3.1 Silicon on insulator (SOI)

Silicon-on-insulator (SOI) is a material system that is used mainly for optical signal processing in telecom applications (Fig. 1.4(a)). An important advantage of the technology is the ability to realize very compact components, due to the high refractive index contrast between the Si waveguide and its surroundings (silicon dioxide and air). As illustrated in Fig. 1.5(a-d), waveguides are structures that can confine light within a certain area and convey it over a given distance[35]. This confinement is done by trapping light in a core of a material with a higher refractive index than the surrounding material. Consequently, light is bundled in a spot around the centre, or a mode. A second merit for SOI is that integrated photonics circuits in silicon-on-insulator can be made in existing CMOS manufacturing lines from semiconductor electronics industry. The current standard, 193 nm deep-UV etching lithography

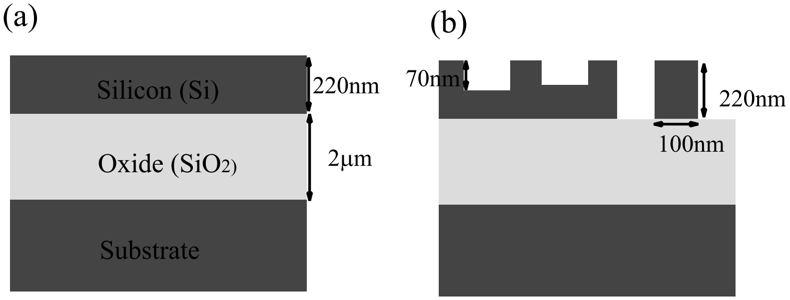

Figure 1.4: (a) Silicon-on-insulator layer structure of an unprocessed wafer. (b) Processing the top-layer of the wafer using deep (220 nm) and shallow (70 nm) etching lithography yields ultra compact optical waveguides and photonic structures.

(Fig. 1.4(b)) allows to define structures smaller than 100 nm on a SOI wafer . Herewith, ultra compact single mode waveguides can be combined to efficient directional couplers, ring resonators with high quality factors and broadband Mach-Zechnder interferometers[36–39]. With these basic componets passive devices have been realized : optical swicthes[40], modulators and wavelength convertors[41]. Yet, in spite of the possibilities, these building blocks to realize all-optical signal processing rely on the creation of charged carriers and are therefore restricted to bit rates of 1Gbit/s. Faster signal processing and active components require the use optical nonlinear - and direct bandgap materials, hampering a wide employment of silicon.

1.3.2 Functionalization of SOI

A strategy to increase the reliance value of Si based photonic integrated circuits is by functionalizing SOI. Up to now, this is tested with mainly - other than QDs - four different material systems and we will consider following criteria for the ideal material on silicon : Low cost, highly nonlinear, direct semiconductor bandgap and easy processing. The first type of materials are chalcogenide doped glasses, which are glasses in

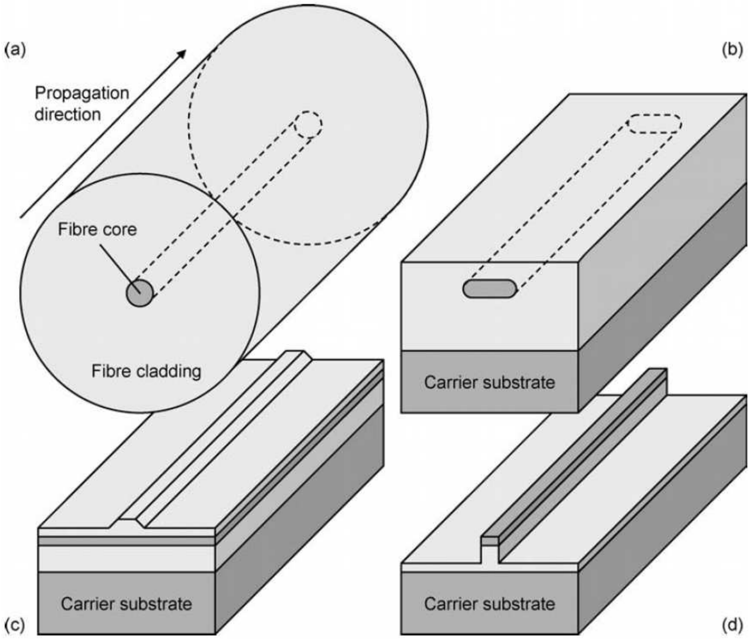

Figure 1.5: Various waveguide cross sections from Bogaerts et al.[42] (a) A single mode optical fibre, with an oxide (glass) core of 9μm and a glass cladding of 125μm diameter. The refractive index contrast between core and cladding is typically lower than 1%. (b) A silica-on-silicon waveguide, with similar dimensions and refractive index contrasts. (c) A typical low-contrast III-V semiconductor ridge waveguide. The refractive index contrast between core and cladding layers is typically in the range 3.2-3.4, with a ridge width of several microns. (d) A high-contrast silicon-on-insulator photonic waveguide with submicron dimensions. The core material is silicon with an refractive index of 3.45, compared to a cladding of SiO_2 and air with refractive indices of 1.45 and 1.0, respectively.

which S, Se, Te in combination with other elements such as Ge, As, Sb, Ga, ... are added. These non-semiconductors exhibit nonlinearities which are 2 orders of magnitude larger than the silicate glass. Functionalization of (non)linear-Si waveguides was reported by means of a coating on Si[43]. Second type of materials are III-V semiconductors, which are particularly suitable for light emission for the sake of their direct bandgap, but show rather restricted nonlinear characteristics. Successfull, but at high cost integration on SOI was reported using 'die to wafer bonding' epitaxial tecchniques[44]. The third type of functional materials are nonlinear polymers, these are non-semiconductor materials possessing a high nonlinearity due their strong electronic polarizability and integration of these polymers on silicon-slot waveguides has been demonstrated[5]. Final type of functionalizing material is graphene, which consists of a single layer of carbon atoms self assembledly resulting in a honeycomb lattice. Optical absorption control of graphene - through gate voltages - in a Si waveguide resulted in a 1.2 Gbit/s modulator[6]. Additionally, graphene flakes were shown to possess high nonlinear optical response suitable for optical communication[45].

1.4 Objective of this work

Besides the above mentioned materials in the previous section and as outlined colloidal QDs are promising for functionalizing SOI. Si nanocrystals were demonstrated for optical switching in SOI around 900 nm[46]. Yet, few reports include the use of colloidal QDs in the more relevant telecom range (1200-1600 nm)[47]. In this context, lead salt semiconductor nanocrystals (PbX and PbX/CdX, X=S,Se) are a captivating class of materials, due to the combination of their adjustable direct bandgap in the near infrared range and a suitability for low cost solution-based processing[48]. This implies that their properties can be tailored for telecom applications. As these lead salt colloidal QDs can be employed for hybrid SOI devices and may offer key answers to many photonic operations : lasing, modulation, wavelength conversion and all optical signal processing, understanding the optical properties of these QD coated SOI waveguides is essential. Therefore the goal of this thesis will be dedicated to resolve this issue.

1.4.1 Outline

The work of this thesis can be divided into four main parts:

- In the second chapter we will highlight the general synthesis route of colloidal quantum dots using the hot injection method. At first, we will provide a synthesis procedure for CdTe QDs from visible till NIR range. Secondly, we will give the synthesis procedure of PbS core- and PbS/CdS core/shell nanocrystals and show their tunability from NIR till mid-IR range. Additionally, the structural-, optical- and stability properties of the above QDs will be discussed.

- In the third chapter we will present a generalised description of the theoretical intrinsic absorption coefficients -which are linked to the particle concentrations- of core, core/shell, multi- and graded shell particles by applying Maxwell-Garnett theory together with the transmission line analogy for determining the particle polarizability in semiconductor spherically shaped particles. The use of the above model will be illustrated for CdTe core-, CdSe/CdS core/shell - and CdSe/ $CdSe_xS_{1-x}$/CdS core/alloy/shell nanocrystals.

- In the fourth chapter we will make a leap from the study of the linear optical properties (chapter 3) towards the description of the optical nonlinearities of nanocrystals. We will report n_2, β and the resulting Figure of Merit values for PbS QDs resonantly excited around the telecom wavelength range (1500-1600 nm). We will make use of the Z-scan technique together with pump-probe four wave mixing (FWM) and determine the time response of the optical nonlinearities.

- In Chapter 5, we will describe the use of the Langmuir-Blodgett technique to obtain thickness controlled depostion of colloidal

QDs on SOI platform. We will coat SOI planarized waveguides with close-packed mono- and multilayers of PbS/CdS QDs and analyze the absorption coefficient through the waveguide absorbance. Experimental data will be compared with simulations and a close formula describing the dielectric function of the QD-layers will be derived. Next, we will determine the waveguide absorbance of silicon-on-insulator strip waveguides coated with PbS/CdS core/shell QDs. Additionally, the morphology of the QD-layer on SOI will be discussed.

- In chapters 6-7 we will discuss the potential use of colloidal QDs for photonic applications. In chapter 6, we will discuss the use of colloidal QDs as a wavelength convertor. We will provide the Figure of Merit values for wavelength conversion of QDs in a SOI platform. In chapter 7, we will demonstrate the use of colloidal QDs as local field sensors in plasmonic arrays.

We will end this thesis by a general conclusion, summarizing the most essential results and give prospects for future research and application directions.

Bibliography

[1] Emmons, R.; Kurdi, B.; Hall, D. G. Buried-oxide silicon-on-insulator structures. I. Optical waveguide characteristics. *Quantum Electronics, IEEE Journal of* **1992**, *28*, 157–163.

[2] Assefa, S. et al. A 90nm CMOS Integrated Nano-Photonics Technology for 25Gbps WDM Optical Communications Applications. *2012 Ieee International Electron Devices Meeting (Iedm)* **2012**.

[3] Assefa, S.; Green, W. M. J.; Rylyakov, A.; Schow, C.; Horst, F.; Vlasov, Y. A.; Optical Society of, A. CMOS Integrated Nanophotonics - Enabling Technology for Exascale Computing Systems. *2011 Optical Fiber Communication Conference and Exposition (Ofc/Nfoec) and the National Fiber Optic Engineers Conference* **2011**.

[4] Green, W. M. J.; Assefa, S.; Van Campenhout, J.; Lee, B.; Yang, M.; Doany, F.; Schow, C.; Rylyakov, A.; Jahnes, C.; Kash, J.; Vlasov, Y. A.; Ieee, Silicon Integrated Nanophotonic High-radix Switch Arrays for Next Generation Computer Systems. *2010 23rd Annual Meeting of the Ieee Photonics Society* **2010**, 512–513.

[5] Koos, C.; Vorreau, P.; Vallaitis, T.; Dumon, P.; Bogaerts, W.; Baets, R.; Esembeson, B.; Biaggio, I.; Michinobu, T.; Diederich, F.; Freude, W.; Leuthold, J. All-optical high-speed signal processing with silicon-organic hybrid slot waveguidesx. *Nature Photonics* **2009**, *3*, 216–219.

[6] Liu, M.; Yin, X.; Ulin-Avila, E.; Geng, B.; Zentgraf, T.; Ju, L.; Wang, F.; Zhang, X. A graphene-based broadband optical modulator. *Nature* **2011**, *474*, 64–67.

[7] Feynmann, R. Theres Plenty of Room at the Bottom. *Theres Plenty of Room at the Bottom*, Pasadena, United States, 1959.

[8] Efros, A. L. Interbrand absorption of light in a semiconductor sphere. *Soviet Physics Semiconductors-Ussr* **1982**, *16*, 772–775.

[9] Ekimov, A. I.; Efros, A. L.; Onushchenko, A. A. Quantum size effect in semiconductor microcrystals. *Solid State Communications* **1985**, *56*, 921–924.

[10] Sargent, E. H. Infrared photovoltaics made by solution processing. *Nature Photonics* **2009**, *3*, 325–331.

[11] Konstantatos, G.; Clifford, J.; Levina, L.; Sargent, E. H. Sensitive solution-processed visible-wavelength photodetectors. *Nature Photonics* **2007**, *1*, 531–534.

[12] Konstantatos, G.; Huang, C.; Levina, L.; Lu, Z.; Sargent, E. H. Efficient Infrared Electroluminescent Devices Using Solution-Processed Colloidal Quantum Dots. *Advanced Functional Materials* **2005**, *15*, 1865–1869.

[13] Yong, P.; Paterson-Beedle, M.; Mikheenko, I. P.; Macaskie, L. E. From bio-mineralisation to fuel cells: biomanufacture of Pt and Pd nanocrystals for fuel cell electrode catalyst. *Biotechnology Letters* **2007**, *29*, 539–544.

[14] Medintz, I. L.; Uyeda, H. T.; Goldman, E. R.; Mattoussi, H. Quantum dot bioconjugates for imaging, labelling and sensing. *Nature materials* **2005**, *4*, 435–46.

[15] Wu, Y. L.; Fu, S.; Tok, A. I. Y.; Zeng, X. T.; Lim, C. S.; Kwek, L. C.; Boey, F. C. Y. A dual-colored bio-marker made of doped ZnO nanocrystals. *Nanotechnology* **2008**, *19*,.

[16] Rhee, S. H.; Suetsugu, Y.; Tanaka, J. Biomimetic configurational arrays of hydroxyapatite nanocrystals on bio-organics. *Biomaterials* **2001**, *22*, 2843–2847.

[17] Talapin, D. V.; Lee, J.-S.; Kovalenko, M. V.; Shevchenko, E. V. Prospects of Colloidal Nanocrystals for Electronic and Optoelectronic Applications. *Chem. Rev.* **2010**, *110*, 389–458.

[18] Reed, M. A.; Aggarwal, R. J.; Matyi, R. J.; Moore, T. M.; Wetsel, A. E. Observation of Discrete Electronic States in a Zero-Dimensional Semiconductor Nanostructure. *Phys. Rev. B* **1988**, *60*, 535–537.

[19] Poole, P.; Allen, C. N.; Marshall, P.; Fraser, J.; Moisa, S.; Raymond, S.; Fafard, S. InAs self-assembled quantum dot lasers grown on [100] InP. *Indium Phosphide and Related Materials Conference, 2002. IPRM. 14th*, 2002; pp 573–576.

[20] Wang, K. L.; Cha, D.; Liu, J.; Chen, C. Ge/Si self-assembled quantum dots and their optoelectronic device applications. *Proceedings of the Ieee* **2007**, *95*, 1866–1883.

[21] Murray, C.; Norris, D. J.; Bawendi, M. G. Synthesis and Characterization of Nearly Monodisperse CdE (E = S, Se, Te) Semiconductor Nanocrystallites. *J* **1993**, *115*, 8706–8715.

[22] Brus, L. E. Electron electron and electron-hole interactions in small semiconductor crystallites - The size dependence of the lowest excited electronic state. *Journal of Chemical Physics* **1984**, *80*, 4403–4409.

[23] Brus, L. Electronic wave functions in semiconductor clusters: experiment and theory. *The Journal of Physical Chemistry* **1986**, *90*, 2555–2560.

[24] Bawendi, M. G.; Steigerwald, M. L.; Brus, L. E. The Quantum-Mechanics of Larger Semiconductor Clusters (Quantum Dots). *Annu. Rev. Phys. Chem.* **1990**, *41*, 477–496.

[25] Kippeny, T.; Swafford, L. a.; Rosenthal, S. J. Semiconductor Nanocrystals: A Powerful Visual Aid for Introducing the Particle in a Box. *Journal of Chemical Education* **2002**, *79*, 1094.

[26] Dabbousi, B. O.; RodriguezViejo, J.; Mikulec, F. V.; Heine, J. R.; Mattoussi, H.; Ober, R.; Jensen, K. F.; Bawendi, M. G. (Cdse)Zns Core-Shell Quantum Dots: Synthesis and Characterization of a Size Series of Highly Luminescent Nanocrystallites. *J. Phys. Chem. B* **1997**, *101*, 9463–9475.

[27] Justo, Y.; Goris, B.; Kamal, J. S.; Geiregat, P.; Bals, S.; Hens, Z. Multiple Dot-in-Rod PbS/CdS Heterostructures with High Photoluminescence Quantum Yield in the Near-Infrared. *Journal of the American Chemical Society* **2012**, *134*, 5484–5487.

[28] Manna, L.; Scher, E. C.; Alivisatos, A. P. Synthesis of soluble and processable rod-, arrow-, teardrop-, and tetrapod-shaped CdSe nanocrystals. *Journal of the American Chemical Society* **2000**, *122*, 12700–12706.

[29] Ithurria, S.; Tessier, M. D.; Mahler, B.; Lobo, R. P. S. M.; Dubertret, B.; Efros, A. L. Colloidal nanoplatelets with two-dimensional electronic structure. *Nature Materials* **2011**, *10*, 936–941.

[30] Tessier, M. D.; Spinicelli, P.; Dupont, D.; Patriarche, G.; Ithurria, S.; Dubertret, B. Efficient Exciton Concentrators Built from Colloidal Core/Crown CdSe/CdS Semiconductor Nanoplatelets. *Nano Letters* **2014**, *14*, 207–213, Times Cited: 0 0.

[31] Nemchinov, A.; Kirsanova, M.; Hewa-Kasakarage, N. N.; Zamkov, M. Synthesis and characterization of type IIZnSe/CdS core/shell nanocrystals. *Journal of Physical Chemistry C* **2008**, *112*, 9301–9307.

[32] De Geyter, B.; Justo, Y.; Moreels, I.; Lambert, K.; Smet, P. F.; Van Thourhout, D.; Houtepen, A. J.; Grodzinska, D.; de Mello

Donega, C.; Meijerink, A.; Vanmaekelbergh, D.; Hens, Z. The different nature of band edge absorption and emission in colloidal PbSe/CdSe core/shell quantum dots. *ACS nano* **2011**, *5*, 58–66.

[33] Li, J. J.; Wang, Y. A.; Guo, W. Z.; Keay, J. C.; Mishima, T. D.; Johnson, M. B.; Peng, X. G. Large-scale synthesis of nearly monodisperse CdSe/CdS core/shell nanocrystals using air-stable reagents via successive ion layer adsorption and reaction. *Journal of the American Chemical Society* **2003**, *125*, 12567–12575, Times Cited: 720 736.

[34] Maiman, T. H. Stimulated optical radiation in ruby. *Nature* **1960**, *187*, 493–494.

[35] Van Stryland, E.; Enoch, E.; Wolfe, M.; Bass, W. *Handbook of Optics*; OSA, 2000.

[36] Almeida, V. R.; Xu, Q. F.; Barrios, C. A.; Lipson, M. Guiding and confining light in void nanostructure. *Optics Letters* **2004**, *29*, 1209–1211.

[37] Baehr-Jones, T.; Hochberg, M.; Wang, G. X.; Lawson, R.; Liao, Y.; Sullivan, P. A.; Dalton, L.; Jen, A. K. Y.; Scherer, A. Optical modulation and detection in slotted Silicon waveguides. *Optics Express* **2005**, *13*, 5216–5226.

[38] Bogaerts, W.; Dumon, P.; Van Thourhout, D.; Taillaert, D.; Jaenen, P.; Wouters, J.; Beckx, S.; Wiaux, V.; Baets, R. G. Compact wavelength-selective functions in silicon-on-insulator photonic wires. *Ieee Journal of Selected Topics in Quantum Electronics* **2006**, *12*, 1394–1401.

[39] Baehr-Jones, T. W.; Hochberg, M. J. Polymer silicon hybrid systems: A platform for practical nonlinear optics. *Journal of Physical Chemistry C* **2008**, *112*, 8085–8090.

[40] Almeida, V. R.; Barrios, C. A.; Panepucci, R. R.; Lipson, M. All-optical control of light on a silicon chip. *Nature* **2004**, *431*, 1081–1084.

[41] Xu, Q. F.; Almeida, V. R.; Lipson, M. Micrometer-scale all-optical wavelength converter on silicon. *Optics Letters* **2005**, *30*, 2733–2735, Times Cited: 53 54.

[42] Bogaerts, W. *Nanophotonic Waveguides and Photonic Crystals in Silicon-on-Insulator*; Ghent university, 2004.

[43] Zakery, A.; Elliott, S. R. Optical properties and applications of chalcogenide glasses: a review. *Journal of Non-Crystalline Solids* **2003**, *330*, 1–12.

[44] Roelkens, G. *Heterogeneous III-V/Silicon photonics: Bonding technology and integrated devices*; Ghent university, 2007.

[45] Hendry, E.; Hale, P. J.; Moger, J.; Savchenko, A. K.; Mikhailov, S. A. Coherent Nonlinear Optical Response of Graphene. *Physical Review Letters* **2010**, *105*,.

[46] Yuan, Z.; Anopchenko, A.; Daldosso, N.; Guider, R.; Navarro-Urrios, D.; Pitanti, A.; Spano, R.; Pavesi, L. Silicon Nanocrystals as an Enabling Material for Silicon Photonics. *Proceedings of the Ieee* **2009**, *97*, 1250–1268.

[47] Moreels, I.; De Geyter, B.; Van Thourhout, D.; Hens, Z. Transmission of a quantum-dot-silicon-on-insulator hybrid notch filter. *Journal of the Optical Society of America B-Optical Physics* **2009**, *26*, 1243–1247.

[48] Moreels, I.; Lambert, K.; Smeets, D.; De Muynck, D.; Nollet, T.; Martins, J. C.; Vanhaecke, F.; Vantomme, A.; Delerue, C.; Allan, G.; Hens, Z. Size-Dependent Optical Properties of Colloidal PbS Quantum Dots. *Acs Nano* **2009**, *3*, 3023–3030.

2

Synthesis of CdTe, PbS and PbS/CdS quantum dots

2.1 Introduction

2.1.1 The hot injection synthesis

Colloidal quantum dots are synthesized using wet chemistry, where especially the hot injection approach leads to highly monodisperse suspensions of nanocrystals. The method combines precursors and ligands or surfactants to control the nucleation and growth of the nanocrystals and stabilize the resulting colloid by steric hindrance. Since its introduction in 1993 for the synthesis of CdS, CdSe and CdTe nanocrystals, the hot injection method[1] has become an established procedure that is widely used by the nanocrystal community. It has been extended to form nanocrystals of a wide range of materials, including semiconductors, metals and metal oxides[2–4] where it typically leads to an outstanding control over nanocrystal size and shape. The use of QDs has been demonstrated for various applications in photonics, including lighting, displays, photovoltaics and photodetection but also for bio-imaging or sensing[5–11]. Far less reports showed the application of the non-linear optical properties of colloidal QDs. In this context, optical switching in photonic circuits has been demonstrated[12].

Detailed studies on the synthesis of CdSe quantum dots have shown that the nucleation and growth of colloidal nanocrystals in the hot injection synthesis is driven by the in-situ formation of a solute or monomer species out of the initial precursors. The precursor injection initiates this solute formation, resulting in a supersaturated reaction mixture in which stable nuclei can form that grow larger by the continued addition of monomer species. An important element of this growth process, leading to the narrow size distributions that are so characteristic of the hot injection synthesis, is size distribution focusing. This is a process in which smaller nanocrystals grow faster than larger nanocrystals and that typically occurs when nanocrystal growth is diffusion limited and the supersaturation is high. At the end of the reaction, when all precursors have been depleted, further growth can still happen by Ostwald ripening[13–15]. This is a process in which the large nanocrystals continue to grow, yet at the expense of the smaller nanocrystals as illustrated in Fig. 2.1. Very often, Ostwald ripening will lead to a broadening of the size distributions and reactions are typically stopped before they enter this growth regime

2.1.2 Quantum dots synthesized in this work

In this work, we have synthesized colloidal quantum dots tailored for applications in nonlinear optics in combination with the silicon-on-insulator photonics platform, i.e., in the wavelength range 1300-1600 nm. This involves materials such as PbS and PbS/CdS QDs, where the bandgap transition can be matched to the photon energy or CdTe, where the photon energy can correspond to half the bandgap energy. The aim of this chapter is to summarize the different synthesis recipes used and provide all the basic materials characteristics we will need throughout this work.

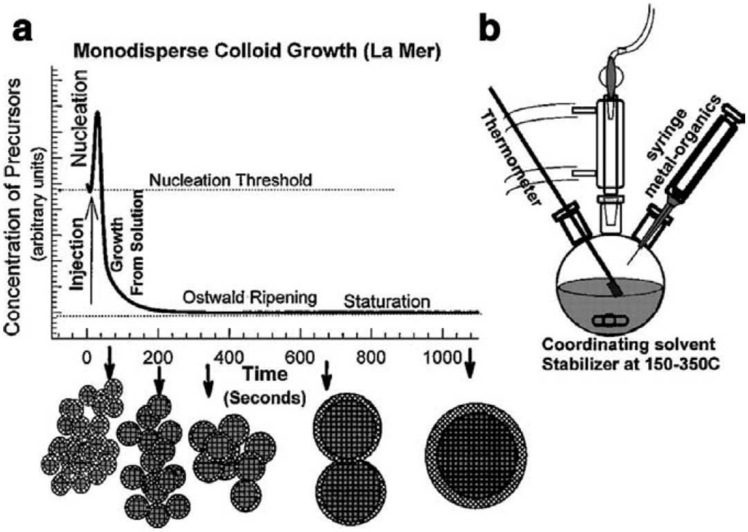

Figure 2.1: Schematic reprinted from Murray et al[16] (a) illustrating the stages of nucleation and growth for monodisperse colloidal nanocrystals. (b) Representation of the synthetic apparatus used in the preparation of monodisperse QDs.

Especially in the case of CdTe, novel synthesis recipes had to be developed to obtain sufficiently large CdTe QDs that have a bandgap in the range 650-800 nm. Thanks to these efforts, it was possible to extend the CdTe QD sizing curve and determine oscillator strengths and absorption coefficients also for large CdTe QDs.

2.2 Synthesis of CdTe QDs

2.2.1 Synthesis procedure

Used chemicals

For the synthesis of CdTe nanocrystals, cadmium oxide (CdO, $>$99.99%, Aldrich) and tellurium (Te, 99.997%, Aldrich) were used to prepare the Cd and Te precursor, respectively. Tetradecylphosphonic acid (TDPA, $>$99% , PCI Synthesis), hexadecylamine (HDA, 98%, Sigma-Aldrich), oleylamine (OLA, 80-90%, Acros Organics) and oleic acid (OA, 90%, Sigma-Aldrich) were used as ligands and technical 1-octadecene (ODE, 90%, Alfa-Aesar) was used as the solvent. Finally, analytical grade methanol, ethanol and toluene, purchased from VWR were used for purification and storage.

Precursor preparation

In a typical synthesis, a CdTDPA (cadmium tetradecylphosphonic acid) complex is prepared as the cation precursor prior to the actual synthesis by adding 6.79 mmol of CdO (0.87244 g) together with 20.52 mmol of TDPA (5.712g) in a three-neck flask. The solid compounds are left under a nitrogen atmosphere at room-temparature for one hour and are then liquefied by heating it to 100°C for 1/2 hour. Next, the temperature of the mixture is *slowly* increased, without bubble forming, to 300°C, where the CdTDPA compound is formed and a colourless solution appears. The solution is then poured in a metal beaker where it solidifies. Afterwards, the CdTDPA is grinded to a fine powder and stored. To obtain the anion precursor, 15 mmol of Te (1.914 g) is added to 10 mL of tri-n-octylphosphine (TOP) solution and the mixture is heated up for 1/2 hour in a nitrogen glovebox. Herafter, the Te is dissolved in the TOP liquid, resulting in a 1.5 M Te in TOP solution with a flash-green color.

Actual synthesis

Various procedures have been used to synthesize monodisperse colloidal zinc-blende (zb) CdTe QDs in the range of 4-6 nm and we refer to [1;17;18] for the literature. For the synthesis of QDs with a diameter of 6-11 nm, we grow them up in a two-step procedure. The first step is the growth of the initial core particles, the *seed QDs* and then in a second step we add continously in time extra precursors in the flask containing the seed particles, a process we will refer to as continuous multiple injection (CMI). As we will show, this method fastens the growth of the large particles and avoids entering the Ostwald-regime by creating sufficient monomers to be consumed for all particles. We will try to optimize each

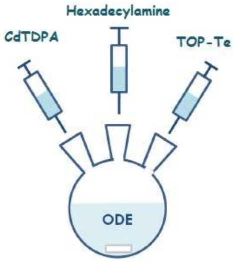

Figure 2.2: Scheme depicting the synthesis of CdTe QDs.

of the two outlined steps. An important point is that the nanocrystals formed in the first step are sufficiently large – meaning a diameter close to 6 nm – to facilitate the second (CMI) step.

In the first step the seed particles are synthesized by the injection of 0.084 g of CdTDPA with a 1:3 Cd to TDPA ratio, followed by 0.1933 g of HDA with a 1:8 Cd to HDA ratio. Added to this is 7.8 mL of octadecene (ODE) in the three-neck flask (Fig. 2.2). The mixture is kept under a nitrogen flow during 1/2 h at room temperature and is then heated up till 100°C for 1.5 h. The anion (Te) precursor is made of 2 mL of a mixture of 3.7 mL ODE, 0.7 mL TOP and 0.1 mL of a 1.5 M TOP-Te solution. The corresponding Cd to Te ratio is 3:2. The anion Te-precursor is injected at a temperature of 280°C, and the temperature drop leads to a growth temperature of 260°C, which is maintained throughout the reaction. The combination of the precursor ratios – 1:8 Cd to HDA and 3:2 Cd tot Te – yielded nanocrystals with sufficiently large diameters suitable for the CMI process. This resulted in QDs with an aborption peak at 690-700 nm, but achieved after 8 hours 20 min of growth, which is a time consuming proces.

Figure 2.3(a) shows normalized absorption spectra recorded on aliquots taken at different times after the start of the reaction. One clearly observes a very slow red shift of the absorption peak with time, indicating an almost inert nanocrystal growth. The duration of the synthesis can be significanly decreased by increasing the injection tempearture to 305°C and letting the QDs grow at 290°C. After 1 h 4 min of growth time (Fig.2.3(b)) the particles reached already a size of 6.0 nm corresponding to an absorption wavelength of 680 nm. As we will show below, the size is determined using TEM-analysis. Moreover, allowing the seed-nanocrystals to grow more than the mentioned duration time yielded Ostwald ripening. In addition, increasing the injection temperature above 305°C is no longer possible as ODE will start to evaporate due to the proximity of the ODE boiling temperature at 315°C.

To reach larger sizes a second injection of cation-anion precursor is made. A good estimate of the additional amount of precursor needed is obtained by calculating the extra amount of CdTe needed to reach the target diameter. In practice, this involves calculating the relative increase in particle volume (R) and rescale the amount of 'precursor' required for the second injection according to R. We illustrate this for a target diameter of 9 nm ($\lambda = 745$ nm), which yields a ratio between initial and second Cd amount injection of 1:4 ($R = 4$). To prepare this precursor, 0.84 g of CdTDPA (1 mmol) is dissolved in 4 mL ODE and heated up till 255°C for 15 min. After cooling to a temperature of 45°C, 0.67 mL of 1.5M TOP-Te solution is added and well mixed. This temperature is sufficiently low to avoid nucleation and high enough to decrease the viscosity of the gel-like mixture. After a reaction time of 64 min of the previously described procedure, 2 mL of the precursor is then loaded in a syringe and injected continuously into the reaction solution using a (PROSENSE B.V.) syringe pump at a rate of 2 mL/h. Fig. 2.3(b) shows the red shift of the absorption spectra from the start of the CMI - using QDs with an exciton peak at 680 nm - towards the end at 40 min of growth time. Clearly the target size is reached from the finally obtained absorbance spectrum, with a bandgap wavelength of ≈740 nm.

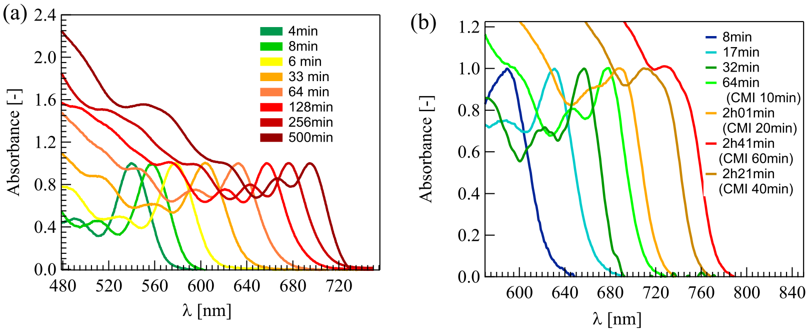

Figure 2.3: (a) Synthesis of CdTe QDs at low injection temperature of 280°C. (b) Synthesis of the CdTe QDs at high injection temperature followed by a CMI process using the nanocrystals grown after 64 min as the seed material.

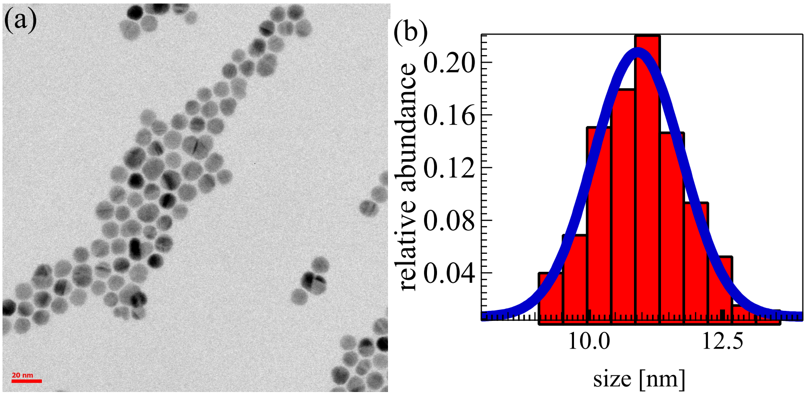

Figure 2.4: (a) TEM image of large zb-CdTe QDs (scalebar: 20 nm) synthesized by the CMI process ($R = 6$). (b) Statistical analysis of the TEM pictures, yielding an average QD-size of 10.9 nm with a size dispersion of 8%.

2.2.2 Basic material properties

The large CdTe QDs synthesized for this work have been used to determine a more extended sizing curve for these quantum dots, which will be outlined in the next section. For this, the average diameter d of quantum dots in different batches and their standard deviation (σ_d) were determined by the analysis of TEM micrographs. In this context, the ratio $\frac{\sigma_d}{d} \times 100$ between the standard deviation and the mean quantum dot diameter – denoted as the size dispersion – is used as a measure of the mono- or polydisperse character of a quantum dot dispersion. Figure 2.4(a) shows a representative TEM micrograph of the CdTe QDs obtained by the synthesis procedure as outlined in section 2.2.1. The samples for the micrographs are prepared by dipping a TEM grid in a 0.5-1 μM CdTe QD dispersion. One sees this results in the formation of small hexagonally close-packed assemblies of QDs, from which a diameter of each QD was determined from the equivalent circular diameter d_{QD}:

$$d_{QD} = \sqrt{\frac{4\,A}{\pi}} \tag{2.1}$$

Here A is the projected surface area of the QDs in the TEM micrographs. By combining multiple TEM images of the CdTe QDs, 300-400 nanocrystals were analysed for each batch. The resulting histogram is shown in Fig. 2.4(b), to which a Gaussian distribution can be fitted. The average diameter and σ_d are directly calculated from the individual diameters, resulting in a number of d=10.98 nm, σ_d=0.90 nm and thus a size dispersion of 8.2% for this sample. These values agree with the ones obtained from the fitted Gaussian distribution. A more elaborate discussion, including a more extensive dataset is given in Kamal et al.[19].

The crystal structure of the synthesized CdTe QDs obtained by the above described procedure are examined by powder X-ray diffraction (XRD). For the XRD measurements the samples are prepared by drying the QD suspensions under a nitrogen flow and resuspending the dry powder in a mixture of 2 volume units of hexane and 4 volume units of heptane. Subsequent drop casting of the QD suspensions on a 1 cm^2 glass plate completes the sample preperations. All the XRD measurements showed the fingerprint features of the zincblende crystal stucture.

An important quantity of colloidal nanocrystal suspensions is the concentration c of particles in the solution. The concentration is obtained through elemental analysis of the QDs dissolved in a HNO_3 solution. The CdTe QDs will decompose in Cd and Te atoms and via inductively coupled mass spectroscopy (ICP-MS), the concentration of the cadmium in solution $\mathrm{C_{Cd}}$ (mg/L) is determined from which c is calculated as:

$$c = \frac{6\mathrm{C_{Cd}}\mathrm{a_{CdTe}}}{8\pi d^3\mathrm{M_{Cd}}}(1+\frac{1}{\rho}) \tag{2.2}$$

Here, $\mathrm{a_{CdTe}} = 0.648$ nm is the zincblende CdTe lattice parameter and ρ is the Cd:Te ratio determined via Rütherford backscattering spectroscopy (RBS). This number is always found to exceed one, which is attributed to an enrichment of Cd at the CdTe nanocrystal surface[19]. $\mathrm{M_{Cd}}$ is the molar mass of cadmium. Table 3.1 illustrates the data for the different QD diameters.

2.2.3 An extended sizing curve

From the absorbance spectrum of each batch, we determine the wavelength λ_g in nanometer from the peak of the first 1S-1S transiton as shown in Fig 2.5(a). Thus the energy E_g in eV of the 1S-1S bandgap

d (nm)	$\mathrm{C_{Cd}}$ (mg/L)	ρ	A_{410} ($\mathrm{cm^{-1}}$)	c (10^{-6}mol/L)
3.19	111.3	1.39	0.199	0.5685
3.73	236.1	1.13	0.429	0.0825
4.14	483.4	1.20	0.286	0.4013
5.20	255.2	1.14	0.466	0.3284
5.67	123.7	1.09	0.221	1.2530
7.65	97.8	1.12	0.297	0.0598
10.97	122.5	1.07	0.360	0.0257

Table 2.1: CdTe diameter d, Cd weight concentrations $\mathrm{C_{Cd}}$ as obtained by ICP-MS measurements, ρ is the RBS Cd:Te ratio, A is the absorbance at 410 nm and the c is the calculated concentration of the suspensions used.

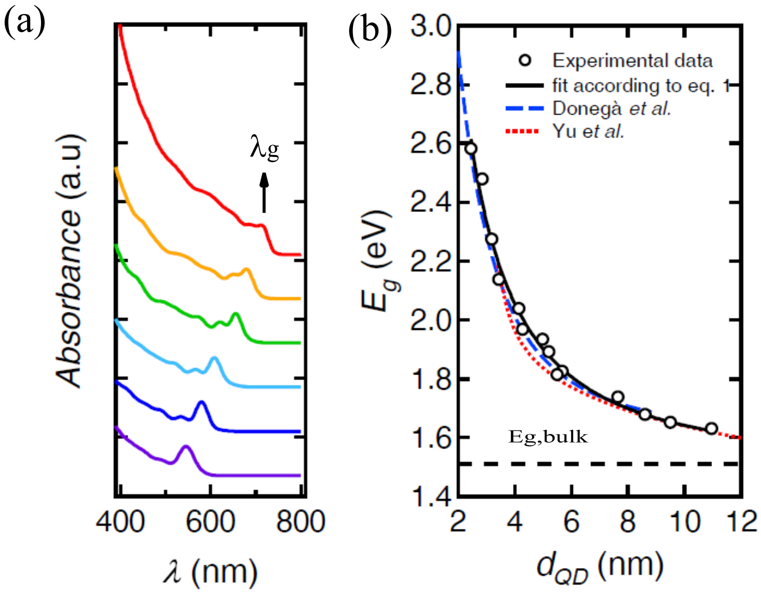

Figure 2.5: (a) Absorption spectra of CdTe nanocrystals with diameter d_{QD} of (top to bottom) 7.65, 5.67, 5.20, 4.41, 3.73 and 3.19 nm determined via TEM. As denoted by the arrow for $d_{QD} = 7.65$ nm the peak of the first 1S-1S exciton transition corresponds to the bandgap wavelength λ_g from which the bandgap energy E_g is calculated. (b) Determined sizing curve of the CdTe QDs relating E_g and d_{QD} as outlined in (a). Markers represents the experimental data which are well fitted to Eq. 2.3. Blue and red sizing curves are respectively according to Donega et al.[20] and Yu et al.[21]. Dashed black line is the bandgap of bulk CdTe.

transition is calculated as $\frac{1239.84}{\lambda_g}$. Plotting the ensuing combinations of diameter and bandgap yields the CdTe sizing curve as shown in Fig. 2.5(b). Here, the experimental data have been fitted to:

$$E_g(d) = 1.51 + \frac{1}{0.048d^2 + 0.29d - 0.09} \tag{2.3}$$

In this expression, the first term is kept fixed at the bandgap of bulk CdTe (1.51 eV) and the three factors in the denominator of the second term have been used as adjustable variables. The resulting fit has been added as a black line to Fig. 2.5(b). Next to the best fit according to Eq. 2.3, the figure shows a blue and a red line that correspond to sizing curves presented by Donega *et al.*[20] and Yu *et al.*[21]. A good correspondance between our sizing curve and that of Donega et al.[20] is obtained, with maximum deviations in diameter of about 0.3 nm. On the other hand, more important deviations up to 0.6 nm are found with the sizing curve of Yu *et al.*[21].

2.2.4 Extinction coefficients

The concentration c as described in section 2.2.2 for the batches summarized in Table 3.1 was determined via ICP-MS, which is an accurate but time consuming and cost increasing method. Additionally, the QDs have to be ’destroyed’ in the nitric acid and therefore it is not a convenient way for use in practice. Nevertheless, the ICP-MS data can serve as a calibration set. The absorbance A at the wavelength of 410 nm, determined via absorption spectroscopy, is linked to c by the Beer-Lambert law :

$$A = \epsilon_{ext} c L \tag{2.4}$$

Here, $L = 1$ cm is the length of the cuvette containing the QD suspension and given c from the ICP-MS data the molar extinction coefficient at 410 nm $\epsilon_{ext,410}$ is calculated. This quantity scales proportionally to the volume of the QDs and writing d as the size of the QDs in nanometer, a best fit to the experimental data yields ($\epsilon_{ext,410}$) in $\mathrm{cm}^{-1}/\mu\,\mathrm{M}$:

$$\epsilon_{ext,410} = 0.0105\, d^3 \tag{2.5}$$

Therefore by knowing $\epsilon_{ext,410}$ and through a measurement of A using absorption spectroscopy – a low cost, non-destructive and fast measurement – the QD-concentration is easily determined via Eq. 2.4. The origin of the scaling of $\epsilon_{ext,410}$ with the volume comes from the independency of the intrinsic absorption coefficient on d, a point we will address and discuss together with $\epsilon_{ext,410}$ in more depth in the next chapter.

2.2.5 Stability under ambient atmosphere

We have studied the evolution of the absorbance spectrum of a batch of 4.9 nm and 10.9 nm CdTe QDs when stored under ambient atmosphere. Figure 2.7 shows the spectra taken at different times during storage. For the smaller sized CdTe QDs a spectral blue shift of 6 nm is noticed after a storage of 20 days, while a 1 nm blue shift is measured during the same period of time for the larger QDs. From the bandgap absorption, an effective size is determined using the sizing curve (Fig. 2.7b-c). The results yield a final decrease in effective size of 1.5 Å and 1.8 Å for the smaller and bigger QDs, respectively. While the final decrease in effective size for smaller QDs is accurately analyzed, the determined value for the larger QDs should be more seen as an estimate. This is because the sizing curve is close to size independent at these large diameters and therefore small varations of the bandgap might lead to large variations in the diameter. Nevertheless, the determined value of size decrease in 20 days (1.8Å) for the larger QDs is similar to the one determined for the smaller QDs (1.5Å), indicating that the induced error might be low.

2.3 Synthesis of PbS QDs

PbS quantum dots are synthesized following the procedure developed by Moreels et al..[22] Here, we summarize the main steps in this synthesis and the most important materials characteristics.

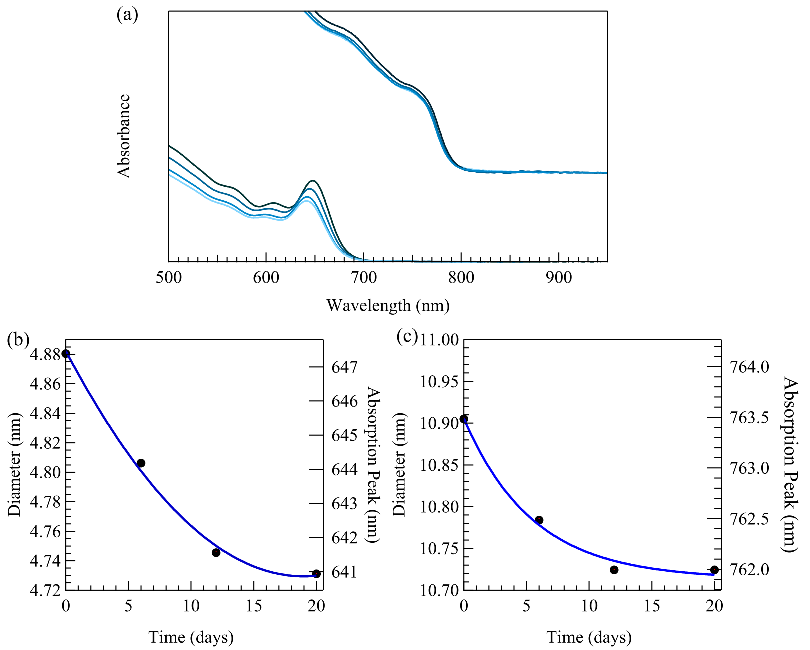

Figure 2.6: (a) Series of CdTe QD spectra for two particle sizes of 4.9 nm and 10.9 nm shown at the bottom and the top, respectively. The spectra are taken at different times during storage at ambient conditions. (b) The decrease in effective size for the bottom spectra in (a) is 1.5 Å in 20 days. (c) The decrease in effective size for the top spectra in (a) is 1.8 Å in 20 days.

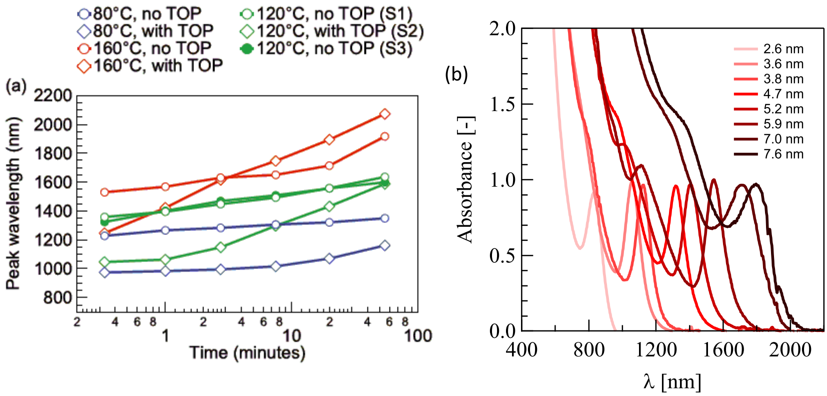

Figure 2.7: ((a) Wavelength position reproduced from[22] of the first 1S-1S aborption peak as function of reaction time and temperature for PbS QDs. The diamond and circle represent the synthesis without TOP and with TOP, respectively. (b) PbS QDs absorption spectra illustrating the spanning from $\approx 800 - 2000\,nm$. The labeling indicates the corresponding size.

2.3.1 Synthesis procedure

Used chemicals

For the synthesis of PbS quantum dots, lead(II) chloride ($PbCl_2$, 99.999%, Alfa-Aesar) and sulfur (S, 99.999%, Strem Chemicals) were used for preparing the initial precursors. Tri-n-octylphosphine (TOP, 97%, Strem Chemicals), oleic acid (OlAc, 90%, Sigma-Aldrich) were used as ligands and oleylamine (OLA, 80-90%, Acros Organics) was used as the solvent. Finally, analytical grade ethanol and toluene, purchased from VWR were used for purification and storage.

Precursor preparation

A sulfur precursor is prepared before the actual synthesis by dissolving 0.16 g (5 mmol) of sulfur in 15 mL of oleylamine (OLA). The solution is heated up in a nitrogen atmosphere (glovebox) till 120°C. After 1/2h of reaction, all the sulfur has dissolved resulting in a 0.33 M OLA-S solution with a dark-red color.

Actual synthesis

Prior to the injection, 3 mmol (0.834 g) of lead(II)cloride ($PbCl_2$) is weighted in a three-neck flask, 7.5 mL of oleylamine (OLA) is added and the mixture is heated up till 125°C and left for 1/2h. A nitrogen flow is send in the flask to remove any evoparating impurities. The solution is then put under a nitrogen atmosphere and brought to the target temperature for injection. Hereafter, 2.25 mL of 0.33 M OLA-S is injected, which typically results in a temperature drop of 5-10°C and the resulting growth temperature is maintained throughout the reaction. Depending on the required particle size, the target temperature and reaction time are determined[22] as shown in Fig. 2.7b. For smaller target sizes (1-3 nm), 375μmol (170 μl) of tri-n-octylphosphine (TOP) is added to the 2.25 mL OLA-S anion precursor at room temperature. This replaces 50% of the OLA-S by TOP-S and results in a wider range of accessible size ranges[22]. After the growth 10 mL of toluene is added to quench the reaction followed by 18 mL of EtOH. The suspension is set for centrifugation. Hereafter, the supernatant is decantated and the QDs are resupsended in 10 mL of toluene.

Ligand exchange. Using solution NMR spectroscopy, the PbS QDs as described above where shown to be capped by oleylamine[22]. This is a labile ligand which results in aggregation and clustering of the PbS QDs during further purification. To avoid this, the OLA ligands are exchanged for oleic acid (OlAc) molecules. Typically, 1.5 mL of OlAc is added together with toluene to the QDs suspension in a 1.5:10 OlAc:toluene ratio. Hereafter, the QDs are precipitated with EtOH and resuspended in toluene. This ligand exchange procedure is repeated and in a final step the QDs are precipitated once more with EtOH to remove any excess of free OlAc in the suspension.

Removal of $PbCl_2$. After the ligand exchange, the PbS QD suspensions still appear to be slightly turbid. This is due to presence of unreacted $PbCl_2$ resulting from the synthesis. The $PbCl_2$ QD suspension are placed in a centrifuge for 5-6 h resulting in a clear supernatant with the QDs in toluene, which is decantated and stored in a fridge.

2.3.2 Basic material properties

The QD material characterizations, e.g. *spectra*, *crystal structure*, *size* and *concentration*, are done relying on literature reports and using absorption spectroscopy. A known volume amount of the QD samples is taken out and the toluene is being dried out using a nitrogen flow. The QDs are resuspend in tetrachloroethylene (C_2Cl_4) liquid. Opposite from toluene, C_2Cl_4 is a transparent liquid in the visible and near-infrared range, allowing for a quantitative characterization of the PbS QDs materials. The measured spectra for the different syntheses with the corresponding sizes are illustrated in Fig. 2.7(b).

Using XRD and high resolution TEM measurements on individual particles[23], the PbS QDs were shown to be quasi-spherical and to have the rocksalt crystal structure, with a lattice parameter equal to bulk PbS (a = 5.936 Å).

2.3.3 Sizing curve

The size of the above described QDs is extracted using the sizing curve of PbS QDs[23] :

$$E_g = 0.41 + \frac{1}{0.283d + 0.0252d^2} \tag{2.6}$$

2.3.4 Extinction coefficients

The concentration c of the PbS QD suspensions described in the previous sections is determined using the Beer-Lambert law at 400 nm as given in Eq. 2.4 and ϵ_{ext} the molar extinction coefficient at 400 nm[22]:

$$\epsilon_{ext,400} = 0.0234\, d^3 \tag{2.7}$$

with d the size in nm and the corresponding unit in $\mathrm{cm}^{-1}/\mu\,\mathrm{M}$.

2.3.5 Stability under ambient atmosphere

The PbS QDs as prepared by the given synthesis procedure and capped by OlAc ligands were shown to be stable under ambient atmosphere[23]. After six weeks following the synthesis, the spectra of the PbS QDs remained unchanged.

2.4 Synthesis of PbS/CdS QDs

2.4.1 Synthesis procedure

Used chemicals

The chemicals needed for PbS/CdS core shell QDs are the same as those mentioned before for the synthesis of PbS core particles. Additionally, diphenyl ether (DPE, $>$99%, Sigma Aldrich) is purchased.

Precursor preparation

Before the actual synthesis a cadmium oleate (CdOA) precursor is prepared by adding 15.58 mmol (2 g) of CdO together with 19.77 mL of OlAc in a three-neck flask. All reagents are loaded in a single flask and put under a nitrogen atomsphere at a temperature of 125°C for 45 min. Next, the temperature is increased till 200°C untill all the compounds are liquefied. Finally, diphenylehter is added to dilute the mixture to a solution with a cadmium concentration of 0.35 M.

Actual synthesis

In the following, the synthesis and material characterization of core shell QDs will be demonstrated for nanocrystals absorbing at 1450 nm. The PbS QDs were prepared using a procedure as described above, where the synthesis conditions were chosen such that oleate capped PbS QDs with a first exciton absorption at 1590 nm – corresponding to a diameter of 6.2 nm – were formed (see blue line in Fig. 2.8). For the CdS shell growth, a cationic exchange procedure was used, starting from a 5.7μM QD dispersion in toluene. The dispersion was heated to 125°C in

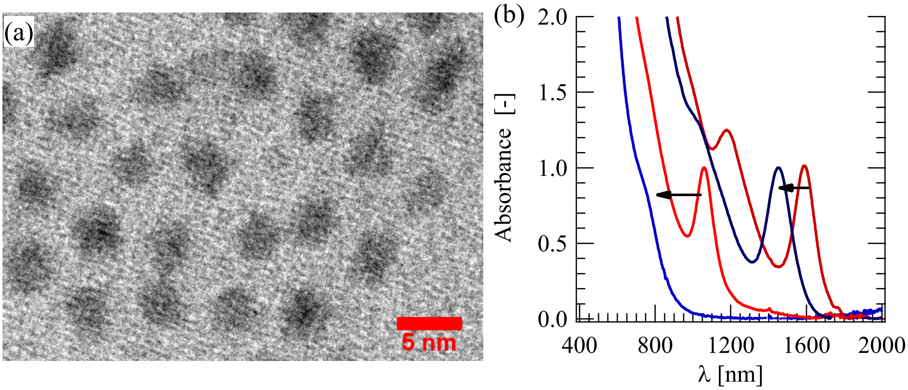

Figure 2.8: (a) TEM image of 6.2 nm PbS/CdS core/shell QDs. (b) The QDs core shell exciton absorption (red line) shows a blueshift, after cationic exchange procedure, compared with the QD core exciton absorption (blue line).

a reaction flask placed in an nitrogen atmosphere. Cadmium oleate was added in a 20:1 Cd to Pb ratio. This starts a cationic exchange process in which the outer Pb^{2+} cations are replaced by Cd^{2+} cations, leading to a heterostructure with a PbS core and a CdS shell. The reaction was stopped by quenching with a double amount of ethanol as compared to the reaction volume. After centrifugation and decantation the PbS/CdS QDs were suspended in toluene.

2.4.2 Basic material properties

Similar to PbS core QDs, the characterization of the PbS/CdS nanocrystals is done relying on literature reports[24;25] and using absorption spectroscopy. Again, a known amount of the QD sample is taken out and the toluene is being dried out using a nitrogen flow. The QDs are resuspended in tetrachloroethylene (C_2Cl_4). The TEM micrograph of the sample is shown in Fig. 2.8(a) and as illustrated in Fig. 2.8(b) the exciton absorption is shifted from 1590 nm to 1450 nm indicating an increase in the bandgap and the formation of a core/shell particle.

To quantify the size of the core particles and the concentration of the QDs it is important to know how the size is affected after the cationic exchange. Zhao et al.[24] showed that by using X-ray diffraction the PbS/CdS quantum dots form a gradual transformation from a rock salt PbS pattern to a zinc blende CdS pattern, confirming the formation of core/shell structured nanocrystals. Moreover, the overall diameter is not expected to change, due to the small difference in the lattices constants of the cubic PbS rock salt (5.94 Å) and cubic zinc blende CdS (5.83 Å). By using TEM analysis this conclusion is further confirmed by various literature reports where the cationic exchange reaction leaves the overall diameter unchanged.

2.4.3 Sizing curve

To estimate the CdS shell thickness and the average diameter d_c of the PbS core particles in the PbS core/shell QDs of our sample, it was shown by Justo et al.[25] that d_c obtained from ICP-OES (inductively coupled plasma- optical emission spectroscopy) is exactly the same value as the core diameter obtained by applying the PbS sizing curve to the peak wavelength λ_{1S-1S} of the first exciton transition of PbS/CdS core/shell QDs. Therefore Eq. 2.6 can be used, but by evaluation at a size equal to d_c:

$$E_g = 0.41 + \frac{1}{0.283 d_c + 0.0252 d_c^2} \tag{2.8}$$

This yields after solving the above equation for $\lambda_{1S-1S} = 1450\,\text{nm}$ ($E_g = 0.855\,\text{eV}$), a d_c value of 5.8 nm. Given the total size d_{tot} of the PbS/CdS core/shell QDs to 6.2 nm, a shell thickness $\delta = \frac{d_{tot}-d_c}{2}$ of 0.4 nm is found.

2.4.4 Extinction coefficients

Unlike PbS core QDs as outlined in in section 2.2.4, the molar extinction coefficient ϵ_{ext} is not expected to merely scale with the volume for PbS/CdS core/shell QDs and therefore a straightforward relation between this quantity and the concentration is not possible. Furthermore, no literature reports the determination of c via this procedure. Other route is reported[25] using the intrinsic absorption coefficient μ_i of PbS/CdS core/shell QDs and it is shown that μ_i depends on the ratio p of the CdS shell volume (V_s) to the total PbS/CdS volume (V_{tot})). In this context, we can rely on their reported ICP-OES data at 400 nm to calculate $\epsilon_{ext,400}$ and suggest following form for the extinction coefficient (see Appendix A.1) :

$$\epsilon_{ext,400} = A_p \, d^3 \tag{2.9}$$

With d the total QD size in nanometer, $\epsilon_{ext,400}$ in $\frac{\mathrm{cm}^{-1}}{\mu\,\mathrm{M}}$ and A_p a prefactor depending on p:

$$A_p = 0.02392 + 3.2599\,10^{-3}\,p - 1.6414\,10^{-3}\,p^2 - 1.2092\,10^{-2}\,p^3 \tag{2.10}$$

In Eq. 2.9, we maintained the volumescaling and fitted the data using a third degree polynomial prefactor. Note that at zero p-values the above prefactor is in line with the reported one for PbS QDs.

2.4.5 Stability under ambient atmosphere

Since PbS QDs were shown to be stable under ambient atmopshere, adding a CdS shell will increase the protection of the core in the core/shell nanocrystals rendering the PbS/CdS QDs to be very robust under ambient atmosphere and therefore suitable for post-treatments and QD-layer depositions.

2.5 Conclusion

CdTe QDs were synthesized with sizes varying from 3 to 11 nm using the hot injection method. The bandgap is tunable between 500 nm and 760 nm, or 1.6-2.48 eV. The large quantum dot size were obtained using a continuous injection of precursors at a controlled reaction time, avoiding Ostwald ripening. The sizing curve of the CdTe QDs is constructed by combining UV-vis-absorption spectroscopy and TEM-imaging. PbS core and PbS/CdS core/shell QDs are synthesized using the hot-injection method. Nanocrystal sizes from 2.5-7.5 nm are obtained with absorption peaks in the range 800-2000 nm or 0.62-1.5 eV.

Bibliography

[1] Murray, C. B.; Norris, D. J.; Bawendi, M. G. Synthesis and characterization of nearly monodisperse CdE (E=S, Se, Te) semiconductor nanocrystallites. *Journal of the American Chemical Society* **1993**, *115*, 8706–8715.

[2] Murray, C. B.; Sun, S. H.; Gaschler, W.; Doyle, H.; Betley, T. A.; Kagan, C. R. Colloidal Synthesis of Nanocrystals and Nanocrystal Superlattices. *IBM J. Res. Dev.* **2001**, *45*, 47–56.

[3] Murray, C. B.; Kagan, C. R.; Bawendi, M. G. Synthesis and characterization of monodisperse nanocrystals and close-packed nanocrystal assemblies. *Annual Review of Materials Science* **2000**, *30*, 545–610.

[4] Talapin, D. V.; Lee, J.-S.; Kovalenko, M. V.; Shevchenko, E. V. Prospects of Colloidal Nanocrystals for Electronic and Optoelectronic Applications. *Chem. Rev.* **2010**, *110*, 389–458.

[5] Liu, Z.; Yin, L.; Ning, H.; Yang, Z.; Tong, L.; Ning, C.-Z. Dynamical Color-Controllable Lasing with Extremely Wide Tuning Range from Red to Green in a Single Alloy Nanowire Using Nanoscale Manipulation. *Nano Letters* **2013**, *13*, 4945–4950.

[6] Sun, B.; Findikoglu, A. T.; Sykora, M.; Werder, D. J.; Klimov, V. I. Hybrid Photovoltaics Based on Semiconductor Nanocrystals and Amorphous Silicon. *Nano Letters* **2009**, *9*, 1235–1241.

[7] Sargent, E. H. Infrared photovoltaics made by solution processing. *Nature Photonics* **2009**, *3*, 325–331.

[8] Clifford, J. P.; Konstantatos, G.; Johnston, K. W.; Hoogland, S.; Levina, L.; Sargent, E. H. Fast, sensitive and spectrally tuneable colloidal quantum-dot photodetectors. *Nature Nanotechnology* **2009**, *4*, 40–44.

[9] Johnston, K. W.; Pattantyus-Abraham, A. G.; Clifford, J. P.; Myrskog, S. H.; MacNeil, D. D.; Levina, L.; Sargent, E. H. Schottky-quantum dot photovoltaics for efficient infrared power conversion. *Applied Physics Letters* **2008**, *92*,.

[10] Michalet, X.; Pinaud, F. F.; Bentolila, L. A.; Tsay, J. M.; Doose, S.; Li, J. J.; Sundaresan, G.; Wu, A. M.; Gambhir, S. S.; Weiss, S. Quantum dots for live cells, in vivo imaging, and diagnostics. *Science* **2005**, *307*, 538–544.

[11] Yebo, N. A.; Sree, S. P.; Levrau, E.; Detavernier, C.; Hens, Z.; Martens, J. A.; Baets, R. Selective and reversible ammonia gas detection with nanoporous film functionalized silicon photonic micro-ring resonator. *Optics Express* **2012**, *20*, 11855–11862.

[12] Yuan, Z.; Anopchenko, A.; Daldosso, N.; Guider, R.; Navarro-Urrios, D.; Pitanti, A.; Spano, R.; Pavesi, L. Silicon Nanocrystals as an Enabling Material for Silicon Photonics. *Proceedings of the Ieee* **2009**, *97*, 1250–1268.

[13] Zhang, H.; Wang, L. P.; Xiong, H. M.; Hu, L. H.; Yang, B.; Li, W. Hydrothermal synthesis for high-quality CdTe nanocrystals. *Advanced Materials* **2003**, *15*, 1712.

[14] Abe, S.; Capek, R. K.; Al, A. B. E. E. T. Tuning the Postfocused Size of Colloidal Nanocrystals by the Reaction Rate : From Theory to Application. *Acs Nano* **2012**, 42–53.

[15] Peng, X. G.; Wickham, J.; Alivisatos, A. P. Kinetics of II-VI and III-V colloidal semiconductor nanocrystal growth: ”Focusing” of size distributions. *Journal of the American Chemical Society* **1998**, *120*, 5343–5344.

[16] Murray, C.; Kagan, C.; Bawendi, M. Synthesis and characterization of monodisperse nanocrystals and close-packed nanocrystal assemblies. *Annu. Rev. Mater. Sci.* **2000**, *30*, 545.

[17] Yu, W. W.; Wang, Y. A.; Peng, X. G. Formation and stability of size-, shape-, and structure-controlled CdTe nanocrystals: Ligand effects on monomers and nanocrystals. *Chemistry of Materials* **2003**, *15*, 4300–4308.

[18] Dorfs, D.; Franzl, T.; Osovsky, R.; Brumer, M.; Lifshitz, E.; Klar, T. A.; Eychmueller, A. Type-I and type-II nanoscale heterostructures based on CdTe nanocrystals: A comparative study. *Small* **2008**, *4*, 1148–1152.

[19] Kamal, J. S.; Omari, A.; Van Hoecke, K.; Zhao, Q.; Vantomme, A.; Vanhaecke, F.; Capek, R. K.; Hens, Z. Size-Dependent Optical Properties of Zinc Blende Cadmium Telluride Quantum Dots. *Journal of Physical Chemistry C* **2012**, *116*, 5049–5054.

[20] Donega, C. d. M.; Koole, R. Size Dependence of the Spontaneous Emission Rate and Absorption Cross Section of CdSe and CdTe Quantum Dots. *Journal of Physical Chemistry C* **2009**, *113*, 6511–6520.

[21] Yu, W. W.; Qu, L. H.; Guo, W. Z.; Peng, X. G. Experimental determination of the extinction coefficient of CdTe, CdSe, and CdS nanocrystals. *Chemistry of Materials* **2003**, *15*, 2854–2860.

[22] Moreels, I.; Lambert, K.; Smeets, D.; De Muynck, D.; Nollet, T.; Martins, J. C.; Vanhaecke, F.; Vantomme, A.; Delerue, C.; Allan, G.; Hens, Z. Size-Dependent Optical Properties of Colloidal PbS Quantum Dots. *Acs Nano* **2009**, *3*, 3023–3030.

[23] Moreels, I.; De Geyter, B.; Van Thourhout, D.; Hens, Z. Transmission of a Quantum-Dot-Silicon-on-Insulator Hybrid Notch Filter. *J. Opt. Soc. Am. B* **2009**, *26*, 1243–1247.

[24] Zhao, H.; Chaker, M.; Wu, N.; Ma, D. Towards controlled synthesis and better understanding of highly luminescent PbS/CdS core/shell quantum dots. *Journal of Materials Chemistry* **2011**, *21*, 8898–8904.

[25] Justo, Y.; Geiregat, P.; Van Hoecke, K.; Vanhaecke, F.; Donega, C.; Hens, Z. Optical properties of PbS/CdS quantum dots. *Journal of Phys. Chem. C* **2013**, *117*, 20171–20177.

3

Linear optical properties of multishell and graded shell quantum dots

3.1 Introduction

In the last decade, significant progress has been made on passivation of QDs. Passivation decreases the influence of the surface on the electrons and holes from the surrounding medium and makes the QDs less vulnerable to photo-oxidation and trap states. Therefore, well passivated nanocrystals show increased photoluminescence quantum yield (PLQY), are chemically robust and stable for post-treatments[1–3]. The prevailing strategy of passivating nanocrystals is by epitaxially growing one or multiple inorganic shell(s) of *larger* bandgap around the QD core, creating so called Type I core/shell QDs[4–8]. As an example, CdSe core QDs are coated with a CdS and/or ZnS shell, yielding nanocrystals[9] with an increased PLQY. Nevertheless, lattice strain at the core/shell interface limits further improvement of the PL. An alternative to core/shell

QDs are graded shell particles[10], *e.g.*, interface alloying between a CdS and a ZnS shell around a CdSe core yields a smooth potential transition at the outer layer of the CdSe/Cd$_x$Zn$_{1-x}$S graded shell QDs, decreasing the interfacial tension and resulting in an almost unity PL quantum yield[11].

In this perspective of increasing progress in colloidal nanocrystal research, characterizing the opto-electronic properties of all of these QDs is essential. Hereby, an important quantity is the intrinsic absorption coefficient μ_{int}, which is related to the molar extinction coefficient. Knowledge of this extinction coefficient in combination with the absorbance spectrum of nanocrystals in a colloidal suspension and the Beer-Lambert law, the concentration of the QDs in the solution can be extracted. In previous works, μ_{int} values were reported for dispersed PbS, PbSe, CdSe, CdTe core QDs[12–15]. Core/shell μ_{int} values are available for PbSe/CdSe and PbS/CdS QDs[16;17]. In contrast, no literature reports on the intrinsic absorption coefficient of CdSe/CdS core/shell or CdSe/CdSe$_x$S$_{1-x}$/CdS core/graded alloy/shell QDs containing an alloyed innershell. Alloying may (unintentionally) rise through thermal diffusion of the atoms at the core/shell interface as illustrated by Tschirner et al.[18] for CdSe/CdS QDs. Alternatively, alloying may be suitably introduced through a control of the precursor anion or cation reactivities[11].

Besides exploiting intrinsic absorption coefficients to fulfill (recent) developments in synthesizing multi- and graded shell QDs, it is important to check the amount of studies available reporting consistently same μ_{int} values for core QDs. This excludes errors introduced as operator-bias. Using this consistency check, molar absorption coefficients for CdSe QDs published by Yu et al.[15], for example, were re-examined by Jasieniak et al.[19] leading to considerably improved values. Similar studies were provided for PbSe and PbS QDs[12;13;20]. Moreover, in the latter studies μ_{int} values were compared with bulk values. Furthermore, together with CdSe, CdTe is one of the first key QDs that was synthesized[21], yet the amount of available studies reporting μ_{int} values are very scarce[15] and none of them were consistently verified or compared with bulk values.

In this chapter we will present a generalised description of the theoretical intrinsic absorption coefficients of core, core/shell, multi- and graded shell QDs by applying Maxwell-Garnett theory toghether with the transmission line analogy for determining the particle polarizability in (semiconductor) spherically shaped particles. Next, we will present a study of the intrinsic absorption coefficient of CdTe QDs at short wavelengths (300 nm) and around the bandgap of the QDs. The μ_{int} values will be obtained by combining UV-vis absorption spectroscopy, elemental analysis together with the sizing curve as determined in the second chapter using TEM-analysis. We will show that integrated μ_{int} values around the bandgap deviate by a factor of 3 from published reports, making the latter ones not reliable for use. Moreover, at short wavelengths, we will identify wavelength regions where size quantization is absent and the absorption coefficient is close to the bulk values. These values yield a reliable standard for use in characterizing CdTe nanocrystal suspensions.

Finally, we will determine the intrinsic absorption coefficient of CdSe/ CdSe$_x$S$_{1-x}$/CdS QDs. Based on Maxwell-Garnett theory for a multilayered particle and an alloying model considering the diffusion of the Se and S atoms at the respective inner CdSe and outer CdS shell, we show that intrinsic aborption coefficients of CdSe/CdS core/shell QDs are comparable to CdSe/ CdSe$_x$S$_{1-x}$/CdS core/alloy/shell QDs within a 5% error of calculation. As a result, μ_{int} values of CdSe/CdS core/shell QDs can be employed to determine the concentration of the alloyed CdSe/CdSe$_x$S$_{1-x}$/CdS QDs. Moreover, our theoretical description is general, as it allows to determine μ_{int} for spherical shaped graded particles and can therefore be used as a model system for all material types of complex layered QDs.

3.2 Theory

3.2.1 Maxwell-Garnett theory for μ

A dilute dispersion of colloidal semiconductor nanocrystals in a organic solvent can be considered as a composite with a Maxwell-Garnett geometry[22–24]. The theory is applicable point-like particles with a complex polarizability α_P that must be spherical and randomly dispersed in a (transparent) dielectric medium (host) with a dielectric constant ε_h. Based on this assumption a complex effective dielectric constant ε_{eff} is derived containing all the information upon interaction of the particles by an optical field:

$$\varepsilon_{eff} = \varepsilon_h \frac{1 + 2f\beta}{1 - f\beta} \tag{3.1}$$

$$\beta = \frac{\alpha_P}{3\, V_{1dot}\, \varepsilon_h} \tag{3.2}$$

These formulae relate ε_{eff} to the volume fraction f of the particles in the composite, *i.e.*, the ratio between the volume of the particles and the total volume of the composite. V_{1dot} is the total volume of a single particle. At low volume fractions ($f << 1$) as is typically the case for a composite of colloidal QDs in dispersion, Eq. 3.1 is simplified using a Taylor expansion up to a first order in f:

$$\varepsilon_{eff} = \varepsilon_h(1 + 3\beta f) + O(f^2) \tag{3.3}$$

$$n_{eff} = \sqrt{\varepsilon_{eff}} = \sqrt{\varepsilon_h}(1 + \frac{3}{2}\beta f) + O(f^2) \tag{3.4}$$

The complex effective refractive n_{eff} allows then to access the effective absorption coefficient $\mu = -\frac{ln(T)}{L}$ – with T the optical transmittance through the composite of a length L – of the QDs dispersed in a (transparent) host with a refractive index n_h:

$$\mu = \frac{4\pi \Im(n_{eff})}{\lambda} = \frac{2\pi}{\lambda\, n_h} \Im(3\,\beta\,\varepsilon_h\, f) \tag{3.5}$$

From this expression we observe that μ scales with the volume fraction and therefore by dividing μ by f, the theoretical intrinsic absorption coefficient μ_{int} is derived :

$$\mu_{int} = \frac{2\pi}{\lambda\, n_h} \Im(3\,\beta\,\varepsilon_h) \tag{3.6}$$

This quantitiy is important, because it yields a property independend of the QD concentration. As we will show, this theoretical expression for μ_{int} can be experimentally verified by analyzing the absorbance (A_λ) at a short wavelength, *e.g.* 300 nm, for various samples of QDs occupying a volume fraction f in a cuvette with a length L:

$$\mu_{int} = \frac{A_\lambda \ln(10)}{f L} \tag{3.7}$$

From the above equation it is clear that a straightforward comparison between expression 3.7 and 3.6 is possible once the parameter β or equivalently the polarizability α_P is known. In literature, formulae for polarizabilities of different types of spherical particles have been provided. At first, solutions for homogeneous spheres are reported, *i.e.*, core or core/shell particles[25;26]. Secondly, graded particles are considered where the material properties vary in space and the dielectric function may depend on the radial position in the particle. In this case, solutions are only given for a continuous dielectric function profile by Dong et al.[27], meaning that the grading should be present throughout the whole particle along the radial direction. In addition, the solution in Dong et al.[27] is only applicable for dielectric function profiles with small slopes. Finally, the solution of an N-layered multishell particle is provided[28].

In our work, we will rely on the latter solution and transform it to be suitable for generally more complex graded particles with a discontinuous or continuous dielectric function profile. Moreover, no restrictions on the profiles will be assumed. Before we will move to the explicit solution of α_P, we will introduce the local field factor, a quantity closely related to μ_{int} and therefore important in understanding the absorbance of colloidal QD dispersions.

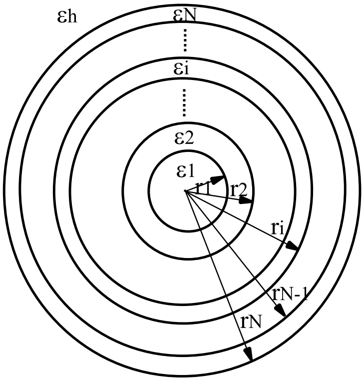

Figure 3.1: A schematic of a N-layered multishell dielectric particle presented together with the respective dielectric constants (ε_i) in each region. ε_h denotes the dielectric function of the surrounding medium (host). $r_1..r_N$ are the radial distances from the particle center to the corresponding shell regions.

3.2.2 Local field factor of multi- and graded shell QDs

The local field factor is defined as the amount of field amplitude that penetrates the centre of the QD as compared to the incoming field. The importance of this quantity can hardly be underestimated as it is directly influenced by the material properties of the QDs and its surrounding medium. For instance, the same amount of QDs dispersed in two different solvents with various refractive indices will result in dissimilar absorbance values, because the local field that the QDs feel in each of the two media is different and influenced by the solvent environment. Based on the above formulation the local field factor reads :

$$f_{LF} = -\frac{\mathbf{E}_{in}.\mathbf{E}_0}{E_0^2} \tag{3.8}$$

$\mathbf{E}_0$ is the incoming field and $\mathbf{E}_{in}$ is the local field that particles internally feel at their centre. For a homogeneous particle the internal electric field is static and is derived as the gradient of the scalar potential Φ:

$$\mathbf{E}_{in} = -\nabla\Phi_{in} \tag{3.9}$$

Based on Gauss's flux theorem[29;30] for a source free medium ($\nabla.\mathbf{E}_{in} = 0$), the solution for the internal potential is reduced to solving the Laplace equation :

$$\nabla^2 \Phi_{in} = 0 \tag{3.10}$$

In spherical coordinates (r,θ,ϕ) – with r the radial distance, θ the polar angle and ϕ the azimuthal angle – the solution for the Laplace equation is seperable and designating the incident field on the spherically shaped particles along the z-axis ($\mathbf{E}_0 = E_0 \mathbf{e}_z$, with $\mathbf{e}_z$ the unit vector along the z-direction) the solution for Equation 3.10 is written as:

$$\Phi_{in} = -A_1 E_0 r \cos(\theta) + B_1 E_0 r^{-2} \cos(\theta) \tag{3.11}$$

Here, A_1 and B_1 are two unknown parameters. At the core of the particles ($r \rightarrow 0$), the field cannot diverge to infinity ($B_1 = 0$) and therefore Equation 3.11 is simplified to the first term :

$$\Phi_{in} = -A_1 E_0 r \cos(\theta) \tag{3.12}$$

The gradient of the above potential within the core of the particles is proportional to $\mathbf{e}_z$ – which is equivalent to $\cos(\theta)\mathbf{e}_r - \sin(\theta)\mathbf{e}_\theta$ in spherical coordinates – and therefore substituting the resulting internal field in Eq. 3.8 yields following convenient result for the local field factor :

$$f_{LF} = A_1 \tag{3.13}$$

This infers that once the amplitude A_1 is found, the local field factor is directly accessed by identifying it A_1. To determine A_1, we consider the multishell geometry given in Fig. 3.1, where the field in the core – denoted as the first region – is related to the field in the adjacent regions by the boundary conditions. Moreover, in each region i a potential Φ_i exists obeying $\nabla^2 \Phi_i = 0$, with a general solution :

$$\Phi_i = -A_i E_0 r cos(\theta) + B_i E_0 r^{-2} cos(\theta) \tag{3.14}$$

The first term is proportional to r, while the second term scales with r^{-2}. The gradient of the latter term is propotional to r^{-3}, typical for a dipole field radiating in the z-direction. These two terms can be understood as inward propagating and reflecting fields. This is an interpretation similar to the one used in transmission line theory in electrical engineering where it is typically used in estimating voltage levels within coaxial cables[31]. Based on the boundary conditions, *i.e*, the normal component of the field displacement $\mathbf{D}_n$ – which equals $\varepsilon\mathbf{E}_n$ – and the electric field along the tangential direction $\mathbf{E}_t$ should be both continuous at a boundary, following relations are derived at the boundary between region $i-1$ and i :

$$\frac{\partial\Phi_i}{\partial\theta} = \frac{\partial\Phi_{i-1}}{\partial\theta} \tag{3.15}$$

$$\varepsilon_i\frac{\partial\Phi_i}{\partial r} = \varepsilon_{i-1}\frac{\partial\Phi_{i-1}}{\partial r} \tag{3.16}$$

Application of these conditions directly to Eq. 3.14 yields :

$$-A_i + B_i r_i^{-3} = -A_{i-1} + B_{i-1}r_{i-1}^3 \tag{3.17}$$

$$\varepsilon_i A_i + 2\varepsilon_i B_i r_i^{-3} = \varepsilon_{i-1}A_{i-1} + 2\varepsilon_{i-1}B_{i-1}r_{i-1}^3 \tag{3.18}$$

These two expressions are rewritten in following type 2×2 matrix forms :

$$\begin{bmatrix} A_{i-1} \\ B_{i-1} \end{bmatrix} = \bar{P}_{i-1} \times \begin{bmatrix} A_i \\ B_i \end{bmatrix}$$

$$\begin{bmatrix} A_i \\ B_i \end{bmatrix} = \bar{R}_{i-1} \times \begin{bmatrix} A_{i-1} \\ B_{i-1} \end{bmatrix}$$

with $\bar{P}_{i-1}$ and $\bar{R}_{i-1}$ the *propagation* and *reflection* matrices, respectively at the boundary $i-1$:

$$\bar{P}_{i-1} = \tfrac{1}{3\varepsilon_{i-1}}\begin{bmatrix} 2\varepsilon_{i-1}+\varepsilon_i & 2(\varepsilon_i-\varepsilon_{i-1})r_{i-1}^{-3} \\ (\varepsilon_i-\varepsilon_{i-1})r_{i-1}^3 & (\varepsilon_{i-1}+2\varepsilon_i) \end{bmatrix}$$

and

$$\bar{R}_{i-1} = \tfrac{1}{3\varepsilon_i}\begin{bmatrix} \varepsilon_{i-1}+2\varepsilon_i & 2(\varepsilon_{i-1}-\varepsilon_i)r_{i-1}^{-3} \\ (\varepsilon_{i-1}-\varepsilon_i)r_{i-1}^3 & (\varepsilon_{i-1}+2\varepsilon_i) \end{bmatrix}$$

Note that indeed $\bar{R}_{i-1} = \bar{P}_{i-1}^{-1}$, or the reflection matrix is the inverse of the propagation matrix. These matrices can be used to relate the electric field amplitude inside and outside the QDs:

$$\begin{bmatrix} A_1 \\ B_1 \end{bmatrix} = \bar{P}_1 \times \bar{P}_2 \times ....\bar{P}_N \times \begin{bmatrix} A_i \\ B_i \end{bmatrix} = \bar{\bar{P}}_N \begin{bmatrix} A_N \\ B_N \end{bmatrix}$$

Here, $\bar{\bar{P}}_N$ includes the individual propagation matrices at the different regions and is conveniently denoted as the total propagation matrix. Similarly, the field amplitude inside and outside the particles is related via the reflection matrices :

$$\begin{bmatrix} A_N \\ B_N \end{bmatrix} = \bar{R}_N \times \bar{R}_{N-1} \times ....\bar{R}_1 \times \begin{bmatrix} A_1 \\ B_1 \end{bmatrix} = \bar{\bar{R}}_N \begin{bmatrix} A_1 \\ B_1 \end{bmatrix} \tag{3.19}$$

with $\bar{\bar{R}}_N$ the resulting total reflection matrix. Recalling that once the field penetrates the core B_1 equals 0 and noting that the field in the outer region (host) arriving from infinity – distance far away from the outer shell – is merely due to the applied field ($A_{N+1} = 1$), a final expression for the local field factor is found :

$$f_{LF} = A_1 = \frac{1}{\left[\bar{\bar{R}}_N\right]_{1,1}} \tag{3.20}$$

This formula can now be employed to obtain closed form expressions for the local field factor of QD core, core/shell and core/shell/shell particle types.

Core particle

Assuming a core particle with $\varepsilon_1 = \varepsilon_c$ and $\varepsilon_2 = \varepsilon_H$ the dielectric functions of the core and the host medium respectively, the local field factor based on Eq. 3.20 reads:

$$f_{LF} = \frac{3\varepsilon_2}{\varepsilon_1 + 2\varepsilon_2} = \frac{3\varepsilon_h}{\varepsilon_c + 2\varepsilon_h} \tag{3.21}$$

In agreement with literature reporting from Ricard et al.[25].

Core/shell particle

Using $\varepsilon_1 = \varepsilon_c$, $\varepsilon_2 = \varepsilon_{sh}$ and $\varepsilon_3 = \varepsilon_H$, the dielectric functions of the core, shell and the host, respectively, Eq. 3.20 yields the local field factor for a core/shell particle type as:

$$f_{LF} = \frac{3^2 \varepsilon_2 \varepsilon_3}{(\varepsilon_1 + 2\varepsilon_2)(\varepsilon_2 + 2\varepsilon_3) + 2(\varepsilon_1 - \varepsilon_2)(\varepsilon_2 - \varepsilon_3)\frac{r_1^3}{r_{tot}^3}} \tag{3.22}$$

Here, r_1 and r_{tot} denote the core and the total radius, respectively. Again this expression is in agreement with a previous result from Neeves et al.[26], confirming the reliance of the procedure used here based on the transmission line analogy.

Core/shell/shell particle

In line with the above results, a close expression can be obtained for a core/shell/shell particle type with $\varepsilon_1 = \varepsilon_c$, $\varepsilon_2 = \varepsilon_{sh,1}$, $\varepsilon_3 = \varepsilon_{sh,2}$ and $\varepsilon_4 = \varepsilon_H$ signifying the dielectric function of the core, inner shell, outer shell and the host, respectively :

$$f_{LF} = \frac{3^3 \varepsilon_2 \varepsilon_3 \varepsilon_4}{(\varepsilon_3 + 2\varepsilon_4)\,\kappa_1 + 2(\varepsilon_3 - \varepsilon_2)\,\kappa_2} \tag{3.23}$$

$$\kappa_1 = \left[(\varepsilon_2 + 2\varepsilon_3)(\varepsilon_1 + 2\varepsilon_2) + 2(\varepsilon_2 - \varepsilon_3)(\varepsilon_1 - \varepsilon_2)\frac{r_1^3}{r_2^3}\right] \tag{3.24}$$

$$\kappa_2 = \left[(\varepsilon_1 + 2\varepsilon_2)(\varepsilon_2 - 2\varepsilon_3)\frac{r_2^3}{r_3^3} + (2\varepsilon_2 + \varepsilon_3)(\varepsilon_1 - \varepsilon_2)\frac{r_1^3}{r_2^3}\right] \tag{3.25}$$

with r_1, r_2 and r_{tot} the respective radius of the inner shell, outer shell and the total particle.

3.2.3 μ solution for a multishell QD

To determine the intrinsic absorption coefficient we recall Equation 3.6, where μ_{int} can be calculated once β is known, a factor depending on the polarizability α_P. The polarizability of a particle, is the ability of the particle to be locally polarized upon excitation with an optical field. This dipole field generates a new field and the strength of this field determines the magnitude of the polarizability. In the previous section, the solution for the strength of this field was determined based on the transmission line anology from electrical engineering of finding the amplitudes of forward and backward propagating electric waves in the different piecewise homogeneous regions (shells). Based on this solution an expression for α_P will be obtained and by appropriately defining the boundaries of the regions : homogeneous core, shells and the inhomogeneous alloyed region, a reliable solution for μ_{int} will be found for a general QD system, *i.e.*, one with an arbitrary type of dielectric function profile.

Having determined the potential of an N-multilayered dielectric particle Φ_{N+1} in the outer region $N+1$ (Fig. 3.1) as shown by Equations 3.14 and 3.19, the possiblity exist to relate this expression to the potential of a dipole $\mathbf{p} = p\mathbf{e}_z$ present in a host medium with a dielectic constant ε_H :

$$\Phi_{N+1} = \frac{\mathbf{p}.\mathbf{e}_r}{4\pi\varepsilon_H r^2} = \frac{\alpha_P E_0 cos(\theta)}{4\pi\varepsilon_H} \tag{3.26}$$

Comparison with Eq. 3.19 yields for the polarizability:

$$\alpha_P = 4\pi\varepsilon_H B_{N+1} \tag{3.27}$$

Given the expression for the intrinsic absorption coefficient (Eq. 3.6), this result is simplified :

$$\mu_{int} = \frac{6\pi\, r_{tot}^3}{\lambda} \Im(\left[\bar{\bar{R}}_N\right]_{2,1} f_{LF}) \tag{3.28}$$

or in the more standard form as outlined in Eq. 3.6:

$$\mu_{int} = \frac{2\pi}{\lambda\, n_h} \Im(3\,\beta\,\varepsilon_h) \tag{3.29}$$

$$\beta = \frac{n_h \left[\bar{\bar{R}}_N\right]_{2,1} f_{LF} r_{tot}}{\varepsilon_h} \tag{3.30}$$

with r_{tot} the total radius of the particle. This equations show that, for spherical multilayered particles dispersed in a transparent host, the intrinsic absorption coefficient depends on the product of the local field factor and the matrix element $\left[\bar{\bar{R}}_N\right]_{2,1}$. While the former factor indicates the amount of power that is permitted to enter the core, the latter factor accounts for the dielectric shielding of the core due to the surrounding shells. Moreover, both factors depend on the dielectric constants $\varepsilon_1..\varepsilon_N$ in the marked regions of the multilayered particle and once this values are known, a direct solution for μ_{int} is obtained for QDs of a multishell type. Interestingly, by a good partitioning (Fig. 3.2) of the different regions of the multishell particle this solution can be extended to following *cases* of particle types :

1. **core/shell/shell**
2. **core/shell/graded alloy**
3. **core/graded alloy/shell**
4. **core/graded alloy**
5. **graded alloy**

From case 1 till case 3, three regions can be distinguished : a core , inner and outer region. Each region can be either alloyed or non-alloyed. An alloyed particle indicates that the composition of the material is a mix of cation or anion bindings, *e.g.* $\mathrm{CdS}_x\mathrm{Se}_{1-x}$. If these mixed bindings are uniformly distributed along the inner or outer shell – homogeneous alloy – of a particle, the solution for μ_{int} for this homogeneous alloys is reduced to finding the solution for the first case, signifying that the dielectric properties of the shell are constant along the alloyed region. In the other cases, the alloy will gradually change composition along the particle and the region could be located at the inner or outer shell. This will result in an inhomogeneous particle, yielding a radial dependence of the dielectic function, which we will denote as $\varepsilon_{alloy}(r)$ for the graded alloyed region in the nanocrystal.

The elegance of the above solution for μ_{int} is that by defining the boundary of the core, shell and the graded alloy and by discritizing the (graded alloy) dielectric function at radial positions r_i one can uses the multishell results of β and μ_{int} , *i.e.*, by combining the geometry given in

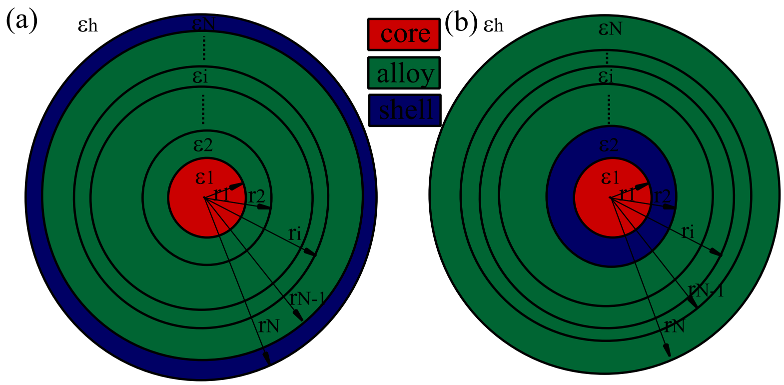

Figure 3.2: Partitioning – allocation of the boundaries – of a multilayered particle to obtain the solution for the particle types in (a) case 3 (core/graded alloy/shell) and (b) case 2 (core/shell/graded alloy).

Fig. 3.1 together with the expressions 3.30, 3.29. The graded alloy material in the particle is then considered as piecewise homogeneous with a uniform dielectric function $\varepsilon_{alloy}(r = r_i)$ along a suffciently small shell thickness ($\Delta\, r = r_{i+1} - r_i$). Figure 3.2 illustrates the allocation of the boundaries for case 3 and case 2. This allows us to derive expressions for the total dielectric function along the nanocrystal radial direction for the different cases of particle types:

1. core/shell/shell

$$\begin{aligned} &\varepsilon_{core} = \varepsilon_1,\, r_{core} = r_1 \\ &\varepsilon_{innershell} = \varepsilon_2,\, r_2 = r_{tot} - r_{core} \\ &\varepsilon_{outershell} = \varepsilon_3,\, r_3 = r_{tot} \end{aligned} \tag{3.31}$$

2. core/graded alloy/shell

$$\begin{aligned}
&\varepsilon_1 = \varepsilon_{core},\, r \leq r_1,\, r_1 = r_{core} \\
&\varepsilon_i = \varepsilon_{alloy}(r = r_i),\, r_1 < r < r_{N-1}, \\
&r_i = r_1 + \frac{r_{N-1} - r_1}{N-2}(i-1),\, i = 2, .., N-2 \\
&\varepsilon_N = \varepsilon_{shell},\, r_{N-1} \leq r \leq r_N\, r_N = r_{tot}
\end{aligned} \tag{3.32}$$

3. core/shell/graded alloy

$$\begin{aligned}
&\varepsilon_1 = \varepsilon_{core},\, r \leq r_1,\, r_1 = r_{core} \\
&\varepsilon_2 = \varepsilon_{shell},\, r_1 < r \leq r_2 \\
&\varepsilon_i = \varepsilon_{alloy}(r = r_i),\, r_2 < r < r_N, \\
&r_i = r_2 + \frac{r_N - r_2}{N-2}(i-2), \\
&i = 3, .., N-1,\, r_N = r_{tot}
\end{aligned} \tag{3.33}$$

4. core/graded alloy

$$\begin{aligned}
&\varepsilon_1 = \varepsilon_{core},\, r \leq r_1,\, r_1 = r_{core} \\
&\varepsilon_i = \varepsilon_{alloy}(r = r_i),\, r_1 < r < r_N, \\
&r_i = r_1 + \frac{r_N - r_1}{N-1}(i-1) \\
&i = 2, .., N-1,\, r_N = r_{tot}
\end{aligned} \tag{3.34}$$

5. graded alloy

$$\begin{aligned}
&\varepsilon_i = \varepsilon_{alloy}(r = r_i),\, 0 < r < r_N, \\
&r_i = \frac{r_N i}{N},\, i = 1, .., N-1 \\
&r_N = r_{tot}
\end{aligned} \tag{3.35}$$

When implementing the above dielectric functions for computing the solution of μ_{int}, N should be large enough for $\left|\frac{(\varepsilon_{i+1}-\varepsilon_i)}{\varepsilon_i}\right|$ to be sufficiently smaller than one. If this condition holds, Δr will be very small enabling the use of Eq. 3.29.

3.3 Absorption coefficient of CdTe QDs

3.3.1 μ at short wavelengths

In the previous chapter we determined the average size of the CdTe nanocrystals using TEM-imaging and we related the size to the 1S-1S absorption peak determining the sizing curve. Apart from the average size, the concentration of (semiconductor) nanocrystals in solution can be determined from the absorption spectra using the intrinsic absorption coefficient (μ_{int}) or the molar extinction coefficient (ϵ_{ext}) at short wavelengths, especially in the ranges around 400 and below 340 nm. For ZnO[32], InAs[33], PbSe[13], PbS[12], CdSe[14] QDs, both quantities have already been compared to bulk values and it has been shown that μ_{int} tends to coincide at short wavelengths. Experimentally, the intrinsic absorption coefficient is provided in Eq. 3.7. This equation relates the absorbance A_λ – measured via absorption spectroscopy – of the dispersed QDs in a cuvette with a length L to the occupied volume fraction f by the QDs. For nanocrystals with a size d and a molar concentration c, the volume fraction is given by :

$$f = cN_A\frac{\pi d^3}{6} \tag{3.36}$$

with N_A Avogadro's constant. The concentration c is obtained through elemental analysis of the QDs dissolved in a $\mathrm{HNO_3}$ solution. The CdTe QDs will decompose in Cd and Te atoms and via inductively coupled mass spectroscopy (ICP-MS), the concentration of the cadmium in solution $\mathrm{C_{Cd}}$ (mg/L) is determined from which c is calculated as:

$$c = \frac{6\mathrm{C_{Cd}}\mathrm{a_{CdTe}}}{8\pi d^3\mathrm{M_{Cd}}}(1+\frac{1}{\rho}) \tag{3.37}$$

$\mathrm{a_{CdTe}}$=0.648 nm is the lattice parameter of a CdTe zincblende (zb) unit cell. ρ is the Cd:Te ratio determined via Rütherford backscattering spectroscopy (RBS) and accounts for the enriched surface of CdTe QDs with an excess of Cd-atoms. $\mathrm{M_{Cd}}$ is the molar mass of cadmium. Table 3.1 illustrates the data for the different QD sizes.

d (nm)	C_{Cd} (mg/L)	ρ	A_{410} (cm^{-1})	c (10^{-6}mol/L)
3.19	111.3	1.39	0.199	0.5685
3.73	236.1	1.13	0.429	0.0825
4.14	483.4	1.20	0.286	0.4013
5.20	255.2	1.14	0.466	0.3284
5.67	123.7	1.09	0.221	1.2530
7.65	97.8	1.12	0.297	0.0598
10.97	122.5	1.07	0.360	0.0257

Table 3.1: CdTe size d, cadmium weight concentrations C_{Cd} as obtained by ICP-MS measurements, ρ is the RBS Cd:Te ratio, A is the absorbance at 410 nm of the CdTe QDs dispersed in toluene and c is the calculated concentration of the suspensions used.

Based on the elemental analysis and absorption spectroscopy and by combining Eq. 3.7 and Eq. 3.36, the spectral dependence of μ_{int} is determined as shown in Fig. 3.3a for different sizes of QDs dispersed in toluene. From the inset in Fig. 3.3a we observe a distinct shoulder feature around 365 nm that shifts from shorter wavelengths for smaller QDs towards 365 nm for larger QDs. In addition, the feature becomes more pronounced for larger QDs. This is a clear signiture of size-quantization effects at 365 nm and has been attributed to the E_1 transition along the initial and final energy states of the Λ direction in the Brillouin zone[35]. Similar observations have been made for the E_1 transition in PbSe QDs along the Σ direcion of the Brillouin zone[36]. Importantly, due to the size-quantization effects in this wavelength region the μ_{int} spectra are not suitable for use as a standard value to determine f or c from an absorbance measurement.

Unlike the wavelength range at 365 nm, size quantization effects are less pronounced around 400 nm or below 340 nm, and the spectra tend to overlap in these regions. This is in line with literature[13], where at regions of higher energy band states and where the bulk spectrum do not possess distinct features, an absence of quantum confinement is found in the QD-spectra. The black line in Fig. 3.3a illustrates this for bulk CdTe ($\mu_{i,th}$) at the denoted wavelengths. The bulk spectrum is calculated based on Eq. 3.6 using the dielectric constants of the bulk CdTe material[37]. Figure 3.3b shows $\mu_{i,310}$ nm and $\mu_{i,410}$ nm as a function of the size d. Both values are largely size independent marking the absence of quantum confinement. The μ_{int} values are averaged yielding a mean intrinsic aborption coefficient $\mu_{i,mean}$ around both wavelengths as shown by the dashed lines. Fig. 3.3c shows that the relative standard deviation for $\mu_{i,mean}$ is minimal at 410 nm. Consequently, the μ_{int} at this wavelength is the proper choice for use as a standard value for the determination of f or c. For the CdTe QDs dispersed in toluene we find :

$$\mu_{i,mean,410} = 7.55\,10^4 \mathrm{cm}^{-1} \tag{3.38}$$

Moreover, this value is only 16% lower than $\mu_{i,th}$ and a similar observation has been made in zb-CdSe QDs[14]. The value in Eq. 3.38 is applicable for QDs dispersed in toluene and can be extended to solvents with a refractive index n_s close to the value of toluene (n=1.52). However, the dependence of μ_{int} on the solvent may involve the dependence of the refractive index on the ligand molecules, which is not well understood, and the value in Eq. 3.38 should be multiplied by $\frac{A_{toluene}}{A_{solvent}}$ (determined from different QD-sizes) for a proper calibration.

3.3.2 μ at the bandgap

Although less consistent than intrinsic absorption coefficients at short wavelengths, literature data are typically available at the bandgap[15]. Following the procedure of Cadimartiri et al.[38], which has been expanded by Moreels et al.[13]., we calculate an energy integrated intrinsic aborption coefficient $\mu_{i,gap,eV}$ at the bandgap transition, by doubling the integrated low energy half of the first exciton absorption peak. The spectra are obtained using the elemental analysis procedure as outlined in the previous section. Alternatively, $\mu_{i,gap,eV}$ can be obtained by normalizing the spectra using the mean value of $\mu_{int,410}$. In this way, $\mu_{i,gap,eV}$ follows from the energy integrated absorbance A_{gap} (eV/cm) of the first absorption peak :

$$\mu_{i,gap,eV} = \frac{A_{gap}}{A_{410}} \mu_{int,410} \tag{3.39}$$

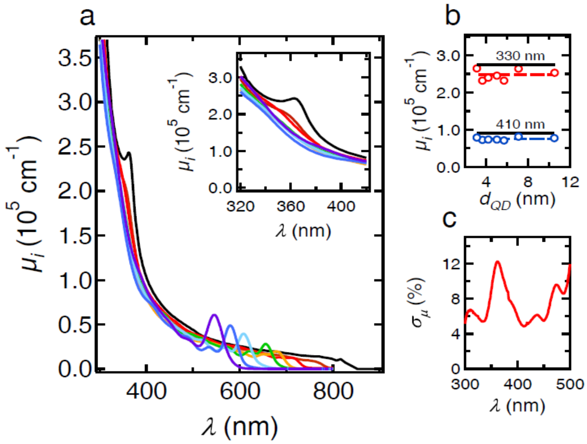

Figure 3.3: (a) Intrinsic absorption coefficient μ_i of different sizes in toluene of CdTe QDs as determined by combining elemental analysis with absorption spectroscopy. The black line represents $\mu_{i,th}$ of bulk CdTe calculated using the bulk dielectric function of CdTe[37]. (Inset) zoom of μ_i-spectra at the short-wavelength range. (b) μ_i at 330 nm and 410 nm of differently sized QDs in toluene (dots), together with the theoretical value μ_{th} (full lines) and the mean values $\mu_{i,mean}$ at the respective wavelengths (dashed lines). (c) Procentual deviation from $\mu_{i,mean}$ at the short-wavelength range calculated using the spectra shown in (a).

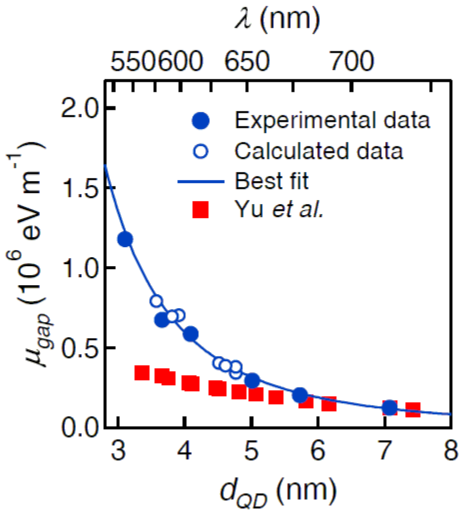

Figure 3.4: Absorption coefficient at the bandgap μ_{gap} as a function of the QD diameter (bottom axis) and the 1S-1S absorption peak (top axis). The filled blue circles represent experimental data obtained by elemental analysis and the open circles are calculated data according to Eq. 3.39. The blue line is the best fit (Eq. 3.40) and the filled squared are converted data from Yu et al.[15].

The normalization accounts for inhomogeneous broadening of the absorbing peak due to the size dispersion. The resulting data for both procedures are illustrated in Fig. 3.4. The QD diameter is obtained using the sizing curve as determined in Chapter 2. Opposite to μ_{int} at 410 nm, size quantization effects are strongly present at the bandgap and μ_{gap} shows a significant increase with decreasing particle size. Moreover, the dependence of μ_{gap} on the size d (nm) can be well fitted with a power law for the sizes used here (3-10 nm). A one-parameter fit yields:

$$\mu_{gap} = \frac{3.599\,10^7}{d^3}(\mathrm{eV\,m^{-1}}) \tag{3.40}$$

This infers that $\mu_{i,gap}$ scales with the inverse of the QD volume. Given that the aborption coefficient is proportional to the volume fraction as $\mu = \mu_{i,gap}\, f$, this shows that for an equal volume occupied by the QDs, smaller QDs are more efficient absorbers as compared to larger QDs at the bandgap transition.

In a previous work, Yu et al.[15] reported wavelength integrated molar extinction coefficients $\epsilon_{ext,gap,\lambda}$. This quantity is transformed to an energy intrinsic aborption coefficient at the bandgap using :

$$\mu_{i,gap,eV} = \frac{6}{\pi log(e) d^3 N_A} \times \frac{e\,E_0\,d^2}{hc} \times \epsilon_{ext,gap,\lambda} \tag{3.41}$$

The second factor accounts for the tranformation from a wavelength to an energy integrated molar extinction coefficient. The resulting data are shown in Fig. 3.4 (filled squares) as a function of peak wavelength (top axis). The corresponding sizes (bottom axis) are calculated according to their published sizing curve[15]. We note that their values are up to 3 times smaller than the ones obtained here. Since, our value of $\mu_{int,410}$ only deviates 16% from the bulk values, the proposed values by Yu et al. are not recommended for use and may give considerable errors.

3.4 Absorption coefficient of CdSe/ CdSe$_x$S$_{1-x}$/ CdS QDs

In this section we will determine the intrinsic absorption coefficient of CdSe/CdS core/shell and CdSe/CdSe$_x$S$_{1-x}$/CdS core/alloy/shell QDs, but prior to that an understanding of the alloying mechanism is needed to properly account for the alloyed layer in the determination of μ_{int} for dispersed CdSe/CdSe$_x$S$_{1-x}$/CdS QDs.

3.4.1 Diffusion induced alloying

The synthesis of the QDs is done starting from CdSe core QDs, where a CdS shell is grown using the selective ion layer deposition method (SILAR)[39]. By comparing TEM images of the CdSe core QDs and the finally obtained nanocrystals after shell growth, core radius r_0 and the total QD radius r_{tot} can be determined. Assuming that after the CdS shell growth, CdSe/CdS core/shell QDs are formed as illustrated in Fig. 3.5a, the shell thickness is thus given by $r_{tot} - r_0$. As shown previously by Tschirner et al.[18], at the edge between the CdSe core and the CdS shell, Se atoms diffuse outwards to the shell, while S atoms diffuse inwards to the core. Hence, an alloyed region is created as shown in Fig. 3.5b. In general, this alloying is expected to be gradually appearing near the CdSe core, while it starts fading out gradually away towards the CdS shell. For simplicity, we assume the alloying to appear abruptly from the CdSe core and vanish abruptly towards the CdS shell, yielding a CdSe$_x$S$_{1-x}$ alloyed region with a well defined thickness denoted as t. Therefore, the core will shrink from a radius value r_0 (Fig. 3.5a) to a value r_c (Fig. 3.5b), and accordingly the CdS shell thickness amounts as $r_{tot} - (t + r_c)$.

The value of r_c and t is found by assuming that the amount of Se atoms before the alloying ($n_{Se,1}$) – through diffusion – is conserved in the nanocrystal after the alloying ($n_{Se,2}$). Furthermore, as the CdSe and CdS unit cells with respective lattice parameters a_{CdSe} and a_{CdS} contain 4 atoms, the total number of atoms within a nanocrystal of radius r is

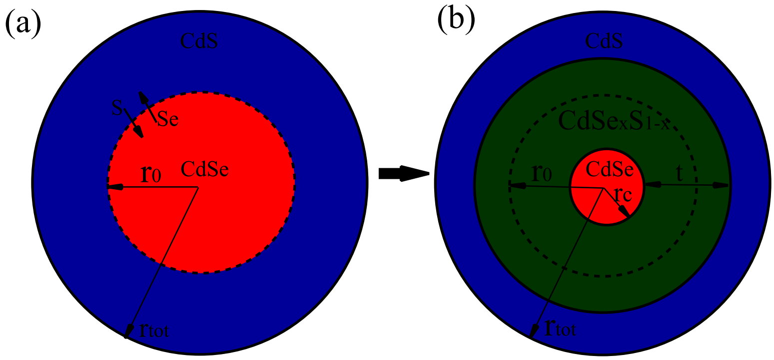

Figure 3.5: (a) An ideal core/shell CdSe/CdS particle (b) through which diffusion of S,Se atoms started and created an alloyed innershell resulting in a shrinking of CdSe core to a size r_c.

given by $\frac{4\pi r^3}{3\,a^3} \times 4$. Accordingly, the Se amounts are determined as:

$$n_{Se,1} = \frac{4\pi r_0^3}{3}\,\frac{4}{a_{CdSe}^3} \tag{3.42}$$
$$n_{Se,2} = \frac{4\pi r_c^3}{3}\,\frac{4}{a_{CdSe}^3} + \left[\frac{4\pi (r_c+t)^3}{3} - \frac{4\pi r_c^3}{3}\right]\frac{4}{x_{Se}\,a_{alloy}^3}$$

Here, x_{Se} is the fraction of Se atoms in the alloyed innershell and sums up together with the fraction of S atoms x_S as one ($x_{Se} + x_S = 1$). In the same expression, a_{alloy} denotes the lattice parameter in the alloyed region of the QDs and in accordance with Vegard's Law[40] has shown to be the weigthed averaged of the CdSe and CdS lattice parameters[41] :

$$a_{alloy} = x\,a_{CdSe} + (1-x)\,a_{CdS} \tag{3.43}$$

As the lattice parameters for cubic CdSe and CdS are approximately equal, above equation is simplified as $a_{alloy} \approx a_{CdSe} \approx a_{CdS}$, with $a_{alloy} \approx 0.61$ nm. Recalling the conservation condition $n_{Se,1} = n_{Se,2}$, the quantities r_c, t, x_{Se} and r_0 are linked as :

$$(r_c + t)^3 + (x_{Se} - 1) r_c^3 + x_{Se}\, r_0 = 0 \tag{3.44}$$

Therefore, by knowing r_0 and assuming a t value, the shrinking of the core to the value r_c can be evaluated using Eq. 3.44 for a given selenium fraction x_{Se}. This will allow to properly account for the alloyed layer while estimating intrinsic absorption coefficients.

3.4.2 μ at short wavelengths

To determine μ_{int} for CdSe/CdS or CdSe/CdSe$_x$S$_{1-x}$/CdS QDs, we at first study how μ_{int} is related for both particle types at a wavelength of 300 nm. To quantify, the dielectric constants of the CdSe core, CdSe$_x$S$_{1-x}$ alloy and the CdS shell material are needed. The core and the shell dielectric constants are found relying on the bulk value of CdSe and CdS denoted as ε_{CdSe} and ε_{CdS}, respectively. The dielectric function of the alloyed region ε_{alloy} is assumed to be the weigthed average of ε_{CdSe} and ε_{CdS} :

$$\varepsilon_{alloy} = x_{Se}\,\varepsilon_{CdSe} + (1 - x_{Se})\varepsilon_{CdS} \tag{3.45}$$

Using the multishell solution as provided by equations 3.32,3.29, μ_{int} is determined as a function of the Se fraction in the alloyed region for different alloy thickness values. Fig. 3.6 illustrates this for samples A,B (see Table 3.2).

In Fig. 3.6a, a maximum of μ_{int} as a function of the selenium fraction is observed for sample A, whilst the error difference between the thickest introduced alloy shell $d = 3.1$ nm and no alloy shell $d = 0$ nm is within 5%. This signifies that (diffusion induced) alloying does not affect significantly the intrinsic absorption coefficient and consequently μ_{int} values for – simple non-alloyed – CdSe/CdS QDs can be employed to – more complex alloyed – CdSe/CdSe$_x$S$_{1-x}$/CdS QDs, synthesized

Sample	Core size (nm)	Total size (nm)
A	3.1	6.6
B	5.4	8.91

Table 3.2: The core and total size (twice radius) of the CdSe/CdSe$_x$S$_{1-x}$/CdS core/alloy/shell QDs used to evaluate μ_{int} for different alloy conditions.

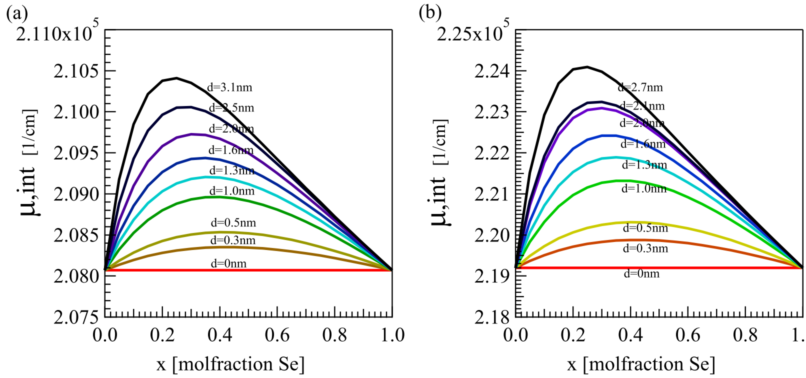

Figure 3.6: (a) Intrinsic absorption coefficients μ_{int} for CdSe/CdSe$_x$S$_{1-x}$/CdS core/alloy/shell QDs a function of the fraction Se ($x_{Se}+x_S=1$) in the alloyed innershell. μ_{int} is calculated based on an abrupt interface between the core and the alloyed layer using parameters of sample A. (b) Similar calculations as in (a), but done with the parameter values of sample B.

based on the SILAR method. The features in Fig. 3.6b for sample B are similar to those observed for sample A, affirming the previous conclusion.

In view of this, μ_{int} of – non-alloyed – CdSe/CdS QDs can now be calculated and experimentally verified for various combinations of core and total QD size, to yield a reliable standard for the concentration determination of CdSe/CdS or CdSe/CdSe$_x$S$_{1-x}$/CdS QDs. Table 3.3 illustrates the data for the different QD sizes. The core and total size of the QDs is determined using TEM imaging. The concentration c of the CdSe/CdS QD samples is determined by noting that the amount of nanocrystals remains unchanged during the SILAR synthesis. Therefore, prior to the SILAR processing of the CdSe core QDs, c is estimated, by employing the elemental analysis procedure as outlined in sec. 3.3 for these QDs. In this procedure, a zinc-blende CdSe lattice parameter a_{CdSe} of 0.615 nm is used and a Cd:Se ratio ρ of 1.22[14] is substituted in Eq. 3.37, accounting for the enriched surface of the CdSe QDs with an excess of Cd-atoms. Based on the elemental analysis and absorption spectroscopy and by combining Eq. 3.7 and Eq. 3.36, the dependence of μ_{int} on the

d_{core} (nm)	d_{tot}	A_{300} (cm^{-1})	c (10^{-6}mol/L)
5.6	7.4	0.358	0.00496
5.06	6.55	0.053	0.05067
3.24	5.6	0.124	0.02907
3.24	3.64	0.075	0.05424
2.48	5.74	0.209	0.05013
2.48	13.3	0.397	0.00726
5.41	7.5	0.484	0.04457
2.72	5.3	0.108	0.03259
2.72	10.61	0.547	0.01829
5.41	10.4	0.743	0.03129

Table 3.3: CdSe core size d_{core}, CdSe/CdS total size d_{tot}, A_{300} is the absorbance at 300 nm of CdSe/CdS QDs dispersed in a choloroform liquid and c is the calculated concentration of the suspensions used.

various combinations of core and total size of the QDs – included as the CdS to the total volume ratio $\frac{V_{CdS}}{V_{tot}}$ – is shown in Fig. 3.7a (red squares). The QDs are dispersed in a chlolorform liquid. The red line is the bulk dependence μ_{th} on $\frac{V_{CdS}}{V_{tot}}$, calculated based on Eq. 3.29 using the dielectric constants of bulk CdSe and CdS . Moreover, this bulk dependence is in a good agreement with the experimental μ_{int} values, yielding a reliable standard for use to determine the concentration of dispersed CdSe/CdS or CdSe/CdSe$_x$S$_{1-x}$/CdS QDs.

3.5 Conclusion

We have analyzed the absorption coefficient of CdTe QDs by combining UV-vis absorption spectroscopy and elemental analysis. At short wavelength of 410 nm the intrinsic absorption coefficient does not show size quantization effects and the obtained values are in good agreement with the bulk value of CdTe. The average of these values can be used as reliable standard for the concentration determination of CdTe nanocrystals. Around the bangap transition we find integrated absorption coefficients that scale inversely proportionally with the QD volume. In addition, these data showed a deviation up to a factor of 3 compared to the values

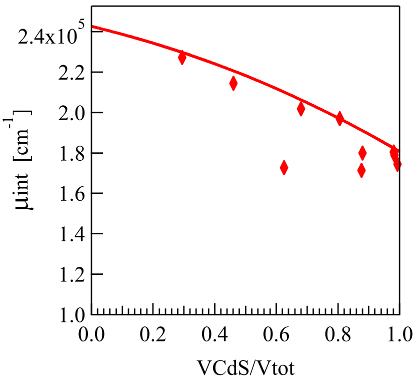

Figure 3.7: The experimental intrinsic absorption coefficient follows nicely the predicted μ_{th} as a function of the CdS volume fraction in the CdSe/CdS core/shell QDs. The CdSe/CdS are dispersed in a cholorofrom liquid.

widely used in literature.

The intrinsic absorption coefficient of CdSe/CdS core/shell CdSe/ CdSe$_x$S$_{1-x}$/CdS core/alloy/shell QDs has been determined. Based on Maxwell-Garnett theory and an alloying model considering the diffusion of the Se and S atoms respectively at the inner and outer CdSe and CdS shell we showed that the intrinsic aborption coefficient of CdSe/CdS core/shell QDs can be used for a CdSe/ CdSe$_x$S$_{1-x}$/CdS core/alloy/shell QDs within a 5% error of calculation.

Bibliography

[1] Reiss, P.; Protiere, M.; Li, L. Core/Shell Semiconductor Nanocrystals. *Small* **2009**, *5*, 154–168, Times Cited: 370 Reiss, Peter/C-2604-2009; LI, Liang/A-9686-2011 379.

[2] Mahler, B.; Spinicelli, P.; Buil, S.; Quelin, X.; Hermier, J.-P.; Dubertret, B. Towards non-blinking colloidal quantum dots. *Nature Materials* **2008**, *7*, 659–664, Times Cited: 266 Spinicelli, Piernicola/F-4706-2012 Spinicelli, Piernicola/0000-0001-8078-6047 266.

[3] Chen, Y.; Vela, J.; Htoon, H.; Casson, J. L.; Werder, D. J.; Bussian, D. A.; Klimov, V. I.; Hollingsworth, J. A. Giant multishell CdSe nanocrystal quantum dots with suppressed blinking. *Journal of the American Chemical Society* **2008**, *130*, 5026–+, Times Cited: 268 269.

[4] Donega, C. d. M. Synthesis and properties of colloidal heteronanocrystals. *Chemical Society Reviews* **2011**, *40*, 1512–1546, Times Cited: 104 de Mello Donega, Celso/B-8020-2009 de Mello Donega, Celso/0000-0002-4403-3627 104.

[5] Eychmuller, A. Structure and photophysics of semiconductor nanocrystals. *Journal of Physical Chemistry B* **2000**, *104*, 6514–6528, Times Cited: 262 Eychmuller, Alexander/G-2354-2010 267.

[6] Mokari, T.; Banin, U. Synthesis and properties of CdSe/ZnS core/shell nanorods. *Chemistry of Materials* **2003**, *15*, 3955–3960, Times Cited: 151 Mokari, taleb/f-1685-2012 153.

[7] Li, D.; Liang, C.; Liu, Y.; Qian, S. Femtosecond nonlinear optical properities of PbS nanoparticles. *Journal of Luminescence* **2007**, *122-123*, 549–551.

[8] van Embden, J.; Jasieniak, J.; Mulvaney, P. Mapping the Optical Properties of CdSe/CdS Heterostructure Nanocrystals: The Effects of Core Size and Shell Thickness. *Journal of the American Chemical Society* **2009**, *131*, 14299–14309, Times Cited: 40 Jasieniak, Jacek/H-3380-2011 40.

[9] Peng, X. G.; Schlamp, M. C.; Kadavanich, A. V.; Alivisatos, A. P. Epitaxial growth of highly luminescent CdSe/CdS core/shell nanocrystals with photostability and electronic accessibility. *Journal of the American Chemical Society* **1997**, *119*, 7019–7029, Times Cited: 1513 1567.

[10] Wang, X.; Ren, X.; Kahen, K.; Hahn, M. A.; Rajeswaran, M.; Maccagnano-Zacher, S.; Silcox, J.; Cragg, G. E.; Efros, A. L.; Krauss, T. D. Non-blinking semiconductor nanocrystals. *Nature* **2009**, *459*, 686–689, Times Cited: 308 Wang, Xiaoyong/D-5956-2012; Wang, Xiaoyong/F-9542-2012 311.

[11] Boldt, K.; Kirkwood, N.; Beane, G. A.; Mulvaney, P. Synthesis of Highly Luminescent and Photo-Stable, Graded Shell CdSe/CdxZn1-xS Nanoparticles by In Situ Alloying. *Chemistry of Materials* **2013**, *25*, 4731–4738, Times Cited: 0 0.

[12] Moreels, I.; Lambert, K.; Smeets, D.; De Muynck, D.; Nollet, T.; Martins, J. C.; Vanhaecke, F.; Vantomme, A.; Delerue, C.; Allan, G.; Hens, Z. Size-Dependent Optical Properties of Colloidal PbS Quantum Dots. *Acs Nano* **2009**, *3*, 3023–3030.

[13] Moreels, I.; Lambert, K.; De Muynck, D.; Vanhaecke, F.; Poelman, D.; Martins, J. C.; Allan, G.; Hens, Z. Composition and size-dependent extinction coefficient of colloidal PbSe quantum dots. *Chemistry of Materials* **2007**, *19*, 6101–6106.

[14] Capek, R. K.; Moreels, I.; Lambert, K.; De Muynck, D.; Zhao, Q.; Vantomme, A.; Vanhaecke, F.; Hens, Z. Optical Properties of Zincblende Cadmium Selenide Quantum Dots. *J. Phys. Chem. C* **2010**, *114*, 6371–6376.

[15] Yu, W. W.; Qu, L. H.; Guo, W. Z.; Peng, X. G. Experimental determination of the extinction coefficient of CdTe, CdSe, and CdS nanocrystals. *Chemistry of Materials* **2003**, *15*, 2854–2860.

[16] De Geyter, B.; Hens, Z. The absorption coefficient of PbSe/CdSe core/shell colloidal quantum dots. *Appl. Phys. Lett.* **2010**, *97*,.

[17] Justo, Y.; Geiregat, P.; Van Hoecke, K.; Vanhaecke, F.; Donega, C.; Hens, Z. Optical properties of PbS/CdS quantum dots. *Journal of Phys. Chem. C* **2013**, *117*, 20171–20177.

[18] Tschirner, N.; Lange, H.; Schliwa, A.; Biermann, A.; Thomsen, C.; Lambert, K.; Gomes, R.; Hens, Z. Interfacial Alloying in CdSe/CdS Heteronanocrystals: A Raman Spectroscopy Analysis. *Chemistry of Materials* **2012**, *24*, 311–318, Times Cited: 18 Thomsen, Christian/E-2295-2012; Hens, Zeger/J-6366-2013 18.

[19] Jasieniak, J.; Smith, L.; van Embden, J.; Mulvaney, P.; Califano, M. Re-examination of the Size-Dependent Absorption Properties of CdSe Quantum Dots. *Journal of Physical Chemistry C* **2009**, *113*, 19468–19474, Times Cited: 95 Jasieniak, Jacek/H-3380-2011; SPIEL, CSIRO/C-2809-2013 95.

[20] Moreels, I.; Lambert, K.; De Muynck, D.; Vanhaecke, R.; Poelman, D.; Martins, J. C.; Allan, G.; Hens, Z. Comment on Size-Dependent Composition and Molar Extinction Coefficient of PbSe Semiconductor Nanocrystals. *Acs Nano* **2009**, *3*, 2053–2053.

[21] Murray, C. B.; Norris, D. J.; Bawendi, M. G. Synthesis and characterization of nearly monodisperse CdE (E=S, Se, Te) semiconductor nanocrystallites. *Journal of the American Chemical Society* **1993**, *115*, 8706–8715.

[22] Maxwell Garnett, J. Colours in metal glasses and in metallic films. *Philos. Tr. Soc-A* **1904**, *203*, 385–420.

[23] Maxwell Garnett, J. Colours in metal glasses, in metallic films and in metallic solutions. II. *Philos. Tr. Soc-A* **1906**, *205*, 237–288.

[24] Mallet, P.; Guérin, C. A.; Sentenac, A. Maxwell-Garnett mixing rule in the presence of multiple scattering: Derivation and accuracy. *Phys. Rev. B* **2005**, *72*, 014205.

[25] Ricard, D.; Ghanassi, M.; Schanneklein, M. C. Dielectric confinement and the linear and nonlinear-optical properties of semiconductor-doped glasses. *Optics Communications* **1994**, *108*, 311–318.

[26] Neeves, A.; Birnboim, M. Composite structures for the enhancement of nonlinear-opitcal susceptibility. *J. Opt. Soc. Am. B* **1989**, *6*, 787–796.

[27] Dong, L.; Huang, J. P.; Yu, K. W.; Gu, G. Q. Dielectric response of graded spherical particles of anisotropic materials. *Journal of Applied Physics* **2004**, *95*, 621–624, Times Cited: 28 huang, jiping/G-7865-2011 29.

[28] Sihvola, A.; Lindell, I. V. Polarizability and effective permittivity of layered and continuously inhomogeneous dielectric spheres. *Journal of Electromagnetic Waves and Applications* **1989**, *3*, 37–60.

[29] Van Stryland, E.; Enoch, E.; Wolfe, M.; Bass, W. *Handbook of Optics*; OSA, 2000.

[30] Boyd, J. *Nonlinear Optics*, 2nd ed.; Elsevier, 2003.

[31] Franchois, A. *Elektromagnetisme II*; Ghent university, 2006.

[32] Lommens, P.; Lambert, K.; Loncke, F.; De Muynck, D.; Balkan, T.; Vanhaecke, F.; Vrielinck, H.; Callens, F.; Hens, Z. The growth of Co : ZnO/ZnO core/shell colloidal quantum dots:

Changes in nanocrystal size, concentration and dopant coordination. *Chemphyschem* **2008**, *9*, 484–491.

[33] Yu, P. R.; Beard, M. C.; Ellingson, R. J.; Ferrere, S.; Curtis, C.; Drexler, J.; Luiszer, F.; Nozik, A. J. Absorption Cross-Section and Related Optical Properties of Colloidal InAs Quantum Dots. *J. Phys. Chem. B* **2005**, *109*, 7084–7087.

[34] *Alivisatos_1996.pdf*.

[35] Chelikowsky, J. R.; Cohen, M. L. Nonlocal pseudopotential calculations for electronic-structure of 11 diamond and zincblende semiconductors. *Physical Review B* **1976**, *14*, 556–582.

[36] Hens et al., Z. Effect of quantum confinement on the dielectric function of PbSe. *Physical review letters* **2004**, *92*, 026808.

[37] Adachi, S.; Kimura, T.; Suzuki, N. Optical-Properties of CdTe - Experimental and Modeling. *Journal of Applied Physics* **1993**, *74*, 3435–3441.

[38] Cademartiri, L.; Montanari, E.; Calestani, G.; Migliori, A.; Guagliardi, A.; Ozin, G. a. Size-dependent extinction coefficients of PbS quantum dots. *Journal of the American Chemical Society* **2006**, *128*, 10337–46.

[39] Li, J. J.; Wang, Y. A.; Guo, W. Z.; Keay, J. C.; Mishima, T. D.; Johnson, M. B.; Peng, X. G. Large-scale synthesis of nearly monodisperse CdSe/CdS core/shell nanocrystals using air-stable reagents via successive ion layer adsorption and reaction. *Journal of the American Chemical Society* **2003**, *125*, 12567–12575.

[40] Vegard, L. Die Konstitution der Mischkristalle und die Raumfüllung der Atome. *Zeitschrift für Physik* **1921**, *5*, 17–26.

[41] Joon Kwon, S.; Choi, Y.-J.; Park, J.-H.; Hwang, I.-S.; Park, J.-G. Structural and optical properties of CdSxSe1x nanowires. *Physical Review B* **2005**, 205312.

4

Nonlinear optical properties of PbS quantum dots

4.1 Introduction

Materials with a large nonlinear third-order susceptibility $\chi^{(3)}$ are needed in a wide range of photonic applications. Materials with a large real part of $\chi^{(3)}$ or equivalently a large nonlinear refractive index n_2 are suitable for optical switching, spectral filtering[1;2], holography gratings[3] and phase modulated photonic applications. Materials with a large imaginary part of $\chi^{(3)}$ or nonlinear absorption coefficient β are used in many applications including fluorescence imaging, optical data storage, microfabrication[4–6] and saturable absorbers for optical limiting and mode locked lasers and generally in photonic applications where an amplitude modulation is required.

Table 4.1 lists values of n_2, β and the corresponding figure of merit FOM ($n_2/\lambda\beta$)– see sec 4.3.3, measured around $\lambda = 1.55\,\mu$m, for typical bulk semiconductors[7;8], chalcogenide glasses[9–11] and nonlinear polymers[12;13]. Materials such as GaAs, Si or silica have a poor FOM around the telecom wavelengths (1.55 μm), making them unsuited for integrated nonlinear photonic devices. A way to enhance their performance is functionalization by the overgrowth with high FOM materials, such as AlGaAs or chalcogenide glasses. However, due to the high cost of vacuum-based deposition routes, these materials are less favorable for large-area processing[14]. This drawback can be overcome by the use of solution-deposited materials with a large FOM. For instance, all-optical signal processing has been recently demonstrated by functionalizing Si slotted waveguides with 2-[4-(dimethylamino)phenyl]-3 -([4(dimethylamino)phenyl]-ethynyl)buta-1,3-diene-1,1,4,4-tetracarbonitrile) (DDMEBT) polymers[15]. An alternative and valuable candidate are colloidal QDs as they are an appealing class of materials, due to the combination of size-tunable optical properties and a suitability for wet processing. They possess a high photo-luminescence efficiency, making them potential light sources in LEDs[16;17] and lasers[18–20] and they have a high and tunable absorption cross-section, enabling the fabrication of efficient near infrared (NIR) photodetectors.[21;22] Furthermore, it has been shown that PbSe QDs have a high and tunable n_2 upon resonant excitation around 1.55 μm.[23] and the use of PbS QD doped glasses as saturable absorbers for passive mode-locking in Yb:KYW and Cr^{4+}:YAG lasers has been demonstrated.[24;25] Recently, Padilha et al. and Nootz et al.[26;27] have investigated the absorption cross sections for non-resonant two photon absorption (TPA) of PbS and PbSe QDs. Other authors have studied the nonlinear optical properties of PbS QDs at wavelengths ranging from 0.5 μm to 1.1 μm.[28–33] Yoshino et al.[34;35] investigated the nonlinear optical properties for PbS QD suspensions with a first exciton peak at 1.33 μm excited in the wavelength range 1.1-1.6 μm. In the same wavelength range Brzozowski et al. reported values for FOM up to 0.3 for PbS QD suspensions with a first exciton peak at 1.39 μm.[36] Savitski et al.[37] have studied the nonlinear absorption of PbS QDs doped glasses in the wavelength range 1.06-1.54 μm.

In spite of this extensive research however, no studies report on n_2, β

and the resulting FOM for PbS QDs resonantly excited around 1.55 μm. Here, we study nonlinear refraction and absorbance of PbS QDs using picosecond pulsed excitation between 1535 and 1565 nm. Using the Z-scan technique in combination with chopped illumination, we find that a dispersion of PbS QDs shows strong nonlinear refraction due to electronic effects. Although related to absorption saturation, we argue that photoinduced intraband absorption also contributes to n_2. Next, using pump-probe four wave mixing (FWM), we determine the time response of the optical nonlinearity. We demonstrate that it contains a nanosecond component at low excitation intensities. With increasing light intensity, the FWM decay contains an additional ~ 100 ps component, which we attribute to the presence of carrier-carrier mediated scattering processes, next to a dip prior to the rise of the FWM signal. This unexpected dip may reflect the destructive interference between two FWM signals, the bleaching of the QD absorption (with a typical time constant set by the exciton lifetime) and photoinduced absorption.

The Z-scan experiments that will be presented in this work are obtained thanks to a collaboration with Prof. P. Kockaert from the Opera-group at the ULB, Brussels. The FWM measurements are done in collaboration with Dr. F. Masia from the University of Cardiff.

4.2 Analysis of non-linear optical properties by Z-scan

4.2.1 Set-up and beam characterization

For the Z-scan measurements[39], we used a setup as shown in Fig. 4.1(a). In brief, a pulsed, Gaussian laser beam with a repetition rate ν is guided toward a lens $L1$ (using for instance a mirror $M1$), which creates a focused Gaussian beam. To correct for possible fluctuations of the laser intensity during the measurement, a small fraction is reflected at beam splitter $BS1$ and monitored at detector $D1$. The linear stage LS translates the sample S along the z-axis through the focus of the Gaussian beam. After passing through the sample, a fraction of the total beam

material	n_2 10^{-13} cm^2/W	β cm/GW	FOM $n_2/(\lambda\beta)$
Fused Silica	0.0027	–	–
Semiconductors			
Si	0.45	0.79	0.37
GaAs	1.59	10.2	0.1
AlGaAs	1.75	0.35	3.2
Chalcogenide glasses			
$Ge_{25}As_{10}Se_{65}$	0.6	0.4	1.0
$Ge_{33}As_{12}Se_{55}$	1.5	0.4	2.4
$As_4S_3Se_3$	1.2	0.15	5
$As_{40}S_{60}$	0.6	$<$0.03	$>$12
Polymers			
DDEMBT	1.7	-	2.19

Table 4.1: The nonlinear refractive index n_2, the nonlinear absorption coefficient β and figure of merit FOM for typical materials, measured around $\lambda = 1.55\,\mu$ m.[7–13;38]

intensity (TBI) is reflected at beam splitter $BS2$ and measured with detector $D2$, while the on-axis intensity (OAI) is measured in the far field of the laser beam with a small aperture A and detector $D3$. The input intensity is set using a variable neutral density filter NDF. The illumination of the sample can be chopped using an electronic shutter ESH. The Gaussian spatial profile induces a lens in a nonlinear sample, creating an extra (de-)focusing of the beam (Fig. 4.1(b)), enabling the determination of n_2. In our experiments, we use a 10 MHz pulsed laser with a pulse duration of $\tau_p \approx 2.5$ ps. τ_p is determined with an optical auto-correlator; the pulses have a Gaussian temporal profile. The beam is spatially characterized by two parameters: the beam waist w_0 (beam radius at the focus) and the Rayleigh length z_R. At a given wavelength λ, both are related through:

$$z_R = \frac{\pi w_0^2}{\lambda M^2} \tag{4.1}$$

where M^2 denotes the beam quality factor, which equals 1 for a Gaussian (diffraction limited) beam. We determine w_0 and z_R with a beam

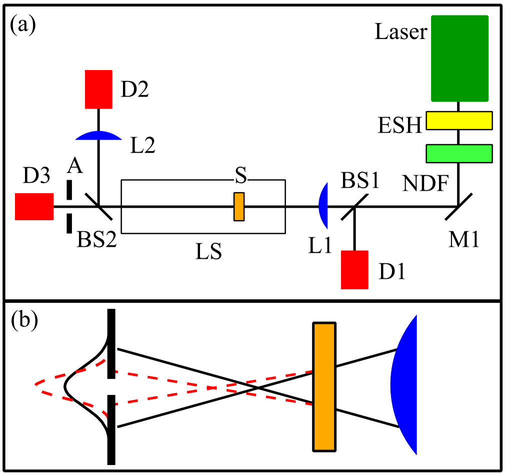

Figure 4.1: (Color online) (a) Schematic representation of the Z-scan setup. (b) Far away from the laser beam focal point, the optical intensity is too low to induce nonlinear effects (full lines). Near the focus, at pre-focal positions, the sample acts as a thin lens, inducing an extra beam divergence in the case of a negative n_2 (dashed lines). This leads to an increased on-axis intensity.

profiler at $\lambda = 1550$ nm. The resulting $w_0 = 47$ μm and $z_R = 3.9$ mm yield $M^2 = 1.17$, confirming that the beam has a Gaussian spatial profile.

Another important characteristic is the on-axis power density at the focus I_0 (referred to as the optical intensity from here on). I_0 equals the maximal power density achieved during a laser pulse. We calculate I_0 from the measured average laser power P:

$$I_0 = \frac{2}{\sqrt{\pi}} \frac{P}{\nu \tau_p \pi w_0^2} \tag{4.2}$$

4.2.2 Derivation of n_2 and β from the Z-scan traces

A calculation of n_2 and β starts from the differential equations which describe the attenuation and phase change of an electric field as it passes through a nonlinear sample with length L.[39] We assume that the sample nonlinearity is limited to the third order ($n = n_0 + n_2 I_0$, $\alpha = \alpha_0 + \beta I_0$) and that the sample length L is much smaller than the Rayleigh length ($L \ll z_R$, thin sample approximation). Using the following substitutions: $q = \beta I_0 L_{eff}$ (L_{eff}: effective sample length)[39] and $x = z/z_R$, this yields for the normalized TBI trace:

$$T_{\mathrm{TBI}}(x) = \frac{(1+x^2)}{q} \ln(1 + \frac{q}{1+x^2}) \tag{4.3}$$

Equation 4.3 enables us to determine q, and therefore β, from a fit to the experimental TBI trace.
The normalized OAI is derived in a similar way:

$$\begin{aligned} T_{\mathrm{OAI}}(x) &= (1+x^2) \,. \\ &\left| \sum_{m=0}^{\infty} \frac{(i\Delta\phi_0)^m (2m+1+ix)}{m!(1+x^2)^m((2m+1)^2+x^2)} \right|^2 \end{aligned} \tag{4.4}$$

For practical calculations, we limit ourselves to an approximation up to the third order in the nonlinear phase shift $\Delta\phi_0$:[23]

$$\begin{aligned} T_{\mathrm{OAI}}(x) &= 1 + \frac{4x}{(x^2+1)(x^2+9)}\Delta\phi_0 \\ &+ \frac{4(3x^2-5)}{(x^2+1)^2(x^2+9)(x^2+25)}\Delta\phi_0^2 \\ &+ \frac{32x(x^2-11)}{(x^2+1)^3(x^2+9)(x^2+25)(x^2+49)}\Delta\phi_0^3 \end{aligned} \tag{4.5}$$

We estimate that the first order approximation (the one most often used in literature) is valid up to $\Delta\phi_0 \approx 0.2$, the second order up to $\Delta\phi_0 \approx 1$ and the third order up to $\Delta\phi_0 \approx 1.75$. The validity is within an error of less than 3.5% in determining the OAI transmission and predicting the focal position (x=0). By fitting the OAI trace to eq. 4.5, we can determine $\Delta\phi_0$ and thus n_2 according to:

$$\Delta\phi_0 = \frac{2\pi n_2 I_0 L_{eff}}{\lambda} \tag{4.6}$$

4.2.3 Thermal effects

When performing Z-scan measurements using a nontransparent material (as is the case here, as we study the *resonant* nonlinearities of PbS QDs around the band gap), the absorbed energy can be converted to heat. The corresponding temperature increase of the sample may also lead to a change in refractive index, due to the thermo-optical coefficient dn/dT. In the center of the laser beam, the higher optical intensity leads to a higher increase in temperature than at the edges of the laser beam. Hence, taking heat diffusion throughout the material into account, a steady state spatial temperature profile will develop at $t \gg t_c$, with $t_c = \frac{w_0^2}{4D}$ the characteristic profile buildup time. D denotes the thermal diffusion coefficient of the medium. If dn/dT differs from zero, the refractive index will follow this temperature profile, leading to a thermal lensing effect[40] (similar to the electronic lensing effect described above).

The resulting OAI trace will also show an anti-resonance. Taking only linear absorption into account, *i.e.*, neglecting nonlinear processes such as TPA, the *thermal* OAI can be described by:[40]

$$T_{\mathrm{OAI,th}}(x) = 1 + \theta \arctan\left(\frac{2x}{x^2+3}\right) \tag{4.7}$$

The equation is valid for a small thermal lens strength θ:

$$\theta = \frac{\alpha_0 L P}{\lambda \kappa}\frac{\mathrm{d}n}{\mathrm{d}T} \tag{4.8}$$

As expected, θ depends only on the average power and is inversely proportional to the thermal conductivity κ, as a larger κ leads to a more rapid heat dissipation.

4.3 Nonlinear refraction n_2 and β for PbS QDs

4.3.1 Fabricated samples

All following measurements (Z-scan and FWM) were performed at room temperature. For our study of the n_2 of PbS QDs, we prepared 12 QD samples. All the samples have a size dispersion of ≈5% . The sample optical properties are very stable in time[41]. Their properties are summarized in table 4.2. The concentrations of all samples are optimized to obtain a clearly measurable $\Delta\phi_0$, while still keeping its value low enough for the fit (equation 4.5) to apply ($\Delta\phi_0 < 1.75$). We use a $L = 1$ mm optical cell for the Z-scan measurements, satisfying $L \ll z_R$. The QDs

sample	size (nm)	λ_0 (nm)	c_0 (μM)
A	3.8	1123	4.95
B	5.2	1408	5.45
C	5.5	1492	6.34
D	5.9	1539	4.91
E	6.1	1574	4.63
F	6.4	1620	4.76
G-I	5.9	1539	0.48,1.37,2.89
J,K	5.9	1539	6.06,9.78
L	5.6	1506	Thin film

Table 4.2: Summary of the different samples used for the Z-scan and FWM experiments. λ_0 denotes the spectral position of the first absorption peak and c_0 the sample concentration.

are suspended in C_2Cl_4, a transparent solvent in the NIR spectral range. Z-scan traces recorded for C_2Cl_4 are featureless both for the TBI and OAI, revealing a negligible n_2 and β of the solvent. To determine the spectral dependence of n_2 for our QD suspensions, Z-scan traces are measured between 1535 and 1565 nm. The intensity dependence of n_2 is measured between 1 and 25 MW/cm^2, at $\lambda = 1550$ nm.

For sample D,E,F, we determine the intensity dependence of the nonlinear absorption coefficient β. Samples D,E,G-K are used to explore the nonlinear absorption further, by positioning the sample at the focus and collecting the sample transmittance T as a function of I_0. I_0 is varied between 0.5 and 25 MW/cm^2, around $\lambda = 1550$ nm. From T, the intensity-dependent absorption coefficient is calculated: $\alpha = \frac{-\ln(T)}{L}$. We use samples D,G-K to determine the concentration dependence of n_2, β and α.

For the FWM measurements we prepared sample L using a 20 μM solution of PbS QDs mixed with a solution 10 m% of polystyrene in toluene. The solution is spincoated with a spinning speed of 1000 rpm on a 0.17mm glass coverslip. The resulting film has an uniform thickness of ≈2 μm and macroscopically homogenous concentration of PbS QDs. The sample is then mounted on another coverslip of same thickness by using Meltmount (Cargille Labs) (refractive index 1.54) as mounting medium. For the FWM experiment the total average intensity used is varied between 0.7 to 89 kW/cm^2, corresponding to peak intensity from 0.054 to 6.9 GW/cm^2.

4.3.2 Excluding thermal effects

Typical OAI and TBI traces for a QD suspension are shown in Fig. 4.2. The OAI shows a strong anti-resonance (Fig. 4.2(a)), that can only be satisfactorily fitted to a sum of eqs. 4.5 and 4.7 (Fig. 4.2(b)). The TBI features an increase in intensity near the focus indicating a negative β (Fig. 4.2(c)). Using the ESH, we switch the laser light between *on* for 2 ms and *off* for a time interval variable between 0 and 64 ms, corresponding to a duty cycle DC between 100$\%$ and 3$\%$, respectively. As shown in Fig. 4.2(a), we find that reducing DC from 100% to 12.5% leads to a steady decrease of the OAI peak and valley amplitude. Below 12.5%, the OAI trace tends towards a limiting trace when DC is further reduced. In addition, no change in the limiting trace is obtained when reducing the on time to 1 ms keeping the same duty cycle. In Fig. 4.2(c), one sees that the TBI remains constant when sweeping the DC.

The above observations indicate that at a DC of 12.5% or more, the OAI is composed of an electronic and a thermal component. Using the fit of the OAI to a sum of an electronic and a thermal non-linearity, we determined dn/dT. Limiting the DC to 12.5% to ensure the low thermal lens strength condition, we obtain a value of -0.9 10^{-4} K^{-1}, which stays constant in the range 1535 nm-1565 nm. Independent measurements of dn/dT for CCl_4, $CHCl_3$ and CH_2Cl_2, performed at visible wavelengths, yield values of about -6 10^{-4} K^{-1}.[42;43] As we find a number of the same order of magnitude, we conclude that the energy absorbed by the QDs is at least partially converted to heat and transferred to the surrounding C_2Cl_4 medium. Using the material properties of C_2Cl_4 (D =7.7 10^{-8} m^2/s)[44], we calculate a t_c of 4.7 ms. Hence, a duty cycle of 7.3% or less is needed to prevent the buildup of a stationary thermal lens. In line with these findings, we fix DC at 3.1% for further measurements. This excludes thermal contributions and allows

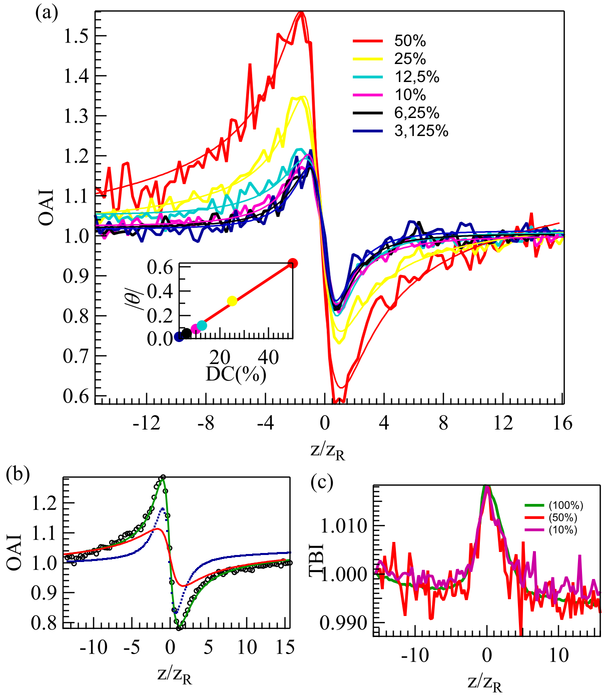

Figure 4.2: (Color online) (a) Typical experimental OAI traces, measured on $\lambda = 1550\,\mathrm{nm}$ for sample D as a function of ESH duty cycle. The OAI shows a strong anti-resonance. Inset: When redcuing the DC the magnitude of the thermal lens strength decreases. (b)Illustration for the traces fitted (black dots) with a sum of equation 4.5 (blue line) and 4.7 (red line) for sample D at a $DC = 12\%$. (c) The corresponding measured TBI traces for sample D. The TBI remains constant when changing the duty cycle and yields an increase around the focus indicating a negative β.

the determination of n_2 by fitting OAI traces using only the electronic contribution of eq. 4.5.

4.3.3 Analyzing n_2 and β

Figure 4.3(a) shows typical OAI traces obtained for sample K at two different light intensities. As indicated in Fig. 4.3(b), this results for the PbS QD concentrations used (4.5-6.5 μM) in a nonlinear refractive index n_2 of the order of $10^{-11}\ \mathrm{cm}^2/\mathrm{W}$, a value independent of I_0 in the intensity range $I_0 = 1 - 25\,\mathrm{MW/cm}^2$ around $\lambda = 1550\,\mathrm{nm}$. By changing the QD concentration in solution, we find that n_2 changes proportionally to the QD volume fraction f (Fig. 4.3(c)). From the regression curve we get a concentration independent intrinsic nonlinear refraction index $n_{2,int} = n_2/f$ of $-1.17\ 10^{-7}$ cm^2/ W, a value of the same order of magnitude as the $-6.5\,10^{-7}\ \mathrm{cm}^2/\mathrm{W}$ measured for PbSe QDs at $\lambda_0 = 1640\,\mathrm{nm}.$[23]. Figure 4.4 represents the spectral dependence of n_2 for samples A–F, measured between 1535 and 1565 nm and rescaled to a concentration value of 5 μM. As the wavelength range is limited, an alternative representation of n_2 is given, in which the abscissa is the difference between the laser wavelength and the absorption wavelength λ_0 of the QDs. In agreement with the n_2-spectrum of PbSe QDs,[23] we find that n_2 is correlated with the absorbance spectrum of the PbS QD suspensions.

A suitable parameter to assess the measured values for n_2 is the figure of merit (FOM$=$ $\delta n/(\lambda\alpha)$). It is a materials property, independent of the QD volume fraction and reflects the maximal nonlinear phase shift that can be achieved when light propagates through a sample, before absorption reduces its intensity too much for nonlinear effects to occur. Within the intensity range studied, we find FOMs that are larger than 1 and that increase with increasing light intensity. Since these values are similar to the FOM of AlGaAs[7] and the chalcogenide glasses[9–11] (table 4.1), PbS QDs are clearly of interest as nonlinear optical materials.

Figure 4.5(a) shows the nonlinear absorption coefficient β as determined for three different PbS samples. In line with the TBI trace given in

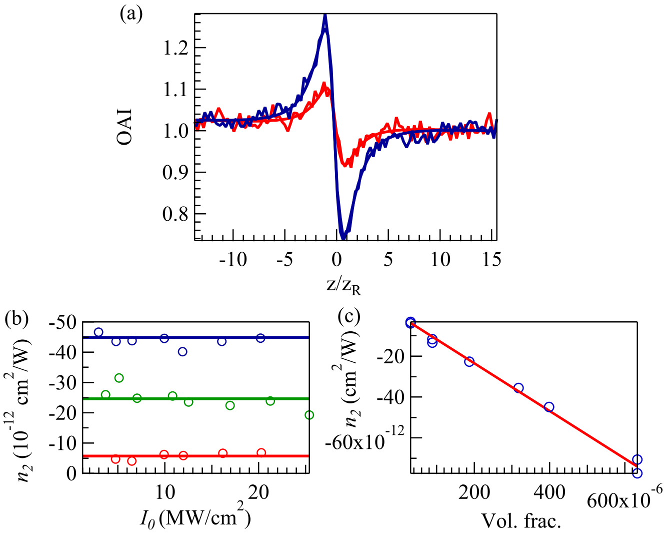

Figure 4.3: (Color online)(a) Measured OAI for sample K at intensities of 2.7 and 8.0 MW/cm^2 at a $DC = 3.1\%$ fitted with equation 4.5. (b) Dependence of n_2 on I_0 for samples J,E,F (blue, green and red dots). n_2 remains constant over the entire intensity range.(c) n_2 increases linearly with the QD volume fraction measured for samples with first absorption peak at 1539 nm (see table 4.2).

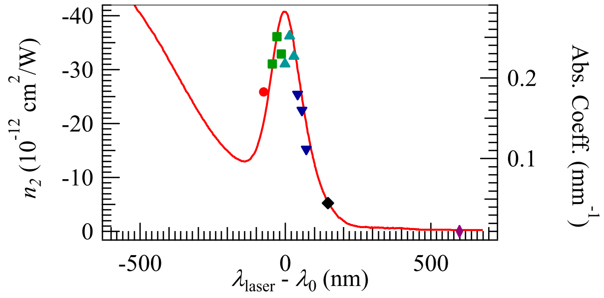

Figure 4.4: (Color online) n_2-spectra around 1550 nm. λ_0 denotes the absorption peak of the sample and λ_{laser} is the varying laser wavelength. n_2 is clearly correlated with the QD absorption coefficient. The symbols are from right to left: diamond (sample A) , square (sample B), downward triangles (sample C), upward triangles (sample D) , squares (sample E) , dot (sample F).

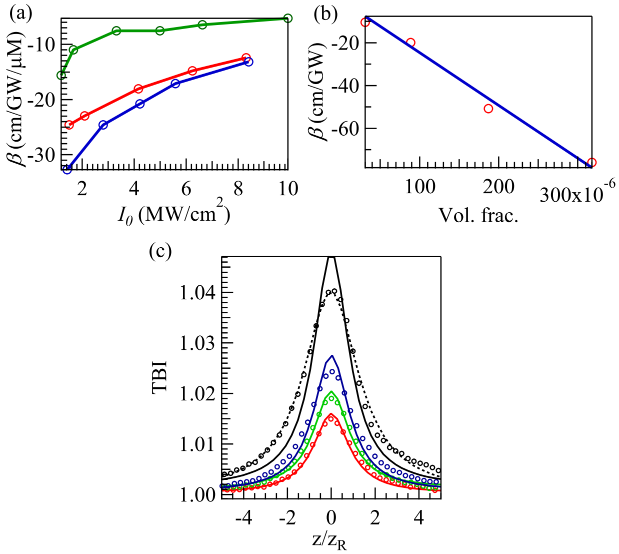

Figure 4.5: (Color online)(a) The magnitude of β (normalized to corresponding concentration) decreases with increasing I_0. Blue,red and green curve corresponds to resp. sample D, E, F. (b) β scales linearly with the QD volume fractions measured for samples with λ_0 =1539 nm. (c) TBI traces for sample D at optical intensities of 1.7, 2.5, 3.7, 8.4 MW/cm^2 fitted with eq. 4.3 (full lines). At I_0=8.4 MW/cm^2 the TBI fits only with eq.4.23 (dotted black line) as it broadens compared with the predicted fit from a true third order non-linearity (full black line).

Fig. 4.2(c), β is negative and is largest for λ_0 closest to the excitation wavelength. Similar to n_2, the magnitude of β increases with the volume fraction. A linear fit yields an intrinsic nonlinear absorption coefficient $\beta_{int} = \beta/f$ of -2.47 10^5 cm/GW. On the other hand, Fig. 4.5(a) indicates that the magnitude of β – as determined from a fit of the TBI to eq. 4.3 – decreases with increasing intensity. In addition, the TBI (Fig. 4.5(c)) broadens at intensities above 8 MW/cm^2 and no longer fits to eq. 4.3.

4.4 Simulation of the QD exciton population

4.4.1 Bandgap exciton population of the QDs

The number of excitations or absorbed photons per unit of volume created per pulse, N_{ph}, equals :

$$N_{ph} = \frac{E_{abs}}{E_{gap}L} \tag{4.9}$$

with L the sample length and E_{abs} the absorbed energy per unit of area following an excitation with a pulse. For $\alpha L << 1$ we find for E_{abs}:

$$E_{abs} = \frac{P}{\nu \pi w_0^2}\alpha(E_{gap})L \tag{4.10}$$

with $\alpha(E_{gap}) \approx \alpha_0(E_{gap})$, with $\alpha_0(E_{gap})$ the linear absorption coefficient at the bandgap energy. This approximation is valid in our case as α maximally decrease with 20% over the measured intensity range (figure 4.5). P_{avg} is the average laser power and is related to I_0 through expression 4.2. The number of excitations per pulse created per QD N_{ex} is :

$$N_{ex} = \frac{N_{ph}}{c_{ex}N_A} \tag{4.11}$$

with c_{ex} the concentration of QDs excited with the laserbeam. c_{ex} is determined as

$$c_{ex} = c_{tot}\int c(E)S(E)dE \tag{4.12}$$

c_{tot} is the total QD concentration and $c(E)dE$ represents the fraction of QDs with a bandgap in the energy range $E, E+dE$. $S(E)$ represents the probability that a QD with bandgap E gets excited with the corresponding laserbeam. $c(E)$ and $S(E)$ are given by :

$$c(E) = \frac{1}{\sqrt{2\pi}\sigma_{inh}} e^{-\frac{(E-E_{gap})^2}{2\sigma_{inh}^2}} \tag{4.13}$$

$$S(E) = e^{\frac{-(E-E_l)^2}{2(\sigma_l^2+\sigma_{hom}^2)}} \tag{4.14}$$

with E_l central energy of the Gaussian laserbeam and $\sigma_l = \frac{\Delta E_l}{2\sqrt{2ln(2)}}$, with ΔE_l, the FWHM of the laserbeam. Similarly $\sigma_l = \frac{\Delta E_{hom}}{2\sqrt{2ln(2)}}$ and $\sigma_{inh} = \frac{\Delta E_{inh}}{2\sqrt{2ln(2)}}$ with ΔE_{hom}, ΔE_{inh} respectively the homogenous and inhomgenous linewidth of the QDs.

As the size dispersion is very small (5%), one can assume the inhomogenuous linewidth to be constant for all QDs[45]. Evaluation of expression 4.12 for c_{ex} yields :

$$c_{ex} = c_{tot} \frac{e^{\frac{-(E_{gap}-E_l)^2}{2(\sigma_{inh}^2+\sigma_l^2+\sigma_{hom}^2)}} \sqrt{\sigma_l^2 + \sigma_{hom}^2}}{\sqrt{\sigma_{inh}^2 + \sigma_l^2 + \sigma_{hom}^2}} \tag{4.15}$$

This leads to a final expression for N_{ex} presuming that we excite with a central laser energy in resonance with the bandgap energy($E_l = E_{gap}$):

$$N_{ex} = \frac{\sqrt{\pi}\tau_p I_0 \alpha_0(E_{gap}) \sqrt{\Delta E_{inh}^2 + \Delta E_l^2 + \Delta E_{hom}^2}}{2E_{gap} c_{tot} N_A \sqrt{\Delta E_l^2 + \Delta E_{hom}^2}} \tag{4.16}$$

The factor $\sqrt{\Delta E_{inh}^2 + \Delta E_l^2 + \Delta E_{hom}^2}$ represents the total linewidth of the QDs.

4.4.2 Occupancy rate equations

We define c_i as the fraction of total QDs which contain i excitons. The number i can maximally reach 8 due to the 8-fold degeneracy of the

HOMO and LUMO levels in the PbS QDs. Within the duration of each incoming pulse the occupancy of the different c_i changes with time due to the absorption and stimulated emission of photons. This yields:

$$\begin{gathered}
\frac{\mathrm{d}c_0}{\mathrm{d}t} = -k_{0,abs}c_0 + k_{1,em}c_1 \\
\frac{\mathrm{d}c_1}{\mathrm{d}t} = k_{0,abs}c_0 - k_{1,abs}c_1 - k_{1,em}c_1 + k_{2,em}c_2 \\
\frac{\mathrm{d}c_2}{\mathrm{d}t} = k_{1,abs}c_1 - k_{2,abs}c_2 - k_{2,em}c_2 + k_{3,em}c_3 \\
\dots \\
\frac{\mathrm{d}c_7}{\mathrm{d}t} = k_{6,abs}c_6 - k_{7,abs}c_7 - k_{7,em}c_7 + k_{8,em}c_8 \\
\frac{\mathrm{d}c_8}{\mathrm{d}t} = k_{7,abs}c_7 - k_{8,em}c_8
\end{gathered} \tag{4.17}$$

Here, $k_{i,abs}$ is the rate of absorption of a state i, which is given by $\frac{i-8}{8}k_{0,abs}$. $k_{0,abs}$ is the rate of absorption by an unexcited state QD, which corresponds to $\frac{\epsilon ln(10)I_0}{N_A E_{gap}}$. With ϵ the molar extinction coefficient determined as: $\frac{2\sqrt{2ln(2)}}{\sqrt{2\pi}}\frac{\epsilon_{int}}{\Delta E_{hom}}$. ϵ_{int} is the integrated molar extinction value which is given by 15.3 $\frac{\mathrm{meV}}{\mu\mathrm{Mcm}}$ [46]. $k_{i,em}$ is the stimulated emitting rate from a state i to a state (i-1) and is given by $\frac{i}{8}k_{0,abs}$.

Between the pulses we assume $c_i \rightarrow 0$, i.e. that the relaxation of the states c_i,i =2..8 is much faster than the laser repetition period of 100 ns. This means that the remaining relaxation contribution is due to 1 μs radiative recombination[46] of state c_1. By implementing this procedure numerically, one can calcuate for a given ΔE_{hom} and I_0 the average number of excitons in the QDs through:

$$< \gamma(t) >=< \sum ic_i(t) > \tag{4.18}$$

The corresponding absorption coefficient will be calculated in the next section using eq.4.19.

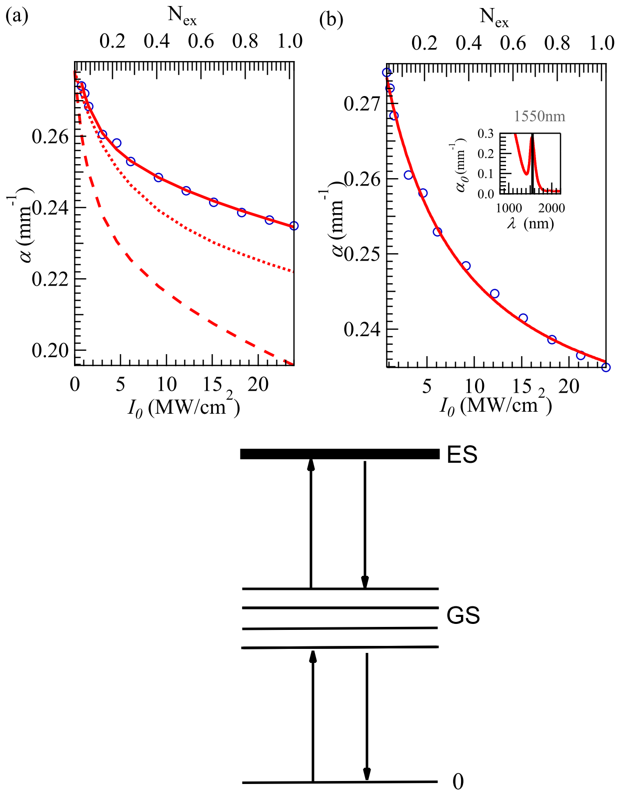

Figure 4.6: (Color online)(a) When we exclude the absorption from an exciton ground state (GS) towards an exciton excited state (ES) (eq. 4.19) the theoretically expected absorption, assuming a QD homogeneous linewidth (ΔE_{hom}) of 18 meV (dashed line), is smaller compared with the measured one (blue circles). Neglecting the contribution of the inhomogenous broadening and assuming the total linewidth is all due to homogenous broadening ($\Delta E_{hom} = \Delta E_{total}$ =58 meV) the corresponding increase in absorption (dotted line) is not sufficient to explain the measurements. If we include the absorption from GS to ES the measurements fits well with rate equation model with ΔE_{hom} =18 meV. (b) Measured α fitted with expression 4.21. Inset: Absorption spectrum (α_0) of sample D.

4.5 Intensity dependence of the absorption coefficient (α)

The broadening of the TBI and the decrease of β with increasing I_0 point towards absorption saturation. To investigate this, we have directly measured the absorbance α as a function of the optical intensity I_0 (sample D and E). The QDs are probed at 1550 nm, on resonance with their band gap transition. Figure 4.6(a) shows that, at low optical power, the linear absorbance α_0 is recovered. In line with the negative nonlinear absorption coefficient, α decreases with increasing I_0, which suggests bleaching induced by state filling.

Assuming an 8-fold degeneracy of the PbS HOMO and LUMO, one expects that the absorbance of a QD decreases linearly with the number of excitons γ it contains, to reach zero when $\gamma = 4$[47]:

$$\alpha = \frac{(8 - 2\gamma)}{8}\alpha_0 \tag{4.19}$$

The expected complete bleaching at $\gamma = 4$ contrasts with conclusions from[48;49], yet forms a relevant starting point to benchmark our results. As a reference, the top axis in Fig. 4.6(a) gives the average number of photons N_{ex} absorbed per QD by a single pulse with an intensity as given by the bottom axis (see calculation above). At the highest light intensities used, N_{ex} reaches one. Since the exciton lifetime of about 1 μs exceeds the 100 ns time delay between successive pulses, this indicates that the measured change of the absorbance is not due to a single pulse event, yet results from the build-up of excitons over several pulses. Based on this picture and eq. 4.19, we have calculated $\alpha(I_0)$ by using a rate equation model involving band gap absorption and stimulated emission (see calculation above). For this calculation, we assumed a homogenous linewidth ΔE_{hom} of the QD's first exciton transition of 18 meV. This is a 300 K value extrapolated from low temperature data determined by exciton dephasing in an ensemble of QDs done with photon-echo spectroscopy[45]. As shown in Fig. 4.6(a), this results in a theoretical $\alpha(I_0)$ considerably smaller than the measured one. The same conclusion holds if ΔE_{hom} is set equal to the total linewidth of 58.5 meV, a value that follows from the FWHM of the first exciton transition in the QD absorption spectrum. In line with our experiment, previous measurements on PbS suspensions[48;49] did not yield complete absorption bleaching at high excitation intensities.

This indicates that an excited QD is a stronger absorber than predicted by eq. 4.19. As shown in Fig. 4.6, a possible origin of this enhanced, photoinduced absorption are intraband transitions that bring the first exciton (labeled as GS in Fig. 4.6) to an excited single exciton state (ES in Fig. 4.6). A similar observation was made in lead salt QD doped glasses[29;37].

If the electrons in the conduction band and the holes in the valence band of excited QDs can be excited to higher energy conduction band or lower energy valence band states, one expects an additional contribution to α that is proportional to the number of excitons:

$$\alpha = \frac{(8-2\gamma)}{8}\alpha_0 + \frac{\gamma}{4}\alpha_{pi} \tag{4.20}$$

Clearly, the occurrence of photoinduced absorption inhibits the bleaching of the QD band gap transition when $\gamma = 4$. If we base our calculation of $\alpha(I_0)$ on eq. 4.20, a fit with the experimental curve yield α_{pi} =0.4 α_0. By including photoinduced absorption in the proposed two-level model, the theory fits well with the experimental results.

Figure 4.6(b) shows that for practical purposes, the experimental $\alpha(I_0)$ can be fitted by extending the expression for the intensity dependence of the absorbance of a two-level system with a non-saturable absorption coefficient α_{ns}[50]:

$$\alpha = \frac{\alpha_0 - \alpha_{ns}}{1 + I_0/I_{sat}} + \alpha_{ns} \tag{4.21}$$

This includes a saturation intensity I_{sat}, which corresponds to the value of I_0 where the absorbance is halfway between α_0 and α_{ns}. Typical values for the fitting are I_{sat} $=$7.2 MW/cm^2 and $\frac{\alpha_{ns}}{\alpha_0}$ =0.8. By using eq. 4.21 to describe $\alpha(I_0)$, we can reinterprete the TBI traces measured in Fig. 4.5(c). For this, we divide the intensity I_0 in eq. 4.21 with a factor $(1 + x^2)$ – where $x = \frac{z}{z_R}$ – to take into account the Gaussian spatial dependence of the intensity :

$$\alpha(x, I_0) = \frac{\alpha_0 - \alpha_{ns}}{1 + I_0/(I_{sat}(1 + x^2))} + \alpha_{ns} \tag{4.22}$$

$$T_{\mathrm{TBI}} = e^{-\alpha(x,I_0)L} \tag{4.23}$$

At low light intensities, eq. 4.23 reduces to eq. 4.3, which holds for a third order non-linearity. With increasing light intensity however, only 4.23 fits to the experimental, broadened TBI traces.

4.6 Four Wave Mixing (FWM)

The Z-scan measurement as described above yields the absolute values of the nonlinear refractive index and absorption coefficient, but it provides no information on the dynamics of the optical nonlinearity. To investigate this, we measure the time-resolved response of the optical nonlinearities using a FWM set-up (Fig. 4.7a) [51]. A Ti:Sapphire laser pumps an optical parametric oscillator (APE OPO) which provides pulses of 150 fs duration around 1.47 μm with 76 MHz repetition rate. The laser beam is split up into 4 components denoted as reference, Pulse 1, Pulse 2 and Pulse 3 (R, P_1, P_2,P_3). The frequencies of the pulses are upshifted using acousto-optical modulators to 79, 80, and 80.6 MHz, for P_1, P_2, and P_3 respectively. This leads to a 1MHz modulation of the carrier density. P_1 and P_2 as well as P_2 and P_3 are mutually time-delayed by τ_{12} and τ_{23} by means of delay stags (DL) with a temporal resolution of 20 fs. All exciting pulses are combined through BS5 and sent through the sample S (thin film) using an oil-immersion microscope objective MO1 with a numerical aperture of NA =1.25.

P_1 creates a coherent polarization in resonance with the band gap transition of the sample. P_2, arrives in time-overlap ($\tau_{12} = 0$) to ensure that the coherent polarization is not lost, and interferes maximally with P_1. The interference of P_1 and P_2 creates a beating pattern within the sample (see Fig. 4.7b). This induces a carrier density modulation of 1 MHz over the pulse repetitions. This modulates the absorption and hence the transmission of the probing pulse P_3, resulting in a measured FWM field

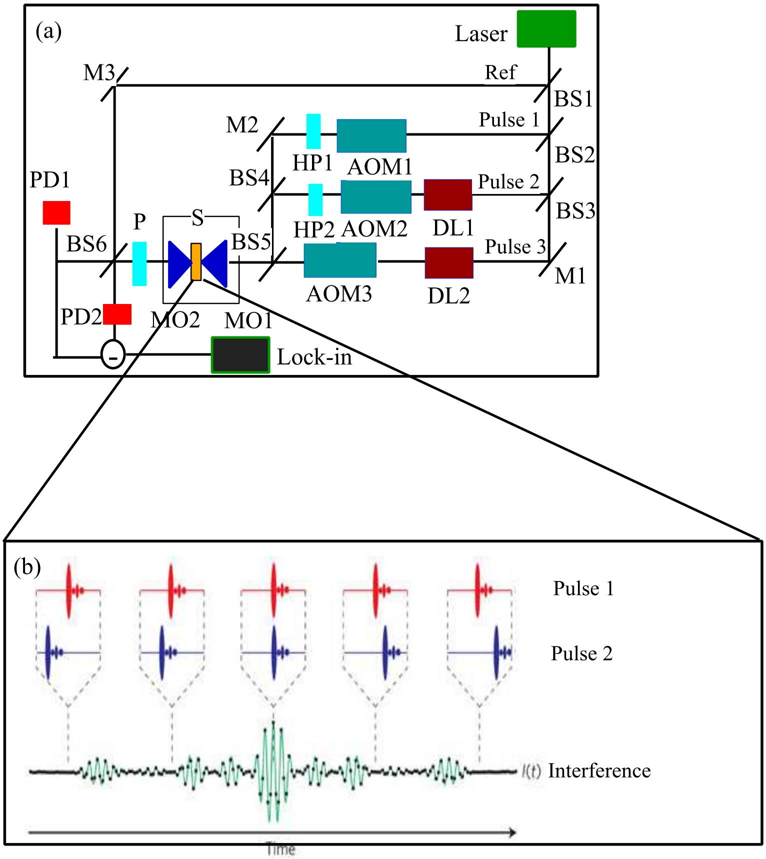

Figure 4.7: (Color online) (a) Schematic representation of the FWM setup as outlined in the text. (b) Schematic representation of the interference of Pulse 1 (red) and Pulse 2 (blue). Pulse 2 is slightly shifted in optical frequency with respect to Pulse 1 creating an interference pattern varying with a beating frequency of 1MHz over the different pulse repetitions.

E_{FWM} proportional to

$$E_{\mathrm{FWM}}(t) \propto \chi^{(3)}(t) E_1 E_2^* E_3(t) \tag{4.24}$$

with the third-order susceptibility $\chi^{(3)}$. $E_{1,2,3}$ are the optical electric fields associated with $P_{1,2,3}$ in the sample, having an amplitude proportional to $\sqrt{I_{1,2,3}}$. The FWM field is measured through its interference with the reference field which is in time overlap with P_3. The dynamics of the modulated carrier density can be obtained by measuring E_{FWM} as a function of the delay τ_{23}. $P_{1,2}$ were chosen linearly co-polarized by half-wave plates (HP). Both were cross-polarized to P_3 and R to reduce the background from the balanced photodetectors (BPD) and maximize the heterodyne detection of the FWM signal.

4.7 Dynamics of optical nonlinearities in PbS QDs

Since the nonlinear optical properties of PbS QDs are related to the creation of excitons, one expects that the relaxation and recombination of these excitons determines the dynamics of their optical non-linearity. We analyzed this nonlinear dynamics using FWM as described in section 4.6. Figure 4.8(a) represents the FWM amplitude as measured on PbS QDs (sample L) excited at λ_{ex} =1470 nm as a function of the time delay between P_2 and P_3. The different traces correspond to different intensities of the P_1 pulse (with P_2 and P_3 having same intensity as P_1) expressed in terms of N_{ex}. N_{ex} has been calculated considering the constructive interference between P_1 and P_2 leading to an effective intensity $4I_1$. The intensity has been tuned such that the FWM experiments correspond to the same range of N_{ex} (0-3) as used in the Z-scan measurements (see Fig. 4.6a). Figure 4.8(a) clearly shows that with increasing excitation intensity, the resolved FWM dynamics has a larger amplitude and a faster decay. Moreover a dip appears at time overlap.
We have analyzed the FWM dynamics using the following response function:

$$\begin{aligned} E_{\mathrm{FWM}}(\tau_{23}) &= \Theta(\tau_{23})(A_1 e^{-\frac{\tau_{23}}{T_1}} \\ &+ A_2 e^{-\frac{\tau_{23}}{T_2}}) + A_{\mathrm{os}}, \end{aligned} \tag{4.25}$$

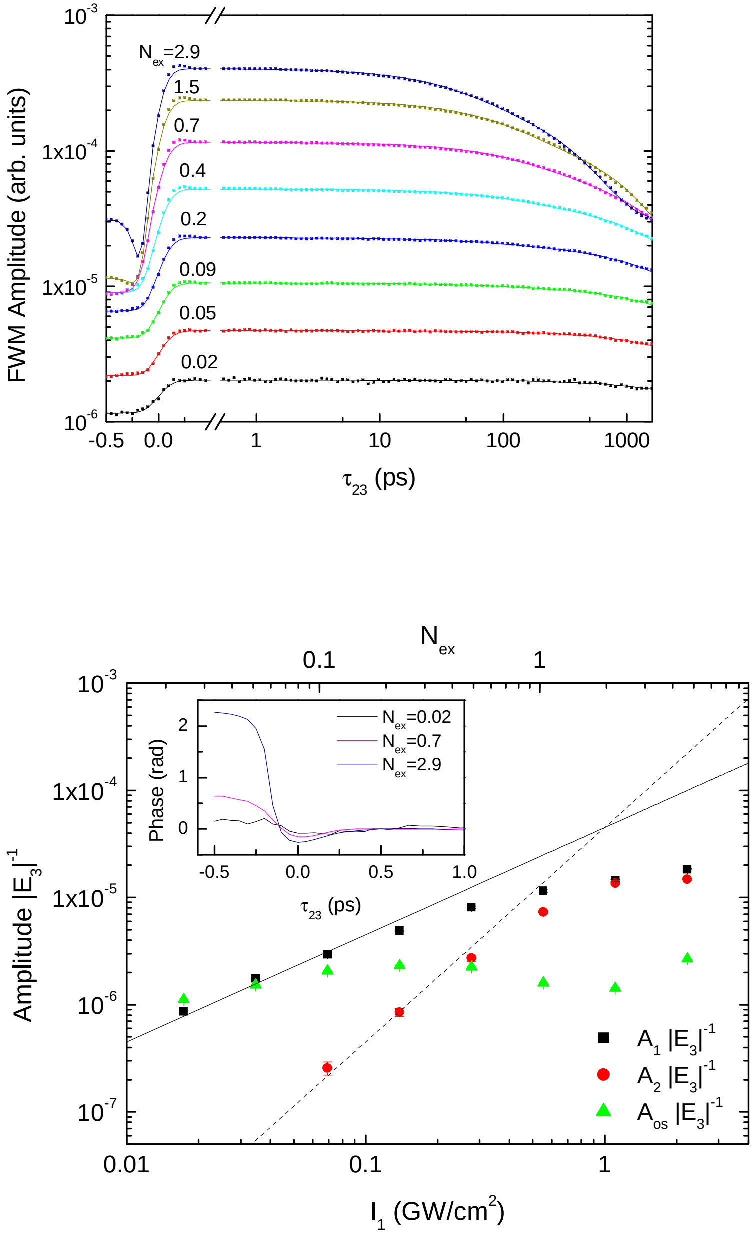

Figure 4.8: (Color online)(a) Measured FWM for sample L as a function of the averaged excitations per QD created per pulse, N_{ex}. (b) Amplitude of each recombination mechanism (see text) divided by the P_3 field amplitude as a function of P_1 intensity (I_1). Solid and dashed lines show a linear and quadratic dependence with the excitation intensity respectively. In the inset: dynamics of the FWM field phase for different excitation intensities around $\tau_{23} = 0$, relative to the phase at $\tau_{23} = 0.5\,$ps.

The sum of two exponentials multiplied by a step function $\Theta(\tau_{23})$ represents the response after the excitation. The offset A_{os} is included to account for the accumulation of excitons/charges over successive pulses since the single exciton lifetime of about 1 μs[41] strongly exceeds the repetition period of the laser (13 ns). The FWM dynamics is then fitted considering the convolution of the response function with a Gaussian pulse intensity autocorrelation, which transforms an instantaneous contribution into the Gaussian pulse autocorrelation and a step-function into an error function. For the contributions A_1 and A_2, we find lifetimes in the range 1–4 ns (T_1) and 45–110 ps (T_2). Fig. 4.8(b) shows the amplitude of each contribution normalized to the amplitude $|E_3|$ of the P_3 field as a function of I_1.

At peak excitation intensities below 0.13 GW/cm^2 ($N_{ex} < 0.17$) the decay is dominated by the nanosecond component. Similar to what was reported previously on PbS QDs of smaller size [51], we attribute this nanosecond dynamics to phonon-assisted single exciton thermalization between the 64 1S-like energy states. This interpretation is confirmed by the linear increase of $A_1/|E_3|$ with the excitation power in the low intensity regime, which indicates a single exciton process.

With increasing optical intensity, the picosecond component becomes more and more important. The time constant T_2 is constant over the intensity range investigated(110 $\pm$ 20 ps), apart for the maximum intensity where it drops to 45 ps. $A_2/|E_3|$ follows a quadratic dependence on excitation intensity and eventually saturates at high I_1. Such dynamics with quadratic intensity dependence could be attributed to Auger–like non-radiative recombination of biexcitons created in a single pulse repetition. However, in smaller PbS dots, where the probability for Auger processes is expected to be larger, we found no evidence of such biexciton recombination [51]. Alternatively, this component can be explained as thermalization of single excitons between the different levels of the ground state mediated by carrier-carrier scattering. Notably, the nanosecond time constant varies from 4.3 ns at 0.02 GW/cm^2 to 0.33 ns at 2.2 GW/cm^2, with a low intensity dependence of $I_1^{-0.27}$ and a high intensity dependence of $I_1^{-1.5}$, further indicating a speeding-up of exciton thermalization at high intensities.

In our FWM experiment, the photoinduced absorption of excitons would result in a decrease of the signal and cannot be distinguished from the dominant absorption bleaching. However, in line with the discussion in the previous section, the presence of photoinduced absorption is supported by the dip observed at negative delays. Its presence at high excitation intensities is due to destructive interference between the left-over signal due to previous pulses and the FWM generated by the P_1-P_2-P_3 pulse sequence with P_3 in time overlap with the reference pulse. The inset of Figure 8(b) shows the dynamics of the FWM field phase for three excitation intensities corresponding to N_{ex} equal to 0.02, 0.7, and 2.9, respectively. At low intensity the phase at negative and positive delays is similar, indicating that the signal measured at negative delays is due to absorption bleaching induced by the left-over exciton density generated by previous pulses. With increasing intensity, the phase difference between the signal at negative and positive delays increases and reaches $\sim 0.75\pi$ for $N_{ex} = 2.9$. This suggests that the origin of the signal at negative delays is different from absorption bleaching.

Thermal effects can produce a phase shift of the FWM signal of $\pi/2$, while photoinduced absorption should give a phase shift of π. Since the measured phase shift exceeds 0.5π, induced absorption is a significant process. [1] The continuous change of the phase difference with intensity indicates that the signals of the induced absorption and the absorption bleaching are not π out of phase. While the resonant absorption bleaching will not be accompanied by a resonant phase component, the photoinduced absorption can, provided that it is not spectrally centered at the excitation wavelengths. This will be the case, e.g. when photoinduced absorption involves transitions to higher energy conduction or valence band states of the QDs.

---

[1] The effect of heating can be neglected. Considering the beam size and the thermal diffusion coefficient of the polystyrene[52], we estimate for the FWM experiment a characteristic heating build up time $2 \cdot 10^3$ time faster than in the Z-scan experiment, with an on state of the excitation $4 \cdot 10^3$ times shorter. As a consequence the heating effects are attenuated by a factor of 2 in the FWM experiment with respect to the Z-scan measurements, where it is negligible.

The observation that photoinduced absorption starts to dominate the FWM signal at negative delays with increasing light intensity may reflect the presence of charges in the QDs, related to the occurrence of Auger events at high exciton densities. As a result of an Auger process, one of the carriers can be trapped by a defect state at high energy or leave the QD to be trapped in its vicinity. In this situation, the cross section of the absorption bleaching broadens as compared to that of resonantly excited QDs in their ground state. On the other hand, the cross section of the photoinduced absorption has most likely a broad spectrum. Hence, it will not be significantly affected by the redistribution of the carriers.

4.8 Discussion

The measurements presented here demonstrate that resonantly excited PbS QDs have a large nonlinear refractive index, with a figure of merit that exceeds one. This optical non-linearity is related to the creation of excitons and to photoinduced absorption – possibly intraband absorption – in already excited QDs. Relaxation and recombination of excitons lead to a complex nonlinear dynamics, with distinct time constants of the order of 100 ps and 1 ns next to the single exciton lifetime of about 1 μs. Furthermore, like PbSe QDs, the n_2 spectrum of PbS QDs shows a bell shape, which contrasts with the dispersive, anti-resonance behavior predicted for the two-level system[50]. This can mean that the optical nonlinearity is dominated by photoinduced absorption, which is typically a spectrally broad process that does not result in the dispersive n_2 of the two-level system. Alternatively, the n_2 spectrum can also have the observed bell shape if biexciton absorption is the dominant process. Although biexciton absorption should also lead to an anti-resonance in n_2, its resonance frequency is slightly red shifted due to the biexciton binding energy[47]. Hence, biexciton absorption will always give a negative contribution to n_2, regardless of the wavelength used.

The Z-scan measurements do not allow for a decomposition of n_2 into the separate contribution from exciton creation and photoinduced absorption. Nevertheless, a number of arguments evidence that the contribution is due to photoinduced absorption. First, opposite to the nonlinear absorption, the nonlinear refraction does not show a tendency to saturate with increasing light intensity. This saturation is expected if only exciton creation contributed to n_2. Second, the intensity dependence of the absorption could only be modeled if we include photoinduced absorption from the exciton ground state to an excited exciton state. Finally, the FWM experiments, revealed that photoinduced absorption dominates absorption bleaching of the probing pulse at negative time delays.

For the FWM experiments, it is also interesting for practical applications, **e.g.** signal modulation, to compare the weight of the ultrafast components (45 -100 ps) with respect to the ’slow’ thermalization contributions. From Fig. 4.8 it is clear that at the regime of high intensities the ultrafast components become equally important or dominate the thermalization contributions. However, one needs up to GW/cm^2 of intensity levels to reach this regime and practical applications might become limited.

4.9 Two photon absorption coupled nonlinearities

In the previous section we investigated the nonlinearity under resonant excitation. A major drawback of the corresponding nonlinearity is the linear absorption, which leads to a strong attenuation of the light intensity, passing through the material. An alternative is to investigate the optical Kerr-effect due to two-photon absorption (TPA), which is inherently a fast process. Possible QDs for these applications are large CdTe QDs (bandgap 650-750 nm) or very small PbS and PbS/CdS QDs (bandgap 800-1000 nm).

Adapting Z-scan set-up for two photon absorption measurements

In contrast to resonant nonlinearities, which are present with excitation at optical intensities in the region 1-10 $\frac{\mathrm{MW}}{\mathrm{cm}^2}$, non-resonant TPA occurs at $1-10\,\frac{\mathrm{GW}}{\mathrm{cm}^2}$. As we do not possess a sufficiently strong laser, this yields that in the z-scan set-up the beamwidth at focus should be reduced from $\approx$ 40 μm to 1-4 μm to obtain the desired optical intensities I_0. We therefore changed the focusing lens in Fig. 4.1 by a microscope objective lens with a high numerical aperture (NA = 0.5). However, these strong focusing hampers an accurate determination of the beam characteristics (beamwidth w_0 and Rayleigh range z_R). z_R is a measure of the spatial extension of the focusing. Existing beamprofilometers show a detection limit of 10 μm. This problem is solved by measuring materials with known n_2 and β values. To determine z_R we prepared a 16 μM PbS QD suspension in toluene mixed with a 10 m% polystyrene in a toluene solution. The solution is spincast on a glass substrate and the PbS QDs are resonantly excited around the bandgap and showed a clear OAI trace. A fit trough the OAI curve yielded $z_R = 13\,\mu\mathrm{m}$. Based on this value we determined the beamwidth via the relation in eq.4.1 ($w_0 = \sqrt{\frac{z_R\lambda}{\pi}}$) as $w_0 = 2.5\mu\mathrm{m}$.

To verify the obtained numerical values we performed TBI-scans on pure silicon. Typically, OAI and TBI scans are executed under the condition where the thickness of the sample L is much smaller as compared to the Rayleigh range z_R[39]. This requirement facilitates the analysis and the analytical expressions as described in sec. 4.2.2 can be applied. From literature we find that β equals $0.8\frac{\mathrm{cm}}{\mathrm{GW}}$[8] at an excitation around 1550 nm for Si. This yields an expected dip of 0.4% for the TBI, a value at the edge of our detection limit. To increase the resolution of the dip we opt for a substrate with a thickness of $L = 500\,\mu\mathrm{m}$, many times larger than the Rayleigh range. Consequently, the focus of the beam will not fall within one single z-position in the sample, but on different z-values spanning over a length $L_{eff}/n_{Si}z_R$ in the sample (Fig. 4.9). n_{Si} is the linear refractive index of Si (3.5) and $L_{eff} = \frac{1-e^{-\alpha L}}{\alpha}$ is the effective sample length of Si. Note that for two-photon absorbing materials $L_{eff} = L$ as the linear loss α equals zero.

Therefore, the *nonlinear interaction increases* and the reliability of the measurements becomes higher. The z-scan OAI and TBI curves of the thick medium can be modeled using a distributed lens model. The medium is considered to act as a stack of thin nonlinear slices (Fig. 4.9b)

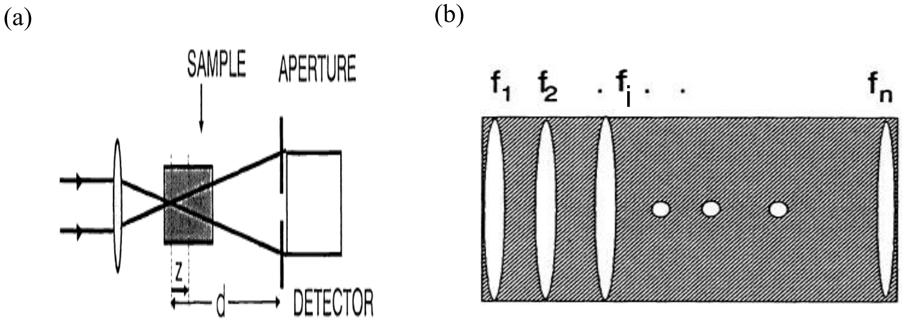

Figure 4.9: (a) Schematic of a thick z-scan experiment. (b) The thick nonlinear medium is considered as a stack thin nonlinear lenses whose focal distance depends on the optical irradiance.

and the laser beam travels through each of these slices sequentially. If coupling of the nonlinearities is neglected between the slices, the normalized transmittance for the OAI and TBI can be calculated from the sequential product of the normalized transmittance of the TBI and OAI of a single thin lens (eq. 4.3,eq. 4.5) where we simplfiy the result up to the first order in the phase shift $\Delta\phi_{0i}$ of the i-th single nonlinear lens:

$$\begin{aligned} T_{\mathrm{OAI}}(x) &= \lim_{\substack{L_i\to 0\\ n\to\infty}} \prod_{i=1}^{n} 1+\frac{4x}{(x_i^2+1)(x_i^2+9)}\Delta\phi_{0i} \\ &\approx \lim_{n\to\infty} exp\left[\sum_{i=1}^{n} 1+\frac{4x}{(x_i^2+1)(x_i^2+9)}\Delta\phi_{0i}\right] \\ &= \left[\frac{((x+l)^2+1)(x^2+9)}{((x+l)^2+9)(x^2+1)}\right]^{\frac{\Delta\phi_R}{4}} \end{aligned} \qquad (4.26)$$

An expression is obtained at $x = \frac{z}{z_R}$, with z the front position of the sample with respect to the focus of the Gaussian beam. $\Delta\phi_{0i} = \Delta\phi_R\Delta x_i$, the nonlinear phase along the length L_i of the i-th thin lens and $\Delta\phi_R = k\Delta n z_R$ is the total phase change along the Rayleigh length with $\Delta x_i = \frac{L_i}{z_R}$. $l = \frac{L}{z_R n_{sample}}$ is the normalized effective length, n_{sample} is the linear refractive index and L the effective length of the sample. In line with above considerations a similar expression can be deduced for the TBI for a thick medium based on the TBI for a single thin nonlinear lens[53;54]:

$$\begin{aligned}
T_{\text{TBI}}(x) &= \lim_{\substack{L_i \to 0 \\ n \to \infty}} \prod_{i=0}^{n} \frac{(1+x_i^2)}{q_i} \ln(1 + \frac{q_i}{1+x_i^2}) \\
&\approx \lim_{n\to\infty} 1 - \frac{1}{2} \sum_{i=0}^{n} \frac{q_i}{1+x_i^2} \\
&\approx \frac{1}{1 + \frac{1}{2}\int_x^{x+l} \frac{q}{1+x'^2} dx'} \\
&= \frac{1}{1 + \frac{1}{2} Q_R \left[tan^{-1}(x+l) - tan^{-1}(x)\right]} \qquad (4.27)
\end{aligned}$$

Fig. 4.10(a) shows the simulated TBI curves, based on eq. 4.27 as a function of l for Q_R=0.008. We see that with increasing l, the dip in the TBI-scans gets deeper and broader making it a signature of a thick nonlinear lens interaction. Fig. 4.10(b) shows TBI curves for the Si wafers analyzed at $\lambda_{ex} = 1550\,\text{nm}$ as a function of the optical intensity determined from w_0 and the incoming power. Based on l $=$11, a value extracted from $z_R = 13\,\mu\text{m}$, we get fit-values for the parameter Q_R=$\beta I_0 n_{Si} z_R$ for the three curves. This yields for β an average value of $0.93\,\frac{\text{cm}}{\text{GW}}$, which is close to the literature value of $0.8\,\frac{\text{cm}}{\text{GW}}$. This analysis illustrates that the beam parameters z_R en w_0 are accurately extracted and should allow to determine the nonlinearities of each two photon material. However, attempts of measuring the nonlinearites of large CdTe and small sized PbS QD-films, yielded OAI-scans that are hard to analyse as they were blurred by scattering.

4.10 Conclusions

We have studied the nonlinear properties of PbS QD suspensions as a function of wavelength, optical intensity and QD volume fraction using the Z-scan technique with picosecond pulses. Knowing the characteristic temperature profile buildup time t_c, we modulated the laser repetition rate and excluded thermal lensing to directly measure the electronic con-

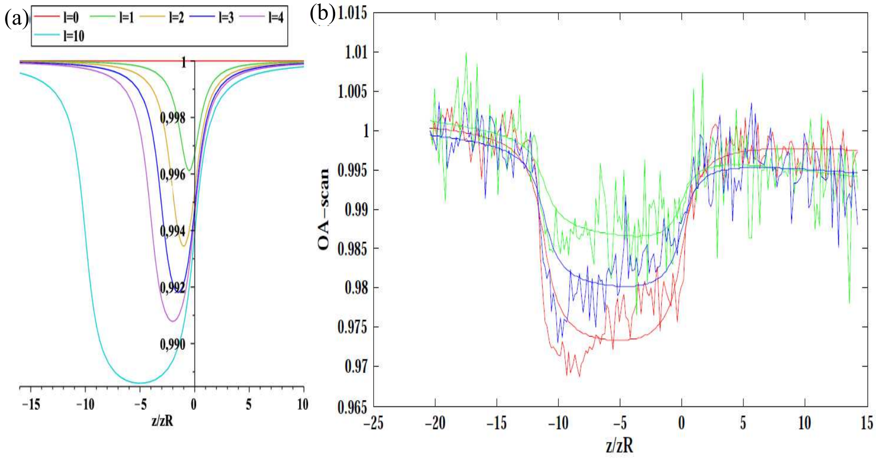

Figure 4.10: (a) Simulation of the TBI for a thick nonlinear medium for Q_R =0.008 as a function of the normalized effective length l. We see the that dip gets broader and wider as l increases. (b) TBI scans at $\lambda = 1550$ nm for a 500 μm thick Si measured at respectively I_0 =3.2, 4.2, 5 $\frac{\mathrm{GW}}{\mathrm{cm}^2}$ (green, blue, red) .

tribution to n_2. The nonlinear refractive index is independent from the intensity and follows the QD absorption spectrum. The FOM is larger than 1 for the PbS QDs and is comparable with PbSe QDs and lead chalcogenide glasses. It is argued that the creation of excitons and the resulting photoinduced absorption in the PbS QDs lie at the origin of the observed n_2 and β. Using transient Four Wave Mixing with 150 fs pulses we proved that at low excitation intensities the dynamics is dominated by single exciton thermalization (ns) and recombination (μs). At higher intensities the FWM signal results in a 100 ps response. This shows that colloidal PbS QDs are efficient and fast nonlinear materials. In combination with the facile integration of PbS QDs with photonic devices using wet deposition techniques and the easy tuning of the QD linear and nonlinear properties ,[55] this opens pathways for all-optical signal processing on photonic platforms.

Bibliography

[1] Priem, G.; Notebaert, I.; Maes, B.; Bienstman, P.; Morthier, G.; Baets, R. Design of all-optical nonlinear functionalities based on resonators. *IEEE Journal of Selected Topics in Quantum Electronics* **2004**, *10*, 1070 – 1078.

[2] Koos, C.; Jacome, L.; Poulton, C.; Leuthold, J.; Freude, W. Nonlinear Silicon-on-Insulator Waveguides for All-Optical Signal Processing. *Opt. Express* **2007**, *15*, 5976–5990.

[3] Petruska, M. A.; Malko, A. V.; Voyles, P. M.; Klimov, V. I. High-performance, quantum dot nanocomposites for nonlinear optical and optical gain applications. *Advanced Materials* **2003**, *15*, 610–613.

[4] Cumpston, B. H. et al. Two-photon polymerization initiators for three-dimensional optical data storage and microfabrication. *Nature* **1999**, *398*, 51–54.

[5] Kawata, S.; Sun, H. B.; Tanaka, T.; Takada, K. Finer features for functional microdevices - Micromachines can be created with higher resolution using two-photon absorption. *Nature* **2001**, *412*, 697–698.

[6] Serbin, J.; Egbert, A.; Ostendorf, A.; Chichkov, B. N.; Houbertz, R.; Domann, G.; Schulz, J.; Cronauer, C.; Frohlich, L.; Popall, M. Femtosecond laser-induced two-photon polymerization of inorganic-organic hybrid materials for applications in photonics. *Optics Letters* **2003**, *28*, 301–303.

[7] Villeneuve, A.; Yang, C. C.; Stegeman, G. I.; Lin, C. H.; Lin, H. H. Nonlinear Refractive-Index and 2 Photon-Absorption near Half the Band-Gap in Algaas. *Appl. Phys. Lett.* **1993**, *62*, 2465–2467.

[8] Dinu, M.; Quochi, F.; Garcia, H. Third-Order Nonlinearities in Silicon at Telecom Wavelengths. *Appl. Phys. Lett.* **2003**, *82*, 2954–2956.

[9] Lenz, G.; Zimmermann, J.; Katsufuji, T.; Lines, M. E.; Hwang, H. Y.; Spalter, S.; Slusher, R. E.; Cheong, S. W.; Sanghera, J. S.; Aggarwal, I. D. Large Kerr Effect in Bulk Se-Based Chalcogenide Glasses. *Opt. Lett.* **2000**, *25*, 254–256.

[10] Harbold, J. M.; Ilday, F. O.; Wise, F. W.; Sanghera, J. S.; Nguyen, V. Q.; Shaw, L. B.; Aggarwal, I. D. Highly Nonlinear as-S-Se Glasses for All-Optical Switching. *Opt. Lett.* **2002**, *27*, 119–121.

[11] Juliet, T. G.; Marin, S.; Erich, P. I.; Vladimir, N. F.; Wesley, A. K.; Max, S. Third Order Nonlinearities in Ge-as-Se-Based Glasses for Telecommunications Applications. *J. Appl. Phys.* **2004**, *96*, 6931–6933.

[12] Esembeson, B.; Scimeca, M. L.; Michinobu, T.; Diederich, F.; Biaggio, I. A High-Optical Quality Supramolecular Assembly for Third-Order Integrated Nonlinear Optics. *Advanced Materials* **2008**, *20*, 4584–4587.

[13] Vallaitis, T.; Bogatscher, S.; Alloatti, L.; Dumon, P.; Baets, R.; Scimeca, M. L.; Biaggio, I.; Diederich, F.; Koos, C.; Freude, W.; Leuthold, J. Optical properties of highly nonlinear silicon-organic hybrid (SOH) waveguide geometries. *Optics Express* **2009**, *17*, 17357–17368.

[14] Coe-Sullivan, S. Quantum dot developments. *Nature Photonics* **2009**, *3*, 315–316.

[15] Koos, C.; Vorreau, P.; Vallaitis, T.; Dumon, P.; Bogaerts, W.; Baets, R.; Esembeson, B.; Biaggio, I.; Michinobu, T.; Diederich, F.; Freude, W.; Leuthold, J. All-optical high-speed signal processing with silicon-organic hybrid slot waveguidesx. *Nature Photonics* **2009**, *3*, 216.

[16] Steckel, J. S.; Snee, P.; Coe-Sullivan, S.; Zimmer, J. P.; Halpert, J. E.; Anikeeva, P.; Kim, L.-A.; Bulovic, V.; Bawendi, M. G. Color-Saturated Green-Emitting Qd-Leds. *Angew. Chem.-Int. Edit.* **2006**, *45*, 5796–5799.

[17] Rogach, A. L.; Gaponik, N.; Lupton, J. M.; Bertoni, C.; Gallardo, D. E.; Dunn, S.; Li Pira, N.; Paderi, M.; Repetto, P.; Romanov, S. G.; O'Dwyer, C.; Sotomayor Torres, C. M.; EychmÃ¼ller, A. Light-Emitting Diodes with Semiconductor Nanocrystals. *Angew. Chem.-Int. Edit.* **2008**, *47*, 6538–6549.

[18] Malko, A. V.; Mikhailovsky, A. A.; Petruska, M. A.; Hollingsworth, J. A.; Htoon, H.; Bawendi, M. G.; Klimov, V. I. From Amplified Spontaneous Emission to Microring Lasing Using Nanocrystal Quantum Dot Solids. *Appl. Phys. Lett.* **2002**, *81*, 1303–1305.

[19] Schaller, R. D.; Petruska, M. A.; Klimov, V. I. Tunable near-Infrared Optical Gain and Amplified Spontaneous Emission Using Pbse Nanocrystals. *J. Phys. Chem. B* **2003**, *107*, 13765–13768.

[20] Klimov, V. I.; Ivanov, S. A.; Nanda, J.; Achermann, M.; Bezel, I.; McGuire, J. A.; Piryatinski, A. Single-Exciton Optical Gain in Semiconductor Nanocrystals. *Nature* **2007**, *447*, 441–446.

[21] McDonald, S. A.; Konstantatos, G.; Zhang, S. G.; Cyr, P. W.; Klem, E. J. D.; Levina, L.; Sargent, E. H. Solution-Processed Pbs Quantum Dot Infrared Photodetectors and Photovoltaics. *Nat. Mater.* **2005**, *4*, 138–U14.

[22] Rauch, T.; Boberl, M.; Tedde, S. F.; Furst, J.; Kovalenko, M. V.; Hesser, G. N.; Lemmer, U.; Heiss, W.; Hayden, O. Near-Infrared

Imaging with Quantum-Dot-Sensitized Organic Photodiodes. *Nat. Photonics* **2009**, *3*, 332–336.

[23] Moreels, I.; Hens, Z.; Kockaert, P.; Loicq, J.; Van Thourhout, D. Spectroscopy of the Nonlinear Refractive Index of Colloidal Pbse Nanocrystals. *Appl. Phys. Lett.* **2006**, *89*, 193106.

[24] Lagatsky, A. A.; Brown, C. T. A.; Sibbett, W. Highly efficient and low threshold diode-pumped Kerr-lens mode-locked Yb : KYW laser. *Optics Express* **2004**, *12*, 3928–3933.

[25] Lagatsky, A. A.; Malyarevich, A. M.; Savitski, V. G.; Gaponenko, M. S.; Yumashev, K. V.; Zhilin, A. A.; Brown, C. T. A.; Sibbett, W. PbS quantum-dot-doped glass for efficient passive mode locking in a CWYb : KYW laser. *Ieee Photonics Technology Letters* **2006**, *18*, 259–261.

[26] Padilha, L. A.; Nootz, G.; Olszak, P. D.; Webster, S.; Hagan, D. J.; Van Stryland, E. W.; Levina, L.; Sukhovatkin, V.; Brzozowski, L.; Sargent, E. H. Optimization of Band Structure and Quantum-Size-Effect Tuning for Two-Photon Absorption Enhancement in Quantum Dots. *Nano Letters* **2011**, *11*, 1227–1231.

[27] Nootz, G.; Padilha, L. A.; Olszak, P. D.; Webster, S.; Hagan, D. J.; Van Stryland, E. W.; Levina, L.; Sukhovatkin, V.; Brzozowski, L.; Sargent, E. H. Role of Symmetry Breaking on the Optical Transitions in Lead-Salt Quantum Dots. *Nano Letters* **2010**, *10*, 3577–3582.

[28] Li, H. P.; Liu, B.; Kam, C. H.; Lam, Y. L.; Que, W. X.; Gan, L. M.; Chew, C. H.; Xu, G. Q. Femtosecond Z-scan investigation of nonlinear refraction in surface modi Â® ed PbS nanoparticles. *Optical Materials* **2000**, *14*, 321–327.

[29] Malyarevich, A. M.; Gaponenko, M. S.; Yumashev, K. V.; Lagatsky, A. A.; Sibbett, W.; Zhilin, A. A.; Lipovskii, A. A. Nonlinear spectroscopy of PbS quantum-dot-doped glasses as saturable

absorbers for the mode locking of solid-state lasers. *Journal of Applied Physics* **2006**, *100*, 23108.

[30] Li, D.; Liang, C.; Liu, Y.; Qian, S. Femtosecond nonlinear optical properities of PbS nanoparticles. *Journal of Luminescence* **2007**, *122-123*, 549–551.

[31] Asunskis, D. J.; Bolotin, I. L.; Hanley, L. Nonlinear Optical Properties of PbS Nanocrystals Grown in Polymer Solutions. *J. Phys. Chem. C* **2008**, *112*, 9555–9558.

[32] Asunskis, D. J.; Bolotin, I. L.; Haley, J. E.; Urbas, A.; Hanley, L. Effects of Surface Chemistry on Nonlinear Absorption of PbS Nanocrystals. *J. Phys. Chem. C* **2009**, *113*, 19824–19829.

[33] Bolotin, I. L.; Asunskis, D. J.; Jawaid, A. M.; Liu, Y.; Snee, P. T.; Hanley, L. Effects of Surface Chemistry on Nonlinear Absorption , Scattering , and Refraction of PbSe and PbS Nanocrystals. *J. Phys. Chem. C* **2010**, *114*, 16257–16262.

[34] Yoshino, F.; Major, A.; Brzozowski, L.; Levina, L.; Sukhovatkin, V.; Sargent, E. H. Picosecond-resolved nonlinear absorption of spin-processible lead sulfide (PbS) nanocrystals from 1100 to 1600 nm. *Proceedings of the Society of Photo-Optical Instrumentation Engineers (Spie)* **2004**, *5361*, 142–149.

[35] Yoshino, F.; Major, A. A.; Levina, L.; Sargent, E. H. Nonlinear refractive properties in lead sulfide (PbS) nanocrystals from 1200 to 1550 nm. *International Quantum Electronics Conference (IQEC) (IEEE Cat. No.04CH37598)* **2004**.

[36] Brzozowski, L.; Sargent, E. H.; Hines, M. A. Resonant nonlinearities and figures of merit of strongly-confined 5.5 nm PbS nanocrystals in the 1150 nm to 1550 nm wavelength range. *CLEO/Pacific Rim 2003. The 5th Pacific Rim Conference on Lasers and Electro-Optics (IEEE Cat. No.03TH8671)* **2003**, *2*, 461.

[37] Savitski, V. G.; Malyarevich, A. M.; Demchuk, M. I.; Yumashev, K. V.; Raaben, H.; Zhilin, A. A. Intensity-Dependent Bleaching Relaxation in Lead Salt Quantum Dots. *J. Opt. Soc. Am. B* **2005**, *22*, 1660–1666.

[38] Milam, D. Review and assessment of measured values of the nonlinear refractive-index coefficient of fused silica. *Applied Optics* **1998**, *37*, 546–550.

[39] Sheikbahae, M.; Said, A. A.; Wei, T. H.; Hagan, D. J.; Vanstryland, E. W. Sensitive Measurement of Optical Nonlinearities Using a Single Beam. *IEEE J. Quantum Electron.* **1990**, *26*, 760–769.

[40] Falconieri, M. Thermo-Optical Effects in Z-Scan Measurements Using High-Repetition-Rate Lasers. *J. Opt. A–Pure Appl. Op.* **1999**, *1*, 662–667.

[41] Moreels, I.; Justo, Y.; De Geyter, B.; Haustraete, K.; Martins, J. C.; Hens, Z. Size-Tunable, Bright, and Stable PbS Quantum Dots: A Surface Chemistry Study. *Acs Nano* **2011**, *5*, 2004–2012.

[42] Valkai, S.; Liszi, J.; Szalai, I. Temperature Dependence of the Refractive Index for Three Chloromethane Liquids at 514.5 Nm and 632.8 Nm Wavelengths. *J. Chem. Thermodyn.* **1998**, *30*, 825–832.

[43] Hassan, E.-K. Thermo-Optical and Dielectric Constants of Laser Dye Solvents. *Rev. Sci. Instrum.* **1998**, *69*, 1243–1245.

[44] Lide, D. *CRC Handbook of chemistry and physics*, 82nd ed.; CRC press, 2001-2002.

[45] Masia, F.; Langbein, W.; Moreels, I.; Hens, Z.; Borri, P. Exciton dephasing in lead sulfide quantum dots by X-point phonons. *Phys. Rev. B* **2011**, *83*, 201309.

[46] Moreels, I.; Lambert, K.; Smeets, D.; De Muynck, D.; Nollet, T.; Martins, J. C.; Vanhaecke, F.; Vantomme, A.; Delerue, C.; Allan, G.; Hens, Z. Size-Dependent Optical Properties of Colloidal PbS Quantum Dots. *Acs Nano* **2009**, *3*, 3023–3030.

[47] Gao, Y.; Talgorn, E.; Aerts, M.; Trinh, M. T.; Schins, J. M.; Houtepen, A. J.; Siebbeles, L. D. a. Enhanced Hot-Carrier Cooling and Ultrafast Spectral Diffusion in Strongly Coupled PbSe Quantum-Dot Solids. *Nano letters* **2011**, *11*, 5471–6.

[48] Istrate, E.; Hoogland, S.; Sukhovatkin, V.; Levina, L.; Myrskog, S.; Smith, P. W. E.; Sargent, E. H. Carrier relaxation dynamics in lead sulfide colloidal quantum dots. *Journal of Physical Chemistry B* **2008**, *112*, 2757–2760.

[49] Nootz, G.; Padilha, L.; Levina, L.; Sukhovatkin, V.; Webster, S.; Brzozowski, L.; Sargent, E.; Hagan, D.; Van Stryland, E. Size dependence of carrier dynamics and carrier multiplication in PbS quantum dots. *Physical Review B* **2011**, *83*, 1–7.

[50] Boyd, J. *Nonlinear Optics*, 2nd ed.; Elsevier, 2003.

[51] Masia, F.; Moreels, I.; Hens, Z.; Langbein, W.; Borri, P. Four-wave-mixing imaging and carrier dynamics of PbS colloidal quantum dots. *Phys. Rev. B* **2010**, *82*, 155302.

[52] Hattori, M. Thermal Diffusivlty of Some Linear Polymers. *Kolloid-Zeitschriflt und Zeitschriflt fur Polymere* **1964**, *202*, 11–14.

[53] Chapple, P.; Hermann, J.; McDuff, R. Power saturation eÂffects in thick single-element optical limiters. *Optical and Quantum Electronics* **1999**, *31*, 555–569.

[54] Tian, J.-G.; Zang, W.-P.; Zhang, C.-Z.; Zhang, G. Analysis of beam propagation in thick nonlinear media. *Applied Optics* **1995**, *34*, 4331.

[55] Moreels, I.; De Geyter, B.; Van Thourhout, D.; Hens, Z. Transmission of a Quantum-Dot-Silicon-on-Insulator Hybrid Notch Filter. *J. Opt. Soc. Am. B* **2009**, *26*, 1243–1247.

5

Optical properties of hybrid quantum dots waveguides

5.1 Introduction

In device applications, colloidal QDs are mostly deposited as close packed nanocrystal thin films, either within a layered stack[2] or as a surface coating[3] where they interact with the internal or evanescent optical field, respectively. A typical example here involves QDs embedded in a resonator, where the coupling of the QD light emission to the resonator modes eventually leads to lasing[4]. Essential to the development and optimization of such QD-based devices is a proper understanding of the optical field in materials with embedded or surface-coated QD films, where the influence of the QD film on the optical field is properly taken into account. In the literature, it is well known that a dilute dispersion of QDs, either in a liquid or a solid host, can be described as an effective optical medium according to the Maxwell-Garnett effective

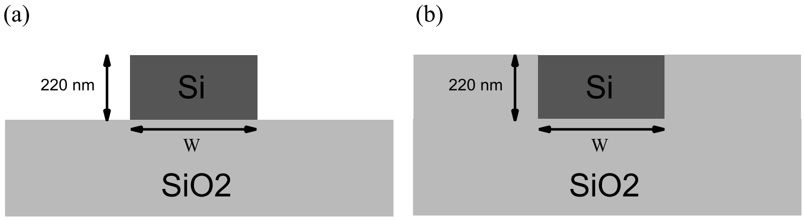

Figure 5.1: (a) Schematic cross section of a silicon-on-insulator strip waveguide (SWGs) with a height of 220 nm and a given width W. (b) Oxide planarization of the SWG described in (a) using a trench isolation process[1] yields a planarized waveguide (PWG) structure.

medium theory in the local field approximation[5]. On the other hand, far fewer studies have addressed the effective medium description of close packed QD films, let alone the experimental investigation and theoretical simulation of the optical properties of hybrid materials containing close packed QD films.

In this chapter, we will first analyze the absorption coefficient of SOI planarized waveguides (PWGs) as illustrated in Fig. 5.1 coated with close packed mono- and multilayers – generally denoted as i-layer with $i = 1, 2, ...$ – of PbS/CdS QDs. We retrieve the fingerprint of the QDs in the waveguide absorbance and find that the absorbance per QD increases with the number of QD layers. The experimental data are compared with simulation results, where the QD i-layers are described as an effective medium in which the optical properties depend on dipolar coupling between neighboring QDs.[6] Close agreement between the experimental values and the simulation results is obtained using the dielectric constant ε_h of the QD host material as the only adjustable parameter. We find that the increased absorbance in thicker layers makes that a higher value of ε_h is needed to match the simulated and the experimental data. We interpret this as a transition from a regime where the field lines coupling the QDs mainly pass through the surroundings (monolayer case) to a situation where these field lines are mainly confined within the QD stack (thicker multilayers). Importantly, the oxide planarization of the strip waveguides (Fig. 5.1a) yielding PWGs is a trench isolation process[1] which consists of six post-processing steps, and consequently increases the cost of the PWG fabrication. As strip waveguides (SWGs) are the backbone of silicon photonics, a profound knowledge of the properties of these directly coated SWGs is essential for device development and a cost-effective fabrication. Therefore we will determine the waveguide absorbance of silicon-on-insulator strip waveguides coated with a monolayer of PbS/CdS core/shell QDs[7]. Using the host permittivity deduced from the study in the PWGs we obtain values for the losses which are in quantitative agreement with the experimental results. This allows to engineer the interaction of colloidal QDs in strip waveguides, which is more relevant for device applications. Based on SEM imaging and the simulated QD absorption coefficient we show that the morphology of the deposited layer directly affects the waveguide absorbance.

This chapter is divided in two main sections : Hybrid QD planarized - and strip waveguides. For the ease of understanding and reading of the results, the main definitions and concepts introduced in the first section will be highlighted or shortly reintroduced in the latter section.

5.2 Hybrid QD/PWGs

5.2.1 Fabrication

Langmuir Blodgett technique

The Langmuir-Blodgett (LB) technique has been first conceptualized by Pockels and developed by Irving Langmuir and his wife Katharine Blodgett in the late 19th century. The technique is very suitable for obtaining a monolayer of a solution processed based material on a solid surface. In the Langmuir-Blodgett technique at first a trough is filled with water covering an area A, which can be controlled by barriers (Fig. 5.2). A few drops of a diluted QD suspension in toluene (or other solvent) are spread out on the water, and the solvent is allowed to evaporate. As the QDs are capped by hydrophobic oleic acid ligands they will stay floating

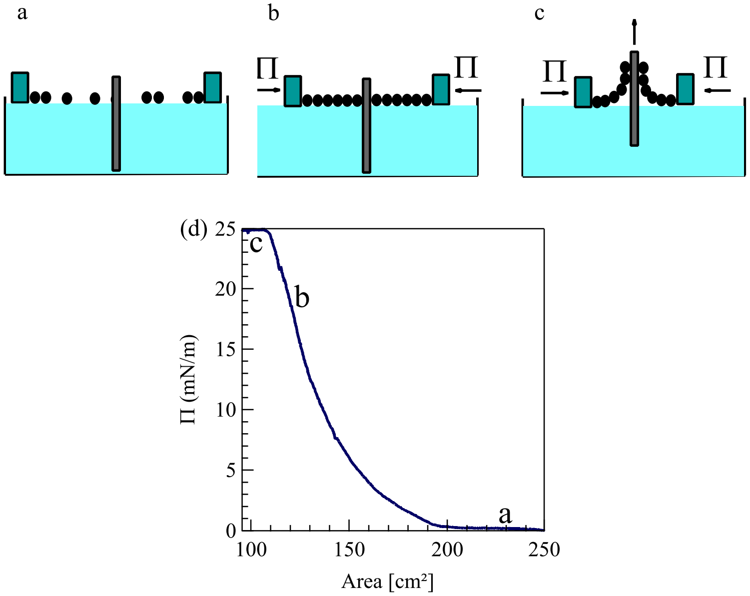

Figure 5.2: Langmuir-Blodgett principle. (a) After solvent evaporation the QDs forms a sub-monolayer. (b) Compression of the QDs in a monolayer. (c) The monolayer is deposited on the substrate at constant surface pressure Π. (d) The Langmuir-Blodgett isotherm shows increasing pressure with lowering the area. The surface pressures of the different regimes as outlined in a-c are indicated in the isotherm.

on the water surface and form islands of nanocrystals in the water. The surface pressure Π of the water interface is monitored with a Wilhelmy plate and is given by :

$$\Pi = \gamma_0 - \gamma \tag{5.1}$$

$$\gamma = \frac{dG}{dA} \tag{5.2}$$

Here, G is the free energy of the surface containing the QD particles, γ_0 is the surface tension of the pure air-water interface and γ is the surface tension of the water surface containing the particles. From the surface pressure the free energy of the particles can be reasoned via Eq. 5.2. The free energy is composed of three contributions : water-air interaction, water-particle and particle-particle interactions[8]. Figures 5.2a-c show the operation principle. As long as the surface area between barriers of the Langmuir trough is large, the nanocrystals can choose their interparticle distance minimizing the free energy By compressing the film the nanocrystal islands arrange (Fig. 5.2b) and when the surface pressure reaches a steep regime (Fig. 5.2d), a monolayer of QDs start to form as the particles can no longer freely arrange. In this regime, reducing the area leads to a decrease of the interparticle distance resulting in a significant increase of the repulsive interparticle interactions and therefore a rise of free energy. Consequently, an increase in the surface pressure[9] is needed to maintain the monolayer formation. When the surface pressure reaches a target value, the compressed monolayer is subsequently transferred to the substrate (Fig. 5.2c) by vertically pulling the substrate out of the water. During the pull out, the area is reduced at constant surface pressure (Fig. 5.2d) . As we will show in the next section, the target value is determined by repeating the LB technique at similar conditions (material amount, substrate), but stopping the procedure at different surface pressures. By inspecting the coated substrates using a microscopy tool (*e.g,* AFM) the target pressure is determined as the value resulting in a uniform coated monolayer. Therefore, once the target surface pressure is known, the LB technique allows not only for obtaining a uniform monolayer, but also for a high control of the layer thickness by repeating the procedure subsequently on the same sample.

Deposition on mica

To deposit a layer on a surface using the LB technique, a known quantity of QDs is dried and redispersed in 33 μL of toluene with a QD concentration of 9μM. Then, this QD solution is spread out on ultrapure water, and the solvent is allowed to evaporate. After evaporation of the toluene, the QD layer is compressed by closing the barriers at a rate of 10 cm^2 min^{-1}. During compression, the pressure is monitored with a Wilhelmy plate attached to a microbalance. At the target pressure, the compressed layer is transferred to the substrate of choice (*e.g.*, mica, glass or SOI waveguides) by vertically pulling it out of the water at a speed of 5 mm min^{-1}. To analyze the quality of the LB layers, we first deposit them on a mica substrate at two different LB target pressures (18 mN/m and 30 mN/m). Mica is chosen as a test substrate as it has a low surface roughness (1 nm) and it allows for an easy check of the layer uniformity using atomic force microscopy (AFM). Fig.5.3(c) shows the corresponding LB-isotherms and Figs.5.4a,c represent AFM topography images of the QD-layer on mica, deposited at 18 and 30 mN/m, respectively. Figs. 5.4b,d show the respective depth profiles of the deposited QD-layers at 18 and 30mN/m. At a pressure of 18 mN/m, we observe a large hole with a depth of ≈ 10 nm. Since this value is in fair agreement with the QD size (6.2 nm) incremented by twice the oleic acid ligand thickness (1.8 nm[10]), we conclude that it indicates the transfer of an incomplete monolayer. At a pressure of 30 mN/m, the depth profile shows variation of ≈ 1 nm in agreement with the mica roughness and therefore the coated surface is smooth, indicating the transfer of a closed packed monolayer. This results provide us with the parameters we need to use for the deposition of PbS/CdS mono- and multilayers on the SOI chips with the oxide planarized waveguides and strip waveguides. In the next section, we will discuss the deposition of the QDs on PWGs and the measured QD loss values.

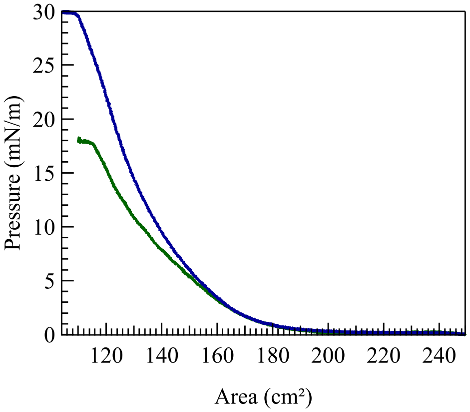

Figure 5.3: LB-isotherms at surface pressures of 18 and 30mN/m.

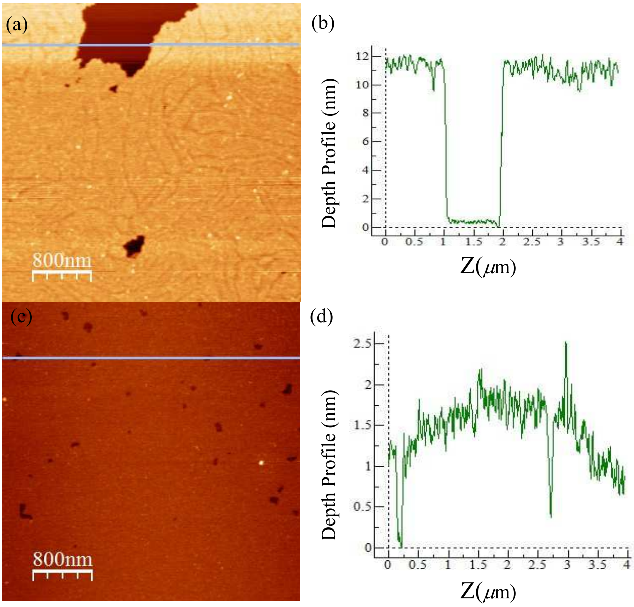

Figure 5.4: (a) AFM profile of the LB deposition at 18mN/m showing a submonolayer on the mica surface. (b) Depth profile corresponding to the drawn line in (a) showing a depth of $\approx 10\,\mathrm{nm}$ in agreement with the QDs size incremented by twice the ligand thickness. (c) AFM profile of the LB deposition at 30mN/m showing a close packed monolayer on the mica surface. (d) Corresponding depth profile shows a variation of 1 nm in agreement with the surface roughness of mica.

5.2.2 Measurements

Absorbance of QD coated PWGs

The PbS/CdS core/shell QDs used in this work were synthesized using the cationic exchange procedure as outlined in Chapter 2. Core diameter and shell thickness were adjusted to have a band gap absorption at $\approx 1450\,\mathrm{nm}$ (see Fig. 5.5(a)). In this way, the long wavelength side of the absorption peak covers the $1500-1550\,\mathrm{nm}$ bandpass window of the SOI grating couplers, which are used to couple light in and out of the waveguides. This will make the QD absorption well discernible in the measurements. Attempts of measuring the QD absorption of only core PbS QDs on the waveguides, showed a blue shift of the QD wavelength spectrum. This has been observed previously for PbS QDs deposited on glass substrates[11]. These optically unstable films will hamper a quantitative study of the QD absorption. The growth of the CdS shell allowed for a better passivation of the PbS core QDs yielding optically stable PbS/CdS particles, which will enable a quantitative comparison between the experimental and theoretical QD absorption. Using the absorption spectrum of the original PbS QDs and the resulting PbS/CdS QDs, core diameter and shell thickness were estimated to be 5.4 and 0.4 nm, respectively[7]. The QDs were locally deposited on the PWGs by combining optical lithography and Langmuir-Blodgett deposition,[11;12] forming strips of 200, 500, 1000 and 1500 μm on otherwise identical waveguides (see Fig. 5.5b). The scanning electron microscopy image shown in Fig. 5.5c (see Fig. 5.6 for an enlarged view) is indicative of the close packing and locally hexagonal ordering of the QDs on top of the PWG, while atomic force microscopy imaging reveals that the PWGs are depressed by $5-10\,\mathrm{nm}$ relative to the surrounding silica, with the QD layer conformally following this geometry (see Fig. 5.5d).

The use of QD strips with different interaction length on identical waveguides enables us to quantify the light absorption in the QD functionalized sections of the PWGs, regardless of coupling losses (see Fig. 5.5b). Indeed, denoting the absorption coefficient of a bare and QD coated PWG α_0 and α, respectively, the net absorption coefficient $\alpha_{QD} =$

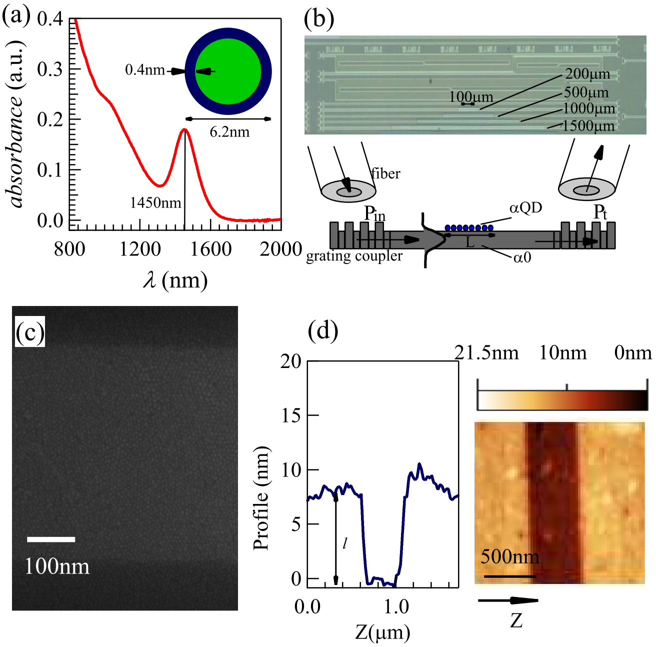

Figure 5.5: (a) PbS/CdS QD spectrum recorded on a dilute QD dispersion in TCE. (b) Cartoon representation of the opitcal field coupled from the fiber through the grating in the QD coated PWG. (c) SEM image of a (topview) PWG coated by a QD monolayer. (d) AFM image and cross section of a PWG coated by a QD monolayer, clearly showing the offset (l) between the top surface of the (slightly submerged) PWG and its silica cladding.

$\alpha - \alpha_0$ of a QD coated PWG can be derived from the transmitted power P_t through PWGs with different QD strip lengths L. More specifically, using the length of and the power transmitted through one of the QD coated waveguides as a reference, the net waveguide absorbance A reads:

$$A = -\ln \frac{P_t}{P_{t,ref}} = (\alpha - \alpha_0)\,(L - L_{ref}) \tag{5.3}$$

In the determination of A we neglect any contribution of the QD emission to the measured P_t, which we will elaborately discuss in section 5.3.4.

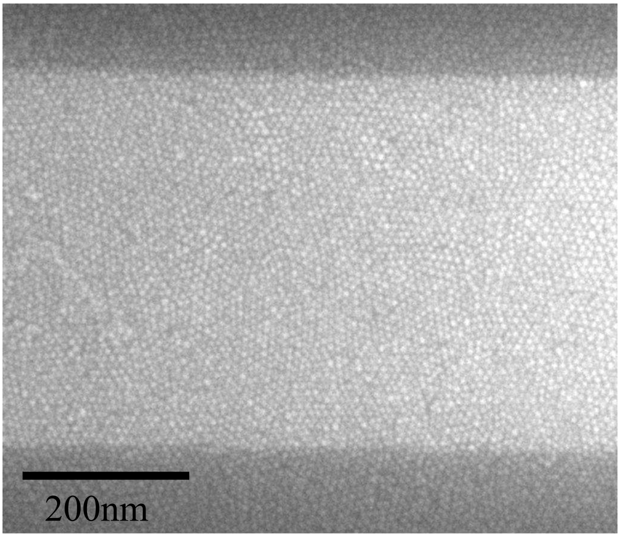

Figure 5.6: Enlarged SEM image of the (topview) PWG coated by a QD monolayer in Fig. 5.5 showing clearly the local hexagonal close packed ordering of the QDs.

Experimental results

The net waveguide absorbance is related to the net waveguide loss (dB) as ($10A\log e$). According to Eq. 5.3, α_{QD} can be obtained from a plot of A versus the strip length difference $\Delta L = L - L_{ref}$. This is exemplified by Fig. 5.7a, which shows A as obtained from measurements on a PWG coated by a PbS/CdS QD 2-layer using the $200\,\mu$m strip as a reference. Clearly, A is proportional to ΔL and α_{QD} can thus be obtained as the slope of the best fitting line passing through the origin. The difference between the absorption coefficient thus obtained – $6.6(3)\,\mathrm{cm}^{-1}$ – and the determined $1.8\,\mathrm{dB/cm}$ (*i.e.*, $0.41\,\mathrm{cm}^{-1}$) loss of an uncoated PWG provides a first indication that the QD coating has a strong influence on the waveguide absorbance. This conclusion is further supported by the wavelength dependence of α_{QD}. As shown in Fig. 5.7b, the α_{QD} spectrum for a mono- and a 2-layer coating strongly resembles the absorption spectrum of the PbS/CdS QDs used in a dilute tetrachloroethylene dispersion. Similar results are obtained using films consisting of

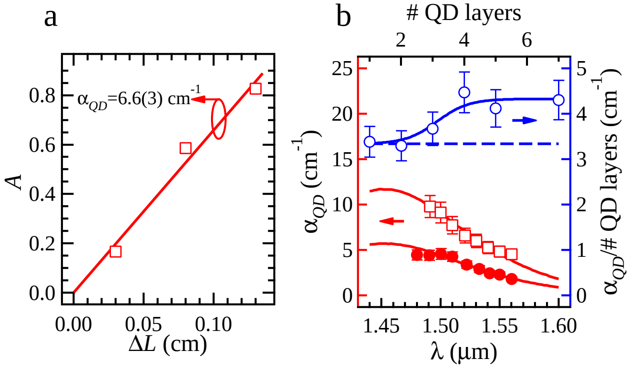

Figure 5.7: (a) (open squares) Absorbance A – as defined by Eq. (5.3) – at 1520 nm as a function of the strip length difference ΔL for PWG coated with a PbS/CdS QD 2-layer strip of 500, 1000, and 1500 μm long using the power transmitted through a similar waveguide with a 200 μm QD 2-layer as a reference and (full line) best fit of the data to a line passing through the origin with an indication of the thus obtained absorption coefficient α_{QD}. (b) (red, left and bottom axis) α_{QD} thus determined as a function of wavelength for a (filled circles) QD monolayer and a (open squares) QD 2-layer coated PWG. The full lines represent the absorption spectrum of dispersed PbS/CdS QDs normalized to match the respectively measured absorption coefficients. (blue, right and top axis) α_{QD} per QD layer at 1520 nm. The full line is a guide to the eye and the dashed line indicates the average value obtained for a monolayer and a 2-layer.

up to 7-layers (see Fig. 5.8). Remarkably, we find a higher absorption coefficient per layer for thicker layers (see Fig. 5.7b), meaning that the absorption cross section of a QD in, *e.g*, a 7-layer is larger than in a monolayer.

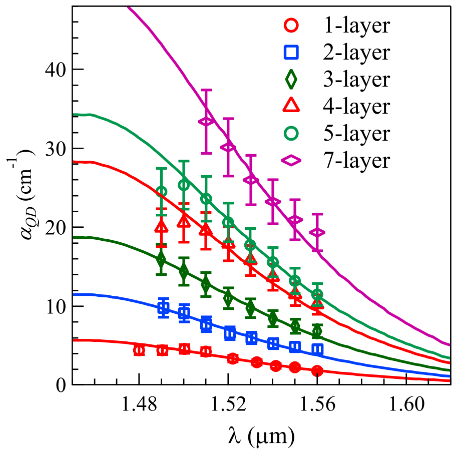

Figure 5.8: Experimental α_{QD}, measured as a function of wavelength for a QD monolayer to a QD 7-layer coated PWG. The full lines represent the absorption spectrum of dispersed PbS/CdS QDs normalized to match the respectively measured absorption coefficients.

5.2.3 Numerical description

Description of the QD-layer

To compare the experimental α_{QD} with model predictions, we use an approach where the real QD i-layer covering the PWG is replaced by an effective medium with a dielectric function ε_{eff} (see Fig. 5.9). Using the real geometry of the PWG – including the slightly submerged waveguide top surface, coated by a 2 nm thin native silica layer – this enables us to extract a theoretical absorption coefficient $\alpha_{QD,th}$ from the simulated effective refractive index $\tilde{n}_{eff} = n_{eff} + \imath\kappa_{eff}$ of the propagating quasi-TE mode:

$$\alpha_{QD,th} = \frac{4\pi\kappa_{eff}}{\lambda} \tag{5.4}$$

This approach however requires that the dielectric function of each material or medium involved is known. For silicon and silica, we use typical values at 1520 nm of 3.45 and 1.45, respectively. For ε_{eff}, we build

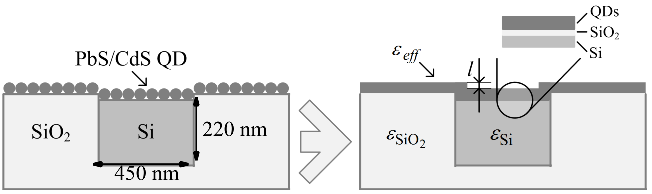

Figure 5.9: Replacement of the real QD film on top of PWG by an effective medium. Indicated are the height difference l between the top surface of the PWG and its silica cladding and the native silica layer in between the PWG top surface and the effective medium representing the QD film.

on the recent finding that the absorption cross section of QDs in close-packed monolayers similar to the ones used here can be well described by taking dipolar coupling between neighboring QDs explicitly into account.[6] As we will show in section 5.2.3, this coupled dipole model (CDM) also applies to all PbS/CdS QD i-layers used in this study. Moreover, it can be extended to yield an expression for ε_{eff}:

$$\varepsilon_{eff} = \varepsilon_h \varepsilon_0 \left(1 + \frac{N_s}{L_t} \frac{a_{QD}}{1 - a_{QD} S} \right) \tag{5.5}$$

Here, N_s is the QD surface density in the layer, L_t is the thickness of the effective layer, a_{QD} is the polarizability of a single PbS/CdS QD and S is the so-called dipole sum, which sums up the influence of the dipolar field of neighboring QDs on an individual QD in the layer. In general, S is different for fields parallel ($S_{\|}$) or perpendicular ($S_{\perp}$) to the QD film. However, the used planarized waveguides here constitutes important advantages and can hardly be underestimated. As their surface is nearly flat, the QD-layer deposition is homogeneous and since the main field component of the quasi-TE modes in the PWG lies parallel to the QD film, only $S_{\|}$ – which was analysed experimentally in[6] – is of relevance here.

Opposite from S, which only depends on the position of the particles relative to each other, a_{QD} is a function of ε_h and the dielectric function $\varepsilon_{QD} = \varepsilon_{QD,R} + \imath \varepsilon_{QD,I}$ of the QDs. While we consider ε_h as an adjustable parameter in this study, we use calculated values – as we will show below – for $\varepsilon_{QD,R}$ and $\varepsilon_{QD,I}$, taking care that they yield the experimental absorption coefficient spectrum of the QDs in a dilute dispersion while obeying the Kramers-Krönig (KK) transformation[13]. Importantly, in this analysis, we assume that the absorption coefficient of the PbS/CdS core/shell QDs at wavelengths shorter than 400 nm can be derived from the bulk dielectric function of PbS and CdS, respectively – as was demonstrated for PbS/CdS QDs[7] – and we neglect possible quantization effects in the CdS shell.

Dielectric constant of the PbS/CdS core shell QDs

The real part ε_R and the imaginary contribution ε_I of the complex dielectric function ε of a dielectric material or equivalently the refractive index n and extinction coefficient κ are both related as :

$$\varepsilon_R = n^2 - \kappa^2 \tag{5.6}$$

$$\varepsilon_I = 2\,n\,\kappa \tag{5.7}$$

In bulk materials, these quantities can be typically determined from a Kramers-Krönig analysis of the absorption coefficient μ, measured with absorbance spectroscopy. κ is directly related to μ as $\frac{4\,\pi\,\kappa}{\lambda}$, and if κ can be determined over a wide enough spectral range, n can be calculated and eventually ε_R and ε_I is determined via equations 5.6-5.7. However, in the case of colloidal quantum dots dispersed in a suspension, calculation is more complicated, as the absorption coefficient is determined by both ε_I and ε_R simultaneously (or n and κ). In this paragraph, we will show how this problem is resolved, allowing for the determination of the real and imaginary part of ε over the entire spectral domain (from energies below the band gap to energies far above).

The dielectric response of a core/shell QD ε_{QD} depends on the complex dielectric function of the core (ε_c) and the shell (ε_{sh}). To determine ε_c and ε_{sh}, we use the iterative matrix inversion (IMI) method as described in[13] for core particles, but we adapt it to the use of a core/shell system. In this method, a self-consistent ε_{QD} is obtained by minimizing the error between the experimentally measured QD intrinsic absorption coefficient $\mu_{i,exp}(\lambda)$ and the intrinsic absorption coefficient $\mu_{i,th}(\lambda)$ as calculated according to the Mawell-Garnett mixing rule in the local field approximation (see also Chapter 3), while requiring that the real and imaginary part of ε_{QD} are obeying the Kramers-Krönig transformations :

$$\varepsilon_{QD,R}(\lambda) = \varepsilon_\infty + \frac{2}{\pi} \wp \int_0^\infty \frac{\lambda^2 \varepsilon_{QD,I}(\lambda')}{\lambda' \left(\lambda^2 - \lambda'^2\right)} \, d\lambda' \tag{5.8}$$

$$\varepsilon_{QD,I}(\lambda) = \frac{-2}{\pi \, \lambda} \wp \int_0^\infty \frac{\lambda^2 \left[\varepsilon_{QD,R}(\lambda') - 1\right]}{\lambda^2 - \lambda'^2} \, d\lambda' \tag{5.9}$$

ε_∞ is a value [equal to 1.5 for PbS[13] and 5.2 for CdS] that accounts for higher energy transitions ($\lambda \to 0$) not observed in experimental ε_I[13;16]. $\wp$ stands for the Cauchy principal value, avoiding the infinite values in the integration. It is clear that if for instance $\varepsilon_{QD,I}$ is known over the entire spectral domain, $\varepsilon_{QD,R}$ can be calculated based on Eq. 5.8. $\mu_{i,exp}(\lambda)$ can be directly determined from the absorbance $A_{susp}(\lambda)$ of a diluted dispersion of PbS/CdS QDs, where we use tetrachloroethylene (TCE) as the solvent:

$$\mu_{i,exp}(\lambda) = \frac{\ln 10 \times A_{susp}(\lambda)}{f_{susp} L_{cuv}} \tag{5.10}$$

Here, f_{susp} denotes the volume fraction of the QDs in the suspension, *i.e.*, the ratio between the volume of all suspended QDs and the total volume of the suspension, while L_{cuv} is the cuvette length (1 cm). In the case of PbX/CdX core/shell QDs (X=S,Se), the correspondence between $\mu_{i,exp}$ and $\mu_{i,th}$ has been confirmed by[7;14], using the expression of $\mu_{i,th}$ according to[15]:

$$\mu_{i,th} = \frac{2\pi}{\lambda n_s} Im \left(3\varepsilon_s \frac{\varepsilon_{sh} \left[\varepsilon_c(3-2q) + 2\varepsilon_{sh} q\right] - \varepsilon_s \left[\varepsilon_c q + \varepsilon_{sh}(3-q)\right]}{\varepsilon_{sh} \left[\varepsilon_c(3-2q) + 2\varepsilon_{sh} q\right] + 2\varepsilon_s \left[\varepsilon_c q + \varepsilon_{sh}(3-q)\right]} \right) \tag{5.11}$$

Here, ε_s, n_s denote the dielectric constant and refractive index of the solvent, respectively, while q is ratio of the shell volume to the total core/shell volume. As shown in Eq. 5.8, $\mu_{i,exp}$ needs to be known over the whole spectral range. However, absorbance spectra are typically measured over a limited spectral range ($\lambda > 400\,\mathrm{nm}$) and therefore we assume that the absorption coefficient $\mu_{i,exp}$ of the PbS/CdS core/shell QDs at wavelengths shorter than 400 nm equals $\mu_{i,th}$, which can be can be derived from Eq. 5.11 using the bulk dielectric function of PbS and CdS, respectively. Furthermore, when implementing the procedure outlined above, we have excluded possible quantization effects in the QD shell and used the dielectric constant of bulk CdS[16] for ε_{sh} over the entire spectral range. The obtained spectral dependence of $\varepsilon_{c,R}$, $\varepsilon_{c,I}$ is shown in Fig. 5.10a.

Coupled Dipole model

Derivation of the effective perimittivity In the coupled dipole model, we consider a collection of polarizable 'point' particles embedded with a volume density N in an 'infinite' extending host with permittivity ε_h[6] (see Fig. 5.11). We can define an effective dielectric constant ε_{eff} for this composite medium by relating the average dielectric displacement to the average electric field:

$$D = \varepsilon_{eff} E = \varepsilon_0 E + P = \varepsilon_0 E + \varepsilon_0(\varepsilon_h - 1)E + Np_0 \qquad (5.12)$$

In the latter sum, the polarization is split into the contribution of the host and the additional contribution of the dipoles p_0 induced on the point particles. The latter term can be rewritten in terms of the polarizability (a_{QD}) of the point particles and the local electric field E_L that polarizes them:

$$Np_0 = N\varepsilon_0 a_{QD} E_L \qquad (5.13)$$

Using the expression derived by[17] for spherically symmetrical core/shell particles, a_{QD} can be expressed as:

$$\begin{aligned} a_{QD} \quad &= \varepsilon_h \frac{V(\varepsilon_{sh} - \varepsilon_h)\left[\varepsilon_{sh} + (\varepsilon_c - \varepsilon_{sh})\frac{1}{3}(1-p)\right] + \ldots}{\left[\varepsilon_{sh} + (\varepsilon_c - \varepsilon_{sh})\frac{1}{3}(1-p)\right]\,\left[\varepsilon_h + \frac{1}{3}(\varepsilon_{sh} - \varepsilon_h)\right] + \ldots} \\ &\quad \frac{\ldots p\varepsilon_{sh}(\varepsilon_c - \varepsilon_{sh})}{\ldots p\frac{1}{3}\varepsilon_{sh}(\varepsilon_c - \varepsilon_{sh})} \end{aligned} \qquad (5.14)$$

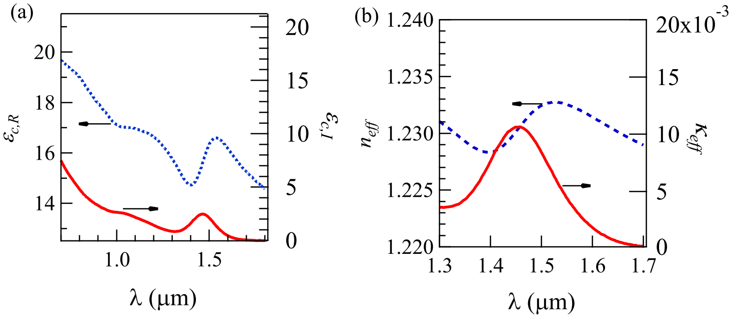

Figure 5.10: (a) The dielectric function of the core (PbS) of PbS/CdS QDs determined using the IMI method for the KK-analysis. Dotted and full line represent respectively $\varepsilon_{c,R}$ and $\varepsilon_{c,I}$. (b) The real part of the complex effective refractive index $\tilde{n}_{eff}$ (dotted line) and the extinction coefficient (full line) extracted from applying the coupled dipole model to the PbS/CdS QD layer.

Here, p denotes the ratio of the volume of the core to the volume of the whole core/shell particle.

In the case of a close packed layer, the local field that drives an individual dipole i is the sum of the external field and the field of the neighboring dipoles j:

$$E_{L,i} = E + \sum_{j \neq i} \beta_{i,j} E_{L,j} \tag{5.15}$$

A crucial element in writing down equation 5.15 is the assumption that because of symmetry reasons, E_L is the same for all particles:

$$E_L = E + S\varepsilon_0 \frac{a_0}{\varepsilon_h} E_L \tag{5.16}$$

Here, S is the dipole sum which contains all contributions from the neighboring particles (j) on the local field driving a central particle (i). For an applied field parallel to the QD film ($S_{\|}$), the dipole sum is given by[6]:

$$S_{\|} = \frac{1}{4\pi} \sum_{j \neq i} \frac{(1 - ikd_{ij})(3\cos^2(\theta_{ij} - 1))e^{ikd_{ij}}}{d_{ij}^3} + \frac{k^2 \sin^2(\theta_{ij}) e^{ikd_{ij}}}{d_{ij}} \tag{5.17}$$

and for a field perpendicular to the QD film ($S_\perp$), the dipole sum reads:

$$S_\perp = \frac{1}{4\pi}\sum_{j\neq i}\frac{(1-ikd_{ij})e^{i(kd_{ij}+\pi)}}{d_{ij}^3}+\frac{k^2e^{ikd_{ij}}}{d_{ij}} \tag{5.18}$$

Here, $k = \frac{2\pi}{\lambda}$ with λ the optical wavelength. The term d_{ij} relates to the distance between particle i and j. The angle θ_{ij} refers to the angle between the polarization of the incident light and the orientation vector from particle i to particle j.

Note that the direction of the applied field has an important consequence on the aforementioned factor S. This is illustrated in Fig. 5.11, where the QDs are considered as point particles (red dots) residing in an infinite host with dielectric constant ε_h. The local field E_L as shown by Eq. 5.16 for a given QD is a sum of the applied field E and the field of neighbouring QDs induced through dipolar coupling. Therefore, if the field is applied parallel to the QD film (Fig. 5.11a), it can be enhanced compared to the field that would exist for a single quantum dot in the host. While for an applied field oriented perpendicular to the QD film, the local field can be decreased compared to the field that would exist for a single QD in the host. The former case is only of relevance here in the PWG since the main component of the applied field lies parallel to the QD film. The latter case needs to be considered for strip waveguides (section 5.2.3), where the quasi-TE field is oriented perpendicular to the QD film at the waveguide edges.

To obtain a consistent expression for N in the case of QD i-layers, we determine it as the ratio between the QD surface density in the layer N_s and the thickness L_t attributed to the i-layer. In this study, we take L_t as the product of the number of layers i and the spacing between close-packed planes in an fcc stacking of QDs. With d the QD diameter (6.2 nm) and l_{lig} the thickness of the ligand shell (taken as 1.8 nm[6;10]), we thus have:

$$L_t = 0.82(d+2l_{lig})\times i \approx 8\times i\,\mathrm{nm} \tag{5.19}$$

Using this definition of N and L_t, ε_{eff} is obtained as:

$$\varepsilon_{eff} = \varepsilon_h\varepsilon_0(1+\frac{N_s}{L_t}\frac{a_0}{1-a_0S}) \tag{5.20}$$

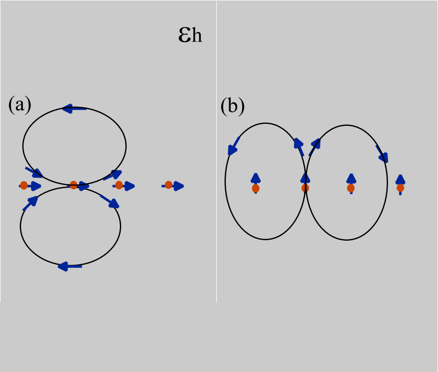

Figure 5.11: Schematic image of QDs represented as point particles (red dots) surrounded by an infinite extending host (grey background) with dielectric constant ε_h. After driving the QDs with an applied field they acquire a dipole moment indicated by the blue arrows. (a) For an applied field parallel to the QD film, dipolar coupling between neighbouring QDs will result in an increase of the field at a given particle. (b) For an applied field perpendicular to the QD film, the coupling due to neighbouring QDs will result in a suppression of the field at a given particle.

In Fig. 5.10b, we plot the spectrum of the real and imaginary part of the refractive index as derived from ε_{eff} for a PbS/CdS QD monolayer with a surface density N_s =1.2 $10^{12}\frac{1}{cm^2}$ and taking ε_h =1 and L_t =8 nm.

Multi-layers The use of the coupled dipole model to analyze the effective permittivity of nanocrystal composites was elaborated by[6] for the case of a single component monolayer on a glass substrate. Their analysis showed a remarkable absorption enhancement effect absent in other effective medium models for dilute systems, such as the Maxwell-Garnett mixing rule. However, the experimental and theoretical analysis was limited to monolayers of QDs. As shown in Fig.5.12b, the ratio between the absorbance of a QD i-layer (on glass) and the number of layers is in a good approximation constant, which means that the same absorption enhancement as for monolayers holds for i-layers. We can thus extend the expression of ε_{eff} that follows from the coupled dipole model to the analysis of QD i-layers. All the layers show a strong hexagonal close packing order as illustrated in Fig. 5.12a for a monolayer of PbS nanocrystals.

5.2.4 Simulations

Combining the geometry of the PWG cross section and the expression for ε_{eff} – based on the coupled dipole model and the self-consistently determined ε_{QD} – the electric field of the guided optical mode in the PWG can be calculated, resulting in theoretical values for $\tilde{n}_{eff}$ and $\alpha_{QD,th}$. As an example, Fig. 5.13a represents the electric field at a wavelength of 1520 nm for a PWG covered by a QD monolayer as obtained using Fimmwave 6.4 full vectorial complex mode solver. The figure clearly shows the overlap between the QD film and the evanescent field, which makes that light absorption by the QDs affects κ_{eff} and leads to a non-zero $\alpha_{QD,th}$. The determination of $\alpha_{QD,th}$ would not be possible trough a transmission measurement of monolayer coated glass in a spectrophotometer as the absorbance would fall within the noise range. As shown in Fig. 5.13b, a close match can be obtained between the simulated and experimental α_{QD} spectrum for a QD monolayer-coated PWG by adjusting ε_h. It should be noted that the ε_h value needed to match the experimental and simulated α_{QD} somewhat depends on the geometry of the PWG. Looking at the AFM cross section of the PWG (see Fig. 5.5d), an exact value of the height difference l between the top surface of the PWG and its silica cladding is hard to determine. Varying l between 6 and $10\,\mathrm{nm}$ as extreme cases, we obtain agreement between experiment and simulation for $\varepsilon_h = 1.0$ ($l = 6\,\mathrm{nm}$) to $\varepsilon_h = 1.16$ ($l = 10\,\mathrm{nm}$). For QDs capped by oleic acid (ε=2.1 at 2000 nm[18]), both figures are relatively low yet they agree with the $\varepsilon_h = 1.0$ found for PbS and CdSe QD monolayers deposited on glass.[6]

The approach as outlined above can be readily extended to simulate α_{QD} for PWG covered by QD i-layers. Using once more ε_h as an adjustable parameter, correspondence between experimental and simulated values can be obtained as shown by the example of a 7-layer in Fig. 5.14. Importantly, the increasing QD absorption cross section with

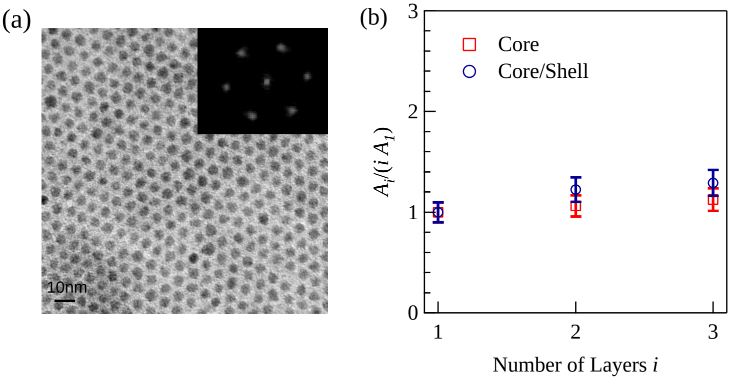

Figure 5.12: (a) Monolayer of PbS nanocrystals deposited on TEM grid. Inset : The fourier image of the monolayer yields a hexagonal diffraction pattern clearly illustrating the strong hexagonal order within the monolayer. (b) The absorbance A_i per layer of i-layers of PbS and PbS/CdS QDs normalized relative to the absorbance of a close packed monolayer at $\lambda = 400$ nm as a function of the number of layers i.

thicker layers makes that a larger ε_h is needed to fit the simulations to the experimental data when the number of layers increases. As shown in Fig. 5.14b and Fig. 5.15, an ε_h in the range of 1.00-1.16 is obtained in the case of a monolayer, whereas values between 1.47 and 1.50 are found for the simulation of the 7-layer using $l = 6$ and $l = 10\,\mathrm{nm}$, respectively. This demonstrates that in the case of a QD i-layer with i close to one, ε_h is not an intrinsic property of the QD film. Since the field lines that couple neighboring QDs in a monolayer mainly pass through the surroundings, the combined effect of the layers surrounding the QDs – air and native silica on silicon – and the organic ligands separating the QDs will determine ε_h in this case. For thicker layers however, the larger part of these coupling fields remains within the QD film. In that respect, the trend shown in Fig. 5.14b can be interpreted as the progressive evolution of ε_h from an extrinsic value, determined by the layer and its surroundings, in the monolayer case to a value that is an intrinsic property of a QD multilayer.

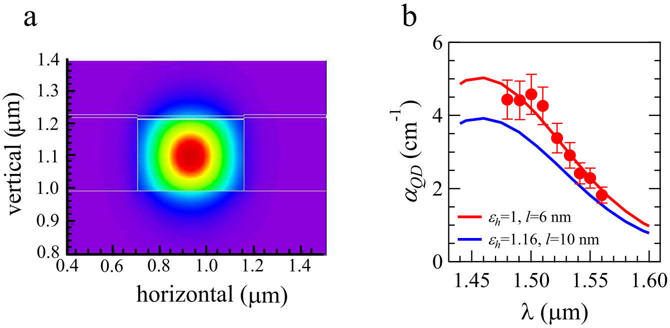

Figure 5.13: (a) Cross-sectional representation of the simulated electric field for 1520 nm light guided by a PWG coated by a QD monolayer. (b) Comparison of the experimental and simulated α_{QD} absorbance spectrum of a QD coated PWG for two different combinations of l and ε_h.

5.3 Hybrid QD/SWGs

In the previous section, we studied the waveguide absorbance of QDs deposited on oxide planarized waveguides (PWGs), which allowed to deduce the host permittivity needed to describe the effective permittivity of the coated layers. In this way, the obtained effective permittivity could be linked with the QD induced waveguide losses using a complex mode-solver (Fimmwave 6.4). Importantly, the oxide planarization of strip waveguides is a trench isolation process[1] which consist of six post-processing steps, and consequently increases the cost of the PWG fabrication. As strip waveguides (SWGs) are the backbone of silicon photonics, a profound knowledge of the properties of these directly coated SWGs is essential for device development and a cost-effective fabrication.

5.3.1 Fabrication

For the fabrication of the QD-layers on the strip waveguides we will rely on the Langmuir-Blodgett technique as explained in section 5.2.1 together with the study of the QD deposition on mica. The results there showed that at surface pressures of 18 mN/m and 30 mN/m the LB depo-

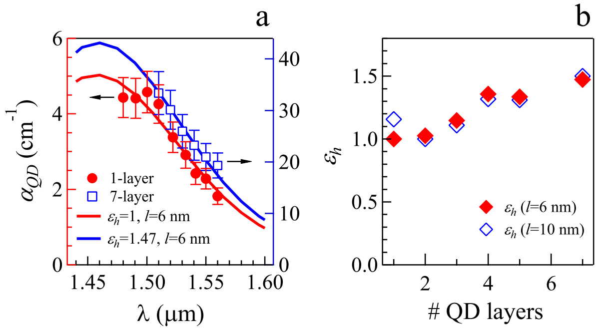

Figure 5.14: (a) Comparison of the experimental and simulated α_{QD} spectrum of a PWG coated with (blue) a QD monolayer and (red) a QD seven layer. The respective axis are scaled by a factor of 7 to allow for a direct comparison of the absorbance per number of layers. (b) Evolution of ε_h values needed to match experimental and simulated absorption coefficient calculated for the extreme case of (red) $l = 6$ and (blue) $l = 10\,\mathrm{nm}$.

sition yielded a sub-monolayer and a uniform close packed monolayer, respectively. Figs. 5.16a-d show SEM images for various samples of QDs deposited on SOI strip waveguides. Figs. 5.16a-b show the top surfaces of LB depositions at the respective pressures of 18 mN/m and 30 mN/m retrieving a sub-monolayer and a close packed monolayer on top of the surfaces, which is in confirmation with of the previous results. Nevertheless, inspecting the side of the waveguides (Fig. 5.16c) we note that some parts of the waveguides *may not be covered* by the QDs. These parts are typically located at the corner between the waveguide edge and the trench. The SEM picture in Fig. 5.16d illustrates this more clearly. These deposition anomalies might affect the measured waveguide absorbance and as we will show need to be considered in our simulations.

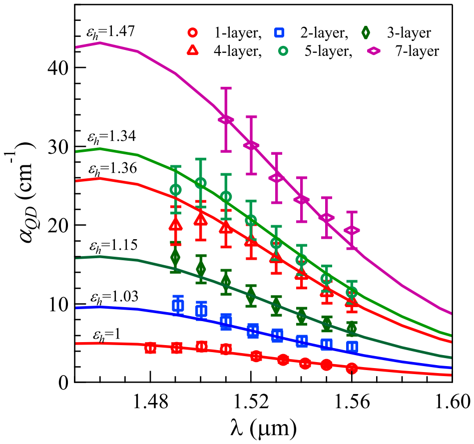

Figure 5.15: The full lines represent the absorption spectrum of the simulated α_{QD} spectrum with the needed ε_h values for l =6nm to match the experimental and simulated absorption coefficient. Similar curves where obtained for $l = 10$nm.

5.3.2 Measurements

Absorbance of QD coated SWGs

In this work, we make use of two different PbS/CdS QD samples, denoted by A and B, with a first exciton peak at 1520 nm and 1450 nm, respectively. The initial PbS core QDs are prepared using a procedure as described by[19–21]. For the CdS shell growth, a cationic exchange procedure was used. The samples are chosen such that the peak wavelength (sample A) or the long wavelength side (sample B) of their first exciton transition falls within the bandpass window of the grating couplers, thus enabling a clear observation of the QD losses through the waveguide absorbance. The waveguide absorbance is monitored using a laser which is wavelength tunable around 1520 nm. The laser light is injected into a polarization controller to maximize the coupled light in the TE-mode grating couplers of the waveguide. Core size, shell thickness and the basic optical characteristics of the PbS/CdS QDs used are summarized in Table 5.1. The QDs are deposited locally on the SWGs using optical lithography combined with Langmuir-Blodgett deposition[12], yielding

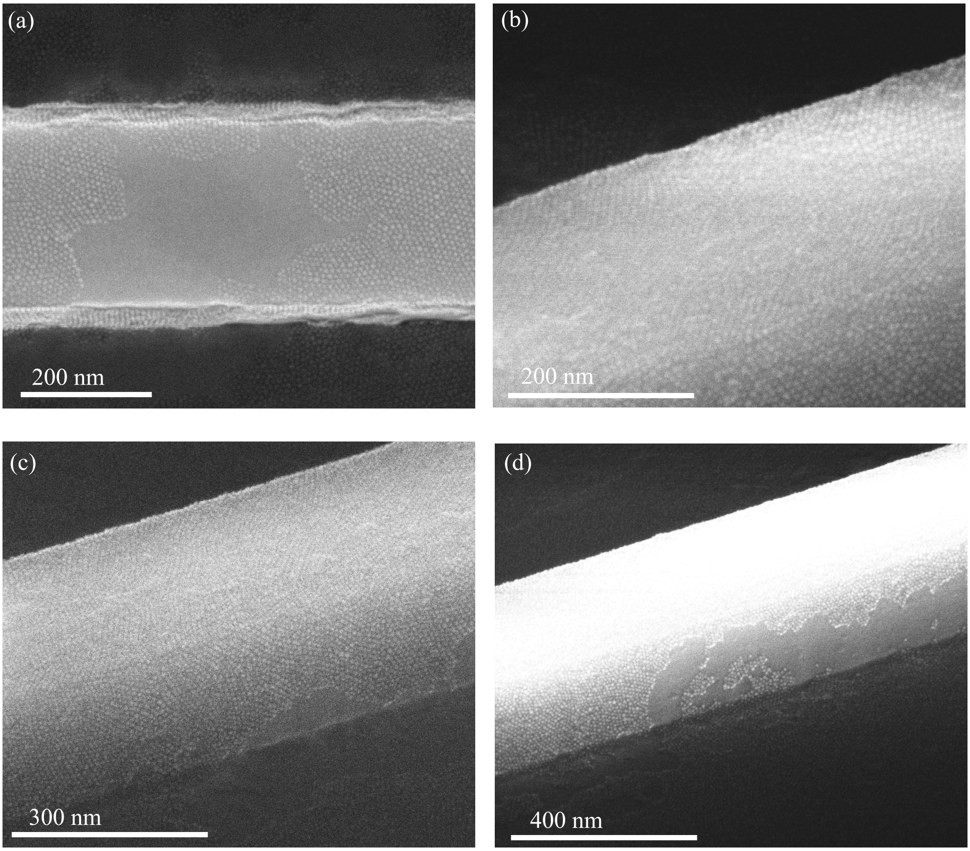

Figure 5.16: SEM images of various QD coated strip waveguides using the LB-technique. (a) Top view image of a QD coated strip waveguide at a surface pressure of 18 mN/m showing a sub-monolayer on top of the waveguide surface. (b) At a surface pressure of 30 mN/m the top surface of the strip waveguide is well covered yielding a uniform close packed monolayer. (c-d) SEM pictures of QD coated strip waveguides (surface pressure of 30 mN/m) showing the sidewalls of the waveguides.

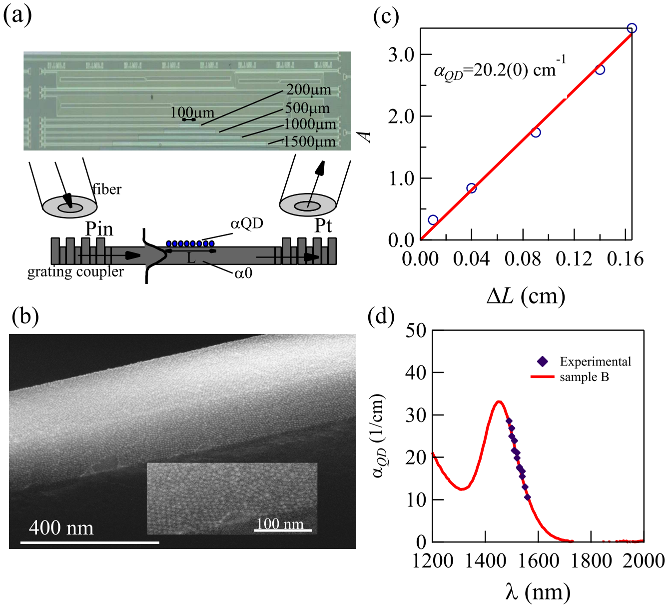

Figure 5.17: (a) Optical microscopy image of a sample with strip waveguides coated by a QD monolayer with various strip lengths and a representation of the optical field coupled from the fiber through the grating in the QD coated SWG. (b) SEM picture illustrating a close packed QD-monolayer coating the strip waveguide. (Inset) Zoom of the SEM image showing clearly discernable quantum dots on the sidewall of the strip waveguide. (c) Absorbance A of sample A – as determined according to Eq. 5.21 – at 1520 nm as a function of the strip length difference. (d) representation of (full red line) absorption spectrum of sample B as recorded in tetrachloroethylene (TCE) and (markers) the measured α_{QD} spectrum for strip waveguides coated by a monolayer of sample B QDs. The absorption spectrum in TCE has been rescaled to stress the correspondence between both quantities.

strips of hexagonally close packed monolayers of QDs on the waveguide (see Fig. 5.17a-b). The strip lengths are varied from 100, to 200, 500, 1000, 1500 and 1750μm. In this way, the QD absorption coefficient α_{QD} can be determined, which is the QD induced loss due to *absorption* in the SWG, excluding any coupling losses. As part of the QDs can re-emit the absorbed photon back into the SWGs, the induced absorption loss may be partly lifted leading to a decrease of α_{QD} and a net QD absorption coefficient α^*_{QD} will be measured. If we define α as the total loss of the QD coated waveguide and α_0 as the loss of a bare waveguide then α^*_{QD} is given by $\alpha - \alpha_0$. Denoting by L and P_t the length of the QD covered part of a strip waveguide and the power transmitted through that waveguide and by L_{ref} and $P_{t,ref}$ the same, yet for a reference waveguide, α^*_{QD} can be determined from the waveguide absorbance A according to:

$$A = -\ln\frac{P_t}{P_{t,ref}} = (\alpha - \alpha_0)\,(L - L_{ref}) \tag{5.21}$$

Fig. 5.17b illustrates A as a function of strip length difference $\Delta L = L - L_{ref}$ for a SWG coated with a PbS/CdS QD monolayer, using the 100 μm strip as a reference. The full line represents the best fit of the data, yielding α^*_{QD} as the slope of $ln\frac{P_t}{P_{t,ref}}$ *vs.* $L - L_{ref}$. As we will show below, the QD emission contribution can be discarded, such that α^*_{QD} equals α_{QD}. In what follows, we will therefore denote the measured net QD absorption coefficient by α_{QD}.

Experimental results

Fig. 5.17c shows that α_{QD} is determined as 20.2cm^{-1} (9 dB/mm) for sample A at 1520 nm. As the typical losses of uncoated waveguides are 0.45cm^{-1}(0.2 dB/mm), this pronounced increase in loss indicates the presence of QDs on the strip waveguide. Similar α_{QD} values are observed for sample B (see Fig. 5.17d), where the wavelength dependence resembles the spectrum of the QDs dispersed in tetracholoroethylene. This clearly shows the interaction of the quantum dots with the optical field in the SWGs.

5.3.3 Numerical description

To compare the experimental QD absorption with model predictions, we use an approach where the real QD layer covering the SWG is replaced by an effective medium with a dielectric function ϵ_{eff}. Using the waveguide geometry as shown in Fig. 5.18a this enables us to extract a theoretical absorption coefficient α_{th} from the simulated effective refractive index $\tilde{n}_{eff} = n_{eff} + i\kappa_{eff}$ of the propagating quasi-TE mode:

$$\alpha_{th} = \frac{4\pi\kappa_{eff}}{\lambda} \tag{5.22}$$

This approach however requires that the permittivity of each material or medium involved is known. For silicon and silica, we use typical values for the refractive index at 1520 nm of 3.45 and 1.45, respectively. For ϵ_{eff} , we use the expression based on the coupled dipole model studied before in section 5.2.3:

$$\varepsilon_{eff} = \varepsilon_h \varepsilon_0 \left(1 + \frac{N_s}{\delta} \frac{a_{QD}}{1 - a_{QD} S} \right) \tag{5.23}$$

Here, δ denotes the assumed thickness of the effective layer (see Table 5.1), which amounts to the nanocrystal diameter increased by 3.6 nm to account for the thickness of the oleate ligand shell[10]. Importantly, the dipole sum S is in general different for fields parallel ($S_{||}$) or perpendicular ($S_{\perp}$) to the QD film. Consequently, S will be different for QDs on top or at the edge of the quasi-TE mode excited SWGs. In contrary to S, which only depends on the position of the particles relative to each other, a_{QD} is a function of the host permittivity ϵ_h and the dielectric function $\epsilon_{QD} = \epsilon_{QD,Re} + i\epsilon_{QD,Im}$ of the QDs. ϵ_h was shown in section 5.2.4 to be an extrinsic property depending on the layer thickness and the surrounding environment of the QDs, where a value of ϵ_h in the range 1-1.16 was determined for a QD monolayer. $\epsilon_{QD,Re}$ and $\epsilon_{QD,Im}$ are calculated values taking care that they yield the experimental absorption coefficient spectrum of the QDs in a dilute dispersion while obeying the Kramers-Krönig transformation[13]. Importantly, in this analysis, we assume that the absorption coefficient of the PbS/CdS core/shell QDs at wavelengths shorter than 400 nm can be derived from the bulk dielectric function of PbS and CdS, respectively as was demonstrated for PbS/CdS QDs[7] and we neglect possible quantization effects in the CdS shell. For the numerical values of ϵ_{eff} we refer to section 5.2.3 as the samples used there for the planarized waveguides are similar to the ones here in strip waveguides and this will allow for a comparison of α_{QD} for both types of waveguides.

5.3.4 Simulations

Given the SWG cross section and the expression for ϵ_{eff} that results from the coupled dipole model and the self-consistently determined a_{QD}, the electric field of the guided optical mode in the SWG can be calculated, resulting in theoretical values for n_{eff} and α_{th}. As an example, Fig. 5.18c represents the electric field along E_x at a wavelength of 1520 nm for a SWG covered by a QD monolayer as obtained using Fimmwave 6.4 full vectorial complex mode solver. The figure clearly shows the overlap between the QD film and the evanescent field, which makes that light absorption by the QDs affects ϵ_{eff} and leads to a nonzero α_{th}.

Results

In Fig. 5.17b, the SEM picture clearly shows a close packed QD monolayer covering the strip waveguide. As outlined in sec. 5.3.1 we note that some parts of the waveguide may not be covered by QDs. These parts are typically located at the corner between the waveguide edge and the trench and might affect the measured waveguide absorbance. Therefore, to account for these possible deposition anomalies in the calculated α_{th}, we start from the schematic geometries as shown in Fig. 5.18a-b, where the waveguides are respectively coated by a QD monolayer covering the whole waveguide surface and a waveguide showing a gap at the SWG corners. t_1 and t_2 denotes respectively the size of this gap at the waveguide edges and trenches. Using a value of $\epsilon_h = 1.16$, the simulated α_{th} is calculated for sample B (see Fig. 5.18d). By setting t_1 equal to

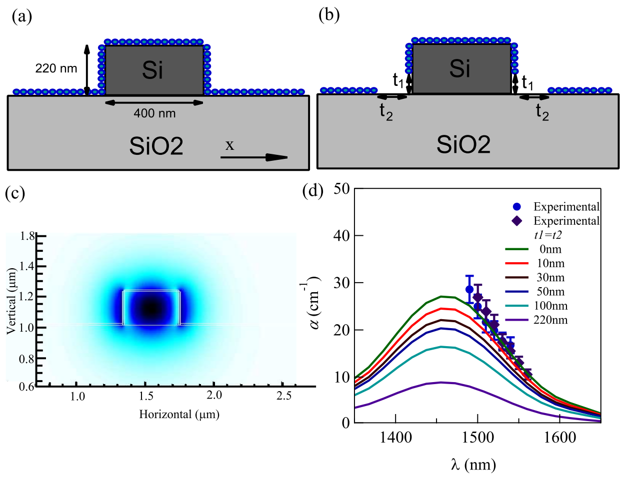

Figure 5.18: (a) Schematic view illustrating a perfect monolayer of PbS/CdS QDs conformally covering the SOI strip waveguide surface. (b) The model structure used to simulate the surface morphology with uncovered parts at the waveguide edges (t_1) and trenches (t_2). (c) The calculated TE field component $|E_x|$ of the quasi-TE mode, for a perfect monolayer showing the clear interaction of the optical mode with the QD top and edge interface layers. The field strength increases from light to dark blue. (d) (lines) the simulated α_{th} spectrum for different values of t_1 and t_2 as indicated ($t_1 = t_2$ for all simulations). The experimental values (blue markers) coincide with the simulated values for $t_1 = t_2 = 0\,\mathrm{nm}$.

t_2 and varing these parameters from 0 nm (a perfect layer) to 220 nm (completely sparse SWG-edges and trenches). A good match between the experimental α_{QD} and the simulated α_{th} is obtained, if t_1 and t_2 equal zero. This indicates that for sample B, the deposition anomalies are minor and the strip waveguide is well covered.

Note that for sample B, α_{QD} is 21 cm^{-1} around 1520 nm. This value is about 6 times larger than the 3.6 cm^{-1} (1.6 dB/mm) measured for a monolayer of QDs deposited on a planarized waveguide (see sec. 5.2)[22]. A first look at the simulated field (Fig. 5.18c) already indicates that this is most likely due to the strong field at the edges of the waveguide. From these simulations, we can calculate the confinement factor Γ, which yields the fraction of the power in the guided mode that passes through the QD-layer. In the case of a strip waveguide, a Γ of 3.6% is calculated. This number is composed of contributions for the QDs covering the SWG edge, top and trench, amounting to 2.1%, 0.96% and 0.55%, respectively. Hence, almost 60% of the total power passing through the QD monolayer on the SWG is attributed to the QDs at the edge. A similar calculation for QDs deposited on a planarized waveguide yields a total Γ of about 0.8%, a number similar to what is obtained for the top surface of the strip waveguide. Since the increase in confinement factor agrees with the increase in absorption coefficient, the strongly enhanced absorption in strip waveguides as compared to planarized waveguides mainly reflects an enhanced Γ, especially due to the waveguide edges being covered by QDs.

For sample A, a value of $\alpha_{QD} = 20.2\,\mathrm{cm}^{-1}$ is experimentally determined at 1520 nm. Here, if we set $t_1 = t_2 = 0$ a value of $26\,\mathrm{cm}^{-1}$ is calculated, overestimating the $20.2\,\mathrm{cm}^{-1}$ value. Fig. 5.19 shows the simulations for different values of t_1 and t_2. Although, we have two degrees of freedom t_1 and t_2, we can determine possible ranges for t_1 and t_2, given the condition that α_{th} needs to match α_{QD} as indicated by the dashed green line in Fig. 5.19. At first, we notice an exponential decrease in α_{th} with increasing t_2, which reflects the decreased influence of the QDs, due to the removal of the QDs near exponentially decaying TE-mode along the x direction. The typical 1/2e decay constant along the x-direction for all the α_{th} curves at the different t_1 values is ≈ 100 nm. Secondly, from the figure we can determine an under- and upperlimit value for t_1, which we will denote as $t_{1,min}$ and $t_{1,max}$. For $t_{1,min}$ a value of 20 nm is found and corresponds to $t_2 = \infty$. This situation represents a totally uncovered waveguide trench and a gap of 20 nm at the SWG-edge. $t_{1,max}$ is determined as 90 nm and corresponds to $t_2 = 0$ nm. This case corresponds to a completely filled trench, while a large gap is present at the waveguide edge. As these values show the extreme cases and given that in practice 0 nm$< t_2 <$200 nm one can expect a t_1 value lying between 20 nm and 90 nm.

In the previous paragraph the ranges of t_1 and t_2 were obtained without taking into account $\approx$10% error of α_{QD}. Moreover, ϵ_h was determined

in the range 1-1.16 and we used a value of 1.16 in the simulations and we have neglected possible scattering losses as these layers will become inhomogeneous around the gaps. All these effects are expected to have very small consequences on the obtained results for t_1 and t_2.
In summary, using an ε_h value determined from the previous result (sec. 5.2)[22], where ε_h is obtained from a simple planar geometry, we are able to model the QD absorption coefficient in more complex strip waveguides. Part of these coated SWGs may not be covered. To account for these possible deposition anomalies, we take into account the morphology of the QD-layer in the simulated absorption coefficients, as discussed in the previous paragraphes.

Emission contribution

In the above discussions, a meaningful comparison of the simulated α_{th} and experimental α^*_{QD} as defined in sec. 5.3.2 was only possible if the re-emission of light absorbed by the QDs in the SWGs can be neglected. Therefore we need to calculate $\frac{QY\eta}{2}$, which is the product of the photoluminescence quantum yield QY and the coupling efficiency η, denoting the photon coupling coefficient from the QD-layer to the propagating mode in the waveguide. Each QD will re-emit the absorbed photon with a probability of $QY \times \frac{\eta}{2}$. If we define $N(z)$ as the amount of photons per unit area per unit time at a certain position z along the propagation direction of the waveguide, then the amount of lost photons dN_{abs} due to QDs within a small section $z, z + dz$ is :

$$dN_{abs} = -\alpha_{QD} N dz \tag{5.24}$$

From the absorbed photons wihtin the section dz, there will be a fraction $\frac{QY\eta}{2}$ re-emitted in the positive z-direction, which will lead to an increase of the photon population. Therefore the amount of emitted photons dN_{em} within the section dz will be :

$$dN_{em} = -dN_{abs} \frac{QY\eta}{2} \tag{5.25}$$

To simplify, we regarded the QDs as all absorbing and emitting around the same wavelength and neglect any reduce of the emitted power due

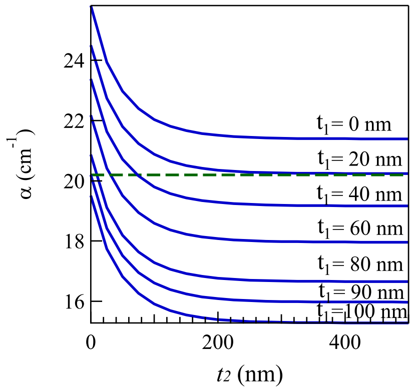

Figure 5.19: Simulated α_{th} for sample A for different combination of t_1 and t_2. The crossing of the experimental α_{QD} (green dashed line) with different α_{th} curves yields allowed values for t_1 and t_2.

to broadening of the QD emission spectrum. In this way, dN_{em} can be seen as an upper limit of the emitted photons around the wavelength of study. The total change of the photonflux dN reads:

$$dN = dN_{abs} + dN_{em} = -\alpha_{QD}(1 - \frac{QY\eta}{2})N \tag{5.26}$$

Integration of the above equation and multiplying the photonflux with the photon energy yields for the power at the end of the waveguide:

$$P(L) = P_0 e^{-\alpha_{QD}(1-\frac{QY\eta}{2})L} \tag{5.27}$$

Therefore, the QD absorption coefficient α_{QD} will be lowered by a factor $1 - \frac{QY\eta}{2}$ yielding a netto loss coefficient:

$$\alpha_{QD}^* = \alpha_{QD}(1 - QY\frac{\eta}{2}) \tag{5.28}$$

The factor 2 in the denominator, accounts for the fact that only half of the spontaneously emitted photons will be collected at one of the waveguide ends. Clearly, if $QY = 1$ and $\eta = 1$, then for each two absorbing QDs, one photon will be emitted with a direction to the waveguide end, and thus the netto loss coefficient will be half the QD absorption coefficient. Otherwise, if $QY \times \eta << 1$, the contribution of the emission to the waveguide loss can be neglected. In the next paragraphs we will estimate the emission contribution ($\frac{QY\eta}{2}$) for both planarized - and strip waveguides yielding conclusions for the measured α_{QD} in these waveguides.

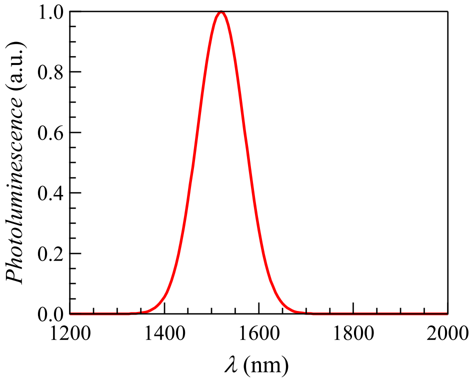

Figure 5.20: Photoluminescence spectrum of the PbS/CdS QDs used in this work after excitation at 750 nm. The QDs are dispersed in tetrachloroethylene. The emission peak is at 1520 nm.

PWGs To estimate the emission contribution in the hybrid QD/PWGs as studied in sec. 5.2, we note that in dispersion, the PbS/CdS QDs used there have a photoluminescence peaking at 1520 nm (see Fig. 5.20) and a quantum yield of 37%, as determined using an integrating sphere[23;24]. When deposited on waveguides, part of this luminescence may be coupled to the waveguides, thus raising the transmitted power and lowering the resulting absorption coefficient. In general, this QY goes down after Langmuir-Blodgett deposition on silicon[25;26], such that the value of 0.37 should be seen as an upper limit. For determining $\frac{\eta}{2}$, we use an FDTD numerical solver to determine the fraction of the power emitted by a dipole oscillator that is coupled to the waveguide modes. The oscillator is located at a distance of 20 nm from the surface, which should be regarded as an average position of the QD-monolayers relative to the waveguide surface. Along the light propagation direction, the oscillator is put at the center of the waveguide and we find that $\frac{\eta}{2}$ amounts to 0.15. Here, we averaged over the three spatial directions in which the dipole can oscillate. This shows that the emitted light ($\frac{QY\eta}{2}$) will amounts to, at its best, 5.6% of the absorbed light. This number falls within the $\approx$10% error of our α_{QD} measurements, and the contribution is therefore discarded.

SWGs To calculate the emission contribution in the hybrid QD/SWGs we first consider sample B (see Table 5.1). This sample is similar to the one used for PWGs and the upperlimit for the QY is 0.37 as discussed in the previous paragraph. For the determination of $\frac{\eta}{2}$ we take into account the waveguide geometry in strip waveguides, the oscillator is located at two positions : On top and at the edge of the SWG surface (Fig. 5.21a-b). Both oscillators are placed at a distance of 5 nm from the SWGs, which is equal to the distance between the QD center positions and the SWG-surface. Along the mode propagation direction, the oscillators are put at the center of the waveguide and we find that $\frac{\eta}{2}$ amounts to 0.125 at 1520 nm for both oscillator locations. Where we averaged over the three spatial directions in which the dipoles can oscillate. This shows that the emitted light ($\frac{QY\eta}{2}$) will amounts to, at its best for 4.6% of the absorbed light (see Fig. 5.21). In line with the conclusion for PWGs, this number falls again within the $\approx$10% error of our α_{QD} measurements, and the contribution of the QD emission is therefore discarded for sample B. For sample A, the emission peak lies beyond 1590 nm (see Table 5.1) and is out of the bandpass range of the grating couplers and therefore the emission contribution needs not te be considered.

Comparison with Maxwell-Garnett

In the previous paragraphs we simulated α_{th} using the effective permittiviy ε_{eff} based on the coupled dipole model (CDM) as given in Eq. 5.23 and clearly demonstrated its relevancy for describing close packed nanocrystal films on SOI waveguides. Other approach for deriving ε_{eff} is based on the Maxwell-Garnett theory, where this model is numerously applied for QDs dispersed in a dilute (liquid) mixture[5]. In the MG theory, ε_{eff} is derived assuming the QDs to be spherical, randomly dispersed and occuping a low volume fraction ($f << 1$) in a

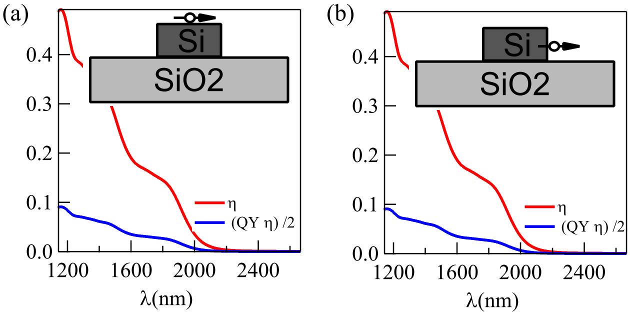

Figure 5.21: (a) Coupling efficiency η and $\frac{\eta QY}{2}$ as a function of the wavelength for a dipole oscillator located 5 nm away from the top waveguide surface. (b) Wavelength dependency of η and $\frac{\eta QY}{2}$ for a dipole oscillator located 5 nm from the edge SWG-surface, which is the distance from the QD center positions and the SWG-surface.

dielectric host. Although the QDs in our films are hexagonally ordered and show a close packed occupation, the MG approach is widely used and therefore it is interesting to verify if MG still applies under the mentioned conditions. We will demonstrate this by comparing the simulated α_{th} value for sample B at 1520 nm for both – coupled dipole and MG – models. As derived in chapter 3, the effective permittivity for QD dilute mixtures based on MG reads:

$$\begin{aligned} \varepsilon_{eff} &= \varepsilon_h \varepsilon_0 \frac{1+2f\beta}{1-f\beta} \\ \beta &= \frac{2a_{QD}}{\pi d^3} \end{aligned} \tag{5.29}$$

Here the parameters a_{QD}, d and ε_h are respectively the QD polarizability, size and host permittivity. f is the effective volume fraction of the QDs, i.e. the fraction of the volume that the QDs occupy with respect to the surrounding ligands and the close packed configuration and f is determined as 0.19. By applying Eq. 5.29 using the same parameter values as in CDM, we determine an α_{th} value of 25.9cm^{-1} based on the MG model. This contrast with the α_{th} value of 21cm^{-1} as determined based on the CDM and consequently this shows that the MG model is not applicable for the hexagonally close packed films on the

SOI waveguides. Interestingly is that the α_{th} value based on the CDM is lower compared to one obtained using MG. This can be understood considering that almost 60% (see sec. 5.3.4) of the light passes through the waveguide edges and the applied quasi-TE field at these edges (see sec. 5.2.3) results in a dipolar coupling with a suppression of the local field compared to the field that would exist for a single QD with the same host, *i.e.,* similar to the low volume fraction approximation within the MG approach as outlined here.

5.4 Conclusions

We have studied light absorption in planarized SOI waveguides functionalized with a top coating of PbS/CdS QD mono- to multilayers. The experimental absorption coefficients can be simulated using an approach where the QD layer is replaced by an effective medium with an effective dielectric function determined by dipolar coupling between neighboring QDs. This approach leaves the host dielectric constant ε_h as the only adjustable parameter and provides a generic scheme to model optical properties of composite materials containing close packed QD films. Using ε_h to match experimental and simulated absorption coefficients, we find that ε_h systematically increases for thicker films. We interpret this as an evolution of ε_h from an extrinsic property, both determined by the QD films and the surrounding layers, to a more intrinsic property of the QD layer. To the best of our knowledge, this is the first demonstration of how ε_h – a typical parameter introduced in effective medium theories – depends on the dimensions of the layer modeled. In addition, we have studied light absorption of colloidal PbS/CdS QDs in SOI strip waveguides. Using Langmuir-Blodgett deposition, close-packed monolayers are formed on the strip waveguides. By analyzing the waveguide absorbance, we show a clear interaction of the QDs with the quasi-TE optical mode. The experimental absorption coefficients due to the presence of the QDs can be simulated using the host permittivity determined in the QD/coated PWGs. Through FDTD simulations we can correct for possible QD emission in the waveguides, which turns out to be negligible in our work. Therefore, the study allows for a complete engineering of absorption and possible emission in (strip) waveguides and as colloidal QDs are easily deposited using wet chemical procedures, these results pave the way for the development of cost-effective silicon photonic devices.

	sample A	sample B
Absorption peak (nm)	1515	1450
Diameter (nm)	7.04	6.2
Shell thickness (nm)	0.66	0.40
Emission peak (nm)	$>$1590	1520
δ (nm)	10.6	9.8
α_{QD} in SWGs (cm^{-1})	20.2	21

Table 5.1: The properties of PbS/CdS core/shell samples determined via optical absorption in a TCE colloidal solution. The emission peak of sample A could not be determined due to the low sensitivity of the InGaAs detector around 1600 nm. α_{QD} is the absorption coefficient at 1520 nm of the QD-layer covering the SWGs that is discussed in sec. 5.3.4.

Bibliography

[1] Baum, C.; Gaddam, S. An improved process, metrology and methodology for shallow trench isolation etch. *In proceeding of Advanced Semiconductor Manufacturing* **2004**.

[2] De Geyter, B.; Komorowska, K.; Brainis, E.; Emplit, P.; Geiregat, P.; Hassinen, A.; Hens, Z.; Van Thourhout, D. From fabrication to mode mapping in silicon nitride microdisks with embedded colloidal quantum dots. *Appl. Phys. Lett.* **2012**, *101*, year.

[3] Moreels, I.; De Geyter, B.; Van Thourhout, D.; Hens, Z. Transmission of a Quantum-Dot-Silicon-on-Insulator Hybrid Notch Filter. *J. Opt. Soc. Am. B* **2009**, *26*, 1243–1247.

[4] Hoogland, S.; Sukhovatkin, V.; Howard, I.; Cauchi, S.; Levina, L.; Sargent, E. H. A solution-processed 1.53 mum quantum dot laser with temperature-invariant emission wavelength. *Opt. Express* **2006**, *14*, year.

[5] Hens, Z.; Moreels, I. Light absorption by colloidal semiconductor quantum dots. *J. Mat. Chem.* **2012**, *22*, 10406–10415.

[6] Geiregat, P.; Justo, Y.; Abe, S.; Flamee, S.; Hens, Z. Giant and Broad-Band Absorption Enhancement in Colloidal Quantum Dot Monolayers through Dipolar Coupling. *ACS Nano* **2013**, *7*, 987.

[7] Justo, Y.; Geiregat, K., Pieter Van Hoecke; Vanhaecke, D. C., Frank; Hens, Z. Optical properties of PbS/CdS quantum dots. *Journal of Phys. Chem. C* **2013**, *117*, 20171–20177.

[8] Lambert, K.; Justo, Y.; Kamal, J. S.; Hens, Z. Phase Transitions in Quantum-Dot Langmuir Films ** CdSe / CdS isotherm Reversibility Light Microscopy. *Langmuir* **2011**.

[9] Lambert, K.; Justo, Y.; Kamal, J. S.; Hens, Z. Phase Transitions in Quantum-Dot Langmuir Films. *Angewandte Chemie (International ed. in English)* **2011**, *50*, 12058–12061.

[10] Moreels, I.; Fritzinger, B.; Martins, J. C.; Hens, Z. Surface Chemistry of Colloidal PbSe Nanocrystals. *J. Am. Chem. Soc.* **2008**, *130*, 15081–15086.

[11] Justo, Y.; Moreels, I.; Lambert, K.; Hens, Z. Langmuir-Blodgett monolayers of colloidal lead chalcogenide quantum dots: morphology and photoluminescence. *Nanotechnology* **2010**, *21*, year.

[12] Lambert, K.; Moreels, I.; Van Thourhout, D.; Hens, Z. Quantum dot micropatterning on si. *Langmuir* **2008**, *24*, 5961–5966.

[13] Moreels, I.; Allan, G.; De Geyter, B.; Wirtz, L.; Delerue, C.; Hens, Z. Dielectric function of colloidal lead chalcogenide quantum dots obtained by a Kramers-Kronig analysis of the absorbance spectrum. *Phys. Rev. B* **2010**, *81*, year.

[14] De Geyter, B.; Hens, Z. The absorption coefficient of PbSe/CdSe core/shell colloidal quantum dots. *Appl. Phys. Lett.* **2010**, *97*, year.

[15] Neeves, A.; Birnboim, M. Composite structures for the enhancement of nonlinear-opitcal susceptibility. *J. Opt. Soc. Am. B* **1989**, *6*, 787–796.

[16] Ninomiya, S.; Adachi, S. OPTICAL-PROPERTIES OF WURTZITE CDS. *J. Appl. Phys.* **1995**, *78*, 1183–1190.

[17] Goncharenko, A. V. Optical properties of core-shell particle composites. I. Linear response. *Chem. Phys. Lett.* **2004**, *386*, 25–31.

[18] Signorell, R.; Bertram, A. Physical chemistry of aerosols. *Phys. Chem. Chem. Phys.* **2009**, *11*, 7759.

[19] Moreels, I.; Lambert, K.; Smeets, D.; De Muynck, D.; Nollet, T.; Martins, J. C.; Vanhaecke, F.; Vantomme, A.; Delerue, C.; Allan, G.; Hens, Z. Size-Dependent Optical Properties of Colloidal PbS Quantum Dots. *Acs Nano* **2009**, *3*, 3023–3030.

[20] Cademartiri, L.; Bertolotti, J.; Sapienza, R.; Wiersma, D. S.; von Freymann, G.; Ozin, G. A. Multigram scale, solventless, and diffusion-controlled route to highly monodisperse PbS nanocrystals. *J. Phys. Chem. B* **2006**, *110*, 671–673.

[21] Pietryga, J. M.; Werder, D. J.; Williams, D. J.; Casson, J. L.; Schaller, R. D.; Klimov, V. I.; Hollingsworth, J. A. Utilizing the lability of lead selenide to produce heterostructured nanocrystals with bright, stable infrared emission. *J. Am. Chem. Soc.* **2008**, *130*, 4879–4885.

[22] Omari, A.; Geiregat, P.; Van Thourhout, D.; Hens, Z. Light absorption in hybrid silicon-on-insulator/quantum dot waveguides. *Opt. Express* **2013**, *21*, 23272–23285.

[23] de Mello, J.; Wittmann, H.; Friend, R. An Improved Experimental Determination of External Photoluminiscence Quantum Efficiency. *Advanced Materials* **1997**, *9*, 230–232.

[24] Porrès, L.; Holland, A.; På lsson, L.-O.; Monkman, A. P.; Kemp, C.; Beeby, A. Absolute measurements of photoluminescence quantum yields of solutions using an integrating sphere. *Journal of fluorescence* **2006**, *16*, 267–72.

[25] Foell, C. A.; Schelew, E.; Qiao, H.; Abel, K. A.; Hughes, S.; van Veggel, F. C. J. M.; Young, J. F. Saturation behaviour of colloidal PbSe quantum dot exciton emission coupled into silicon photonic circuits. *Opt. Epxress* **2012**, *20*, 10453.

[26] Quintero-Torres, R.; Foell, C. A.; Pichaandi, J.; van Veggel, F. C. J. M.; Young, J. F. Photoluminescence dynamics in solid formulations of colloidal PbSe quantum dots: Three-dimensional versus two-dimensional films. *Appl. Phys. Lett.* **2012**, *101*, 121904.

6

Prospects of colloidal quantum dot absorption for photonic applications

6.1 Introduction

In the present days, it is difficult to imagine life without communication. In the early century this communication was mainly conducted using (slow and high loss) electrical – twisted pair or coaxial – cables. But, the growth of internet use has led to a need of more bandwith and there has been increased dependence on (fast) optical communication in the past few decades. This idea of all-optical networking is being implemented commercially or developed for different systems. Long-reach transmission systems, enabling transport information at long distances (20 km - 3000 km) from one to another part of the world, are commercialized. Short distance communication systems (10 m - 20 km) have made their presence with an increased reliance on optical communication. As examples, server-to-server data transport and fiber-to-the-home (FTTH) applications start to become commercialized in certain locations. FTTH is a concept of full optical connection in the last kilometer – in stead of classical coax-cable – from a central provider to the user at home, allowing access to larger bandwith.

Unlike off-chip systems, *i.e.* long haul and short reach communication, on-chip communication systems and computing applications are under development and will rely more and more on the use of optics and photonics[1]. In an optical communication system light is send from a transmitter through a communication or transmission channel and is send to a receiver. The collection of the communication links together with other devices providing information exchange and processing is called a network. Communication for long distances is typically fiber based as single mode fibers are low loss (0.2 dB/km at 1550 nm) and have a potential speed bandwith of up to 101.7 Tb/s (Terabits per sec)[1] to be employed for traffic[2;3]. Moreover, wavelength can be used to perform complex functions as routing and switching. In this context, wavelength division multiplexing (WDM) is a technology which combines a number of optical carrier (data) signals onto the optical fiber by using different wavelengths of laser light[4]. This technique offers a very effective way of using the fiber bandwith directly in the wavelength domain, instead of the time domain; *E.g.* by using 10 wavelengths (channels) one can increase the information transport by a factor of 10. The number of wavelengths in a WDM network determines the number of independent paths or adresses that can be used and this number should be large enough to fulfill a needed information capacity. It is very common that this number is not sufficient to support a large number of nodes in a network leading to an increased blocking probability[5]. This rises if a given output port for a certain wavelength channel is occupied by earlier data traffic then other succeeding data with the same wavelength can not be routed to the output port until the earlier data traffic has left the given port. A way to overcome this limitation is by converting one wavelength to another belonging to a free data channel, hence the need

---

[1] *i.e.* a data speed reached by the use of 370 data channels and therefore the current potential bandwith per channel is 290 Gigabits/s

for *wavelength conversion*.

Besides the motivation for wavelength conversion to reduce the blocking probability, it allows to increase the flexibilty of networks. Wavelength conversion permits network management into smaller subnetworks and allows flexible wavelength assignments within the subnetwork as illustrated in Fig 6.1. The networks operators (1-2) can manage their own network and wavelength conversion could allows for communications between subnetwork 1 and subnetwork 2.

In this chapter we will discuss the possible implementation of a PbS/CdS QD based wavelength convertor in a silicon-on-insulator platform. We will define a figure of merit (FOM), which is a measure of the transforming capability of the QD wavelength convertor, for silicon on insulator strip waveguides. We will perform simulations for obtaining this FOM for QD-coated strip waveguides. At first we will introduce the concepts and definitions to understand the simulated results by considering conversion on a microsecond timescale. Although, this is a very slow process for practical use it will allow us to deduce analytically an expression for the FOM and we will obtain a first estimate of the interaction lengths needed for the QD-layer covering the SWGs. Next, we will perform simulations on a much faster ps timescale, where we will demonstrate the use of the QDs as a 10 GHz speed wavelength convertor for different telecom bands : O-band (1274-1346 nm), C-band (1530-1565 nm) and L-band (1565-1625 nm). By appropriately tuning the bandgap of the QDs, the wavelength conversion can be perfomed either within different telecom bands or from a short - to a longer wavelength band, *e.g.* from the O- to the L-band. In the former case, the bandgap of the QDs needs to match the wavelength region of the needed band and the conversion is done by involving the interband absorption transition of the QDs first 1S-1S energy level. While, in the latter case the bandgap of the QDs needs to be chosen around the wavelength region of the short band and the conversion is performed involving the intraband aborption transitions from the QDs valence and conduction bands.

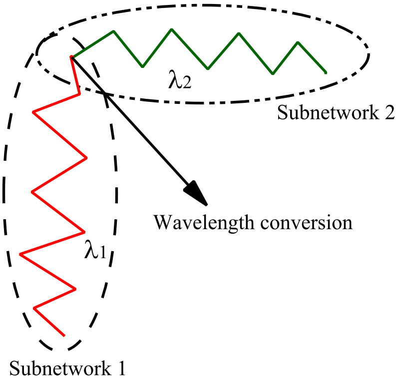

Figure 6.1: Schematic illustration of managing a large network into smaller subnetworks – illustrated here for two subnetworks – using wavelength conversion. Network operators 1,2 are responsable for their subnetwork with wavelength assignments λ_1 and λ_2, respectively.

6.2 Light propagation in a dielecric medium

In the previous chapter we have described the use of waveguides and more specifically, strip and planarized waveguides. Nevertheless, we did not describe in detail how the propagating modes are related to Maxwell's equations and their resulting asborption coefficient in a waveguide. As our wavelength convertor is absorption based and consists of a QD-layer and the SOI waveguide, both need to be considered for an optimal operation. However, we will focus in this chapter only on the simulation of the QD-layer and address the issues that could be considered for further optimizing the waveguide part. Consequently, we will rely on absorption coefficients obtained in the previous chapter and before we describe the simulation of the QD-layer we will deepen our insight into how (dielectric) waveguides are described to address the possible issues properly.

6.2.1 Maxwell's equations

A dielectric waveguide is an important concept in present day optical communication technology. The purpose of an optical waveguide is guiding light. The most known dielectric waveguide is the glass fibre, which is a key building block of the internet. Another example is a dielectric waveguide on a photonic integrated circuit (PIC), which guides light between different components in the PIC. Depending on the desired functionality, optimization of the geometry of the waveguide to target a certain field distribution is desired. Fields propagating in a (strip) waveguide can be described by a superposition of solutions (eigenmodes) of these waveguides. The interaction of light with matter is generally described by Maxwell's equations :

$$\nabla \times \mathbf{E} = -\frac{\partial \mathbf{B}}{\partial t} \tag{6.1}$$

$$\nabla \times \mathbf{H} = \frac{\partial \mathbf{D}}{\partial t} + \mathbf{J} \tag{6.2}$$

$$\nabla . \mathbf{D} = \rho \tag{6.3}$$

$$\nabla . \mathbf{B} = 0 \tag{6.4}$$

Here, **E**, **H**, **D** and **B** are the electric field, the magnetic field, the electric displacement and the magnetic displacement , respectively. These quantities are related to each other by the constitutive relationships. These are given for dielectric and non-magnetic materials as :

$$\mathbf{D} = \varepsilon(\mathbf{r})\mathbf{E} \tag{6.5}$$

$$\mathbf{B} = \mu_0 \mathbf{H} \tag{6.6}$$

where ε is the permittivity and generally depends on the position $\mathbf{r} = (x, y, z)$ within the material. μ_0 is the permeability of vacuum. Taking the charge sources – free charge density ρ and the current **J** – to be zero for a piecewise homogeneous dielectric medium with piecewise constant permittivity ε, the above equations can be rewritten and the optical waves should satisfy the wave equation (together with respective boundary conditions) :

$$\nabla^2 \mathbf{E} - \mu_0 \varepsilon \frac{\partial^2 \mathbf{E}}{\partial t^2} = 0 \tag{6.7}$$

This equation is valid for a non-dispersive medium or for a monochromatic field, provided ε is a spectral quantity evaluated at the wavelength of this field.

6.2.2 Eigenmodes of a waveguide

The solution of the wave equation Eq. 6.7 for a 2D waveguide – with the permittivity depending only on the x and y coordinates and is invariant along the z-direction – yields the eigenmodes as :

$$\mathbf{E}(x, y, z) = e(x, y) e^{-j(\beta z - \omega t)} \tag{6.8}$$

$$\mathbf{H}(x, y, z) = h(x, y) e^{-j(\beta z - \omega t)} \tag{6.9}$$

$$\beta = k_0 \tilde{n}_{eff} = \frac{\omega}{c} \tilde{n}_{eff} \tag{6.10}$$

with β the propagation constant and $\tilde{n}_{eff}$ the complex effective refractive index resulting from solving the wave equation. This value is important as it directly influences the phase and attenuation of the light waves propagating through the waveguide. Following the latter equation, the phase velocity of light as it propagates through the waveguide is given by :

$$v_p = \frac{\omega}{\Re\left[\beta\right]} = \frac{c}{\Re\left[\tilde{n}_{eff}\right]} \tag{6.11}$$

This shows, that in a waveguide, the optical waves propagate with a phase velocity which is slowed down by a factor $\Re\left[\tilde{n}_{eff}\right]$ compared to the speed of light in air or vacuum. On the other hand, the imaginary value of the effective refractive index $\Im\left[\tilde{n}_{eff}\right]$ makes the optical waves undergo an attenuation associated with an absorption coefficient as :

$$\alpha_0 = \frac{4\pi \, \Im[\tilde{n}_{eff}]}{\lambda} \tag{6.12}$$

Here, α_0 is the loss associated with a given mode and is is conveniently called the modal loss. As shown in the previous chapter, this quantity is experimentally accessible through determining the waveguide absorbance. Alternatively, the imaginary part of $\tilde{n}_{eff}$ can be theoretically analyzed by using the complex electromagnetic variational theorem[6]. This provides an expression for the change in propagation constant β resulting from a small change in some parameter, such as the frequency or the refractive index of the medium :

$$\Delta\beta = \frac{\int\int\left[\Delta(\omega\varepsilon_0 n^2)\mathbf{E}.\mathbf{E}^* + \Delta(\omega\mu_0)\mathbf{H}.\mathbf{H}^*\right]dxdy}{2\int\int\Re\left[\mathbf{E}_t \times \mathbf{H}_t^*\right].\mathbf{e}_z dxdy} \tag{6.13}$$

If the refractive index is changed then one finds in a first order Δn perturbation :

$$\Delta\beta = \omega\frac{\int\int\left[(\varepsilon_0 n\Delta n)\mathbf{E}.\mathbf{E}^*\right]dxdy}{\int\int\Re\left[\mathbf{E}_t \times \mathbf{H}_t^*\right].\mathbf{e}_z dxdy} \tag{6.14}$$

Assuming the refractive index n_S of a layer S changes by Δn_S. One can show that the change in propagation constant can be found as follows :

$$\Delta\beta = \frac{\omega}{c}\,\Gamma\,\Delta n_S \tag{6.15}$$

$$\Gamma = \frac{n_g\int_S\int\varepsilon\left|E\right|^2 dxdy}{n_s\int\int\varepsilon\left|E\right|^2 dxdy} \tag{6.16}$$

with Γ an overlap integral and represents the fraction of mode energy density confined in the layer S. Γ is called the confinement factor. Therefore the change in propagation vector is proportional to Δn_S and also the fraction of modal energy inside the layer S. This waveguide perturbation theory can be used to calculate the change in β in the presence of a lossy material (or gain). Suppose a non-aborbing layer coating the waveguide becomes lossy and the imaginary part of the layer refractive index acquires a non-zero value given by :

$$n_s \rightarrow n_s + i\,\frac{c\,\alpha_m}{2\,\omega} \tag{6.17}$$

with α_m is the material loss of the coating layer. Then we can take the index perturbation Δn_S to be :

$$\Delta n_S = i\,\frac{c\,\alpha_m}{2\,\omega} \tag{6.18}$$

The change in propagation constant becomes according to Eq. 6.15 :

$$\Delta\beta = i\Gamma\alpha_m \tag{6.19}$$

Identifying this expression with Eq. 6.10 results in :

$$\alpha_0 \; = \; \alpha_m\Gamma \tag{6.20}$$

In this expression we did not account for the intrinsic losses due to the waveguide. Similar to the perturbation calculation of the coating layer S, in general, one needs to account for the intrinsic losses by considering the change in the propagation constant in the waveguiding layer. This will result in summing up an additional factor to Eq. 6.20, composed of the product of the material loss of the waveguide and the mode confinement factor within the waveguide. However, in the previous chapter the modal loss due to intrinsic scattering was shown to be negligible in the waveguide layer compared to the QD-layer induced losses. Consequently, α_0 can be merely attributed to the QD-layer coating the waveguides.

6.3 Wavelength conversion

6.3.1 Wavelength conversion on SOI

For the simulation of QD-based wavelength conversion on SOI, we consider the configurations as shown in Figs. 6.2a-c for three cases that will be studied in this chapter, where we excite a sample with a laser source around 1550 nm delivering 10 μs or 10 ps pulses with a given pump fluence, i.e. energy per unit area ($\frac{\mathrm{J}}{\mathrm{cm}^2}$). The sample is a silicon strip waveguide coated with a PbS/CdS monolayer of QDs with an absorption coefficient α_0 of 20$\frac{1}{\mathrm{cm}}$ (Γ = 3.6%) – as determined in Chapter 5 – at the bandgap wavelength of 1550 nm. The QD-layer covers a length L on the SWGs. The sample is excited with a pump pulse at the bandgap of the QDs and therefore changes the absorption of the QD-layer. This induced absorption change is monitored by a continuous wave (CW) probe beam. For simplicity, we assume the QD-layer to be uniformly

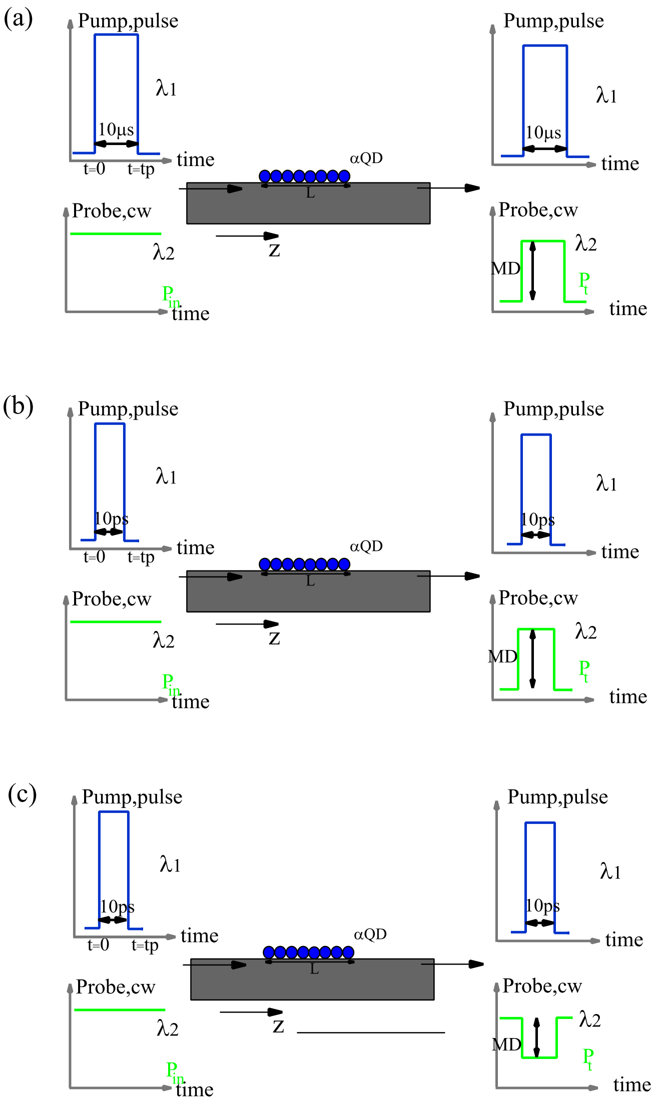

Figure 6.2: Schematic image of a QD-coated strip waveguide illustrating the wavelength conversion of the QD-layer from the pump pulse (blue) to the CW probe beam (green) for three cases discussed in this chapter. All signals are drawn in transmission. MD indicates the modulation depth or height. t_p denotes the pulse width. (a) In this case both pump and probe wavelengths are around the bandgap wavelength of the QDs and the QD-layer is pumped by a 10 μs pump pulse, resulting in an increase in transmission. (b) Similar case to (a) employing absorption bleach, but using a 10 ps pump pulse. (c) Wavelength conversion employing intraband absorption for a 10 ps pump pulse yields a probe signal with a dip in transmission.

excited along the z-direction by an incoming pulse of rectangular shape. In Fig. 6.2a the induced absorption change is due to *absorption bleach* (AB) at the bandgap of the QDs, rendering the QDs to become transparent (bleach) and this can be seen by setting the probe wavelength near the pulse wavelength as illustrated by the green signal. As an example, a 10μs pump pulse at 1550 nm can be converted to the probe with a wavelength of 1552 nm. Similarly, wavelength conversion can be made using a 10 ps pump pulse as drawn in Fig. 6.2b. Due to the decrease of the absorption around the bandgap wavelength in both cases (Fig. 6.2a-b) this results in an increase in transmission for the probe signal. In Fig. 6.2c intraband absorption is employed for a 10 ps pump pulse. Here and unlike absorption bleach, probe wavelengths are considered that result in a dip in transmission. This can be understood by supposing absorption bleaching of the QDs at the bandgap wavelength induced by a pump pulse. This will create electrons and holes in the HOMO and LUMO of the QDs and at wavelengths corresponding to energy transitions below the bandgap of the QDs, where unexcited QDs are naturally transparent, upon excitation efficient photoinduced *intraband absorption* (IA) appears[7]. Therefore, if the pump pulse has a wavelength at 1550 nm, *e.g.* probing at 1650 nm will yield a wavelength conversion together with an inversion of the pump pulse to the probe beam.

6.3.2 Important parameters

To characterize the induced absorption change we introduce the differential absorption ratio (DAR) :

$$DAR(t,\lambda) = \frac{|\Delta\alpha(t,\lambda)|}{\alpha(t^{*},\lambda)} \tag{6.21}$$

The induced absorption change $\Delta\alpha(t,\lambda)$ is the difference between the absorption coefficient at a variable time t after the pulse arrival and at a fixed moment t^{*}. This is the point of time that follows or equals t and where a minimal absorption coefficient is recorded. The differential absorption ratio is defined as the absolute value of the induced absorption change of the probe beam, at a wavelength λ, divided by the absorption coefficient of the probe at the time t^*. A maximal induced absorption change will therefore lead to a maxmim value of the DAR, which can be seen as a figure of merit (FOM), independent of the QD-interaction length L. The figure of merit is a measure of the wavelength conversion capability of the QD-layer for a given pump fluence. Based on this definition the FOM can be calculated from Eq. 6.21 for a beam probing the bleached transitions (AB) at a wavelength λ_g near the bandgap or probing the intraband transitions at a wavelength λ_p corresponding to transitions below the bandgap (IA).

The absorption coefficient $\alpha(t)$ of the excited QD-layer can be estimated from the average number of excitons $\gamma(t)$ present in each quantum dot at a time t. For the absorption coefficient related to AB it reads :

$$\alpha = (1 - \frac{2\gamma}{g})\alpha_0 \tag{6.22}$$

For the IA it yields :

$$\alpha = \frac{2\gamma}{g}\frac{\alpha_0}{\xi} \tag{6.23}$$

Here α_0 is the absorption coefficient of the unexcited QD-layer (modal loss) at the bandgap wavelength and $g = 8$ is the degeneracy of the PbS/CdS 1S-1S energy level and in the latter expression $\xi \approx 10$ and accounts for the 10 times smaller oscillator strength of the intraband as compared to the bandgap transition[7]. In the next sections we will determine γ based on a occupancy rate equation model for μs and ps pulses. Although the μs wavelength conversion is very slow and for practical use is undesirable, it will allow to introduce the concepts to describe the exciton occupancy of the QDs via the rate equations and as we will show yields an analytical expression for γ. This will provide us with a first estimate of the needed interactions lengths for wavelength conversion of QD-coated SWGs.

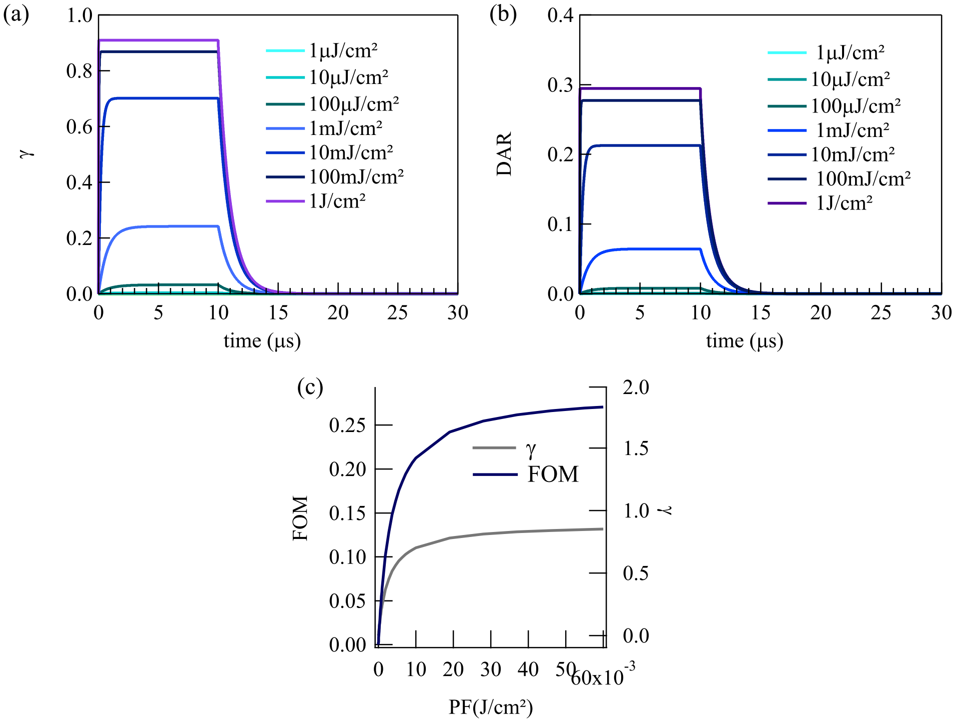

Figure 6.3: (a) The time dependence of c_1, which equals the average number of excitons γ for a 10μs rectangular shaped pulse arriving at $t_0 = 0\,$s. (b) The differential absorption ratio (DAR) as defined for different pumpfluences of the incoming pulse. (c) The DAR depedendency on the pumpfluence (PF) at a time of 10μs (FOM) after the pulse arrival shown as the blue curve with the magnitude values in the left axis. (right axis) γ at 10μs as a function of the PF shown as the grey curve.

6.4 Microsecond wavelength conversion

6.4.1 Occupancy rate equations

To determine γ we at first define c_0 and c_1 as the fraction of total QDs which are unexcited and contain a single exciton, respectively. Important here is that we will assume the Auger recombination rate to be much higher as compared to the absorption rate of photons by a given QD. Practically, this condition is fulfilled because the achievable photon flux levels will be low in a pulse with a width of 10 μs. Consequently, if any biexcitons are created the Auger rate will be so high and result in a negligible fraction of biexcitons within the pulse. Therefore, the rate equations describing the occupancy can be limited to the unexcited state $i = 0$ (c_0) and the single excited state $i = 1$ (c_1) – in which c_1 equals γ as the single excited state is the only contributor to the exciton population – of the QDs:

$$\begin{aligned} \frac{\mathrm{d}c_1}{\mathrm{d}t} &= k_{0,abs}(t)c_0 - k_{1,em}(t)c_1 - \frac{c_1}{\tau_1} \\ c_0 + c_1 &= 1 \end{aligned} \tag{6.24}$$

$k_{0,abs}(t)$ is the rate of absorption of an unexcited QD and for a rectangluar shaped pulse arriving at time t_0 it yields :

$$\begin{aligned} k_{0,abs}(t) &= k_{0,abs} \quad t_0 < t \leq t_p \\ &= 0 \qquad\quad t > t_p \end{aligned} \tag{6.25}$$

with $k_{0,abs} = \sigma J_p$, with σ the QD absorption crossection and J_p the photon flux density, i.e. the amount of photons per unit time and area within the the pulse. σ can be calculated as :

$$\sigma = \frac{\alpha_m\,\delta}{N_s} \tag{6.26}$$

$$= \frac{\alpha_0\,\delta}{\Gamma\, N_s} \tag{6.27}$$

with $\alpha_0 = 20\frac{1}{\mathrm{cm}}$ and $\Gamma = 0.036$ as outlined in section 6.2, $N_s = 1.2\,10^{12}$ cm^{-2} is the surface density of the QDs in the layer and $\delta = 10.6$ nm is the

QD-layer thickness. All these parameters were determined in the previous chapter. The calculation based on Eq. 6.27 results in a σ value of 4.9 10^{-16} cm^2. J_p is related to the pump fluence PF - energy per pulse per unit area - for the rectangular shaped pulse as :

$$J_p = \frac{PF}{E_{fot}\,\tau_p} \tag{6.28}$$

Here E_{fot} is the energy of the photons at the respective wavelength of excitation and $\tau_p = t_p - t_0$ is the temporal pulse width. $k_{1,em}(t)$ is the stimulated emission rate from the first excited state c_1 to the unexcited state c_0 and is given by $\frac{1}{64}\,k_{0,abs}(t)$. The probability prefactor $\frac{1}{64}$ can be understood as follows. The value in the denominator accounts for the 64 possible transitions between the 8-fold degenerate HOMO and LUMO energy levels. While the value of 1 in the numerator of the prefactor is explained as a single excited QD can only emit to one available energy level in the HOMO. The last term in Eq. 6.24 considers the spontaneous radiative recombination of the excited QD with a single exciton and a lifetime τ_1 of 1μs as determined by Moreels et al.[8].

Equation 6.24 can be solved analytically and yields for a pulse coming into the waveguide at a time t_0 and exciting the QD-layer strip with initial fraction $c_1(t_0)$:

$$\begin{aligned} c_1(t) &= \left(c_1(t_0) + \frac{k_{0,abs}}{k_{0,abs} + k_{1,em} + \frac{1}{\tau_1}}\right)\left(e^{-(k_{0,abs}+k_{1,em}(t)+\frac{1}{\tau_1})(t-t_0)}\right) - \ldots \\ &\quad \frac{k_{0,abs}}{k_{0,abs} + k_{1,em} + \frac{1}{\tau_1}} && t_0 < t \leq t_p \\ &= c_1(t_p)e^{-(\frac{(t-t_0)}{\tau_1})} && t > t_p \end{aligned} \tag{6.29}$$

For an incoming pulse on a unexcited QD-layer ($c_1(t_0) = 0$) above expression is simplified to:

$$\begin{aligned} c_1(t) &= \frac{k_{0,abs}}{k_{0,abs} + k_{1,em} + \frac{1}{\tau_1}}\left(e^{-(k_{0,abs}+k_{1,em}(t)+\frac{1}{\tau_1})(t-t_0)}\right) && t_0 < t \leq t_p \\ &= c_1(t_p)e^{-(\frac{(t-t_0)}{\tau_1})} && t > t_p \end{aligned} \tag{6.30}$$

6.4.2 Figure of merit

Since the bi- and multiexciton contribution to the QD occupancy is negligible, the average number of excitons at each time t equals $c_1(t)$. By combining Eq. 6.21 and Eq. 6.22 we explicitly determine DAR. Fig. 6.3a shows the time dependence of γ for different PF values. Initially at $t_0 = 0$ all the QDs are unoccupied followed by an uprise of γ to a value which is maintained during the left over time of the pulse. During this time a minimal absorption value $\alpha(t^*)$ is recorded. After the end time t_p of 10 μs, c_1 decreases with a recombination constant of $\approx 1\mu$s and all the excited QDs head back to the unexcited state. Consequently, the absorption coefficient after the exciton relaxation (background absorption) equals α_0 and corresponds to the maximal absorption value. Fig. 6.3b shows the DAR – calculated based on Eq. 6.21– for the different PF values and in Fig. 6.3c we plot the FOM and $\gamma(t_p)$ as a function of the PF values. At lower PF values, the FOM increases by augmenting the PF while at pump fluence values of 10-20$\frac{\mathrm{mJ}}{\mathrm{cm}^2}$ the FOM tends to level off to a value of 0.27, which is not strongly altered by increasing the PF as the QDs become more occupied by a single exciton ($\gamma \approx 0.9$). We note that indeed the 0.27 value is close to the $\frac{1}{3}$ upperlimit for the FOM of single occupied QDs. The upperlimit is determined by consdering the maximal induced absorption change ($\frac{1}{4}\,\alpha_0$) and the minimal absorption coefficient ($\frac{3}{4}\,\alpha_0$). Hence, the ratio of both yields the $\frac{1}{3}$ upperlimit value for the FOM.

6.4.3 Modulation Depth

The FOM is an intrinsic measure of the conversion capability and is suitable to describe the QD-layer conversion capablity, but for practical design of devices a more extrinsic measure is the modulation depth (or height), also named modulation, which is by definition :

$$MD\,[dB] \;=\; 10\log_{10}\frac{T^*}{T} \tag{6.31}$$

Here, T and T^* are respectively the transmission of the probe beam of the wavelength convertor in the on state (digital 1) with respect to the off state (background or the digital 0). The modulation depth is expressed in decibel (dB)[2] and as an example a MD value of 10 means that the outcoming signal after transmission in the on state is 10 times higher as compared to the signal in the off state. The modulation is related to the FOM as :

$$MD\,[dB] = 10 \times FOM \times \alpha(t^*) \times L \tag{6.32}$$

Note that MD is proportional to FOM and given that $\alpha(t^*) = \alpha_0$ the second term equals 1 in the above equation and the modulation is directly linked to the QD-layer parameters α_0 – expressed in $1\frac{1}{\mathrm{cm}}$ – and L. Assuming a target modulation of 3dB, which is 50% change in transmission between the on and off state, and given that $\alpha_0 = 20\frac{1}{\mathrm{cm}}$ (9 dB/mm) we find for a $FOM \approx$ 0.25 ($PF = 5\frac{\mathrm{mJ}}{\mathrm{cm}^2}$), a QD-interaction length L of 0.6 mm – with a corresponding 5 dB transmission loss – is needed to achieve the target modulation. This value of L is practically feasible on a SWG and is a motivation for investigating much faster, but with more complex exciton dynamics, picosecond wavelength conversion.

6.5 Picosecond wavelength conversion

6.5.1 Occupancy rate equations

In section 6.4 we described wavelength conversion at the microsecond timescale, and we defined c_0 and c_1 as the fraction of QDs with respectively none and a single exciton. The analysis was limited to this levels as the PF in practice is not sufficient to trigger the creation of bi- and

---

[2] sometimes it is expressed per unit length in dB/cm

$\tau_1{}^8$	1 μs	τ_5	8 ps
$\tau_2{}^7$	82 ps	τ_6	6 ps
$\tau_3{}^7$	32 ps	τ_7	4 ps
$\tau_4{}^7$	13 ps	τ_8	3 ps

Table 6.1: The used time constants for implementing in the occupancy rate equations.

multiexcitons and overcome the Auger rate. In what follows, we will analyze picosecond scale wavelength conversion (Fig. 6.2b-c), where a high PF is enforceable and therefore Auger recombination will be included in our analysis. We define c_i as the fraction of QDs that contain i excitons and based on the 8-fold degeneracy of the HOMO and LUMO levels in PbS/CdS QDs this yields for the change of c_i within and after a pulse :

$$\begin{aligned}
\frac{\mathrm{d}c_0}{\mathrm{d}t} &= -k_{0,abs}(t)c_0 + k_{1,em}(t)c_1 + \frac{c_1}{\tau_1} \\
\frac{\mathrm{d}c_1}{\mathrm{d}t} &= k_{0,abs}(t)c_0 - k_{1,abs}(t)c_1 - k_{1,em}(t)c_1 + k_{2,em}(t)c_2 - \frac{c_1}{\tau_1} + \frac{c_2}{\tau_2} \\
\frac{\mathrm{d}c_2}{\mathrm{d}t} &= k_{1,abs}(t)c_1 - k_{2,abs}(t)c_2 - k_{2,em}(t)c_2 + k_{3,em}(t)c_3 - \frac{c_2}{\tau_2} + \frac{c_3}{\tau_3} \\
&\dots \\
\frac{\mathrm{d}c_7}{\mathrm{d}t} &= k_{6,abs}(t)c_6 - k_{7,abs}(t)c_7 - k_{7,em}(t)c_7 + k_{8,em}(t)c_8 - \frac{c_7}{\tau_7} + \frac{c_8}{\tau_8} \\
\frac{\mathrm{d}c_8}{\mathrm{d}t} &= k_{7,abs}(t)c_7 - k_{8,em}(t)c_8 - \frac{c_8}{\tau_8}
\end{aligned} \tag{6.33}$$

With $k_{i,abs}(t)$ the rate of absorption of a state i, which is given by $\frac{(i-8)^2}{8^2}k_{0,abs}(t)$. The absorption rate of the unexcited QDs $k_{0,abs}(t)$ is presented in Eq. 6.25 and $k_{i,em}(t)$ is the stimulated emission rate from a state i to a state (i-1) and is given by $\frac{i^2}{8^2}k_{0,abs}(t)$. τ_i ($i > 1$) are the Auger multiexciton recombination times from a state i to a state (i-1) and τ_1 is the radiative 1μs single exciton recombination time. The τ_i values are summarized in Table 6.1. The values τ_2, τ_3 and τ_4 are taken from a transient absorption report on PbSe QDs[7], while τ_5-τ_8 are obtained from extending the reported values assuming quadratic Auger scaling[9;10]. The coupled rate equations 6.33 are solved numerically using an in-house build solver by assuming 10 ps rectangular shaped pulses with a given PF ($\frac{\mathrm{J}}{\mathrm{cm}^2}$). This results in calculated c_i values together with the average number of excitons $\gamma(t)$ at each time t within or after a pulse:

$$\gamma(t) = \sum ic_i(t) \tag{6.34}$$

From the solution of c_i in time we identify three dynamic regimes: The

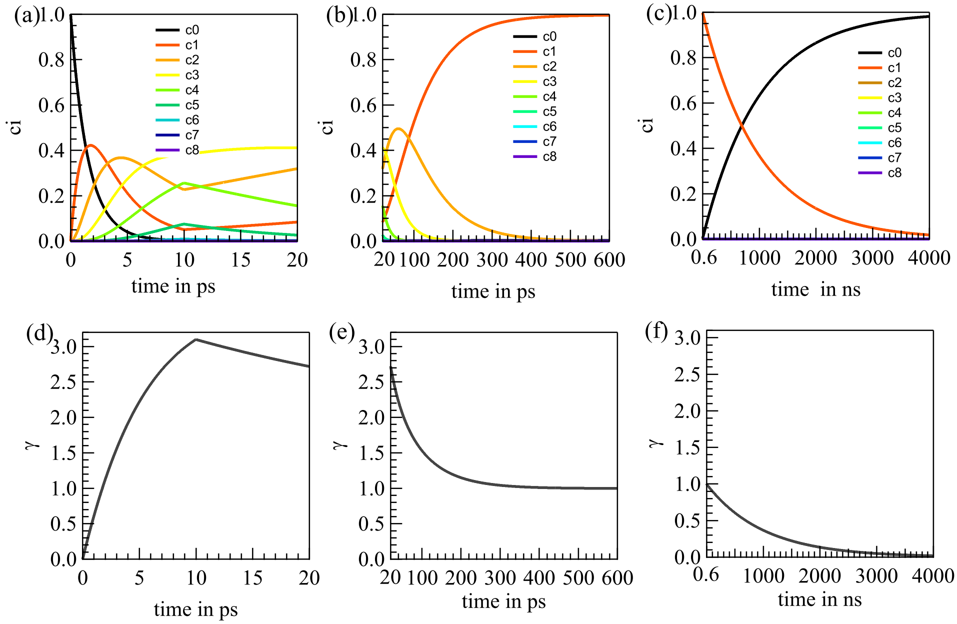

Figure 6.4: (a) The fraction of QDs with i excitons (c_i) as a function of time plotted on a timescale from 0 to 20 ps illustrating the build up of c_i assuming a 10 ps pulse with a pumpfluence $PF = 2\,\frac{\mathrm{mJ}}{\mathrm{cm}^2}$ and an initially unexcited QD-layer. (b) c_i plotted in a timescale from 20 till 600 ps illustrating the creation and Auger recombination of the multiexcitons. (c) c_i plotted in a timescale from 600 ps till 4000 ns showing the radiative single exciton recombination. (d-e-f) The average number of excitons within a QD ($\gamma(t)$) calculated using Eq. 6.34 at the different timescales, respectively for the conditions outlined in (a).

exciton build up within the pulse, the Auger and the single exciton recombination regime as shown in Figure 6.4. The first regime is illustrated in Fig. 6.4a with c_i plotted from the arrival time $t_0 = 0$ ps of the pulse till $t = 20$ ps, showing the build up of c_i within the 10 ps pulse for a PF of 2 $\frac{\mathrm{mJ}}{\mathrm{cm}^2}$ and an initially unexcited QD-layer by setting $c_0(t_0) = 1$. At this PF after the pulse up to 5 multiexcitons per QDs are created. The fractions c_4 (light green) and c_5 (dark green) start to relax as time proceeds increasing the tri- and biexciton fractions c_3 and c_2. In the second regime shown in Fig. 6.4b, c_2 and c_3 reach their maximum followed by a a fast decrease at a timescale of $\approx$ 100 ps due to the Auger recombination leaving the QDs with only single excitons. Finally, in the third regime where c_i is plotted in Fig. 6.4c at a timescale from 600 ps till 4000 ns, c_1 decreases simultaneously with an increase of c_0 due to radiative single exciton recombination. It is clear that in the second regime, the dynamics are fast enough and the best to be exploited. Additionally, in this regime, the QDs are left with single excitons after a certain time, which we will set to be 600 ps and conveniently call the loss at this time the background absorption coefficient. Figures 6.4d-e-f show the resulting average number of excitons within a QD ($\gamma(t)$) calculated using Eq. 6.34 at the different timescales as outlined above. Fig. 6.4d shows that up to 3.1 excitons per QD are created after the pulse.

6.5.2 Figure of merit

Given the average number of excitons at each time t, the differential absorption ratio (DAR) as given in Eq. 6.21 is calculated. From the discussion in the previous section, we showed that after a pulse excites the QD-layer, a single exiton resides after $\approx$ 600 ps. Generally the amount of excitons, that remains as a background, depends on the PF of the pulse; It is clear that if a pulse train (bit sequence) arrives each bit will excite the QD-layer, which contains an initial amount of excitons equal to the background of the previous bit. Therefore, we will assume an initially excited QD-layer containing a single exciton ($\gamma(t_0) = 1$) for the calculation of the figure of merits for the absorption bleach and in-

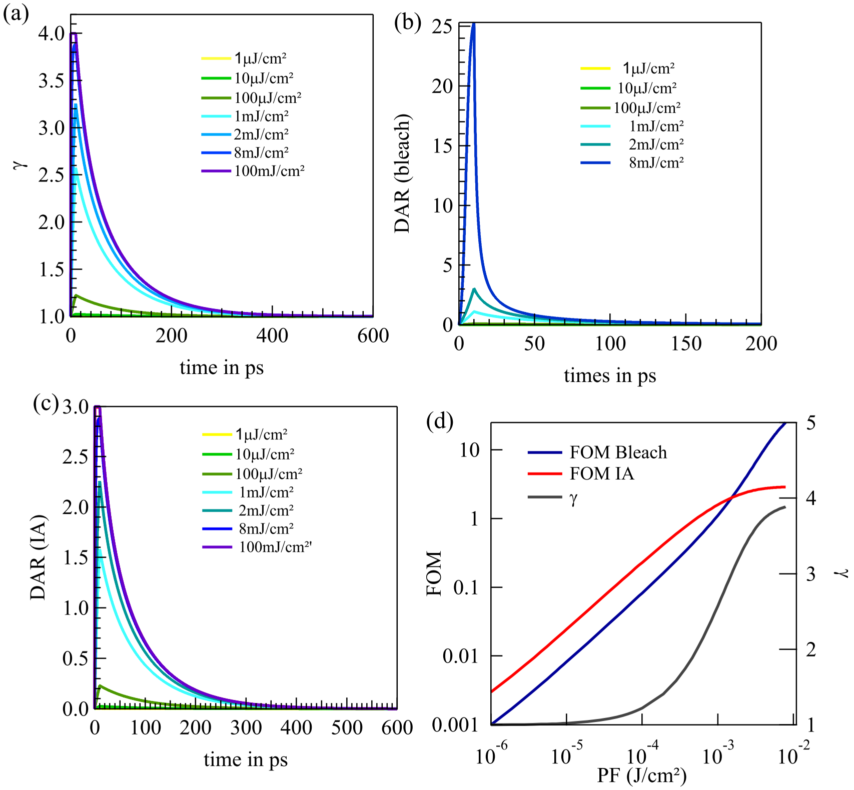

Figure 6.5: (a) The average number of excitons within a QD (γ) as a function of time assuming an initially excited QD-layer with one exciton on average additionally excited by a 10 ps pulse with different PF values as denoted in the graph. (b) The differential absorption ratio (DAR) for the absorption bleach based wavelength convertor as a function of time. (c) DAR for the intraband based wavlength convertor as a function of time. (d) (left axis) The PF dependence of the DARs for respectively the absorption bleach (blue color) and intraband absorption convertor (red color) evaluated at the peak values (Figure Of Merit) of Fig.(b) and Fig.(c). (right axis) The maximum number of created γ evaluated at the peak value of Fig.(a)

traband absorption based convertor. The specific choice of $\gamma(t_0)$ equals 1 is not random, but allows for stable operation of the wavelength convertor and will be more clarified in section 6.5.5. Figure 6.5a shows γ as a function of time for different PF values, while Fig. 6.5b illustrates DAR for the absorption bleach converter. At a PF value of $8\,\frac{\mathrm{mJ}}{\mathrm{cm}^2}$ and $t =$10 ps DAR reaches its maximum value - which corresponds to the FOM - of 25. This is one order of magnitude larger as compared to the μs conversion discussed previously, indicating a more efficient wavelength convertor. The origin of this efficiency is the high induced absorption change $\Delta\alpha$ together with fully exploiting of all the possible exciton transitions (minimal $\alpha(t^*)$). Fig. 6.5c shows DAR for the intraband transition converter, Similar to the absorption bleach convertor, at the same PF and time values DAR reaches very high values, up to 3 indicating optimal operation at this time. With this respect and given the different nature of the transitions associated with IA and AB, a quantitative comparison between FOM of both is only relevant if one compares the resulting modulation depths (or heights), which we will discuss in the next section. Moreover, from both graphs Fig. 6.5b-c we observe that for times in the range 50-200 ps DAR strongly decreases and almost vanishes. Consequently, bit sequences can be wavelength converted with a speed from ≈5 to 20 GHz. In the left axis of Fig. 6.5d we show PF dependence of the FOMs for respectively the bleach (blue color) and intraband transition based convertor (red color). For completeness of the needed parameters we plot on the right axis of Fig. 6.5d the the maximum number of created excitons $\gamma(t_p)$ (grey color) determined by evalutating the peak values in Fig. 6.5a.

In the above discussion, the speed is intrinsically limited for the wavelength convertor by the Auger recombination time of the QDs. Moreover, as this is the underlying mechanism for the IA and AB based wavelength convertors, the operation speed for both – IA and AB – convertors is the same. Additionally, changing the 10 ps pulse width to shorter durations will not result in a higher speed, because the Auger recombination time is much longer compared with the pulse duration.

6.5.3 Modulation Depth

Based on the FOMs for the IA and AB wavelength convertor we estimate the modulation depth as defined in section 6.4.3 as :

$$MD_{AB}[dB] = +10 \times FOM_{AB} \times |\alpha(t^*)| \times L \tag{6.35}$$

$$MD_{IA}[dB] = -10 \times FOM_{IA} \times |\alpha(t^*)| \times L \tag{6.36}$$

The modulation is proportional to the FOM, but we note that the sign of the modulation is negative for intraband absorption (decrease of transmission) and positive for absorption bleach (increase of transmission). The second term in the multiplications can be estimated from Eq. 6.22-6.23 once γ is known at the time t^*, which equals t_p for the AB - and 600 ps for IA convertor. The resulting modulation depths are summarized in Table 6.2 for a QD-layer with α_0 =20$\frac{1}{\text{cm}}$, $PF = 1.7\frac{\text{mJ}}{\text{cm}^2}$ and $\gamma(t_p) = 3.11$.

	FOM	$\frac{\alpha(t*)}{\alpha_0}$	MD (dB/cm)
AB	2.3565	0.2235	10.53
IA	2.1062	0.025	-1.053

Table 6.2: The used figure of merit FOM and $\frac{\alpha(t*)}{\alpha_0}$ values for intraband absorption (IA) and absorption bleach (AB) employed in the QD-layer needed to calculate the modulation depth of the wavelength convertor as given in Eq. 6.36 for a QD-layer exicted with a PF =1.7$\frac{\text{mJ}}{\text{cm}^2}$.

Assuming a target modulation of 3dB and given the MD for AB convertor, an interaction length L of 2 mm is needed to achieve the target modulation. While a length of ≈2 cm is needed for the IA convertor to achieve the same modulation of 3dB. The longer interaction length needed for the IA convertor is due to the 10 times smaller oscillator strengh of the IA with respect to the AB transition. Therefore it is very favorable to employ AB around the bandgap of the QDs, *e.g.* for wavelength conversion from 1550 to 1551 nm, or more general for wavelength conversion within the C and L-telecom bands (1530-1565 nm and 1565-1625 nm, respectively). Changing the bandgap of the QDs to smaller energies (1310 nm) permits conversion of signals from lower telecom bands such as conversion from the O-band (1274-1346 nm) to the C- or L-band by employing IA in the QD-layer. Note that due to the negative sign of the modulation, the QD-layer will not only act as wavelength convertor, but can serve as a NOT port for an incoming bit sequence.

6.5.4 Distribution of QD-excitons after a pulse

An important step in the analysis before, was the determination of the number of excitons created per pulse $\gamma(t_p)$ given the photon flux density J_p (Eq. 6.28) and the absorption crossection σ. This was done by solving the occupancy rate equations explicitly at the times within the pulse. This approach contrasts with the one used in transient absorption spectroscopy of colloidal nanocrystal solutions, where the probability that a QD has i excitons is described by a Poissonian distribution[9;11;12]:

$$P(i, N_{eh}) = \frac{N_{eh}^{i} e^{-N_{eh}}}{i!} \tag{6.37}$$

with $N_{eh} = J_p \, \sigma \, \tau_p$, the Poissonian average number of excitons. Fig. 6.6a shows the occupancy distribution c_i (i =1...8) calculated numerically assuming a QD-layer with an occupancy of one exciton per QD followed by a the pulse excitation for different PF values. From the blue curve, on average 3 excitons – calculated based on Eq. 6.34 – are created per QD at a PF value of $2\frac{\mathrm{mJ}}{\mathrm{cm}^2}$. Remarkably, assuming a Poisson distribution with the same PF value yields N_{eh} =6.6, meaning that one needs on average twice more equivalent Poisson excitations N_{eh} to initiate the same amount of average number excitons after a pulse. Furthermore, the difference is not only in $\gamma(t_p)$, but in the distribution shapes as well. Assuming a Poisson and an occupancy rate equation based distribution – conveniently called occupancy distribution – with the same average amount of excitons, which we will set to be 3, yields a Poissonian distribution (red line) that extends broader over i and is lower in amplitude as compared to the occupancy distribution. These discrepancies are due to the different nature of accessed transitions in our case – at excitation energies around the nanocrystals bandgap – and

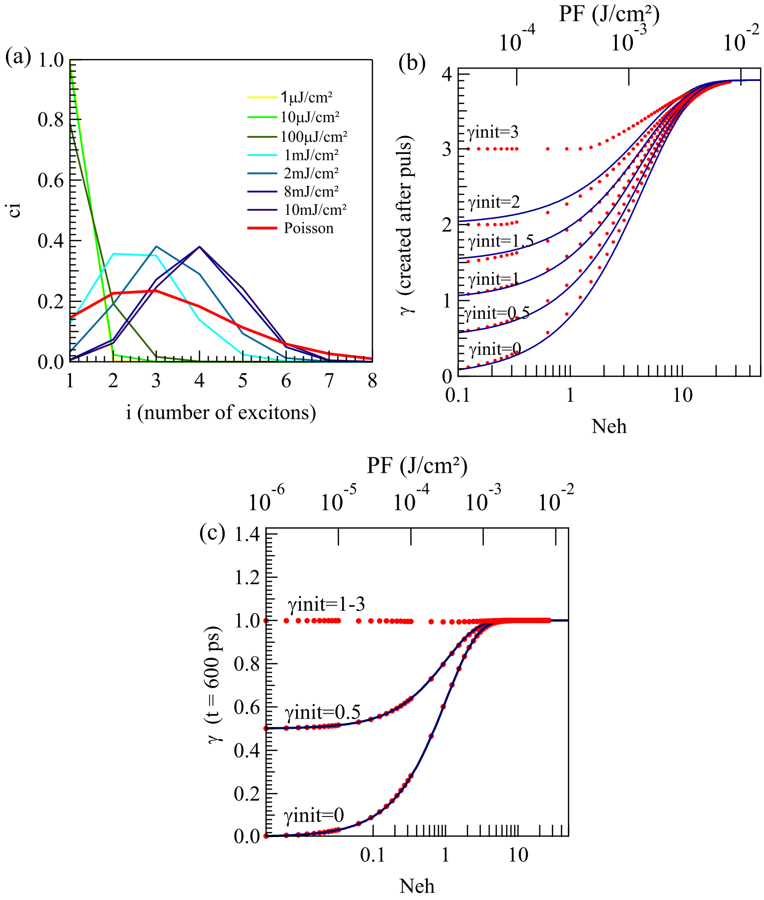

Figure 6.6: (a) The distribution of the number of excitons i created after pulse for different PF levels. The QD distributions are different from a Poissonian (red line) as illustrated at a PF of $2\frac{\mathrm{mJ}}{\mathrm{cm}^2}$, which corresponds on average to 3 excitons per QD calculated using Eq. 6.34. (b) The average number of created excitons after a 10 ps pulse ($\gamma(t_p)$) as a function of the number of equivalent Poisson excitations N_{eh} for a QD-layer containing respectively 0,1,2 and 3 excitons per QD before the pulse (γ_{init}). As the distribution is not Poissonian N_{eh} is not equal to $\gamma(t_p)$, but we can relate both by fitting all the data based on expression 6.38 using a global analysis procedure (continuous blue lines). (c) The average number of created excitons after 600 ps of the pulse arrival - $\gamma(600\,ps)$ - as a function of N_{eh} for a QD-layer containing respectively 0,0.5,1,2 and 3 excitons per QD before the pulse. Similar to Fig.(b), the data can be related to N_{eh} by fitting all the data based on expression 6.39 (continuous blue lines).

in transient absorption spectroscoy, where the excitations energies are larger than the bandgap. Due the high absorption crossection and the high density of states at these short excitation wavelengths[11], the creation of single, bi- and multiexcitons is equiprobable at the beginning and at the end of the pulse allowing the use of a Poisson distribution. While in our case, *e.g.* the creation of tri- and multiexcitons at the end of the 10 ps pulse depends on the creation of single and biexcitons at the beginning of the pulse as shown in Fig. 6.4a.

Since N_{eh}, which we will denote as the equivalent Poisson excitation, is an inclusive quantity containing all the energy and absorption parameters (PF, J_p, σ, τ_p), describing the QD-layer with this quantity would allow for using the simulated FOMs and the resulting MD values for a general QD-layer excited at the bandgap wavelength for different parameter values. Consequently, it is desired to relate N_{eh} and $\gamma(t_p)$ as shown in Fig. 6.6b for a QD-layer with initially different occupancies before the pulse arrival (γ_{init}= 0, 1.5, 2, 3). These curves of $\gamma(t_p)$ allow for a direct calculation of the FOM and MD. Interestingly, the numeric values can be described analytically with following proposed expression :

$$\gamma(t_p) = \frac{2}{g} + (\gamma_{init} - \frac{2}{g})e^{-B_{tp}\,N_{eh}} \tag{6.38}$$

Taking the degeneracy g and B_{tp} as free parameters we fit the numeric data points to Eq.6.38 by using a global fit analysis, where all the data points are fit by one expression given the different γ_{init} values. From the fits we obtain g equals 7.8 or $\frac{2}{g}$ $=$3.9 and B $=$0.229. The fitting constants are valid for γ_{init} values from 0 up to 2.

In line with the above description of $\gamma(t_p)$, the average number of excitons at 600 ps - $\gamma(600\,ps)$ - can be related to N_{eh} as illustrated in Fig. 6.6c for a QD-layer with γ_{init} $=$0,0.5,1,2 and 3 excitons per QD before the pulse. Using a gobal fit analysis, the numeric values are described as :

$$\begin{aligned} \gamma(600\,ps) &= A - (\gamma_{init} - A)\,e^{-B_{600\,ps}\,N_{eh}} \;\; \gamma_{init} < 1 \\ &= 1 \;\; \gamma_{init} \geq 1 \end{aligned} \tag{6.39}$$

A and $B_{600\,ps}$ are the free parameters and the fit yields $A\ = 1$ and $B = 0.981$.

6.5.5 Condition of stable operation

An important requirement for the wavelength convertor is a stable operation for an incoming bit sequence. There are two types of stability : the first type is stability of the background absorption, i.e. the absorption left over after 600 ps of the pulse arrival and the second type is the stability of the modulation depth (height). Both can be influenced by a change of N_{eh} or γ_{init} denoted as ΔN_{eh} and $\Delta\,\gamma_{init}$, repsectively. For the former type, the background absorption is proportionial to $\gamma(600\,ps)$ and from Fig. 6.6c we note that if γ_{init} is larger than one, the resulting $\gamma(600\,ps)$ is one regardless of the value of N_{eh}. This can be exploited by sending a set-pulse to the unexcited QD-layer yielding a stable background before the bit sequence arrives. The amount of N_{eh} needed to trigger the stable background is deduced from assuming a creation of $\gamma(t_p)$ value larger than one and is determined from equation 6.38:

$$N_{eh} > 1.29 \tag{6.40}$$

Accordingly, more than 1.29 equivalent Poisson excitations are needed to achieve a stable background for an arbritray bit sequence arriving at a speed of $\approx$ 5 to 20 GHz. The second type of stability is the modulation, which scales with the product of the FOM and $\frac{\alpha(t^*)}{\alpha_0}$ and is therefore directly proportional to $\gamma(t_p)$. Usually a bit will be designated a time span and can arrive at a time before 600 ps yielding a larger γ_{init} for the following bit. Consequently, it is important to know how the modulation varies if γ_{init} changes and from Eq. 6.38 this can be obtained :

$$\Delta\,\gamma(t_p) = e^{-B_{t_p}N_{eh}}\,\Delta\gamma_{init} \tag{6.41}$$

Here $\Delta\gamma(t_p)$ will yield the modulation change and remarkably the factor before the variation $\Delta\gamma_{init}$ is smaller than one, *e.g.* if γ_{init} increases by 20%, $\Delta\gamma(t_p)$ and therefore the modulation will be maximally altered by 20%. Since the exponential factor strongly decreases with increasing N_{eh}, the change in MD will be much less by increasing the amount of equivalent Poisson excitations. Another influence on the stability of the modulation occurs if N_{eh} changes as a consequence of a direct drop off or increase in signal energy (PF). With this respect, a similar analysis yields the same conclusions for the depedendency of the change in modulation with respect to ΔN_{eh}. The variation of the MD is maximally limited by ΔN_{eh} and strongly decreases by increasing N_{eh}.

6.5.6 Influence of the waveguide on the convertor

To concentrate on the proof-of-concept we simulated the QD-layer without regarding the influence of the waveguide, which will be beyond the scope of this thesis. Nevertheless we will highlight some of the possible problems and also discuss influence of the spectral bandwith of the QDs and the power consumption on the figure of merit.

Non uniform excitation profile

In our simulation a uniform excitation profile was assumed yielding a uniform FOM along the z-direction as shown in Fig. 6.2. But, as evidenced in section 6.2 and via Eq. 6.20 any mode will be subject to a loss when propagating through the waveguide which will no reduce the PF along the z-direction and correspondingly decrease N_{eh} and the FOM. The drop off in the FOM results in a lower modulation (Eq. 6.36) and a smaller PF value will cause the set-pulse to obtain a N_{eh} value that is not sufficiently large to trigger a stable background for the convertor. Hence, for a given waveguide geometry and a QD-layer thickness, the operation of the wavelength convertor will be theoretically limited to an effective interaction length L_{eff}. If the physical interaction length L is larger than L_{eff}, the operation of the convertor will become practically inefficient. Otherwise, if L is much smaller than L_{eff}, there will be no reduction in the wavelength convertor's modulation. In this case one can increase the modulation for a given L, by either increasing α_m or the confinement factor Γ. An increase of the QD-layer thickness from a mono to a multilayer will augment both α_m – as demonstrated in previous chapter – and Γ. Furthermore, optimizing the waveguide by solving the wave equation Eq. 6.7 for different geometries and layer thicknesses, will result in propagating modes possessing high evanescent fields interacting with the QD-layer and therefore increase Γ. Therefore, the modulation will be larger for a given L.

TPA induced free carrier absorption

A second issue that might rises up is free carrier absorption (FCA). If a pulsed beam excites a QD coated silicon on insulator (SOI) strip waveguide, part of the incoming energy will be absorbed by the QD-layer, while the other part could be absorbed by the silicon layer. If light is aborbed by the silicon layer it will generate electrons and holes in the silicon. These additional charges are unbound (free carriers) and can absorb part of the propagating waveguide mode yielding free carrier absorption[13]. The linear absorption of silicon is only present at wavelengths larger than the bandgap of silicon, and its contribution is not relevant for our wavelength convertors operating in the telecom range (1274-1625 nm). Nevertheless , as we work with high PF, two photon absorption (TPA) induced free carriers in silicon are not excluded. TPA occurs when silicon absorbs two subsequent photons with a total energy equal or larger than the bandgap energy of silicon. Avoiding TPA induced FCA might require a reduced PF and N_{eh} and lead to a reduction of the FOM and therefore hampers an efficient modulation of the QD wavelength convertor. But, the solutions as outlined above for the non uniform excitation in the waveguide apply here as well and will improve the modulation of the convertor. Alternatively, rather than using an SOI waveguide a silicon nitride platform could be used with a major advantage that it is transparent from UV till midIR range and it is an insulator as compared to semiconductor silicon and therefore FCA will be excluded. A drawback will be the low refractive index contrast between the silicon nitride ($n = 2$) and air ($n = 1$) resulting in a lower effective refractive index and Γ. For all described solutions, simulation of the waveguide geometry in both - SOI and silicon nitride - platforms will be needed to obtain large values for Γ and consequently obtain an optimal lead salt QD-based wavelength convertor in the telecom range.

Power consumption

The figure of merit that are used in this work this do not intrinsically account for the spectral bandwidth of the QDs or the power consumption E_{cons}, *i.e.*, total amount of energy needed per pulse. If one would increase the bandwith of the QDs this will result in a decrease of the absorption coeffient α_0 and therefore a decrease of the absorption rate k_0. Consequently, there will be less photon absorption events per pulse and this will lead eventually to a decrease of the figure merit. The power consumption will be a superposition of the loss due to the background – which is needed for the stability of the convertor, and the loss of power per pulse. In Fig. 6.5d we show the result of the figure of merit as a function of the pump fluence. Based on the pump fluence values in this graph one can determine the power consumption (see example below). Furthermore, one can repeat the calculation of the figure of merit, but then as a function of the spectral bandwith to obtain a complete idea of how these two parameters (power and bandwidth) would modify the figure of merit. The power consumption can be calculated once the effective area A_{eff} of the mode within the waveguide is known :

$$E_{cons} = PF\, A_{eff} \tag{6.42}$$

As an example for a strip waveguide with typical dimensions 450 nm × 220 nm, we can estimate the effective area of the mode from the waveguide geometry and find a value for A_{eff} as $10^{-8}\,\mathrm{cm}^2$. For a FOM value of 1 a PF of $10^{-3}\,\frac{\mathrm{mJ}}{\mathrm{cm}^2}$ is needed to maintain wavelength conversion (similar amount of PF is needed for the background stability), which corresponds to a power consumption E_{cons} of 10 pJ per pulse.

6.6 Conclusion

We have demonstrated through simulations the use of lead salt QDs excited around their bandgap as a wavelength convertor in silicon on insulator waveguides. We have introduced important concepts to simulate the figure of merits for slow microsecond and fast picosecond wavelength conversion. Figure of merit values larger than 25 and 3 are achieved for the absorption bleach and intraband absorption based convertor, respectively. Operation speeds are feasible of ≈ 5 to 20 GHz for the different telecom bands : O-band (1274-1346 nm), C-band (1530-1565 nm) and L-band (1565-1625 nm). By appropriately tuning the bandgap of the QDs, the wavelength conversion can be perfomed either within different telecom bands or from a short - to a longer wavelength band. Although, the occupancy distribution is different from a Poisson distribution, by introducing an equivalent Poisson excitation quantity an easy determination of the average number of excitons is allowed. This provided us with simple expressions for controlling the background - and modulation stability of the PbS/CdS QD wavelength convertor. Finally, we have highlighted the prospects for further optimizing the wavelength convertor.

Bibliography

[1] Zhang, L.; Yang, M.; Jiang, Y.; Regentova, E. Architectures and routing schemes for optical network-on-chips. *Computers and Electrical Engineering* **2009**, *35*, 856–877.

[2] Sanferrare, R. J. Terrestrial lightwave systems. *At and T Technical Journal* **1987**, *66*, 95–107.

[3] Qian, D.; Huang, M.-F.; Ip, E.; Huang, Y.-K.; Shao, Y.; Hu, J.; Wang, T. 101.7-Tb/s (370×294-Gb/s) PDM-128QAM-OFDM Transmission over 3×55-km SSMF using Pilot-based Phase Noise Mitigation. *Optical Fiber Communication Conference/National Fiber Optic Engineers Conference 2011*, 2011; p PDPB5.

[4] Zhang, L.; Yang, M.; Jiang, Y.; Regentova, E. Wavelength conversion in WDM networks. Lasers and Electro-optics Society. *Lasers and Electro-optics Society AnnualMeeting* **1997**, *1*, 88–89.

[5] Barry, R. A.; Humblet, R. A. Models of blocking probability in all-optical networks with and without wavelength changers. *IEEE Journal on Selected Areas in Communication* **1996**, *14*, 858–867.

[6] Berk, A. Variational principles for electromagnetic resonators and waveguides. *Antennas and Propagation, IRE Transactions on* **1956**, *4*, 104–111.

[7] De Geyter, B.; Houtepen, A. J.; Carrillo, S.; Geiregat, P.; Gao, Y.; ten Cate, S.; Schins, J. M.; Van Thourhout, D.; Delerue, C.; Siebbeles, L. D. A.; Hens, Z. Broadband and Picosecond Intraband

Absorption in Lead-Based Colloidal Quantum Dots. *Acs Nano* **2012**, *6*, 6067–6074.

[8] Moreels, I.; Lambert, K.; Smeets, D.; De Muynck, D.; Nollet, T.; Martins, J. C.; Vanhaecke, F.; Vantomme, A.; Delerue, C.; Allan, G.; Hens, Z. Size-Dependent Optical Properties of Colloidal PbS Quantum Dots. *ACS Nano* **2009**, *3*, 3023–3030.

[9] Klimov, V. I.; Mikhailovsky, A. A.; Xu, S.; Malko, A.; Hollingsworth, J. A.; Leatherdale, C. A.; Eisler, H. J.; Bawendi, M. G. Quantization of multiparticle Auger rates in semiconductor quantum dots. *Science* **2000**, *290*, 314–317.

[10] Klimov, V. I.; McGuire, J. A.; Schaller, R. D.; Rupasov, V. I. Scaling of multiexciton lifetimes in semiconductor nanocrystals. *Physical Review B* **2008**, *77*,.

[11] Schins, J. M.; Trinh, M. T.; Houtepen, A. J.; Siebbeles, L. D. A. Probing formally forbidden optical transitions in PbSe nanocrystals by time- and energy-resolved transient absorption spectroscopy. *Physical Review B* **2009**, *80*,.

[12] Klimov, V. I. Optical nonlinearities and ultrafast carrier dynamics in semiconductor nanocrystals. *Journal of Physical Chemistry B* **2000**, *104*, 6112–6123.

[13] Soref, R. A.; Bennett, B. R. Electrooptical effects in silicon. *Ieee Journal of Quantum Electronics* **1987**, *23*, 123–129.

7

Colloidal QDs for plasmon applications

7.1 Introduction

7.1.1 Rationale

In this chapter will discuss the use of metallic structures, in particular arrays of metallic rods with subwavelength dimensions (nanorods). An interesting property of these nanorods – also called nanoanttenas – in array as shown in Fig. 7.1 is that they exhibit strong resonances – *i.e.* more energy is removed from an incident optical beam at resonance than off resonance – which are called plasmonic modes. A detailed explanation on the type, nature of this modes and the used terminology in this paragraph will be provided in sec. 7.1.2.

In 2001, a class of plasmonic modes which manifest as resonances that can be excited or observed in the near-field (NF) but not in the far-field (FF), so-called dark modes, were theoretically predicted[1]. These dark resonances have attracted much interest in recent years, as they hold supreme qualities for the realization of SPASERS[2;3], subwavelength guiding of optical radiation with suppressed radiative losses[4], plasmonic analogs of electromagnetically induced transparency[5–7], and cloaked sensors[8]. In particular, theoretical work by Alu and Engheta suggests that it is possible to strongly suppress the FF radiation from a nanorod while preserving an enhanced NF sensitivity[8;9] – an optical counterpart to radio frequency minimum scattering antennas. As pointed out by Garcia de Abajo[10], by having an enhanced interaction with its local environment but a minimum interaction with distant sources and detectors, such a minimum scattering antenna is effectively seeing (locally) without being seen (a distance away from the antenna).

The motivation for this work is to demonstrate experimentally the suggested existence of the NF together with a suppression of the FF. With this respect, we will show that a periodic array of plasmonic nanorods can be designed to display a local minimum in its FF extinction but a maximum in the average NF enhancement in the plane of the array. The simulated structures are fabricated by means of electron beam lithography. But to observe the existence and enhancement of the NF in these fabricated structures, materials – coating the nanorod arrays as an overlay – are needed that are capable of locally interacting with the NF. In this context, colloidal quantum dots are very suitable candidates. Due their small sizes (2-5 nm) compared to the wavelength ($\approx$ 900 nm) and the array dimensions ($\approx$ 40 - 300 nm) they are capable of sensing the enhanced local fields. Furthermore, their excitation and emission frequencies can be tuned – as shown in the first chapter of this dissertation – to fit within the excitation and emission bands of the nanorod arrays. Before we will move to the experimental section, we will at first introduce the plasmon concepts that are needed to understand the results.

The results in this work were obtained in the FOM-institute AMOLF-TU/e and Philips Research Laboratories thanks to a collaboration with S. Rodriguez.

7.1.2 Plasmonic phenomena

When an electromagnetic wave with a wavevector k and an angular frequency ω propagates through a bulk metal, the component of an applied optical feld, *e.g.*, in the y direction varies as $E_y e^{[i(k_y - i\omega t)]}$. The sign of this electric field and therefore the sign of the corresponding force (-eE_y) on an electron alternates between positive and negative with a speed equal to the frequency of the wave. In the metal lattice, this force enables the displacement of the free electrons with respect to the ionic cores, resulting in a force pulling the electrons back to their original position. This electron cloud oscillates back and forth with the same excitation frequency as the applied field. The oscillation of the electron cloud is in antiphase with the applied field, such that only in a thin layer of the metal, near the *surface* (the skin depth) a reflected electromagnetic field is generated. The oscillation is at it's strongest in resonance, corresponding to the plasmon frequency. Such oscillating surface waves are called surface plasmon polaritons or surface plasmon resonances (SPRs). Surface plasmon resonances are surface waves – obtained as solutions of the macroscopic Maxwell equations (see Chapter 6, section 2) – that propagate along a metal-dielectric interface and decay in both media[11–13].

Over the years interest has shifted from bulk metals to metal nanoparticles and nanostructures as their local field reaches high values compared to the incident optical field. The plasmon waves in the nanostructures are called local surface plasmon resonances (LSPRs) as the surface waves are limited 'locally' to the nanostructure. The metal nanoparticles or structures exhibit sizes which are much smaller as compared to the wavelength of excitation (d $<<$ λ), and their plasmon frequency is tunable by the permittivity of the surrounding environment. The combination of high electric field and high sensitivity for the surrounding medium opens up the possibility for use in biosensing (to detect small concentrations of molecules), solar cells, spectroscopy and signal enhancement for imaging.

Moreover, if the size of the nanostructures becomes comparable to the wavelength of excitation ($d \approx \lambda$), then apart from the surrounding material one needs to account for the geometry of the nanostructure. Typical examples are nanoantennas or nanorods. Here, due to the geometry of the structure, electromagnetically induced transparency (EIT)[4;5;14] can appear in a single nanoantenna. In EIT, destructive interference between two localized modes (two solutions of the Maxwell equations), induces a narrow frequency transparency window within a broad resonance. One of the two modes, hereafter called bright, couples strongly to radiation and has a broad linewidth. The other mode, hereafter called dark, couples weakly to radiation and has a narrow linewidth. Dark modes have attracted interest for the realization of spasers[2;15], subwavelength guiding of optical radiation[4], enhanced spontaneous emission[16], and sensing[17;18].

In addition, by using regular multiple arrays of nanostructures (Fig. 7.1) the local field can be further enhanced by not only involving the geometry and the medium permittivity, but also the distance between the regular nanoantennas. Remarkably , the surface plasmon waves are not limited locally to the nanostructure, but can be extended throughout a large lattice, generating so called surface lattice resonances (SLRs)[19]. SLRs are complex combinations of localized surface plasmon resonance (LSPRs) on the single nanorods and diffractive orders present due to the periodicity of the structure. The SLRs arise from the enhanced radiative coupling of LSPRs, and occur close to the Rayleigh anomalies (RAs). These are associated with light incident at grazing angles – where new diffracted order appears – and diffracted parallel in the plane of array. Therefore, besides the surface plasmon waves – SLRs and (L)SPRs – RAs are an additional optical phenomenon that needs to be considered in these arrays.

Furthermore, in the field of metallic nano-optics the above optical antennas are frequently designed to manipulate the spectrum of radiation in the near field (NF), but characterized at the far field (FF)[20]. At resonance, one expects an enhancement of the optical system repsonse, typically associated with an increased light extinction. But in the presence of surface waves, the resonant condition needs to be reconsidered. The radiation spectrum may be different in the near field (NF) compared to the far field (FF)[21–24]. Consequently, a frequency of maximum NF enhancement may not coincide with an extinction maximum.

In this chapter, we will evidence through finite-difference in time-domain (FDTD) simulations and experiments that a periodic (diffractive) array of plasmonic nanorods supports a maximum NF enhancement and a FF-induced transparency at the same frequency and angle of incidence. Thus, at the same energy and in-plane momentum. This effect can be seen as the counterpart of the electromagnetically induced transparency, but for a collection of regular arrays. In this work the bright and the dark modes are both collective resonances (their quality factors increase with the number of particles in the array[15]) rather than localized. Finally, we will point out how a NF resonance can be reached with a FF-induced transparency through a proper choice of the length of the nanorods. Furthermore, the simulated results are evidenced by measuring an enhanced emission of quantum dots in the vicinity of the array at an energy and in-plane momentum for which the FF extinction is minimized.

7.2 Experimental near field enhancement in gold nanoanttena arrays

7.2.1 Fabrication of the nanoantennas

The fabrication of the gold nanoantennas is done by means of electron beam lithography and a 2×2 mm^2 periodic array of gold nanoantennas onto a silica substrate is obtained. The antennas have dimensions of 270×80×40 nm^3, and the lattice constants are $a_x = 600$ nm and $a_y = 300$ nm. A 600 nm layer of PbS/CdS core/shell quantum dots in a polystyrene (PS) matrix is spincoated, henceforth referred as the QD-layer, on top of the array. The QDs emit at a peak energy of 1.33 eV (930 nm) with a full width at half maximum of 280 meV. Additionally,

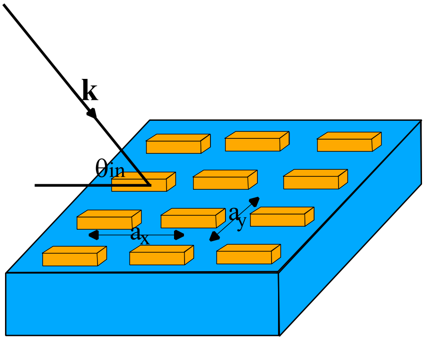

Figure 7.1: An array of gold nanorods (or nanoantennas) on a glass substrate. At the partical combination of incidence angles and photon energies, the surface lattice resonances can be excited.

a similar QD-layer is made, but spincoated directly on a silica substrate. This sample without the manufactured nanoantennay arrays will be used a reference.

7.2.2 Measurement of the near and far field extinction

Figure 7.2a shows the measured variable angle FF extinction, given by 1-T_0, with T_0 the zeroth order transmission through the QD-layer, nanoantenna array and the substrate normalized to the transmission of the reference sample. The measurements are shown as a function of the incident photon energy and the wave vector component $k_{||}$ parallel to the long axis of the nanorods $\mathbf{k}_{||} = k_0 sin(\theta_{in})\mathbf{e}_x$ with k_0 the magnitude of free space wave vector. The incident light is s-polarized, *i.e.*, along the polarization parallel to the short axis of the nanoantennas. The (+1, 0) and (-1, 0) RAs are indicated by the white solid and dash-dot lines, respectively. These are diffraction orders radiating in the plane of the array, and their dispersion follows the conservation of the parallel component of the wave vector, *i.e.*, $\mathbf{E}(k_{||}) = \frac{\bar{h}c}{n} \left|k_{parallel}\right| + m \left|G_x\right|$, where m is the order of diffraction and $G_x = \frac{2\pi}{a_x}$ is the x-component of the reciprocal lattice vector.

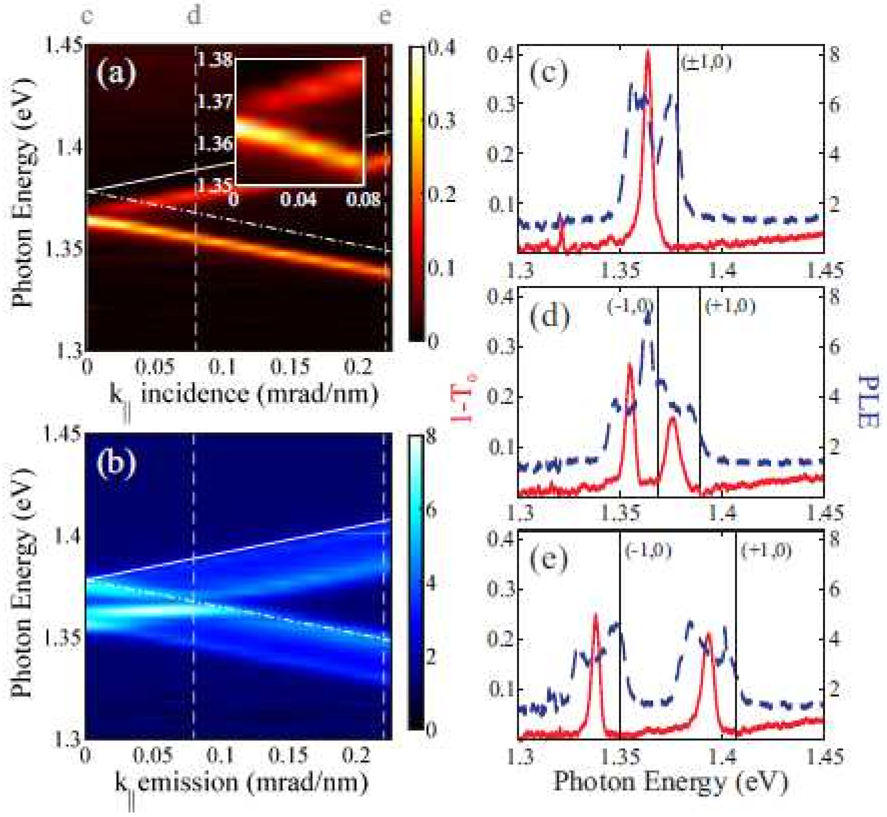

Figure 7.2: Experimental dispersion relations in (a) Extinction, and (b) PhotoLuminescence Enhancement (PLE), for the nanoantenna array described in the text. The photon energy and wave vector component parallel to the surface refer to the (a) incident and (b) emitted radiation. The solid and dash-dot white lines indicate the (+1, 0) and (-1, 0) RAs, respectively. The inset in (a) shows a magnified view of the low $k_{\|}$ region, where the gap opens. Figures (c)-(e) show the extinction as a solid red line and PLE as a dashed blue line for (c) $k_{\|} = 0$, (d) $k_{\|} = 0.1$ rad/μm, and (e) $k_{\|} = 0.22$ rad/μm; the latter two cases are indicated by the dashed lines in (a) and (b). The PLE in (d) shows a peak at an energy for which the extinction is minimized.

An effective refractive index of $n = 1.50$ is used due to the underlying substrate and the QD-layer superstrate to calculate the Rayleigh anomalies. The two peaks in extinction following the dispersion of the RAs on the low energy side correspond to the excitation of the surface lattice resonances[25–31]. The mutual coupling of the SLRs leads to the opening of a frequency gap in their dispersion relation (*anti-crossing*). The inset in Fig. 7.2a displays an enlarged view of this gap. Notice that the dispersion of the bright (-1,0) SLR flattens and the extinction increases near the anti-crossing, which occurs near normal incidence. This indicates the formation of standing waves with an enhanced density of optical states at the band edge. A narrowing linewidth and diminishing extinction are observed for the (+1,0) SLR, which are clear signitures of subradiant damping[32;33].

7.2.3 Measurement of the photoluminescence enhancement

The measurement of the variable angle photoluminescence enhancement (PLE) is done by exciting the sample with a 514 nm line of an Ar/Kr laser at a fixed angle (9°) of incidence, and the and the s-polarized emission is collected as a function of θ_{em}, the angle of the detector with respect to the normal. The PLE is shown as a function of the emitted photon energy and wave vector component parallel to the long axis of the antennas, $\mathbf{k}_{||} = k_0 sin(\theta_{em})\mathbf{e}_x$. Figure 7.2b illustrates the PLE, given by $\frac{I_{in}}{I_{out}}$, with I_{in} and I_{out} the emission from the QD-layer inside and outside the nanoantenna array, respectively. The PLE displays features approximately in line with those in extinction (although broader). Although this similarity, a detailed inspection reveals a non-resemblance between the PLE and the extinction for some values of $k_{||}$. In Figs. 7.2c-e we plot the spectra at the values of $k_{||}$ indicated by the dashed lines in Figs. 7.2a and 7.2b, with the extinction as solid red lines and the PLE as dashed blue lines, respectively. At $k_{||} = 0$ (Fig. 7.2c), a single peak in extinction associated with the bright (-1,0) SLR arises at 1.363 eV. The PLE displays two peaks with a $\approx$ 6-fold enhancement: one at 1.36 eV corresponding to the bright (-1,0) SLR, and another at 1.375 eV corresponding to the dark (+1,0) SLR. We attribute the enhancement of the QD emission by the (+1,0) SLR, which is dark in the FF, to the local nature of the excitation. As it was shown in a recent work[32], the dark and bright character of SLRs has its origin in the symmetry of the modes. However due to their small size (3 nm) as compared the array dimensions, the QD emitters are sensitive to the local field rather than the global symmetry of the array, which allows for their interaction with dark modes[1]. Figure 7.2d shows the spectra at $k_{||} = 0.08\,\text{rad}/\mu\text{m}$, where the extinction displays peaks at 1.376 eV and 1.354 eV corresponding to the (+1,0) and (-1,0) SLRs, respectively. The PLE also shows two broad features centered at approximately the same energies, but more striking is the narrow (60 meV full width at half maximum) feature at 1.364 eV leading to a $\approx$ 7-fold enhancement of the QD emission. Notice that at the same energy the FF extinction is very low. It is remarkable that at an energy and in-plane momentum for which the nanoantennas scatter minimally when probed from the FF there is an emission enhancement that is superior to the one observed for the bright mode at $k_{||} = 0$. The physics behind this NF resonance at a FF anti-resonance is the focus in the next section. For comparison, we show in Fig. 7.2e the measurements at $k_{||} = 0.22\,\text{rad}/\mu\text{m}$, where two broad features in the PLE are observed near the energies of the (-1,0) and (+1,0) SLRs in extinction, as previous work has shown[29].

7.3 Simulations of the near field enhancement in plasmon arrays

7.3.1 Simulation domain

In order to understand the conditions leading to a NF resonance at a FF anti-resonance, we simulate an array of nanorods with dimensions 250 $\times$ 110 $\times$ 40 nm^3 using in-house developed FDTD model. The computational domain consists of a unit cell with Bloch-Floquet boundary conditions on the sides and perfectly matched layers on the top and bottom. The incident light wave is polarized along the short axis of the nanorods and propagates from the top to downwards within computional domain. The arrays of gold nanorods we examine are in a rectangular lattice with constants $a_x = 600\,\text{nm}$ and $a_y = 300\,\text{nm}$. A homogeneous medium of refractive index $n = 1.46$ (silica) surrounds the nanorods. The dielectric function of gold is taken from Palik[34], and fitted in the spectral range of interest with a Drude model:

$$\varepsilon(\omega) = \varepsilon_\infty - \frac{\omega_p^2}{\omega^2 + i\frac{\omega}{\omega_c}} \tag{7.1}$$

with $\varepsilon_\infty = 2.13$, $\omega_p = 1.13\,10^{16}$ rad/s and $\omega_c = 1.38\,10^{16}$ rad/s. The transmittance, T, is calculated by integrating the vertical time-averaged Poynting vector on a plane below the array and normalizing this to that of the incident field. The scattered reflected energy is obtained by an integration on a plane above the nanorods using the scattered field only (by subtracting the incident field). To compare the PLE with model predictions we investigate the NF strength and compute the near-field intensity enhancement (NFIE) $\frac{|E|^2}{|E_0|^2} = \frac{I}{I_0}$, with E the total electric field and E_0 the incident field, both at a plane intersecting the nanorods at their mid-height.

7.3.2 Simulation of the near field intensity enhancement

Figure 7.3 illustrates the FF and NF spectra. Fig. 7.3a,b,d,e show in color the transmittance, reflectance, NFIE and 1-R_0-T_0, respectively as a function of the incident photon energy and $k_\parallel$. The (+1,0) and (-1,0) Rayleigh anomalies are indicated by the magenta solid and dash-dot lines, respectively. The two dips (peaks) in T_0 (R_0) are redshifted with respect to the RAs and following their dispersion the surface lattice resonances. The SLR associated with the (-1,0) order is bright, as its dispersion flattens and its extinction increases near normal incidence. In contrast, a narrowing linewidth and diminishing extinction – fingerprint of subradiant damping – are observed for the (+1,0) SLR as $k_\parallel$ decreases and the mode becomes dark at normal incidence[32]. The mutual coupling of bright and dark SLRs leads to an anti-crossing in their dispersion relation at $k_\parallel = 0$, *i.e.*, a frequency gap opens[32]. This anti-crossing leads to a small gap near 1.37 eV in Figs. 7.3a and 7.3b. Much larger gaps were reported for identical lattices with different nanorod sizes by Rodriguez et al.[32].

The NFIE features in Fig. 7.3d are very similar to those observed in R_0 and T_0 in the high $k_{\|}$ regime, but a strong discrepancy arises near $k_{\|} = 0.1$ rad/μm. Figure 1(e) shows 1-R_0-T_0, which for energies below the RAs is exactly the absorptance in the metal. As expected, there is a close correspondence between absorption and NFIE. In Fig. 7.3c we plot cuts of Figs. 7.3a and 7.3b at $k_{\|} = 0.1$ rad/μm, and Fig. 7.3f shows cuts of Figs. 7.3d and 7.3e at the same value of $k_{\|}$, which is indicated by the vertical dashed line in all dispersion diagrams. The dips (peaks) in T_0 (R_0) at 1.355 and 1.385 eV in Fig. 1(c) correspond to SLRs associated with the (-1,0) and (+1,0) diffraction orders, respectively. A FF-induced transparency is observed as a dip (peak) in R_0 (T_0) between the two SLRs. In contrast, Fig. 7.3f displays a single peak in the NFIE and in absorptance at the same energy of the FF-induced transparency.

7.3.3 Controlling the near field intensity enhancement

The contrast between the FF and NF spectrum of this nanorod array derives from the interference between the SLRs, and the associated retardation of the scattered field along the nanorod length. These processes are governed by the geometry of the nanorods, and in particular their length L. Figure 7.4 shows T_0 in (a) and NFIE in (b), as a function of L, for arrays with dimensions L nm × 110 nm × 40 nm illuminated by a plane wave with $k_{\|} = 0.8$ rad/μm. The 110 nm width and 40 nm height of these nanorods are identical to those reported in Rodriguez et al.[32], so direct comparison can be made for $L = 450$ nm. The high- and low-energy features correspond to the (+1,0) and (-1,0) SLRs. Their energy and linewidth vary with L due to retardation and radiative damping. Notice that for $L \geq 250$ nm the (+1,0) SLR is bright, whereas the (-1,0) SLR is dark, as reported in Rodriguez et al.[32]. The SLR properties are interchanged for $L \leq 250$ nm, such that flattening of the band occurs for the (-1,0) SLR and subradiant damping onsets for the (+1,0) SLR,

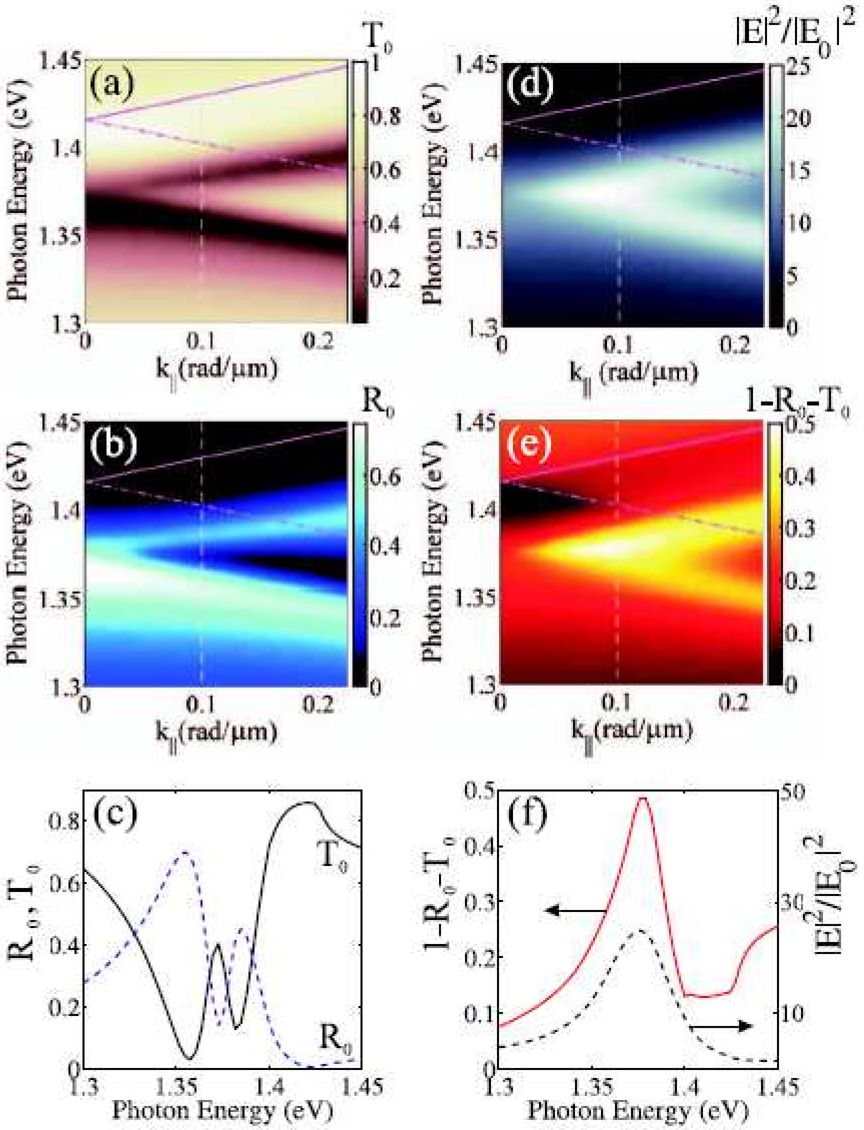

Figure 7.3: Zeroth-order (a) transmittance T_0, (b) reflectance R_0, and (c) cut-of (a) and (b) at $k_{\|} = 0.1$ rad/μm. (d) 1-R_0-T_0, (e), average NFIE at a plane intersecting the nanorods at their midheight, and (f) cut-of (d) and (e) as solid red line at $k_{\|} = 0.1$ rad/μm. In (a), (b), (d), and (e), $k_{\|} = 0.1$ rad/μm is indicated by the vertical dashed lines; the solid and dash/dot lines indicate the (+1, 0) and (-1, 0) RAs. The nanorods have dimensions of 250 nm × 110 nm × 40 nm.

as observed in Fig. 7.3. Particularly interesting is the regime 230 nm $\leq L \leq$ 270 nm, where T_0 displays an anti-crossing characteristic of coupled modes, but the NFIE displays a crossing of the two modes. In this regime the structure has a resonant NF at an FF-induced transparency, as discussed for Fig. 7.3.

7.3.4 Field profile at the anti-crossing condition

The field profile at the photon energy and $k_{\|}$ of the NF resonance at the FF-induced transparency is shown in Fig. 7.5. Figure 7.5a shows the total electric field enhancement $\frac{|E|^2}{|E_0|^2}$ in color and the scattered field as arrows. The four hot-spots near the corners of the nanorods and the scattered field show the quadrupolar character of the mode. The inclined incidence breaks the symmetry of the mode, which manifests as a stronger field enhancement on the right side of each nanorod. This broken symmetry leads to a nonvanishing dipole moment, which allows the excitation of this mode and a finite extinction. Figure 7.5b shows the differences in phase between the scattered and incident fields, i.e., $\phi_{sca} - \phi_{inc}$. Two values, which are $(-0.6 \pm 0.15)\pi$ (light blue) and $(0.5 \pm 0.15)\pi$ (dark blue), prevail throughout space. Their difference, 1.1π, is close to the out-of-phase condition of π, thus resulting in a suppression of scattering. The phase distribution in Fig. 7.5b corresponds to the formation of a standing wave. The interference of two counter-propagating surface polaritons creates the standing wave.

In view of this, we observe a clear qualitative agreement between the extinction and the NFIE by using QDs as local field sensors. Altough, it is not entirely clear to us why the extinction is significantly lower in the experiments than in the simulations. Nevertheless, the above results show the potential for hybrid plasmonic/photonic applications.

7.4 Conclusion

A periodic array of plasmonic nanorods was shown to exhibit a resonant NF and FF-induced transparency at the same photon energy and

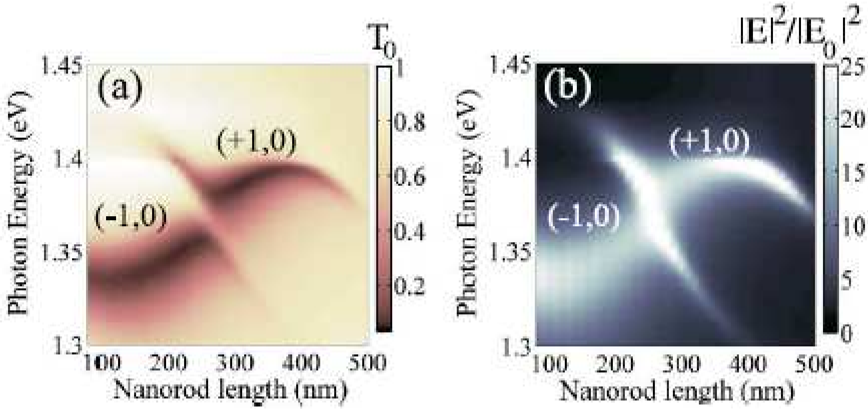

Figure 7.4: (a) Zeroth-order transmittance T_0 and (b) NFIE at a plane intersecting the nanorods at their mid-height. Arrays of nanorods with width = 110 nm, height = 40 nm, and variable length, are illuminated by a plane wave with $k_{parallel} = 0.8\,\text{rad}/\mu\text{m}$. The labels near the SLRs indicate the associated diffraction order.

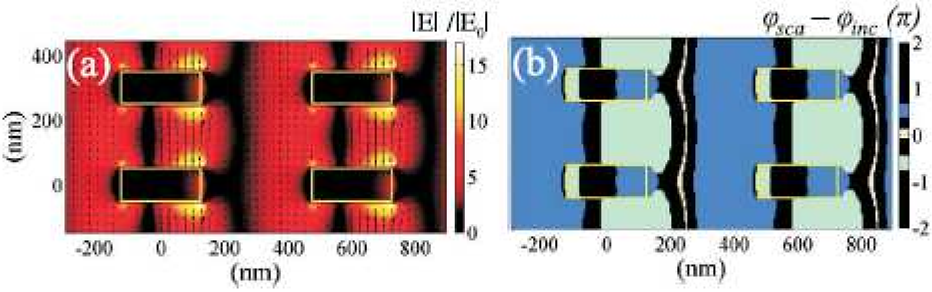

Figure 7.5: (a) Field enhancement (in color scale) and real part of the scattered field at an arbitrary phase (arrows) and (b) phase difference between the scattered and incident field in units of π. Both (a) and (b) are calculated at a plane intersecting the nanorods (delimited by the yellow lines) at their mid-height. The incident photon energy and in-plane wave vector correspond to the NF resonance at the FF-induced transparency.

in-plane momentum. We envisage this counterintuitive behavior to enable many of the key functionalities (e.g., enhanced light emission and sensing) pursued by plasmonic EIT analogs, but with the benefit of a collective resonance at the expense of tight field localization. Additionally, this behavior is being experimentally proven using QDs as local field sensors.

Bibliography

[1] Stockman, M. I.; Faleev, S. V.; Bergman, D. J. Localization versus delocalization of surface plasmons in nanosystems: Can one state have both characteristics? *Physical Review Letters* **2001**, *87*, 167401.

[2] Bergman, D. J.; Stockman, M. I. Surface plasmon amplification by stimulated emission of radiation: Quantum generation of coherent surface plasmons in nanosystems. *Physical Review Letters* **2003**, *90*,.

[3] Li, K. R.; Stockman, M. I.; Bergman, D. J. Enhanced second harmonic generation in a self-similar chain of metal nanospheres. *Physical Review B* **2005**, *72*, year.

[4] Liu, M.; Lee, T.-W.; Gray, S. K.; Guyot-Sionnest, P.; Pelton, M. Excitation of Dark Plasmons in Metal Nanoparticles by a Localized Emitter. *Physical Review Letters* **2009**, *102*,.

[5] Zhang, S.; Genov, D. A.; Wang, Y.; Liu, M.; Zhang, X. Plasmon-induced transparency in metamaterials. *Physical Review Letters* **2008**, *101*,.

[6] Yannopapas, V.; Paspalakis, E.; Vitanov, N. V. Electromagnetically induced transparency and slow light in an array of metallic nanoparticles. *Physical Review B* **2009**, *80*, year.

[7] Liu, N.; Langguth, L.; Weiss, T.; Kaestel, J.; Fleischhauer, M.; Pfau, T.; Giessen, H. Plasmonic analogue of electromagnetically

induced transparency at the Drude damping limit. *Nature Materials* **2009**, *8*, 758–762.

[8] Alu, A.; Engheta, N. Cloaking a Sensor. *Physical Review Letters* **2009**, *102*,.

[9] Alu, A.; Engheta, N. Cloaking a Sensor. *Metamaterials* **2010**, *4*,.

[10] de Abajo, F. Seeing without being seen. *Physics* **2009**, *2*,.

[11] Raether, H. Surface-plasmons on smooth and rough surfaces and on gratings. *Springer Tracts in Modern Physics* **1988**, *111*, 1–133.

[12] Ebbesen, T. W.; Lezec, H. J.; Ghaemi, H. F.; Thio, T.; Wolff, P. A. Extraordinary optical transmission through sub-wavelength hole arrays. *Nature* **1998**, *391*, 667–669.

[13] Janssen, O. T. A.; Urbach, H. P.; t Hooft, G. W. On the phase of plasmons excited by slits in a metal film. *Optics Express* **2006**, *14*, 11823–11832.

[14] Tassin, P.; Zhang, L.; Koschny, T.; Economou, E. N.; Soukoulis, C. M. Low-Loss Metamaterials Based on Classical Electromagnetically Induced Transparency. *Physical Review Letters* **2009**, *102*,.

[15] Rodriguez, S. R. K.; Schaafsma, M. C.; Berrier, A.; Rivas, J. G. Collective resonances in plasmonic crystals: Size matters. *Physica B-Condensed Matter* **2012**, *407*, 4081–4085.

[16] Rodriguez, S. R. K.; Murai, S.; Verschuuren, M. A.; Rivas, J. G. Light-Emitting Waveguide-Plasmon Polaritons. *Physical Review Letters* **2012**, *109*,.

[17] Hao, F.; Sonnefraud, Y.; Van Dorpe, P.; Maier, S. A.; Halas, N. J.; Nordlander, P. Symmetry Breaking in Plasmonic Nanocavities: Subradiant LSPR Sensing and a Tunable Fano Resonance. *Nano Letters* **2008**, *8*, 3983–3988.

[18] Neubrech, F.; Pucci, A.; Cornelius, T. W.; Karim, S.; Garcia-Etxarri, A.; Aizpurua, J. Resonant Plasmonic and Vibrational Coupling in a Tailored Nanoantenna for Infrared Detection. *Physical Review Letters* **2008**, *101*,.

[19] Carron, K. T.; Fluhr, W.; Meier, M.; Wokaun, A.; Lehmann, H. W. Resonances of two-diminensional particle gratings in surface-enhanced Raman-scattering. *Journal of the Optical Society of America B-Optical Physics* **1986**, *3*, 430–440.

[20] Bharadwaj, P.; Deutsch, B.; Novotny, L. Optical Antennas. *Advances in Optics and Photonics* **2009**, *1*, 438–483.

[21] Shchegrov, A. V.; Joulain, K.; Carminati, R.; Greffet, J. J. Near-field spectral effects due to electromagnetic surface excitations. *Physical Review Letters* **2000**, *85*, 1548–1551.

[22] Bryant, G. W.; De Abajo, F. J. G.; Aizpurua, J. Mapping the plasmon resonances of metallic nanoantennas. *Nano Letters* **2008**, *8*, 631–636.

[23] Ross, B. M.; Lee, L. P. Comparison of near- and far-field measures for plasmon resonance of metallic nanoparticles. *Optics Letters* **2009**, *34*, 896–898.

[24] Gallinet, B.; Martin, O. J. F. Relation between near-field and far-field properties of plasmonic Fano resonances. *Optics Express* **2011**, *19*, 22167–22175.

[25] Zou, S. L.; Schatz, G. C. Narrow plasmonic/photonic extinction and scattering line shapes for one and two dimensional silver nanoparticle arrays. *Journal of Chemical Physics* **2004**, *121*, 12606–12612.

[26] Kravets, V. G.; Schedin, F.; Grigorenko, A. N. Extremely narrow plasmon resonances based on diffraction coupling of localized plasmons in arrays of metallic nanoparticles. *Physical Review Letters* **2008**, *101*,.

[27] Auguie, B.; Barnes, W. L. Collective resonances in gold nanoparticle arrays. *Physical Review Letters* **2008**, *101*,.

[28] Chu, Y.; Schonbrun, E.; Yang, T.; Crozier, K. B. Experimental observation of narrow surface plasmon resonances in gold nanoparticle arrays. *Applied Physics Letters* **2008**, *93*,.

[29] Vecchi, G.; Giannini, V.; Rivas, J. G. Shaping the Fluorescent Emission by Lattice Resonances in Plasmonic Crystals of Nanoantennas. *Physical Review Letters* **2009**, *102*,.

[30] Vecchi, G.; Giannini, V.; Rivas, J. G. Surface modes in plasmonic crystals induced by diffractive coupling of nanoantennas. *Physical Review B* **2009**, *80*,.

[31] Giannini, V.; Vecchi, G.; Rivas, J. G. Lighting Up Multipolar Surface Plasmon Polaritons by Collective Resonances in Arrays of Nanoantennas. *Physical Review Letters* **2010**, *105*,.

[32] Rodriguez, S. R. K.; Abass, A.; Maes, B.; Janssen, O. T. A.; Vecchi, G.; Rivas, J. G. Coupling Bright and Dark Plasmonic Lattice Resonances. *Physical Review X* **2011**, *1*,.

[33] Ropers, C.; Park, D. J.; Stibenz, G.; Steinmeyer, G.; Kim, J.; Kim, D. S.; Lienau, C. Femtosecond light transmission and subradiant damping in plasmonic crystals. *Physical Review Letters* **2005**, *94*,.

[34] Palik, E. *Handbook of Optical Constants of Solids*; Academic, 1985.

8

General conclusion

8.1 Conclusion

In this work we have aimed to surpass some of the milestones on the way of progressing the field of colloidal quantum dots and their integration in a photonic platform. Throughout the thesis we have tackled various challenging topics. In this chapter we will summarize the main results, discuss the important links between them and highlight the prospects for future research and applications.

8.1.1 Synthesis

We have succesfully synthesized CdTe QDs with sizes varying from 3 to 11 nm using the hot injection method. The bandgap is tunable between 500 nm and 760 nm, or 1.6-2.48 eV. This bangap energy corresponds to twice the photon energy of the range used in telecom applications, *i.e*, 1300 nm-1600 nm. The large quantum dot sizes were obtained by introducing a continuous multiple injection method, whereby precursors are continuously injected at a controlled reaction time, avoiding Ostwald ripening. We determine the crystal structure with XRD and show that the CdTe QDs have a zincblende crystal structure with the same lattice parameter as their respective bulk material. Due to quantum confinement, the particle size determines the bandgap of the QD material. By combining UV-vis-absorption spectroscopy and transmission electron microscopy imaging, we correlate both the size and the bandgap and construct a sizing curve for the CdTe QDs. In this way, size and size dispersion can be calculated from the spectral position of the first absorption peak determined by measuring the absorbance of the nanocrystal suspension. The CdTe synthesis yields nearly stable particles with a 1-6 nm blue shift of the absorption peak in 20 days, corresponding to a particle size reduction of 1.5-1.8 Å. Further optimzation of the surface chemistry might avoid this small particle size reduction. Additionally we have synthesized PbS QDs for use in the NIR-midIR wavelength region. By controlling the growth temperature of the PbS nanocrystals from 60 to 180°C, nanocrystal sizes from 2.5-7.5 nm are obtained with absorption peaks in the wavelength range 800-2000 nm.

8.1.2 Linear optical properties

An important quantity in a nanocrystal suspension is the particle concentration. It can be determined from the absorbance spectrum if we know the molar extinction - or the intrinsic absorption coefficient. In this part we have analyzed the (linear) optical properties of the synthesized CdTe QDs in the previous part and focused more specifically on the absorption coefficient of CdTe QDs. We determine the atomic concentrations (ICP-MS), cation-anion atomic ratios (RBS), lattice parameter, particle size and the absorbance spectrum of the QDs (UV-vis absorption spectroscopy) and calculate the intrinsic absorption coefficient. At a short wavelength of 410 nm the intrinsic absorption coefficient does not show quantum confinement effects and the obtained values are in good agreement with the bulk value of the CdTe material. The average of these values can be used as a reliable standard for the concentration determination of CdTe nanocrystals. Around the bandgap transition we find integrated absorption coefficients that scale inversely proportionally with the QD volume. Most importantly, these data show a deviation up to a factor of 3 compared to the values widely used in literature. Futhermore, we studied a new class of QDs in the visible wavelength range, CdSe/CdS core/shell and CdSe/ CdSe$_x$S$_{1-x}$/CdS core/alloy/shell QDs. We determine the intrinsic absorption coefficient of these multishell QDs. Based on Maxwell-Garnett theory and an alloying model considering the diffusion of the Se and S atoms respectively at the inner and outer CdSe and CdS shell we show that intrinsic aborption coefficients of CdSe/CdS core/shell QDs can be employed for CdSe/ CdSe$_x$S$_{1-x}$/CdS core/alloy/shell QDs within a 5% error of calculation. In view of this results, the inroduced model is valuable for ongoing research in multishell and alloyed QD systems. Moreover, we show that the absorption coefficient is still correlated with the local field factor as defined for core systems.

8.1.3 Nonlinear optical properties

Having explored the linear optical properties of the colloidal QDs in the previous part, we study (high optical power) nonlinear properties of colloidal PbS QD suspensions as a function of wavelength, optical intensity and QD volume fraction using the Z-scan technique with picosecond pulses. Knowing the characteristic temperature profile buildup time t_c, we modulate the laser repetition rate and exclude thermal lensing to directly measure the electronic contribution to the nonlinear refractive index n_2. The nonlinear refractive index is independent from the intensity and follows the QD absorption spectrum. Figure of merits larger than one are obtained for the PbS QDs and are larger compared with crystalline silicon (0.37). By introducing a rate equation model, the amount of excitons in the QDs is calculated. The creation of excitons and the resulting photoinduced absorption in the PbS QDs lies at the origin of the observed n_2 and the nonlinear absorption coefficient β. Using transient Four Wave Mixing (FWM) with 150 fs pulses we prove that at low excitation intensities the dynamics is dominated by single exciton thermalization (ns) and recombination (μs). At higher intensities the FWM signal results in a 100 ps response. This shows that colloidal PbS QDs are efficient and fast nonlinear materials.

8.1.4 Light absorption in hybrid/SOI waveguides

In this chapter, we have analyzed the absorption coefficient of SOI planarized waveguides (PWGs) coated with close-packed mono- and multilayers of PbS/CdS QDs. We retrieve the fingerprint of the QDs in the waveguide absorbance and find that the absorbance per QD increases with the number of QD layers. The experimental data are compared with simulation results, where the QD multi-layers are described as an effective medium in which the optical properties depend on dipolar coupling between neighboring QDs. Close agreement between the experimental values and the simulation results is obtained using the dielectric constant ε_h of the QD host material as the only adjustable parameter. We find that the increased absorbance in thicker layers makes that a higher value of ε_h is needed to match the simulated and the experimental data. We interpret this as a transition from a regime where the field lines coupling the QDs mainly pass through the surroundings (monolayer case) to a situation where these field lines are mainly confined within the QD stack (thicker multilayers). In addition we determine the waveguide absorbance of silicon-on-insulator strip waveguides (SWGs) coated with a monolayer of PbS/CdS core/shell QDs. Using the host permittivity deduced from the study in the PWGs we obtain values for the losses which are in quantitative agreement with the experimental results. This allows to engineer the interaction of colloidal QDs with strip waveguides. Based on SEM imaging and the simulated QD absorption coefficient we show that the morphology of the deposited layer directly affects the waveguide absorbance. Using 3D FDTD simulations we show that the QD-emission can be excluded from the measured waveguide absorbance in the SWGs and the PWGs.

8.2 Prospects

In chapters 6-7 we demonstrate the use of colloidal QDs as wavelength convertor and as a local field sensor.
We perform simulations for wavelength conversion based on colloidal PbS/CdS QDs integrated on silicon on insulator waveguides. We introduce a figure of merit FOM as a measure of the conversion capability. At a slow microsecond timescale FOM values of 0.9 are obtained, while at faster picosecond time scale FOM values up to 25 are achieved. At this timescale, we demonstrate the use of the QDs as 10-20 GHz bandwidth wavelength convertor for different telecom bands : O-band (1274-1346 nm), C-band (1530-1565 nm) and L-band (1565-1625 nm). By appropriately tuning the bandgap of the QDs, the wavelength conversion can be perfomed either within different telecom bands or from a short - to a longer wavelength band, *e.g.* from the O- to the L-band. In the former case, the bandgap of the QDs requires to match the wavelength region of the needed band and the conversion is done by involving the interband absorption transition of the QDs first 1S-1S energy level. While, in the latter case the bandgap of the QDs needs to be tuned around the wavelength region of the short band and the conversion is performed involving the intraband aborption transitions from the QDs valence and conduction bands.

Furhermore, we demonstrate the employment of PbS/CdS QDs as local field sensors in plasmonic arrays. The high quality factor (Q≈1000) in this arrays enables an efficient interaction with the QD-layer. The plasmonic arrays support surface lattice resonances which interacts with the optical field in a different way in the near field (NF) and the far field (FF), respectively. The NF can be seen as the local field of the plasmonic arrays, while the FF is typically the observed field upon transmission through these arrays. Due to the combination of the small sizes of the QDs as compared to the dimension of the arrays (≈ 100 nm) and their highly luminescent emission properties, the QDs are suitable to be excited with the NF, where they emit photons detectable in the FF. This renders the QDs as efficient local field sensors of the NF for the far field.

Finally, we have shown that the used colloidal QDs posess many new functionalities, they are efficient and fast nonlinear materials and the optical properties on chip can be quantitatively determined enabling simulation supported device modeling and optimization (*e.g.* QD based lasers and solar cells). In combination with the facile integration with photonic devices using wet deposition techniques and the easy tuning of the QD linear and nonlinear properties this opens pathways for a bright future with novel applications in (and beyond) the field of photonics.

List of Publications

International Publications, Proceedings and Awards

[1] Omari, A.; Xie, W.; Geiregat, P.; Van Thourhout, D.; Hens, Z. Modeling the Optical Properties of Low-Cost Colloidal Quantum Dot Functionalized Strip SOI Waveguides. *IEEE Journal of Selected Topics in Quantum Electronics* **2014**, *20*, 1–6.

[18] Omari, A.; Geiregat, P.; Van Thourhout, D.; Hens, Z. Light absorption in hybrid silicon-on-insulator/quantum dot waveguides. *Optics Express* **2013**, *21*, 23272–23285.

[3] Rodriguez, S. R. K.; Janssen, O. T. A.; Lozano, G.; Omari, A.; Hens, Z.; Rivas, J. G. Near-field resonance at far-field-induced transparency in diffractive arrays of plasmonic nanorods. *Optics Letters* **2013**, *38*, 1238–1240.

[4] Omari, A.; Moreels, I.; Masia, F.; Langbein, W.; Borri, P.; Van Thourhout, D.; Kockaert, P.; Hens, Z. Role of interband and photoinduced absorption in the nonlinear refraction and absorption of resonantly excited PbS quantum dots around 1550 nm. *Physical Review B* **2012**, *85*,.

[5] Kamal, J. S.; Omari, A.; Van Hoecke, K.; Zhao, Q.; Vantomme, A.; Vanhaecke, F.; Capek, R. K.; Hens, Z. Size-Dependent Optical Properties of Zinc Blende Cadmium Telluride Quantum Dots. *Journal of Physical Chemistry C* **2012**, *116*, 5049–5054.

[6] Hens, Z.; Omari, A.; Geiregat, P.; Van Thourhout, D. Optical properties of SOI waveguides functionalized with close-packed quan-

tum dot films. *15th International Conference on Transparent Optical Networks, Proceedings*, Cartagena, Spain, 2013; pp 1–4.

[7] Geiregat, P.; Omari, A.; Justo Zarraquiños, Y.; Van Thourhout, D.; Hens, Z. Absorption enhancement in 2D nanocrystal superlattices through near-field dipolar coupling: a novel optical phenomenon at the nanoscale. *Laser Science to Photonics Applications, Abstracts,CLEO*, San Jose, California United States, 2013.

[8] Omari, A.; Geiregat, P.; Van Thourhout, D.; Hens, Z. Assessing colloidal quantum dot optical properties through free standing layers on photonic waveguides. *European Material and Research Society Conference*, Strasbourgh, France, 2013.

[9] Omari, A.; Geiregat, P.; Van Thourhout, D.; Hens, Z. Modelling colloidal quantum dots on SOI photonic waveguides. *European Material and Research Society Conference*, Strasbourgh, France, 2013.

[10] Omari, A.; Geiregat, P.; Van Thourhout, D.; Hens, Z. Probing the optical constants at the nanoscale of colloidal prepared films through optical waveguides. *NWO Scientific meeting on Chemistry related to Physics and Material Sciences*, Veldhoven, Netherlands, 2013.

[11] Omari, A.; Shinchi, H.; Geiregat, P.; Van Thourhout, D.; Hens, Z. Characterisation of PbS/CdS Qdot absorption on SOI waveguides. *Poceedings Symposium IEEE Photonics Society Benelux*, Mons, Belgium, 2012; pp 295–298.

[12] Rodriguez, S. R. K.; Janssen, O. T. A.; Lozano, G.; Omari, A.; Hens, Z.; Rivas, J. G. Near Field Resonance at Far Field Antiresonance: Plasmonically Enhanced Light Emission with Minimum Scattering Nanoantennas. *Gordon Research Conference*, Waterville, Maine, United States, 2012.

[13] Omari, A.; Moreels, I.; Masia, F.; Langbein, W.; Borri, P.; Van Thourhout, D.; Kockaert, P.; Hens, Z. Nonlinear optical prop-

erties due to inter and intraband transitions in PbS quantum dots. *7th International Conference on Quantum Dots*, Santa Fe, United States, 2012.

[14] Rodriguez, S. R. K.; Janssen, O. T. A.; Lozano, G.; Omari, A.; Hens, Z.; Rivas, J. G. Diffractively Induced Transparency: Near Field Resonance at Far Field Anti-resonance. *Materials Research Society, Spring Meeting*, San Francisco, United States, 2012.

[15] Omari, A.; Moreels, I.; Masia, F.; Langbein, W.; Borri, P.; Van Thourhout, D.; Kockaert, P.; Hens, Z. Nonlinear Optical properties of PbS quantum dots. *European Material and Research Society Conference*, Nice, France, 2011.

[16] Omari, A.; Moreels, I.; Van Thourhout, D.; Kockaert, P.; Hens, Z. Nonlinear optical characterization of PbS nanocrystals. *NWO Scientific meeting on Chemistry related to Physics and Material Sciences*, Veldhoven, Netherlands, 2011.

[17] Omari, A. Optical nonlinearities of PbS quantum dots. *Ph.D. Engineering Symposium*, Ghent, Belgium, 2010.

[18] Omari, A. Award for the quality of the latest research in semiconductor nanostructures and their applications to electronic, optoelectronic and photonic devices. *Rewarded at the 30th anniversary of the European Research and Material Science Conference*, Strasbourg, France, 2013.

A

Molar extinction coefficient of core/shell nanocrystal suspensions

In this appendix we will explain the relation between the molar extinction coefficient ϵ and the absorption coefficient μ (see Chapter 3) of colloidal nanocrystal suspensions. We start from the absorbance A in a cuvette which is defined as :

$$A = -\log(\mathrm{T}) \tag{A.1}$$

and on the other hand μ is given by :

$$\mu = \frac{-\ln(\mathrm{T})}{\mathrm{L}} \tag{A.2}$$

with T the transmission through a cuvette of a length L. The intrinsic absorption coefficient μ_{int} is related to μ as :

$$\mu = \mu_{int}\, f \tag{A.3}$$

with f the volume fraction that the nanocrystals occupy in the suspension (or more general in the composite), which can be explicitly related to the quantum dot diameter d_{QD} and the nanocrystal concentration c in the suspension :

$$f = \frac{\pi\, d_{QD}^3}{6}\, N_A\, c \tag{A.4}$$

Here, N_A is Avogadro's constant. In a solution, the absorbance A at a given wavelength is linked to ϵ and the concentration through the Lambert-Beer's law:

$$A = \epsilon\, c\, L \tag{A.5}$$

After some basic algebra using Eq. A.1-Eq. A.5, we obtain an expression relating the molar extinction coefficient through Lamber-Beer's law :

$$\epsilon = \left[\mu_{int}\, \frac{\pi}{6}\, N_A\, ln(10)\right]\, d_{QD}^3 \tag{A.6}$$

It is clear from this equation that this has the form :

$$\epsilon = \mathrm{A_p}\, d^3 \tag{A.7}$$

with $\mathrm{A_p}$ a prefactor. Equation A.6 generally holds for any type of nanocrystal (core, core/shell, ..), but as μ_{int} depends on the shell volume to the total volume ratio p for core/shell nanocrystals as shown in literature[1], we added a p subscript to the prefactor in Eq. A.7 to denote that the prefactor is related to p. In the aforementioned literature report, experimental data is provided for μ_{int} for PbS/CdS QDs dispersed in a tetrachloroethylene (TCE) liquid (see Fig. A.1a). This data allows us to determine $\mathrm{A_p}$ using equations A.6-A.7. The calculated results are shown in Fig. A.1b. By fitting the points using a third order polynomial we obtain an explicit relation for the prefactor as a function of p:

$$\mathrm{A_p} = 0.02392 + 3.2599\, 10^{-3}\, p - 1.6414\, 10^{-3}\, p^2 - 1.2092\, 10^{-2}\, p^3 \tag{A.8}$$

---

[1] Y. Justo et al., Optical properties of PbS/CdS quantum dots., *Journal of Physical Chemistry C*, **2013**, 117, p 20171

This is the relationship that is reported in Chapter 2, sec. 2.4.4.
The μ_{int} values in Fig. A.1 were shown to be reliable in the reported literature (see the procedure outlined in Chapter 3) and consequently the obtained prefactor A_p can be used reliably to determine the molar extinction coefficient of PbS/CdS nanocrystal suspensions.

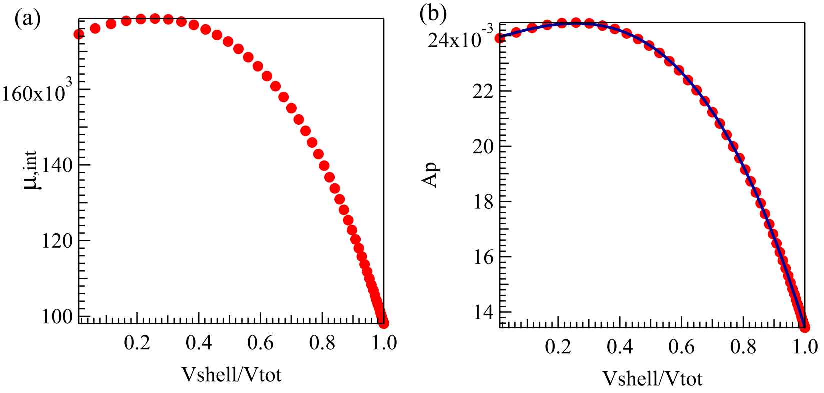

Figure A.1: (a) Intrinsic absorption coefficient μ_{int} of PbS/CdS QDs dispersed in a tetrachloroethylene liquid. (b) Calculation of $\mathrm{A_p}$ based on Eq. A.6 and the data in (a) for μ_{int}. The points are fitted are to a third order polynomial yielding expression A.8 for the prefactor as a function of the shell to the total volume ratio $p = \frac{V_{shell}}{V_{tot}}$.